



University of Cambridge
Department of Applied Mathematics
and Theoretical Physics

The effects of stochastic forces on the evolution of planetary systems and Saturn's rings

Hanno Rein

This dissertation is submitted for the degree of Doctor of Philosophy.

June 14, 2010



St John's College
Cambridge



Abstract

The increasing number of discovered extra-solar planets opens a new opportunity for studies of the formation of planetary systems. Their diversity keeps challenging the long-standing theories which were based on data primarily from our own solar system. Resonant planetary systems are of particular interest because their dynamical configuration provides constraints on the otherwise unobservable formation and migration phase.

In this thesis, formation scenarios for the planetary systems HD128311 and HD45364 are presented. N-body simulations of two planets and two dimensional hydrodynamical simulations of proto-planetary discs are used to realistically model the convergent migration phase and the capture into resonance. The results indicate that the proto-planetary disc initially has a larger surface density than previously thought.

Proto-planets are exposed to stochastic forces, generated by density fluctuations in a turbulent disc. A generic model of both a single planet, and two planets in mean motion resonance, being stochastically forced is presented and applied to the system GJ876. It turns out that GJ876 is stable for reasonable strengths of the stochastic forces, but systems with lighter planets can get disrupted. Even if a resonance is not completely disrupted, stochastic forces create characteristic, observable libration patterns.

As a further application, the stochastic migration of small bodies in Saturn's rings is studied. Analytic predictions of collisional and gravitational interactions of a moonlet with ring particles are compared to realistic three dimensional collisional N-body simulations with up to a million particles. Estimates of both the migration rate and the eccentricity evolution of embedded moonlets are confirmed. The random walk of the moonlet is fast enough to be directly observable by the Cassini spacecraft.

Turbulence in the proto-stellar disc also plays an important role during the early phases of the planet formation process. In the core accretion model, small, metre-sized particles are getting concentrated in pressure maxima and will eventually undergo a rapid gravitational collapse to form a gravitationally bound planetesimal. Due to the large separation of scales, this process is very hard to model numerically. A scaled method is presented, that allows for the correct treatment of self-gravity for a marginally collisional system by taking into account the relevant small scale processes. Interestingly, this system is dynamically very similar to Saturn's rings.

Preface and Acknowledgements

This thesis is the result of my own work and includes nothing which is the outcome of work done in collaboration except where specifically indicated.

The formation scenario presented in chapter 2 was done in collaboration with Professor Wilhelm Kley and has been published as a highlighted article in *Astronomy and Astrophysics* (Rein et al. 2010). The analysis of chapter 3 is based on Rein & Papaloizou (2009). The results of chapter 5 are the outcome of work done in collaboration with Geoffroy Lesur and Zoë Leinhardt. I have contributed more than two thirds to all of these studies. In particular, all simulations and their analysis have been performed by myself. The analytic calculation in appendix C has been made by Professor John Papaloizou.

I would like to thank my supervisor, Professor John Papaloizou, for his time and support during the last three years. I would like to thank Zoë Leinhardt, Geoffroy Lesur, Sijme-Jan Paardekooper, Gordon Ogilvie, Aurélien Crida, James Stone and Adrian Barker for stimulating discussions. For proofreading a draft of this thesis, I would like to thank Min-Kai Lin, Adrian Barker, Katy Richardson, Zoë Leinhardt, Aurélien Crida and Chris Donnelly. I appreciate the help of Professor Wilhelm Kley who provided me with data for various code comparisons.

This work was supported by an Isaac Newton studentship and an STFC studentship (ST/F003803/1). I am grateful for financial support for travel from St John's College Cambridge, the Department of Applied Mathematics and Theoretical Physics, the Institute for Advanced Study in Princeton, AstroSim, the Cambridge Philosophical Society and the Tokyo Institute of Technology. I would also like to thank the Isaac Newton Institute in Cambridge for their support and hospitality during the DDP workshop and associated conferences.

I would like to thank the 800th Anniversary Team for the permission to reprint the drawing of Isaac Newton, copyright Quentin Blake 2009.

Contents

Abstract	v
Preface and Acknowledgements	vii
Contents	viii
1 Introduction	1
1.1 Methods of detecting extra-solar planets	2
1.2 Observed objects	4
1.3 Formation of planets	5
1.4 Evolution of planetary systems	9
1.5 Mean motion resonances	11
2 The dynamical origin of the multi-planetary system HD45364	13
2.1 The planetary system HD45364	14
2.2 N-body simulations	16
2.3 Hydrodynamical simulations	22
2.4 Other scenarios for the origin of HD45364	30
2.5 Comparison with observations	31
2.6 Conclusions	34
3 The survival of mean motion resonances in a turbulent disc	37
3.1 Basic equations	38
3.2 Numerical simulations	51
3.3 Two planets with stochastic forcing	58
3.4 Formation of HD128311	66
3.5 Conclusions	71
4 Stochastic migration of small bodies in Saturn's rings	73
4.1 Basic equations governing the moonlet and ring particles	75
4.2 Effects leading to damping of the eccentricity of the moonlet	77
4.3 Processes leading to the excitation of the eccentricity of the moonlet	81
4.4 Processes leading to a random walk in the semi-major axis of the moonlet	84
4.5 Numerical Simulations	87

4.6	Results	89
4.7	Conclusions	99
5	Planetesimal formation in a turbulent disc	101
5.1	Orders of magnitude	102
5.2	Methods	105
5.3	Numerical simulations	107
5.4	Results	110
5.5	Discussion and implications	118
6	Summary	121
6.1	Main results	121
6.2	Future work	123
	Appendices	127
A	Orbital elements	129
B	Dissipative forces	133
C	Response calculation of particles on horseshoe orbits	137
C.1	Interaction potential	137
C.2	Response calculation	138
C.3	Unperturbed horseshoe motion	139
C.4	Evaluation of the induced epicyclic amplitude	139
C.5	Numerical verification	140
D	N-body simulations with GravTree	143
D.1	Hill's equations	143
D.2	Symplectic integrator	144
D.3	Gravity calculation	146
D.4	Boundary conditions	147
D.5	Collision detection	150
D.6	Optimisations	151
D.7	Tests	152
D.8	Visualisations	155
E	Hydrodynamical simulations with Prometheus	159
E.1	Navier-Stokes equations	159
E.2	Discretisation	162
E.3	Tests	165
E.4	Visualisations	172
	Bibliography	175

Für meine Mutter.

Introduction

And if the fixed Stars are the Centers of other like systems, these, being form'd by the like wise counsel, must be all subject to the dominion of One, [...].

Isaac Newton, General Scholium, translated by Motte, 1729

In 1713 Isaac Newton wrote this sentence in an essay attached to the third edition of his famous *Principia Mathematica*. In other words, he expected to see planets around other stars. Almost three centuries later, astronomers discovered the first planet beyond our own solar system, a so-called exo-planet. The number of known planets has increased rapidly ever since. To date, 461 extra-solar planets have been discovered (Schneider 2010). At least 10% of all nearby solar type stars host planets (Cumming et al. 2008). With this tremendous observational success, it is now the theoreticians' turn to explain the discovered systems. One important aspect is to find out if, and if so why, these systems formed differently compared to the solar system.

In this chapter, first the discoveries of exo-planets in recent years are presented. Then, suggested formation scenarios of planets, planetary systems and their evolution are reviewed.

This thesis discusses stochastic phenomena in a range of astrophysical systems. The analytic model presented in chapter 3 is the key in understanding the effects of stochastic forces and turbulence in those systems. It forms the basis of the physical understanding in many celestial systems in which stochastic forces are present.

A detailed formation scenario of the planetary system HD45364 is presented in chapter 2. In chapter 3 another formation scenario is presented, this time for the planetary system HD128311. Both systems are resonant systems and their dynamical states provide important constraints on their formation history.

HD45364 formed most likely in a massive disc and had a phase of rapid convergent migration. On the other hand, the current observed orbital parameters of the system

HD128311 are consistent with the formation in a strongly turbulent disc.

In chapter 4, these formalism developed in chapter 3 is applied to Saturn's rings and a moonlet. Saturn's rings also exert stochastic forces. The rings, together with embedded moons, resemble a small scale version of the proto-planetary disc.

Finally, the issue of numerical convergence in simulations of planetesimal formation is discussed in section 5. Planetesimals are likely to form in turbulent proto-stellar discs via gravitational instability. It turns out that the system can be simulated consistently only if the relevant small scale processes are included. The dynamical evolution is then very similar to Saturn's rings, except that the final clump is gravitationally bound.

In chapter 6 we summarise the results. The main numerical codes that have been used in chapters 2, 3, 4 and 5 are described in the appendices E and D.

1.1 Methods of detecting extra-solar planets

For thousands of years, the observation of planets was limited to the major planets of our own solar system. Since then, our knowledge of the solar system has been growing constantly and has reached an overwhelming magnitude. However, the fundamental question of whether we inhabit a special place in the universe or not hasn't been answered yet. This is deeply linked to our spiritual desire to know if there are lifeforms on other planets. Luckily, we are living in a time of great technological and scientific progress and it is not unreasonable to assume that those questions can be answered within the next 50 years.

The first steps have already been taken, namely the discovery of planets beyond our own solar system. Various groups around the world have successfully detected exoplanets using different techniques. Each method has both advantages and disadvantages which will be summarised in this section. This is important because the sparse information that we get from these observations determines the predictability of theoretical studies.

Radial velocity measurements. Most planets have been discovered by the radial velocity (RV) method. A periodic Doppler shift in the spectral lines of the host star can be measured with high precision spectroscopy. The Doppler effect occurs because the star is moving around the centre of mass (of both the star and the planet). Only the radial part of this movement is measurable. The period of the oscillation is simply the planet's orbital period. The mass of the star can be calculated by stellar evolution models. If we assume that we observe the system in the plane of the planet's orbit, we can then use Newton's third law $M_{\odot}v_{\odot} = m_p v_p$, where M_{\odot} , m_p , v_{\odot} and v_p are the masses and velocities of the host star and the planet respectively, to calculate the planet's mass.

This method biases the detection of massive planets on short orbits (hot Jupiters) as the gravitational influence of the planet on the star (and therefore the measured v_{\odot}) is bigger in those cases. Note that there is a degeneracy in the inclination i because it is not possible to measure the non-radial part of the velocity. Thus, we can only get a lower limit on the mass of the planet and the mass might actually be larger:

$$m_{p,\text{real}} \geq m_{p,\text{real}} \cdot \sin i = m_p. \quad (1.1)$$

Because of this degeneracy, only a limited number of parameters can be obtained by the RV method. Finding orbital parameters of multiplanetary systems beyond the planet masses and the orbital periods is even more challenging. Each new planet adds 7 degrees of freedom, such that solutions are highly degenerate. Especially the fitting of the eccentricities is very unreliable (see discussion in chapter 2). Furthermore, it is difficult to find precise orbital parameters for very long period planets as it can take many years to sample a full period of the light curve.

The first extra-solar planet discovered by the radial velocity method is 51 Pegasi b (Mayor & Queloz 1995).

Transit light curves. Another method that has been very successful is the transit method. This is mainly due to space based missions such as CoRoT and Kepler. The idea is to find planets by observing variations in the star light caused by transits of planets in front of the host stars. This effect also occurs in our own solar system, known as Mercury and Venus transits. However, transits of extra-solar planets are rare because the host star, the exo-planet and the Earth must be aligned exactly in one line for a transit to occur. The first exo-planet discovered by the transit method is OGLE-TR-56 b (Konacki et al. 2003).

The transit method is capable of measuring the density ρ of exo-planets, a parameter inaccessible to the RV method. It is even possible to do spectroscopy on the atmosphere of the planet during the transit and the secondary transit (when the planet is occulted by the star) to create a temperature map of the exo-planet (Knutson et al. 2007).

Furthermore, the Rossiter-McLaughlin effect allows one to measure the sky projected angle between the orbit and the rotation axis of the host star. To do that, one has to combine transit and RV measurements. A recently submitted paper suggests that a large number of planets might be on retrograde orbits (Triaud et al, in preparation).

Dedicated ground and space based missions promise to detect a large number of planets in the near future. Furthermore, by observing tiny variations in the transit timing (TTV) and transit duration (TDV), it might be possible to find other planets in systems in which only one planet is transiting. Even the possibility to discover exo-moons has been discussed (Kipping et al. 2009).

Gravitational microlensing. Planets can also be discovered by gravitational microlensing. If the star is aligned in one line with the Earth and a bright object in the background (e.g. another star), the light from the background object bends around the star and can be detected by an increase in luminosity. A planet in an orbit around the star disturbs the light curve and theoretical models can determine the planet's mass and some orbital parameters. This event happens only once per star, so good timing and a global collaboration is needed to perform a continuous measurement of the light curve. The orbital parameters cannot be determined with high precision because one only obtains a snapshot of the system without any dynamical evolution. The first exo-planet was discovered by gravitational microlensing in 2004 by Bond et al..

Direct imaging. In 2004 Chauvin et al. reported the first detection of a giant planet candidate by direct imaging. Since then, several planetary systems have been imaged. These are all massive planets, far away from the host star (hundreds of AU). Maybe the most interesting of those planets is Fomalhaut b, which seems to be embedded in a debris disc (Kalas et al. 2008). As all those planets have long orbital periods, it is, similar to the gravitational microlensing method, difficult to determine the precise orbital configuration, especially in multi-planetary systems.

Pulsar timing. Despite the recent success of the detection methods presented above, the first exo-planet was discovered using the pulsar timing method (Wolszczan & Frail 1992) by measuring slight variations in the regular timings from a pulsar. This is sensitive down to very small mass planets. However, pulsars are rare compared to normal stars and the focus has shifted away from the pulsar timing method.

1.2 Observed objects

Extrasolar planets have been observed around a variety of parent stars from pulsars to solar-type stars to M-dwarfs (see e.g. Chauvin et al. 2004; Wolszczan & Frail 1992) indicating that planet formation is common and successful in a broad range of environments. Almost all extra-solar planetary systems are distinct from the solar system.

Many of the detected objects are so-called hot Jupiters. Their size and mass is comparable to Jupiter, but their orbits are very close to their host star (≈ 0.05 AU). Most methods described above bias the detection in favour of these objects.

The existence of hot Jupiters was very surprising because in the solar system all gas giants are located beyond several AU. This still results in difficulties for planet formation theories, although planetary migration is one solution, as described below.

Other observed objects are very heavy and are more likely to be brown dwarfs rather than planets. The International Astronomical Union (IAU) defines an extra-solar planet as follows:

Objects with true masses below the limiting mass for thermonuclear fusion of deuterium (currently calculated to be 13 Jupiter masses for objects of solar metallicity) that orbit stars or stellar remnants are *planets* (no matter how they formed). The minimum mass/size required for an extra-solar object to be considered a planet should be the same as that used in our Solar System. (WGESp 2003)

Thus, many of the massive objects, at separations of hundreds of AU, detected by direct imaging, could actually be brown dwarfs.

In cases where the planet's mean density can be observed, evolutionary models seem to be in broad agreement with observations, although many hot Jupiters have a large surface temperature and are subject to tidal heating. Their atmospheres are not well understood and first studies show a broad range of possible configurations. Observations furthermore suggest that their densities might be rather low (see e.g. Anderson et al. 2010).

The Holy Grail for exo-planet hunters is another Earth-like planet that orbits the host star within the habitable zone. At the present day, the planet that is closest to one Earth mass is Gliese 581 e which has a mass of approximately 2 Earth masses (Mayor et al. 2009).

1.3 Formation of planets

1.3.1 Accretion disc

Stars form out of giant gas clouds that become gravitationally unstable. Because of angular momentum conservation, an accretion disc forms around every new star. As the name suggests, an accretion disc will eventually accrete most of its material onto the star, leaving only a small fraction of it as planets or a debris disc in orbit around the star. Observations of accretion rates in proto-planetary discs suggest that accretion timescales are of the order of a few 10^5 years (Enoch et al. 2008).

Usually one assumes that the Navier-Stokes equations are a good approximation to describe the fluid motion within the disc. However, to reproduce the measured accretion rates, a purely molecular viscosity is not efficient enough. It is generally believed that this large viscosity originates from turbulence (Pringle 1981). The mass flux in a steady state Keplerian disc is then given by

$$\dot{M} = 3\pi\nu\Sigma, \quad (1.2)$$

where ν is the effective kinematic viscosity and Σ the surface density. From observations of proto-stars, a value of $\nu \sim 10^{-5}\text{AU}^2/(\text{yr}/2\pi)$ has been inferred, but with considerable uncertainty.

The magneto rotational instability (MRI, Balbus & Hawley 1991) is the most likely candidate to be responsible for the anomalous value of ν which is often characterised using the Shakura & Syunyaev (1973) α parameter, defined as $\alpha = \nu/(c_s^2/\Omega)$, with c_s being the local sound speed and $2\pi/\Omega$ being the orbital period. For the most likely situation of small or zero net magnetic flux, recent MHD simulations have indicated $\alpha \approx 10^{-2} - 10^{-3}$. This value is very uncertain when realistic values of the actual transport coefficients are employed due in no small part to numerical resolution issues (see Fromang & Papaloizou 2007; Fromang et al. 2007). Which parts of proto-planetary discs are adequately ionised, or constitute a dead zone, is also an issue (Gammie 1996; Sano et al. 2000).

Putting aside all those issues for a moment, the MRI always creates density fluctuations in the disc, resulting in a stochastic force that is exerted on embedded planets which are otherwise decoupled from the gas motion (ignoring migration, which is a laminar effect and acts on timescales much longer than one orbit). In this thesis, we do not attempt to simulate the MRI directly and rather describe it in an empirical way. We therefore avoid all problems mentioned above and can understand the physical scaling of our results. Only two quantities are needed for our analytic model, the root mean square value of the stochastic gravitational force and the corresponding auto correlation time. Laughlin et al. (2004) propose a more complicated model, in which random modes with random decay times create a gravitational potential that is supposed to mimic the MRI. Our, much simpler and more intuitive description, allows us to survey a large parameter space and understand the resulting physical processes, as discussed in chapter 3.

1.3.2 Minimum mass solar nebula and snowline

A standard model of a proto-planetary disc assumes a steady state and a vertical equilibrium (see also appendix E.1.2). The gas and dust components are furthermore assumed to be fully mixed. The resulting disc is flared, although still geometrically

thin. For sufficiently low mass accretion rates ($\leq 10^{-8}M_{\odot}/\text{yr}$) the dominant heating source is stellar irradiation (Chiang & Goldreich 1997).

Hayashi (1981) prescribes the so-called minimum mass solar nebula (MMSN) which is comprised of just enough mass to make all planets of the solar system. This model became the standard disc model and has been used excessively in recent years with different normalisations. One can describe the surface density and temperature profiles as

$$\Sigma(r) = \Sigma_0 \left(\frac{r}{r_0}\right)^{-p} \quad T(r) = T_0 \left(\frac{r}{r_0}\right)^{-q}. \quad (1.3)$$

Typical normalisation values at $r_0 = 1 \text{ AU}$ are $\Sigma_0 = 1700 \text{ g cm}^{-2}$ and $T_0 = 280 \text{ K}$. Standard values of p range from 0 to $5/3$, those of q from $1/2$ to $3/4$ (Hayashi 1981; Cuzzi et al. 1993). The typical mass of the disc is about one percent of the stellar mass. Although the choice of disc model is essential for most aspects of planet formation, little emphasis has been placed on alternatives (see e.g. Desch 2007; Crida 2009).

To form planets and planetary cores, dust is an important ingredient (see also below). In the model of Hayashi ($q = 1/2$), the radius at which temperatures drop below 170 K is around 2.7 AU . At larger radii, the temperatures are low enough for water ice to exist. This transition radius is called the snow line. Recent studies, including more detailed models of accretional heating and radiative transfer show that the snow line could come as close as 1 AU (Sasselov & Lecar 2000).

1.3.3 Planet formation mechanism

Planets are believed to form in proto-stellar discs as a natural by-product of star formation. These discs are made of the same material as the star itself: gas and dust. Current theories give two possible explanations of the formation of giant planets inside the disc. Both models favour planet formation at large radii, beyond the snowline. However, it is important to keep in mind that the process of planet formation itself is not directly observable (yet), leaving theory and numerical simulations to fill in the blanks between observations of hot circumstellar discs around young stars and planets orbiting main sequence stars.

Core accretion

One of the most important unanswered questions in the theory of planet formation is to find out what the mechanism for planetesimal formation is, i.e., the process by which the building blocks of planets are formed. In the core accretion model, solid components of the disc stick together, forming bigger and bigger objects until a core of

about 15 Earth masses is formed (Bodenheimer & Pollack 1986; Pollack et al. 1996a). The proto-planet can then start to accrete gas and form a gas giant.

Again, there are two main theories for planetesimal formation via the core accretion model: mutual collisions (e.g., Hayashi et al. 1977) and gravitational instability in the dust layer (Goldreich & Ward 1973). In the first hypothesis, dust particles grow as the result of accretion-dominated collisions. Although the formation of planetesimals by mutual collisions is consistent with meteoritic evidence, the collision speed between dust particles (or aggregates) must be much slower than the typical velocity dispersion in a standard proto-stellar disc to avoid destructive collisions (Blum & Wurm 2008). In addition, the planetesimal formation process is so slow that metre-sized particles are in danger of spiralling into the star before growing large enough to decouple from the gas (Weidenschilling 1977b). Even if km-sized planetesimals were able to form, they would be in danger of being ground down again by mutual collisions (Stewart & Leinhardt 2009).

Gravitational instability is often considered to be a solution to most of these problems because the intermediate sizes are avoided all together. In this theory, the dust layer becomes dense enough for the Keplerian shear and velocity dispersion of the dust particles to be unable to support the dust against its own self gravity. The dust then collapses into clumps that eventually cool via drag forces and mutual collisions into planetesimals. Many different groups have been working on this subject. Until recently, the focus has been on quiet, non-turbulent, and low density regions of the accretion disc (see e.g., Michikoshi et al. 2009, 2007; Tanga et al. 2004).

However, the turbulent gas in the proto-planetary nebula stirs the dust, which increases the velocity dispersion of the dust particles. Several ideas have been proposed to overcome the turbulence-induced mixing of the dust particles and create localised clumps. For example, Cuzzi et al. (2008) suggest that the same turbulence that stirs the dust on larger scales may also collect the dust particles on small scales. A similar idea was proposed by Johansen et al. (2007), in which dust particles are localised into clumps promoted by both turbulence and the streaming instability (Youdin & Goodman 2005). These dense clumps then become gravitationally unstable. A third hypothesis suggests that large structures, such as vortices, may be able to collect and protect dust particles from the turbulent background (Barge & Sommeria 1995; Lyra et al. 2009).

In chapter 5, we focus on the gravitational collapse in a very dense and turbulent region of the proto-planetary disc. We look carefully at the numerical requirements of modelling gravitational instability accurately and test the validity of using super-particles in a high density region. The results suggest that some of the early results of gravitational collapse from other authors may have been too optimistic.

Gravitational fragmentation

In this model, gas planets form directly as a result of gravitational instability within the disc (Boss 2001); no solid core is needed. However, the planet can accrete dust particles later on, and hence form a core.

For the gravitational instability to occur, it is necessary to have a Toomre Q parameter of order unity (Toomre 1964). The precise criterion depends strongly on the thermodynamics on the disc, especially the cooling time. However, it is unlikely that the physical conditions in a proto-planetary disc are compatible with this constraint. If so, this is most likely to occur at large radii (~ 100 AU). It therefore cannot be the formation mechanism for most discovered exo-planets.

1.4 Evolution of planetary systems

1.4.1 Migration

Many observed planets are very close to their host star. It is implausible that they have formed at such small radii (see section 1.3.2), even taking into account the strong selection effect of discovering close in exo-planets (see section 1.1).

Tidal interactions with the proto-planetary disc give the planet some radial mobility and might therefore be the solution to this problem (Goldreich & Tremaine 1980). The mutual angular momentum exchange depends on many parameters of both the planet and the disc. Several population synthesis simulations were able to reproduce the observed mass-period distribution using migration (e.g. Ida & Lin 2004). Planet migration can be classified in the following four main categories.

Type I

Planets are completely embedded in a proto-planetary disc for sufficiently low mass. Density waves are excited in the disc, both interior and exterior to the planet, at so-called Lindblad resonances. The waves carry angular momentum and produce a torque on the planet that leads to planetary migration (Goldreich & Tremaine 1979). The direction of migration depends on parameters of the disc model such as the gradients of the surface density, sound speed and scale height (Ward 1997). In most cases, the outer torque is bigger than the inner one and the planet migrates inward. This effect is called type I migration.

If the migration rate is very fast, low mass planets are in danger of spiralling into the star within the disc lifetime. The precise speed and direction in a realistic disc model are still subject to debate, where recently the focus has been on non-isothermal equations

of state and the effects of co-rotation torques (Paardekooper et al. 2010; Paardekooper & Papaloizou 2009).

Type II

If the planet is massive enough, it can open a gap in the disc. For most disc models about a Jupiter mass is needed to clear a clean gap. The process is similar to the gaps opening in Saturn's rings with moons orbiting within the gap. The gap establishes a flow barrier to the disc material, effectively locking the planet to the viscous disc evolution (Lin & Papaloizou 1986). Thus, the planet still migrates, the regime being called type II migration. However, the migration timescale is set by the disc evolution timescale which is in general much longer than the type I migration timescale.

Type III

In a disc with a relatively large surface density (several times the MMSN), the density distribution in the co-orbital region of the planet can be asymmetric. This leads to a self-sustained torque that is proportional to the migration rate. In this regime, called type III migration, the planet can fall inward on a timescale much shorter than the disc evolution time obtained for type II migration, even shorter than the timescales associated with type I migration. The planet moves faster than the disc can respond to its perturbation, thus maintaining an asymmetry. The net torque can cause both inward or outward migration (Pepliński et al. 2008a,b,c).

In chapter 2 we present the first observable indication that type III migration is indeed responsible for shaping planetary systems.

Type IV

The different migration regimes have all been studied in quiet non-turbulent discs. However, a proto-planetary disc is thought to be at least partially turbulent (see section 1.3.1). Assuming the simplest scenario in which the effects of turbulence and the net migration are separable, one can describe the stochastic migration as a diffusion process in a distribution of planets on top of the net orbital migration, described above. We call this regime type IV.

This idea leads to a Fokker-Planck description (Adams & Bloch 2009). There are two limits to this approach. The first, in which the net migration dominates and the effects of turbulence are negligible (mostly for heavy planets). The second, in which the net migration can be ignored and the turbulence driven diffusion dominates on short timescales (mostly for small mass planets and planetesimals). We are in an intermediate regime if the migration and diffusion timescales are comparable. It is unlikely that the

interplay of stochastic migration and net migration plays an important role in determining the final semi major axis of planets because the associated timescales would have to be very similar. However, resonant systems are more sensitive to stochastic forces and might therefore provide observational constraints on the strength of turbulence that was present at early times.

So far, only preliminary work has been done on studying the effect of the turbulence on resonances (Adams et al. 2008; Nelson & Papaloizou 2004). If the turbulence is active long enough, it will eventually kick the planets out of resonance. This might happen even if the stochastic forces are not strong enough to cause significant orbital migration. However, the timescale needed for destroying a resonance is not well constrained. New results on this issue are presented in chapter 3.

1.5 Mean motion resonances

Resonances in celestial mechanics can occur when there is a simple numerical relation between two frequencies (Murray & Dermott 2000). For example, a planet could feel a periodic gravitational force from another planet that is a multiple of its own orbital frequency. This can either lead to an unstable situation in which angular momentum is exchanged until the resonance ceases to exist or a planet gets ejected from the system, or a stable configuration.

Resonances can form when dissipative forces act on the planets, for example in a proto-planetary disc (see e.g. Malhotra (1993) and appendix B). When there are two (or more) planets in the disc, the migration rates might differ for various reasons. One possibility is that the planets are in different migration regimes (see section 1.4.1). The resulting differential migration changes the ratio of orbital periods P_i and the ratio of semi major axes a_i . These ratios are related by Kepler's third law, $(T_1/T_2)^2 = (a_1/a_2)^3$.

The planets can become locked into a mean motion resonance (MMR) if the ratio of orbital periods gets close to a rational number q/p with small integers q and p , e.g. $1/2, 1/3$ or $2/3$. The numbers p and q can be interpreted as the number of completed orbits after the same time. Some of these resonances are stable and planets can stay in resonance over a long period of time, migrating together and keeping the ratio of their orbital periods constant. Beside the presence of Hot Jupiters, resonance capturing is admitted as strong evidence that planets undergo a phase of orbital migration. This idea was successful in explaining the observed resonant multi-planet systems GJ876 and 55 Cancri (Lee & Peale 2001; Snellgrove et al. 2001) which are in a 2:1 resonance. In chapter 2, we discuss the first successful formation scenario for a system that is in a 3:2 resonance.

The dynamical origin of the multi-planetary system HD45364

Truth is ever to be found in simplicity, and not in the multiplicity and confusion of things.

Issac Newton, unpublished manuscript, Frank E. Manuel 1974

The recently discovered planetary system HD45364, which consists of Jupiter- and Saturn-mass planets, is very likely in a 3:2 mean motion resonance. The standard scenario for forming planetary commensurabilities involves convergent migration of two planets embedded in a proto-planetary disc. However, when the planets are initially separated by a period ratio larger than two, convergent migration will most likely lead to a stable 2:1 resonance, incompatible with current observations.

Rapid type III migration of the outer planet crossing the 2:1 resonance is one possible way around this problem. Here, we investigate this idea in detail. We present an estimate of the required convergent migration rate in section 2.1.2 and confirm this with N-body simulations in section 2.2 and hydrodynamical simulations in section 2.3. If the dynamical history of the planetary system had a phase of rapid inward migration that forms a resonant configuration as we suggest here, then we predict that the orbital parameters of the two planets will always be very similar and should show evidence of that.

We use the orbital parameters from our simulation to calculate a radial velocity curve and compare it to observations in section 2.5. Our model provides a fit that is as good as the previously reported one. However, the eccentricities of both planets are considerably smaller and the libration pattern is different. Within a few years, it will be possible to observe the planet-planet interaction directly and thus distinguish between these different dynamical states.

This is the first prediction of orbital parameters for a specific extra-solar planetary system derived from planet migration theory alone. It provides strong evidence on how the system formed.

2.1 The planetary system HD45364

2.1.1 The standard formation scenario and its problems

The planets in this system have masses of $m_1 = 0.1906M_{\text{Jup}}$ and $m_2 = 0.6891M_{\text{Jup}}$ and are orbiting the star at a distance of $a_1 = 0.6813$ AU and $a_2 = 0.8972$ AU, respectively (Correia et al. 2008). The period ratio is close to 1.5. This alone does not imply that the planets are in a 3:2 mean motion resonance. However, a stability analysis shows that the three body system (two planets and a star) is only stable if the planets are in a 3:2 mean motion resonance. Furthermore, the region of greatest stability also contains the best statistical, Keplerian fit to the radial velocity measurements (Correia et al. 2008).

In the core accretion model, a solid core is firstly formed by dust aggregation. After a critical core mass is attained (Mizuno 1980), the proto-planet accretes a gaseous envelope from the nebula (Bodenheimer & Pollack 1986).

As explained in more detail in section 1.3.2, the planets have most likely formed further out in cooler regions of the proto-stellar disc as water ice, which is an important ingredient for dust aggregation, can only exist beyond the snow line. The snow line is generally assumed to be at radii larger than 2 AU (Sasselov & Lecar 2000).

When the planets have obtained a substantial part of their mass, they migrate due to planet disc interactions (see section 1.4.1). Although the details of this process are still being hotly debated, the existence of many resonant multiplanetary systems and hot Jupiters supports this idea and suggests that planets preferably migrate inwards. Both planets in the HD45364 system are inside the snow line, implying that they should have migrated inwards significantly.

The migration rate depends on many parameters of the disc such as surface density, viscosity, and the mass of the planets. The planets are therefore in general expected to have different migration rates, which leads to the possibility of convergent migration. In this process the planets approach orbital commensurabilities. If they do this slowly enough, resonance capture may occur (Goldreich 1965), after which they migrate together maintaining a constant period ratio thereafter.

Studies by several authors have shown that when two planets, either of equal mass or with the outer one more massive, undergo differential convergent migration, capture into a mean motion commensurability is expected provided that the convergent migration

rate is not too fast (Snellgrove et al. 2001). The observed inner and outer planet masses are such that, if (as is commonly assumed for multiplanetary systems of this kind) the planets are initially separated widely enough that their period ratio exceeds 2, a 2:1 commensurability is expected to form at low migration rates (e.g. Nelson & Papaloizou 2002; Kley et al. 2004).

Pierens & Nelson (2008) have studied a similar scenario where the goal was to resemble the 3:2 resonance between Jupiter and Saturn in the early solar system. They also find that the 2:1 resonance forms in early stages; however, in their case the inner planet had the higher mass, whereas the planetary system that we are considering has the heavier planet outside. In their situation the 2:1 resonance is unstable, enabling the formation of a 3:2 resonance later on, and the migration rate can stall or even reverse (Masset & Snellgrove 2001).

For the planetary system HD45364, this standard picture poses a new problem. Assuming that the planets have formed far apart and were not much smaller during the migration phase, the outcome is almost always a 2:1 mean motion resonance, not 3:2 as observed. The 2:1 resonance that forms is found to be extremely stable. One possible way around this is a very rapid convergent migration phase that passes quickly through the 2:1 resonance.

2.1.2 Avoiding the 2:1 mean motion resonance

We found that, if two planets with masses of the observed system are in a 2:1 mean motion resonance, which has been formed via convergent migration, this resonance is very stable. An important constraint arises, because at the slowest migration rates, the 2:1 resonance is expected to form rather than the observed 3:2 commensurability provided the planets start migrating outside any low-order commensurability.

We can estimate the critical relative migration timescale $\tau_{a,\text{crit}}$ above which a 2:1 commensurability forms with the condition that the planets spend at least one libration period migrating through the resonance. The resonance's semi-major axis width Δa associated with the 2:1 resonance can be estimated from the condition that two thirds of the mean motion difference across Δa be equal in magnitude to 2π over the libration period. This gives

$$\Delta a = \frac{\omega_{lf} a_2}{n_2} \quad (2.1)$$

where a_2 and n_2 are the semi major axis and the mean motion of the outer planet, respectively. The libration period $2\pi/\omega_{lf}$ can be expressed in terms of the orbital parameters (see e.g. Goldreich 1965; Rein & Papaloizou 2009, and also chapter 3) but is here measured numerically, for convenience. If we assume the semi-major axes of the two

planets evolve on constant (but different) timescales $|a_1/\dot{a}_1| = \tau_{a,1}$ and $|a_2/\dot{a}_2| = \tau_{a,2}$, the condition that the resonance width is not crossed within a libration period gives

$$\tau_{a,\text{crit}} \equiv \left| \frac{1}{1/\tau_{a,1} - 1/\tau_{a,2}} \right| \gtrsim 2\pi \frac{a_2}{\omega_{lf} \Delta a} = 2\pi \frac{n_2}{\omega_{lf}^2} \quad (2.2)$$

to pass through the 2:1 MMR.

If the planets of the HD45364 system are placed in a 2:1 resonance with the inner planet located at 1 AU, the libration period $2\pi/\omega_{lf}$ is found to be approximately 75 yrs. Thus, a relative migration timescale shorter than $\tau_{a,\text{crit}} \approx 810$ yrs is needed to pass through the 2:1 resonance. For example, if we assume that the inner planet migrates on a timescale of 2000 years, then the outer planet has to migrate with a timescale of

$$\tau_{a,2,\text{crit}} \lesssim 576 \text{ yrs.} \quad (2.3)$$

2.2 N-body simulations

We ran N -body simulations to explore the large parameter space and confirm the estimate from the previous section. In an N -body simulation all objects (stars, planets) are treated as point masses interacting only gravitationally with each other. To model the planet-disc interaction, one can explicitly add dissipative and stochastic forces. Thus, the total force acting on an object i is a sum of the following terms

$$\vec{F}_i = \vec{F}_i^{\text{gravity}} + \vec{F}_i^{\text{indirect}} + \vec{F}_i^{\text{a-damping}} + \vec{F}_i^{\text{e-damping}} + \vec{F}_i^{\text{stochastic}}. \quad (2.4)$$

The first term is due to the gravitational interaction. In units where $G = 1$ we have

$$\vec{F}_i^{\text{gravity}} = \sum_{j \neq i} m_i m_j \frac{\vec{r}_j - \vec{r}_i}{|\vec{r}_j - \vec{r}_i|^3}, \quad (2.5)$$

where we sum over all particles in the system, except the i -th particle. In the heliocentric coordinate system which is used here, the star is located at a fixed position at $\vec{r} = 0$. That brings about an additional indirect term as we are in an accelerated, non-inertial frame,

$$\vec{F}_i^{\text{indirect}} = - \sum_j m_i m_j \frac{\vec{r}_j}{|\vec{r}_j|^3}. \quad (2.6)$$

The next two terms in equation 2.4 are due to the laminar planet-disc interaction. In a first approximation the interaction damps the semi-major axis a and the eccentricity e on time scales τ_a and τ_e , respectively. The exact terms depend on the orbital parameters of the planet and are given in appendix B. It is common practice to define the ratio between the timescales $K \equiv \tau_a/\tau_e$. To obtain those timescales, we have to

compare the N-body simulations to full hydrodynamical simulations which will be done in the following section. An N-body simulation is much faster than a hydrodynamical simulation and thus can be integrated over a longer time span. This is essential because resonance capturing and migration act on timescales $\approx 1000 - 10000$ years and we might even want to integrate over millions of years. The last term in equation 2.4 adds stochastic forces, simulating the turbulent nature of proto-planetary discs. The implementation is discussed in chapter 3.

Newton's second law together with equation 2.4 forms a system of ordinary differential equations. To solve them, a new N-body code has been developed which is highly modular and easily expandable. It incorporates different modules for stochastic forces, migration, data output and time-stepping.

The choice of integrator depends on the problem. The following algorithms have been implemented:

Runge-Kutta Method (RK4) The classical, fourth order Runge-Kutta method is a widely-used standard integrator. It is an explicit method that needs four function evaluations per time-step. The main disadvantage of the RK4 method is the fixed time-step. We have to set a specific value at the beginning of the computation that is not refined later on.

Runge-Kutta-Fehlberg Method (RK45) The Runge-Kutta-Fehlberg method is a fifth order explicit method with an embedded fourth order method (Fehlberg 1969). We can use the two different results to estimate the numerical error and a new time-step. We repeat the step with a smaller time-step if the error is larger than a specified limit *eps*.

Midpoint Method The midpoint method belongs to the class of second order Runge-Kutta methods. Due to the low order it is not efficient to use it on its own, but it is used as a sub-timestep integrator by the Bulirsch-Stoer Method.

Bulirsch-Stoer Method (BS) This method (Stoer & Bulirsch 2002; Press et al. 1992) is based on a stepwise extrapolation. For each time-step we calculate the new positions and velocities several times with different sub-time-steps Δt_i using the modified midpoint method. We then perform an extrapolation to a *perfect* sub-step in the limit where $\Delta t \rightarrow 0$. This allows the use of very large time-steps while still obtaining a high accuracy. We can also use the extrapolation to estimate the error and thus make the method adaptive.

The code has been used in Rein & Papaloizou (2009) and Rein et al. (2010), usually with the Bulirsch-Stoer integrator and a precision of $\epsilon = 10^{-11}$. A symplectic integrator

has not been implemented, although it would have better long term conservation properties. This is because the integrator would formally not be symplectic any more once velocity dependent forces have been added. This is the case in all simulations presented here, which include either migration or stochastic forces. Note that in some cases it is possible to find a symplectic integrator for systems with velocity dependent forces, for example for Hill’s equations (Quinn et al. 2010). Such an integrator (a modified version of the leap-frog algorithm) has been used in shearing sheet calculations of planetary rings, presented in chapter 4.

2.2.1 Parameter space survey

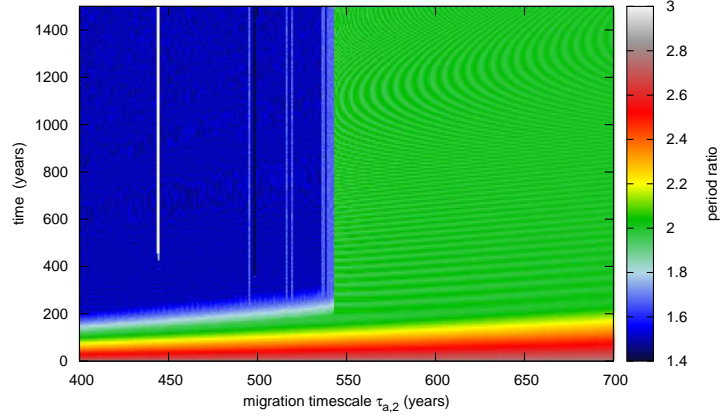
With the new N-body code, we can now easily scan the parameter space and confirm the analytic estimate of the critical migration rate needed to capture into the 3:2 resonance.

We place both planets on circular orbits at $a_1 = 1$ AU and $a_2 = 2$ AU initially. The migration timescale for the inner planet is fixed at $\tau_{a,1} = 2000$ yrs, while the migration timescale for the outer planet is varied. In figures 2.1, 2.2 and 2.3 we plot the period ratio P_2/P_1 and the eccentricities of both planets as a function of time t for different migration timescales $\tau_{a,2}$. In all cases, there is a sharp transition of the final resonant configuration from 2:1 to 3:2 at around $\tau_{a,2} \approx 550$ yrs. This value agrees closely with the analytic estimate given by equation 2.3. Note that once the planets are in resonance, the eccentricities quickly reach an equilibrium value as the planets migrate adiabatically.

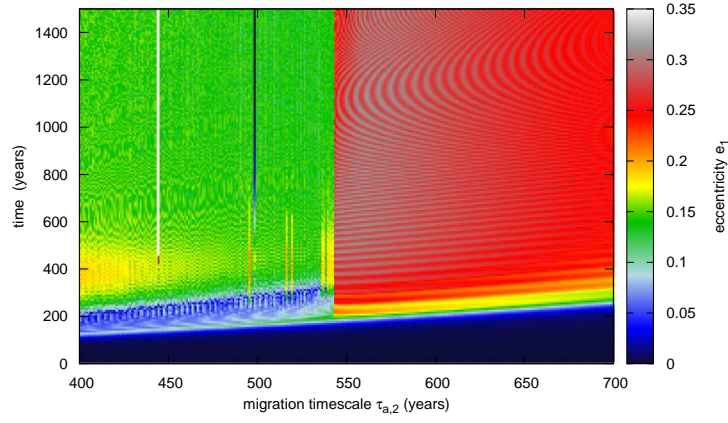
In figure 2.2 the eccentricity damping corresponds to $K = 30$ and is therefore three times stronger than in figure 2.1. A value of $K = 30$ is rather high and probably unphysical. It can be seen that a smaller eccentricity damping timescale pushes the boundary towards a longer migration time-scale. Although this effect is rather weak (a three times stronger eccentricity damping shifts the boundary by only 4%), it can be easily understood within the toy model presented above. The eccentricities have to rise quickly, while the planets are within the resonance width. This is more difficult for short eccentricity damping timescales.

In figure 2.3 the eccentricity damping corresponds to $K = 1$ and is therefore ten times weaker than in figure 2.1. Again, a value of $K = 1$ is probably unphysical. This results in a rapid rise of eccentricities as soon as the planets are in resonance. Systems that are in a 3:2 resonance become unstable within a few thousand years. On the other hand, systems that are in a 2:1 resonance remain stable, although eccentricities are high ($e_1 \sim 0.5$).

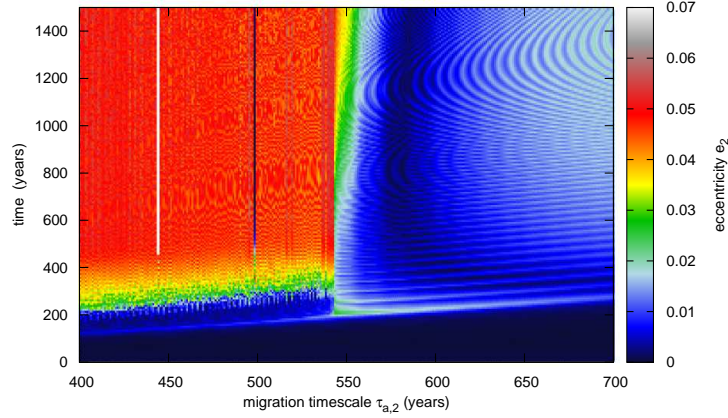
The results show clearly that, if the planets begin with a period ratio exceeding two, to get them into the observed 3:2 resonance, the relative migration time has to be shorter than what is obtained from the standard theory of type II migration applied to



(a) Period ratio P_2/P_1 as a function of time (y -axis) and migration timescale of the outer planet $\tau_{a,2}$ (x -axis).

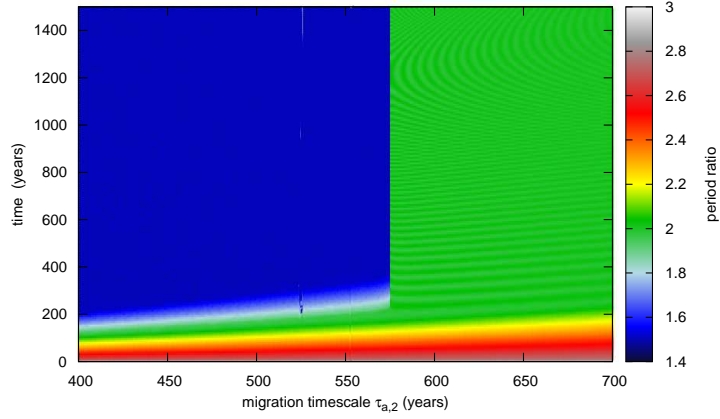


(b) Eccentricity of the inner planet e_1 as a function of time (y -axis) and migration timescale of the outer planet $\tau_{a,2}$ (x -axis).

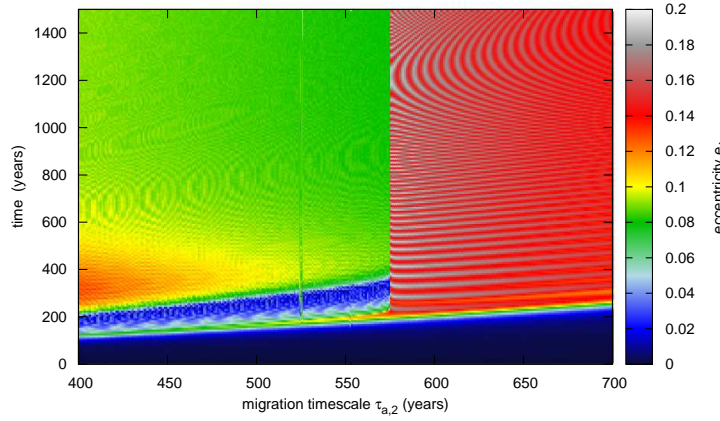


(c) Eccentricity of the outer planet e_2 as a function of time (y -axis) and migration timescale of the outer planet $\tau_{a,2}$ (x -axis).

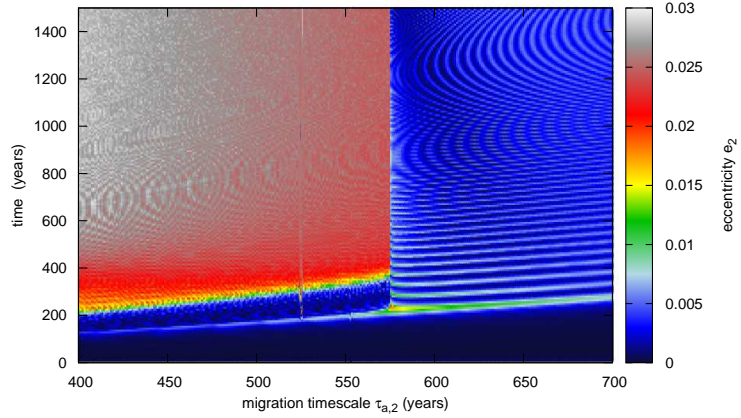
Figure 2.1: Parameter space survey. The migration timescale of the inner planet is $\tau_{a,1} = 2000$ yrs. The eccentricity damping is given through $K \equiv \tau_a/\tau_e = 10$.



(a) Period ratio P_2/P_1 as a function of time (y -axis) and migration timescale of the outer planet $\tau_{a,2}$ (x -axis).

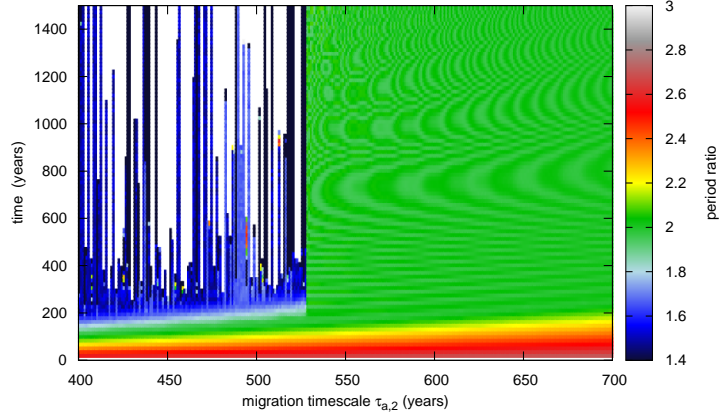


(b) Eccentricity of the inner planet e_1 as a function of time (y -axis) and migration timescale of the outer planet $\tau_{a,2}$ (x -axis).

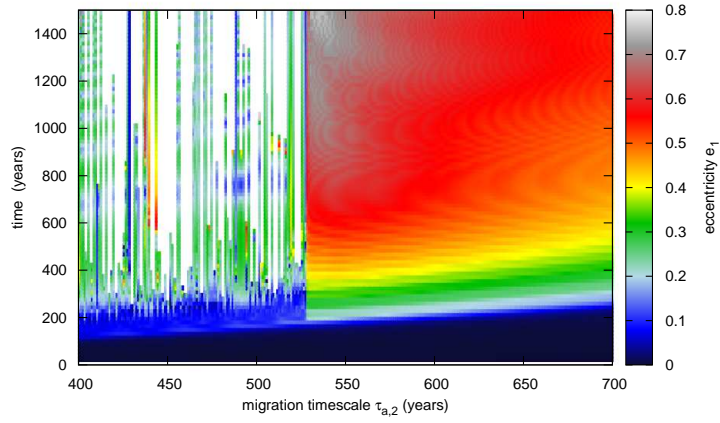


(c) Eccentricity of the outer planet e_2 as a function of time (y -axis) and migration timescale of the outer planet $\tau_{a,2}$ (x -axis).

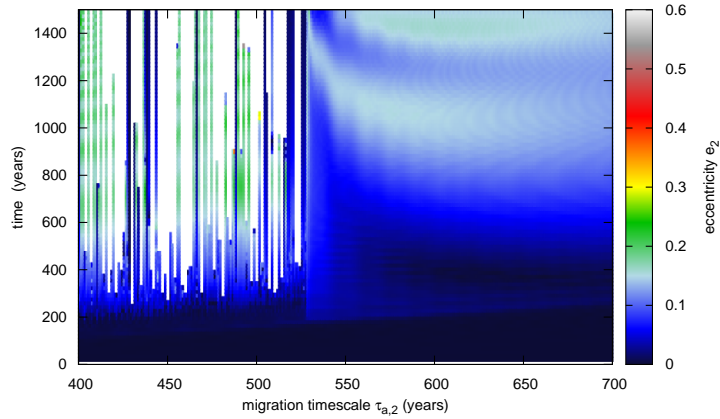
Figure 2.2: Parameter space survey. Same parameters as in figure 2.1 except $K \equiv \tau_a/\tau_e = 30$.



(a) Period ratio P_2/P_1 as a function of time (y -axis) and migration timescale of the outer planet $\tau_{a,2}$ (x -axis).



(b) Eccentricity of the inner planet e_1 as a function of time (y -axis) and migration timescale of the outer planet $\tau_{a,2}$ (x -axis).



(c) Eccentricity of the outer planet e_2 as a function of time (y -axis) and migration timescale of the outer planet $\tau_{a,2}$ (x -axis).

Figure 2.3: Parameter space survey. Same parameters as in figure 2.1 except $K \equiv \tau_a/\tau_e = 1$. Many systems eject one or more planets, indicated by the white colour (on the left).

Run	H/R	b/H	Σ	N_r	N_ϕ	Result
F1	0.05	0.6	0.001	768	768	3:2
F2	0.05	0.6	0.0005	768	768	3:2 D
F3	0.05	0.6	0.00025	768	768	2:1 D
F4	0.04	0.6	0.001	768	768	3:2 D
F5	0.07	0.6	0.001	768	768	3:2
R1	rad	1.0	0.0005	300	300	3:2

Table 2.1: Parameters for some of the hydrodynamic simulations. The second column gives the disc aspect ratio, the third column the softening length in units of the local scale height and the fourth column gives the initial surface density. The fifth and sixth columns give the number of radial and azimuthal grid points used and finally the simulation outcome is indicated in the last column.

these planets in a standard model disc (Nelson et al. 2000). In that case one expects this timescale to be larger than 10^4 years, being effectively the disc evolution timescale. However, it is possible to obtain the required shorter migration timescales in a massive disc in which the planets migrate in a type III regime (see e.g. Masset & Papaloizou 2003; Pepliński et al. 2008a). In this regime, the surface density distribution in the co-orbital region is asymmetric, leading to a large torque which is able to cause the planet to fall inwards on a much shorter timescale than the disc evolution time obtained for type II migration. Other parameters such as the eccentricity damping timescale do not have a strong effect on capture probabilities.

We explore the feasibility of this scenario in more detail in the following sections.

2.3 Hydrodynamical simulations

Two-dimensional, grid-based hydrodynamic simulations of an accretion disc with two gravitationally interacting planets were performed to test the rapid migration hypothesis. The simulations performed here are similar in concept to those performed by Snellgrove et al. (2001) of the resonant coupling in the GJ876 system that may have been induced by orbital migration resulting from interaction with the proto-planetary disc. We performed studies using the FARGO code (Masset 2000) with a modified locally isothermal equation of state. Those runs are indicated by the letter **F**.

Willy Kley also ran simulations including viscous heating and radiative transport using the RH2D code. Those runs are indicated by the letter **R** and more details can be found in Rein et al. (2010).

Further simulations have been performed with a new hydrodynamics code called Prometheus, which is described in appendix E. The code is similar to FARGO, using operator splitting, a staggered grid and fast orbital advection. However, it can be

run in two dimensions (cylindrical grid) and in three dimensions (spherical coordinates). Furthermore, it includes a particle and an MHD module.

2.3.1 Initial configuration and computational set up

We use a system of units in which the unit of mass is the central mass M_* , the unit of distance is the initial semi-major axis of the inner planet, r_1 , and the unit of time is $(GM_*/r_1^3)^{-1/2}$. Thus the orbital period of the initial orbit of the inner planet is 2π in these dimensionless units. The parameters for some of the simulations we conducted, as well as their outcomes, are given in table 2.1.

In all simulations presented here, the mass ratio of the inner and outer planet is $q_1 = 2.18 \cdot 10^{-4}$ and $q_2 = 7.89 \cdot 10^{-4}$, respectively. The mass ratios adopted are those estimated for HD45364. The initial separation of the planets is $r_2/r_1 = 1.7$. The viscosity is chosen to be $\nu = 10^{-5}$. The simulations have the inner and outer boundary of the 2D grid at $r_i = 0.25$ and $r_o = 3.0$, respectively. In all simulations, a smoothing length $b = 0.6 H$ has been adopted, where H is the disc thickness at the planet's position. This corresponds to about 4 zone widths in a simulation with a resolution of 768×768 . The role of the softening parameter b that is used in two-dimensional calculations is to account for the smoothing that would result from the vertical structure of the disc in three dimensional calculations (e.g. Masset et al 2006). We find that the migration rate of the outer planet is only independent of the smoothing length if the sound speed is given by equation 2.7 (see next section).

The planets are initialised on circular orbits, slowly turning on their mass in the first 5 orbits. We assume there is no mass accretion, so that these remain fixed in the simulation (see discussion in Pepliński et al. 2008a, and also Sect. 2.4). The initial surface density profile is constant, and tests indicate that varying the initial surface density profile does not change the outcome very much. The total disc mass in the simulations listed in table 2.1 ranges from 0.014 to 0.055 solar masses. Non-reflecting boundary conditions have been used throughout this chapter.

2.3.2 Equation of state

The outer planet is likely to undergo rapid type III migration, and the co-orbital region will be very asymmetric. We find, in accordance with Pepliński et al. (2008a), that the standard softening description does not lead to convergent results (for a comparative study see Crida et al. 2009). Because of the massive disc, a high density spike develops near the planet. Any small asymmetry will then generate a large torque, leading to erratic results. We follow the prescription of Pepliński et al. (2008a) and increase the sound speed near the outer planet since the locally isothermal model breaks down in

the circum-planetary disc. The new sound speed is given by

$$c_s = [(h_s r_s)^{-n} + (h_p r_p)^{-n}]^{-1/n} \cdot \sqrt{\Omega_s^2 + \Omega_p^2}, \quad (2.7)$$

where r_s and r_p are the distance to the star and the outer planet, respectively. Ω_s and Ω_p are the Keplerian angular velocity and h_s and h_p are the aspect ratio, both of the circumstellar and circum-planetary disc, respectively. The parameter n is chosen to be 3.5, and the aspect ratio of the circum-planetary disc is $h_p = 0.4$. The sound speed has not been changed in the vicinity of the inner, less massive planet as it will not undergo type III migration and the density peak near the planet is much lower.

In radiative simulations (R), we go beyond the locally isothermal approximation and include the full thermal energy equation, which takes the generated viscous heat and radiative transport into account. In this radiative formulation, the sound speed is a direct outcome of the simulation, so we do not use equation 2.7 (Rein et al. 2010).

2.3.3 Simulation results

We find several possible simulation outcomes. These are indicated in the final column of table 2.1, which gives the resonance obtained in each case with a final letter D denoting that the migration became ultimately divergent, resulting in a loss of the commensurability. We find that convergent migration could lead to a 2:1 resonance that was set up in the initial stages of the simulation (F3). Cases F1, F2, F4, F5, R1 provide more rapid and consistent convergent migration than F3 and can attain a 3:2 resonance directly.

Thus avoidance of the attainment of sustained 2:1 commensurability and the effective attainment of 3:2 commensurability required a rapid convergent migration, as predicted by the N-body simulations and the analytic estimate (see section 2.1.2). That is apparently helped initially by a rapid inward migration phase of the outer planet which shows evidence of type III migration. The outer planet went through that phase in all simulations with a surface density higher than 0.00025, and a 3:2 commensurability was obtained. Thus, a surface density comparable to the minimum solar nebula (MMSN, Hayashi 1981), as used in simulation F3, is not sufficient to allow the planets undergo rapid enough type III migration. As soon as the planets approach the 3:2 commensurability, type III migration stops due to the interaction with the inner planet and the outer planet starts to migrate in a standard type II regime.

This imposes another constraint on the long-term sustainability of the resonance. The inner planet remains embedded in the disc and thus potentially undergoes a fairly rapid inward type I migration. If the type II migration rate of the outer planet is slower than the type I migration rate of the inner planet, then the planets diverge and the resonance is not sustained. A precise estimate of the migration rates is impossible in

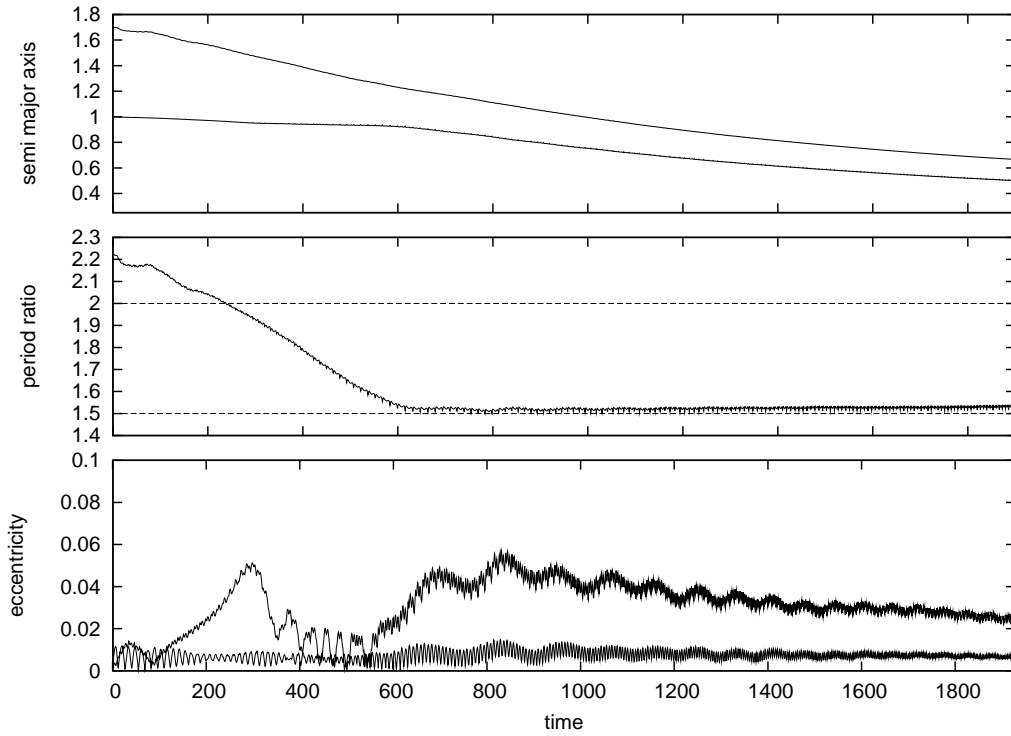


Figure 2.4: The semi-major axes (top), period ratio P_2/P_1 (middle), and eccentricities (bottom) of the two planets plotted as a function of time in dimensionless units for run F5 with a disc aspect ratio of $h = 0.07$. In the bottom panel, the upper curve corresponds to the inner planet.

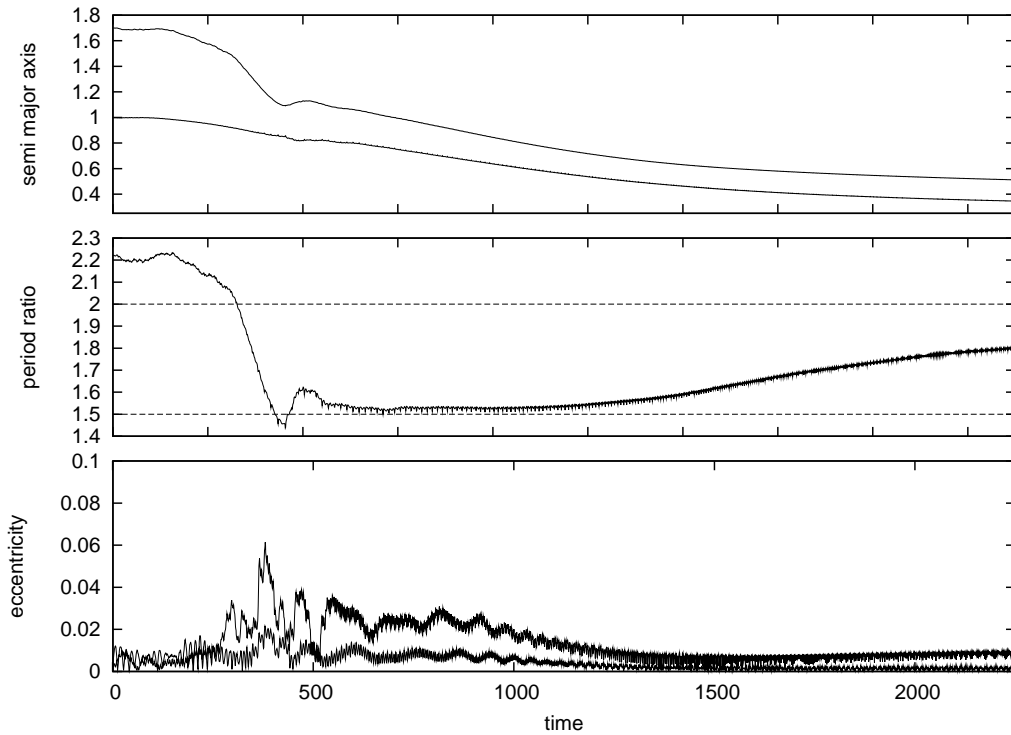


Figure 2.5: Same plot as above for simulation F4 with a disc aspect ratio of $h = 0.04$.

late stages, as the planets interact strongly with the density structure imposed on the disc by each other.

Accordingly, outflow boundary conditions at the inner boundary that prevent the build up of an inner disc are more favourable to the maintenance of a 3:2 commensurability because the type I migration rate scales linearly with the disc surface density. However, those are not presented here, as the effect is weak and we stop the simulation before a large inner disc can build up near the boundary.

The migration rate for the inner planet depends on the aspect ratio h . It is decreased for an increased disc thickness (Tanaka et al. 2002). That explains why models with a large disc thickness (F5,R1) tend to stay in resonance, whereas models with a smaller disc thickness (F2,F4) tend towards divergent migration at late times. The larger thickness is consistent with radiative runs (R1) which give a thickness of $h \sim 0.075$ (see Rein et al. 2010).

As an illustration of the evolution of typical configuration (F5) that forms and maintains a 3:2 commensurability during which the orbital radii contract by a factor of at least ~ 2 we plot the evolutions of the semi-major axes, the period ratio, and eccentricities in figure 2.4. We also provide surface density contour plots in figure 2.6 after 20, 40, 60, 80, 100, 120, 140, 160 and 180 initial inner planet orbits. The eccentricity peak in figure 2.4 at $t \sim 300$ comes from passing through the 2:1 commensurability. At $t \sim 800$, the 3:2 commensurability is reached and maintained until the end of the simulation. The surface density in this simulation is approximately 5 times higher than the MMSN at 1 AU (Hayashi 1981).

We also present an illustration of the evolution of the semi major axes and eccentricities, as well as surface density plots from a simulation (F4) that does form a 3:2 commensurability, but loses it because the inner planet is migrating too fast in figures 2.5 and 2.7. One can see that a massive inner disc has piled up. This and the small aspect ratio of $h = 0.04$ make the inner planet go faster than the outer planet, which has opened a clear gap. The commensurability is lost at $t \sim 1200$.

In the radiative run R1, the initial type III migration rate is slower when compared to run F5 because the surface density is lower. After the the 2:1 resonance is passed, the outer planet migrates in a type II regime, so that the capture into the 3:2 resonance appears later. However, the orbital parameters measured at the end of the simulations are very similar to any other run that we performed. This indicates that the parameter space that is populated by this kind of planet-disc simulation is very generic.

We tested the effect of disc dispersal at the late stages in our models to evolve the system self-consistently to the present day. In model F5 after $t = 2000$ we allow the disc mass to exponentially decay on a timescale of $\tau_{dis} \sim 2000$. This timescale is shorter than the photo-evaporation timescale (Alexander et al. 2006). However, this scenario

is expected to give a stronger effect than a long timescale (Sándor & Kley 2006). In agreement with those authors, we found that the dynamical state of the system does not change for the above parameters. At a late stage, the resonance is well established and the planets undergo a slow inward migration. Strong effects are only expected if the disc dispersal happens during the short period of rapid type III migration, which is very unlikely. We observed that the eccentricities show a trend toward decreasing and the libration amplitudes tend toward slightly increasing during the dispersal phase. However, these changes are not different than what has been observed in runs without a disappearing disc.

Even though we use a high surface density in our simulations, the Toomre Q parameter is still larger than unity at the outer boundary (typically 1.8). This gives us confidence that we do not need to include the effects of self-gravity in the calculation. Furthermore, it is not expected that self-gravity plays an important role for the migration rate of the outer planet which undergoes type III migration (M.K. Lin, private communication).

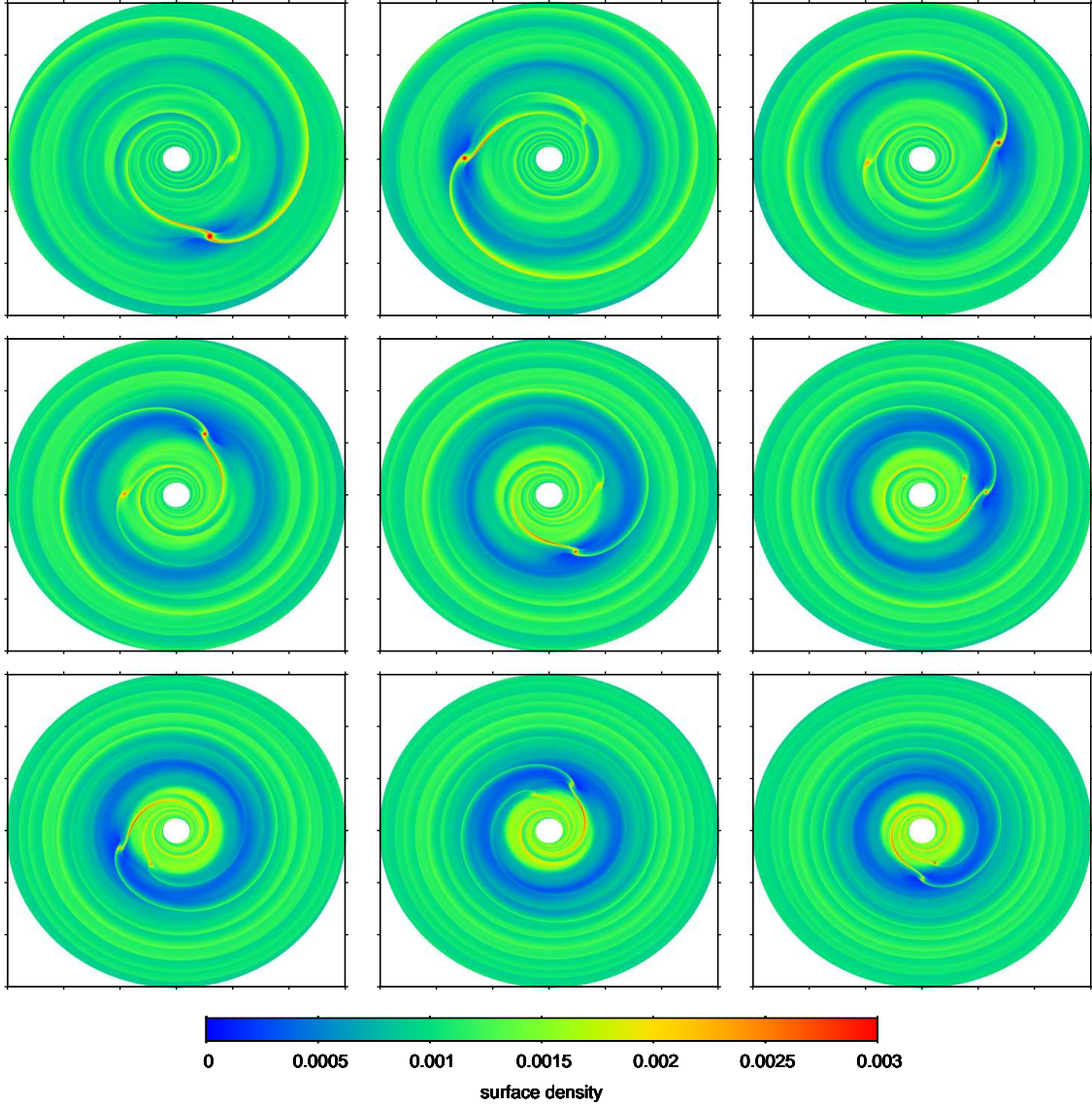


Figure 2.6: Surface-density contour plots for simulation F5 after 20, 40, 60, 80, 100, 120, 140, 160 and 180 inner planet orbits. At the end of the type III migration phase, the outer planet establishes a definite gap, while the inner planet remains embedded at the edge of the outer planet’s gap.

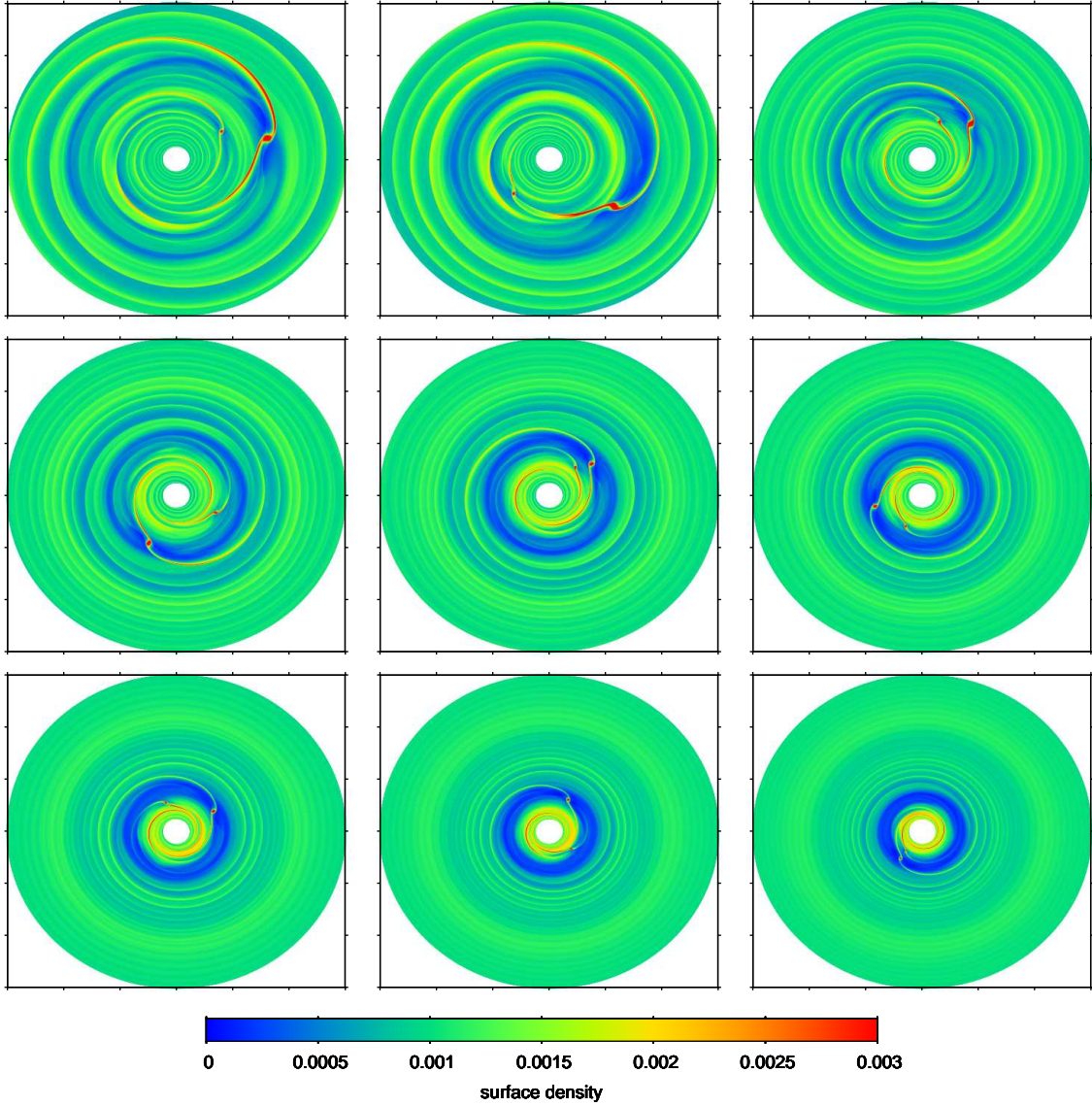


Figure 2.7: Surface-density contour plots for simulation F4 after 20, 40, 60, 80, 100, 120, 140, 160 and 180 inner planet orbits. The extended 1D grid is not shown.

2.4 Other scenarios for the origin of HD45364

In the above discussion, we have considered the situation when the planets attain their final masses while having a wider separation than required for a 2:1 commensurability, and found that convergent migration scenarios can be found that bring them into the observed 3:2 commensurability by disc planet interactions. However, it is possible that they could be brought to their current configuration in a number of different ways as considered below. It is important to note that, because the final commensurable state results from disc planet interactions, it should have similar properties to those described above when making comparisons with observations.

It is possible that the solid cores of both planets approach each other more closely than the 2:1 commensurability before entering the rapid gas accretion phase and attaining their final masses prior to entering the 3:2 commensurability. Although it is difficult to rule out such possibilities entirely, we note that the cores would be expected to be in the super earth mass range, where in general closer commensurabilities than 2:1 and even 3:2 are found for typical type I migration rates (e.g. Papaloizou & Szuszkiewicz 2005; Cresswell & Nelson 2008). One may also envisage the possibility that the solid cores grew in situ in a 3:2 commensurability, but this would have to survive expected strongly varying migration rates as a result of disc planet interactions as the planets grew in mass.

Another issue is whether the embedded inner planet is in a rapid accretion phase. The onset of the rapid accretion phase (also called phase 3) occurs when the core and envelope mass are about equal (Pollack et al. 1996b). The total planet mass depends at this stage on the boundary conditions of the circum-planetary disc. When these allow the planet to have a significant convective envelope, the transition to rapid accretion may not occur until the planet mass exceeds $60M_{\oplus}$ (Wuchterl 1993), which is the mass of the inner planet (see also model J3 of Pollack et al. 1996b, and models of Papaloizou & Terquem 1999). Because of the above results, it is reasonable that the inner planet is not in a rapid accretion phase.

Finally we remark that proto-planetary discs are believed to maintain turbulence in some part of their structure. Using the prescription of Rein & Papaloizou (2009), we can simulate the turbulent behaviour of the disc by adding stochastic forces to an N-body simulation (see also chapter 3). These forces will ultimately eject the planets from the 2:1 resonance should that form. Provided they are strong enough, this can happen within the lifetime of the disc, thus making a subsequent capture into the observed 3:2 resonance possible.

We confirmed numerically that such cases can occur for moderately large diffusion coefficients (as estimated by Rein & Papaloizou 2009). However, this outcome seems to be the exception rather than the rule. Should the 2:1 resonance be broken, a planet-

planet scattering event appears to be more likely. In all the simulations we performed, we find that only a small fraction of systems (1% - 5%) eventually end up in a 3:2 resonance.

2.5 Comparison with observations

Table 2.2 lists the orbital parameters that Correia et al. (2008) obtained from their best statistical fit of two Keplerian orbits to the radial velocity data. The radial velocity data collected so far is insufficient for detecting any interactions between the planets. This is borne out by the fact that the authors did not obtain any improvement in terms of minimising χ^2 when a 3-body Newtonian fit rather than a Keplerian fit was carried out. However, a stability analysis supports the viability of the determined parameters, as these lie inside a stable region of orbital parameter space. The best-fit solution shows a 3:2 mean motion commensurability, although no planet-planet interactions have been observed from which this could be inferred directly. It is important to note that the large minimum χ^2 associated with the best-fit that could be obtained indicates large uncertainties that are not accounted for by the magnitudes of the errors quoted in their paper.

There are two main reasons why we believe that the effective errors associated with the observations are large. First, many data points are clustered and clearly do not provide a random time sampling. This could result in correlations that effectively reduce the total number of independent measurements. Second, the high minimum χ^2 value that is three times the quoted observational error indicates that there are additional effects (e.g. sunspots, additional planets, etc.) that produce a jitter in the central star (M. Mayor, private communication), which then enhances the effective observational error.

No matter what process generates the additional noise, we can assume in a first approximation that it follows a Gaussian distribution. We then have to conclude that the effective error of each observation is a factor ~ 3 larger than reported in order to account for the minimum χ^2 , given the quoted number of ~ 60 independent observations. Under these circumstances, we would then conclude that any fit with $\sqrt{\chi^2}$ in the range 2 – 4 would be an equally valid possibility.

In the following, we show that indeed a variety of orbital solutions match the observed RV data with no statistically significant difference when compared to the quoted best fit by Correia et al. (2008). As one illustration, we use the simulation F5 obtained in section 2.3. We take the orbital parameters at a time when the orbital period of the outer planet is closest to the observed value and integrate them for several orbits with our N-body code. The solution is stable for at least one million years. There are only

Parameter	Unit	Correia et al. (2008)		Simulation F5	
		b	c	b	c
$M \sin i$	[M_{Jup}]	0.1872	0.6579	0.1872	0.6579
M_*	[M_{\odot}]		0.82		0.82
a	[AU]	0.6813	0.8972	0.6804	0.8994
e		0.17 ± 0.02	0.097 ± 0.012	0.036	0.017
λ	[deg]	105.8 ± 1.4	269.5 ± 0.6	352.5	153.9
ϖ^a	[deg]	162.6 ± 6.3	7.4 ± 4.3	87.9	292.2
$\sqrt{\chi^2}$			2.79	2.76 ^b (3.51)	
Date	[JD]		2453500	2453500	

Table 2.2: Orbital parameters of HD45364b and HD45364c from different fits.

^aNote that ϖ is not well constrained for nearly circular orbits.

^bRadial velocity amplitude was scaled down by 8%.

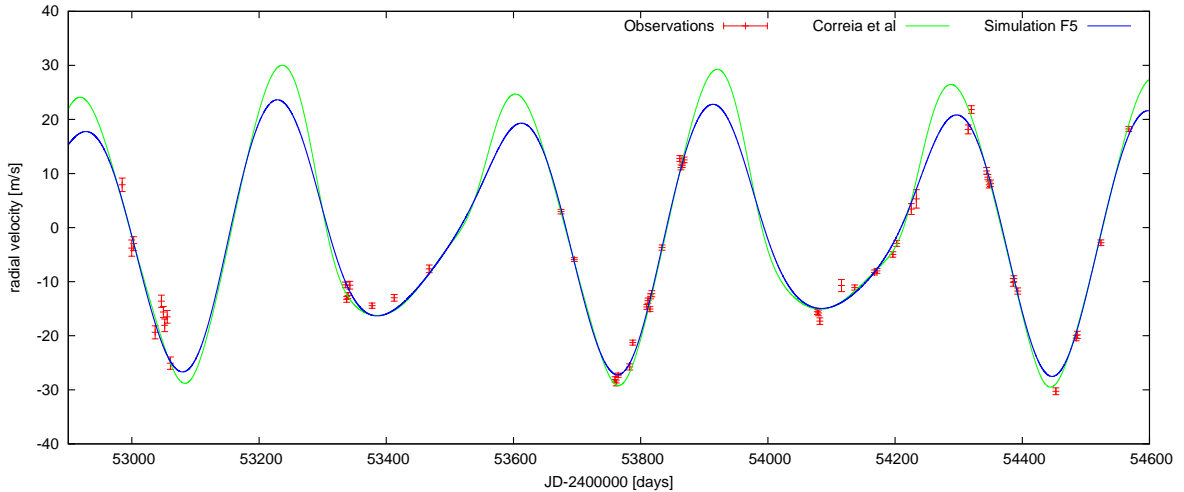


Figure 2.8: Comparison of different orbital solutions. See text for a description of the different models. Radial velocity measurements (red points) and the published orbital solution (green curve) are taken from Correia et al. (2008).

two free parameters available to fit the reflex motion of the central star to the observed radial velocity: the origin of time (epoch) and the angle between the line of sight and the pericentre of the planets.

We can safely assume that the planet masses and periods are measured with high accuracy and that only the shape of the orbit contains large errors. Our best fit results in an unreduced $\sqrt{\chi^2}$ value of 3.51. According to the above discussion, this solution is statistically indistinguishable from a solution with $\sqrt{\chi^2} \sim 2.8$.

It is possible to reduce the value of χ^2 even further, when assuming that the planet masses are not fixed. In that case, we have found a fit corresponding to $\sqrt{\chi^2} = 2.76$ where we have reduced the radial velocity amplitude by 8% (effectively adding one free parameter to the fit). This could be explained by either a heavier star, less massive

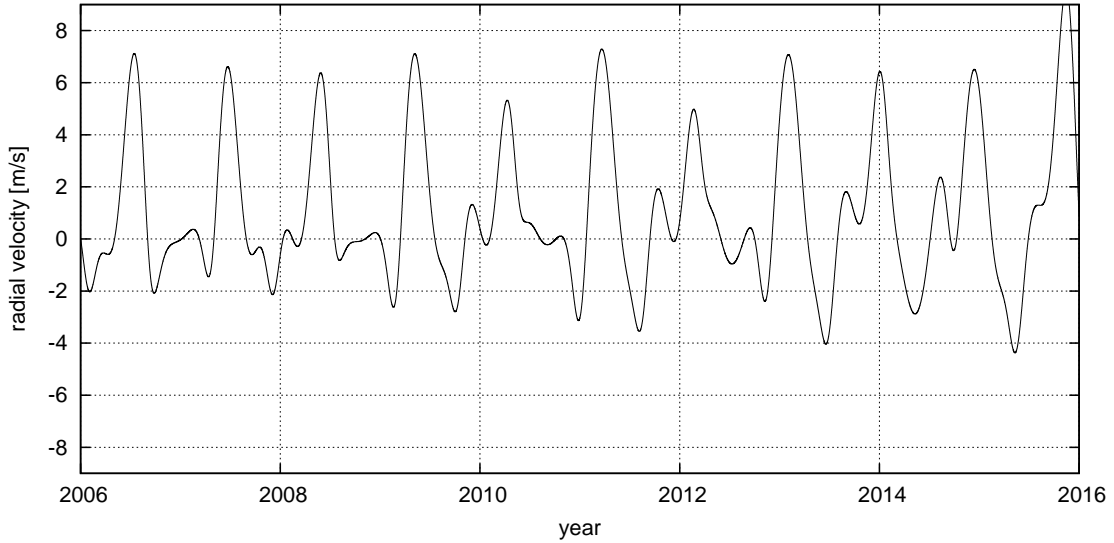


Figure 2.9: Difference in radial velocity between the previously reported fit by Correia et al. (2008) and the new fit obtained from simulation F5.

planets, or a less inclined orbit. The orientation of the orbital plane has been kept fixed ($i = 90^\circ$) in all fits.

The results are shown in figure 2.8. The blue curve corresponds to the outcome of simulation F5 and we list the orbital parameters in table 2.2. We also plot the best fit given by Correia et al. (2008) for comparison (green curve). In accordance with the discussion given above, it is very difficult to see any differences in the quality of these fits, which indeed suggests that the models are statistically indistinguishable.

However, there is an important difference between the fits obtained from our simulations and that of Correia et al. (2008). Our models consistently predict lower values for both eccentricities e_1 and e_2 (see table 2.2). Furthermore, the ratio of eccentricities e_1/e_2 is higher than the previously reported value of 1.73. The eccentricities are oscillating and the ratio is on average ~ 3 .

This in turn results in a different libration pattern: the slow libration mode (see figure 3a in Correia et al. 2008) that is associated with oscillations of the angle between the two apsidal lines is absent, as shown in figure 2.10. Thus there is a marked difference in the form the interaction between the two planets takes place.

It is hoped that future observations will be able to resolve this issue. The evolution of the difference in radial velocity over the next few years between our fit from simulation F5 and the fit found by Correia et al. (2008) is plotted in figure 2.9. There is approximately one window each year that will allow further observations to distinguish easily between the two models. The large difference at these dates is not caused by the secular evolution of the system, but is simply a consequence of smaller eccentricities.

All runs that yield a final configuration with a 3:2 MMR are very similar in their

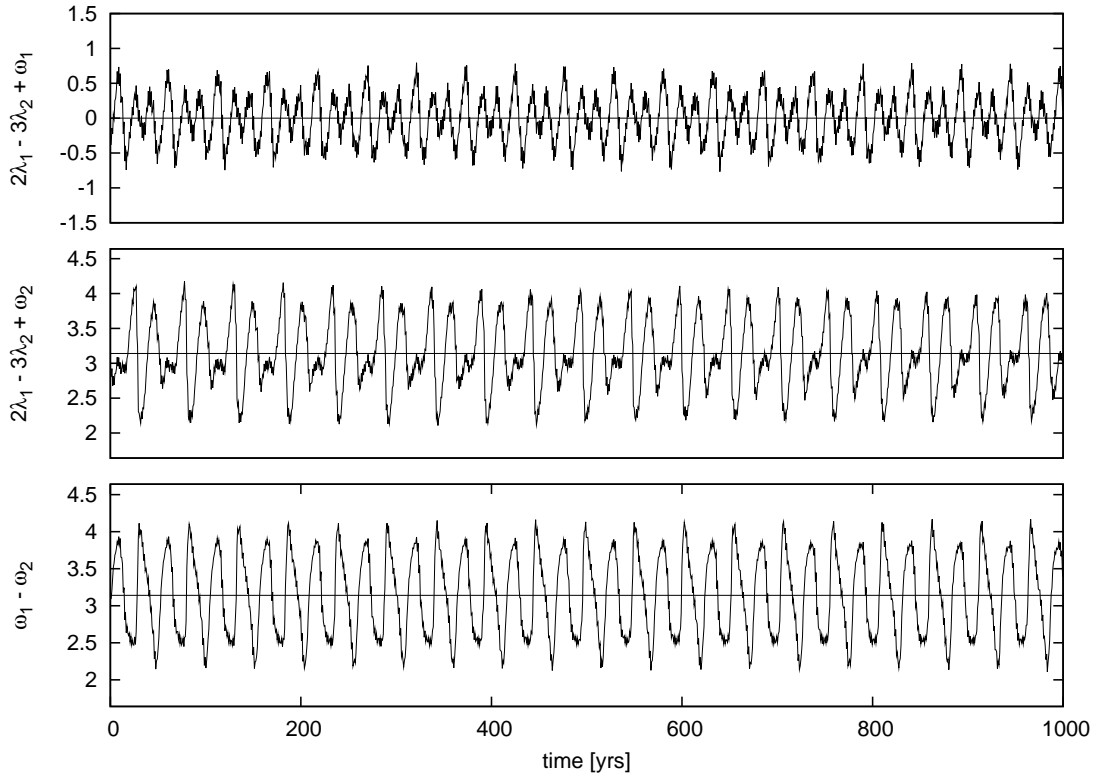


Figure 2.10: Evolution of the resonant angles $\phi_1 = 2\lambda_1 - 3\lambda_2 + \varpi_1$, $\phi_2 = 2\lambda_1 - 3\lambda_2 + \varpi_2$, $\varpi_1 - \varpi_2$ for simulation F5 using the parameters given in table 2.2. The angles are measured in radians.

dynamical behaviour, as found for model F5. They are characterised by an antisymmetric ($\varpi_2 - \varpi_1 \sim \pi$) state with a relatively small libration of ϕ_1 and ϕ_2 . This is a generic outcome of all convergent disc-planet migration scenarios that we performed.

2.6 Conclusions

The planets in the multi-planetary system HD45364 are most likely in a 3:2 mean motion resonance. This poses interesting questions on its formation history. Assuming that the planets form far apart and migrate with a moderate migration rate, as predicted by standard planet formation and migration theories, the most likely outcome is a 2:1 mean motion resonance, contrary to the observation of a 3:2 MMR.

In this chapter, we investigated a possible way around this problem by letting the outer planet undergo a rapid inward type III migration. We presented an analytical estimate of the required migration rate and performed both N-body and hydrodynamical simulations.

We find that it is indeed possible to form a 3:2 MMR and avoid the 2:1 resonance, thus resembling the observed planetary system using reasonable disc parameters. Hydrodynamical simulations suggest that the system is more likely to sustain the resonance

for high aspect ratios, as the migration of the inner planet is slowed down, thus avoiding divergent migration.

Finally, we used the orbital configuration found in the hydrodynamical formation scenario to calculate a radial velocity curve. This curve was then compared to observations and the resulting fit has an identical χ^2 value to the previously reported *best fit*.

Our solution is stable for at least a million years. It is in a dynamically different state, both planets having lower eccentricities and a different libration pattern. This is the first time that planet migration theory can predict a precise orbital configuration of a multiplanetary system. This might also be the first direct evidence for type III migration if this scenario turns out to be true.

The system HD45364 remains an interesting object for observers, as the differences between the two orbital solutions can be measured in radial velocity within a couple of years.

The survival of mean motion resonances in a turbulent disc

Every body continues in its state of rest, or of uniform motion in a right line, unless it is compelled to change that state by forces impressed upon it.

Isaac Newton, *Principia Mathematica*, 1687

As shown for the system HD45364 in chapter 2, resonant configurations can be established as a result of dissipative forces acting on the planets which lead to convergent migration. The previous chapter assumes a laminar disc. However, in general the disc is thought to be turbulent because, as discussed in more detail in chapter 1, the molecular viscosity is not large enough to drive the observed outward angular momentum flux. The most promising mechanism to drive turbulence is the magneto-rotational instability, MRI (Balbus & Hawley 1991), although other possibilities are still being discussed (see e.g. Lesur & Papaloizou 2009).

In this chapter, we study the effects of density perturbations in the disc resulting from any kind of turbulence on planetary systems. We do not solve the full 3D magneto hydrodynamics equations, but rather assume a parametrisation for the forces acting on planets. This has two main advantages. First, we can understand the relevant dynamical processes much more easily. Second, there is a large diversity of simulations of the MRI in the literature which exhibit different diffusion coefficients, varying by several orders of magnitude. By parametrising the forces, we avoid these difficulties altogether.

Using this approach, we study the response of both a single planet and planetary systems in a 2:1 mean motion commensurability to stochastic forcing. The forcing could for example result from MRI turbulence. We first develop an analytic model from first

principles. We can isolate two distinct libration modes for the resonant angles which react differently to stochastic forcing.

Systems are quickly destabilised if the magnitude of the stochastic forcing is large. The growth of libration amplitudes is parametrised as a function of the diffusion coefficient and other relevant physical parameters. We also perform numerical N-body simulations with additional stochastic forcing terms to represent the effects of disc turbulence. These are in excellent agreement with the analytic model.

Stochastic forcing due to disc turbulence may have played a role in shaping the configurations of observed systems in mean motion resonance. It naturally provides a mechanism for accounting for the HD128311 system, for which the fast mode librates and the slow mode is apparently near the borderline between libration and circulation.

3.1 Basic equations

We begin by writing down the equations of motion for a single planet moving in a fixed plane under a general Hamiltonian H in the form (see e.g. Snellgrove et al. 2001; Papaloizou 2003)

$$\dot{E} = -n \frac{\partial H}{\partial \lambda} \quad (3.1)$$

$$\dot{L} = - \left(\frac{\partial H}{\partial \lambda} + \frac{\partial H}{\partial \varpi} \right) \quad (3.2)$$

$$\dot{\lambda} = \frac{\partial H}{\partial L} + n \frac{\partial H}{\partial E} \quad (3.3)$$

$$\dot{\varpi} = \frac{\partial H}{\partial L}. \quad (3.4)$$

Here the angular momentum of the planet is L and the energy is E . For a Keplerian orbital motion around a central point mass M we have

$$L = m \sqrt{GMa(1 - e^2)} \quad \text{and} \quad (3.5)$$

$$E = -\frac{GMm}{2a}, \quad (3.6)$$

where G is the gravitational constant, a the semi-major axis and e the eccentricity (see appendix A). For an elliptical orbit around a point mass, equation 3.3 results in a linear growth of the mean longitude

$$\lambda = n(t - t_0) + \varpi, \quad (3.7)$$

where n is the mean motion, t_0 being the time of periastron passage and ϖ being the longitude of periastron. All other equations of motion are trivial as the right hand side equates to zero.

3.1.1 Additional forcing of a single planet

In order to study phenomena such as stochastic forcing, we need to consider the effects of an additional external force per unit mass \mathbf{F} , which may or may not be described using a Hamiltonian formalism. However, as may be seen by considering general coordinate transformations starting from a Cartesian representation, the equations of motion are linear in the components of \mathbf{F} . Because of this we may determine them by considering forces of the form $\mathbf{F} = (F_x, F_y)$ for which the Cartesian components are constant. Having done this we may then suppose that these vary with coordinates and time in an arbitrary manner. Following this procedure we note that when \mathbf{F} , as in the above form is constant, we can derive the equations of motion by replacing the original Hamiltonian with a new Hamiltonian defined through

$$H \rightarrow H - m(F_x x + F_y y) = H - m(\mathbf{r} \cdot \mathbf{F}). \quad (3.8)$$

The additional terms proportional to the components of \mathbf{F} correspond to the Gaussian form of the equations of motion (Brouwer & Clemence 1961).

The various derivatives involving \mathbf{r} can be calculated by elementary means and expressed in terms of E, L, λ and ϖ . One thus finds additional contributions to the equations of motion 3.1 - 3.4, indicated with a subscript F , in the form

$$\dot{L}_F = m \left(\frac{\partial}{\partial \lambda} + \frac{\partial}{\partial \varpi} \right) (\mathbf{r} \cdot \mathbf{F}) = m (\mathbf{r} \times \mathbf{F}) \cdot \hat{\mathbf{e}}_z \quad (3.9)$$

$$\dot{E}_F = mn \frac{\partial}{\partial \lambda} (\mathbf{r} \cdot \mathbf{F}) = m (\mathbf{v} \cdot \mathbf{F}) \quad (3.10)$$

$$\dot{\varpi}_F = -m \frac{\partial}{\partial L} (\mathbf{r} \cdot \mathbf{F}) \quad \text{or equivalently} \quad (3.11)$$

$$\dot{\varpi}_F = \frac{\sqrt{(1-e^2)}}{nae} \left[F_\theta \left(1 + \frac{1}{1-e^2} \frac{r}{a} \right) \sin f - F_r \cos f \right] \quad (3.12)$$

$$\dot{\lambda}_F = -m \left(\frac{\partial}{\partial L} + n \frac{\partial}{\partial E} \right) (\mathbf{r} \cdot \mathbf{F}) = \left(1 - \sqrt{1-e^2} \right) \dot{\varpi}_F + \frac{2an}{GM} (\mathbf{r} \cdot \mathbf{F}), \quad (3.13)$$

where the true anomaly f is defined as the difference between the true longitude and the longitude of periastron, $f = \theta - \varpi$ (see also appendix A). Note that from equation 3.10 we obtain

$$\dot{a}_F = -\frac{2a\dot{n}}{3n} = \frac{2(F_r e \sin f + F_\theta (1 + e \cos f))}{n\sqrt{1-e^2}}. \quad (3.14)$$

and from equation 3.9 together with equation 3.10 we obtain

$$\dot{e}_F = \frac{L(2E\dot{L} + L\dot{E})}{G^2 m^3 M^2 e}. \quad (3.15)$$

In the limit $e \ll 1$ this becomes (ignoring terms $O(e)$ and smaller)

$$\dot{e}_F = F_r \frac{1}{an} \sin f + F_\theta \frac{1}{an} 2 \cos f. \quad (3.16)$$

Furthermore in this limit we may replace f by $f = \lambda - \varpi = n(t - t_0)$.

Note that the above formalism results in equation 3.12 for $\dot{\varpi}_F$, which diverges for small e as $1/e$. This comes from the choice of coordinates used and is not associated with any actual singularity or instability in the system. This is readily seen if one uses $h = e \sin \varpi$, and $k = e \cos \varpi$ as dynamical variables rather than e and ϖ . The former set behave like Cartesian coordinates, while the latter set are the corresponding cylindrical polar coordinates. When the former set is used, potentially divergent terms $\propto 1/e$ do not appear. This can be seen from equations 3.12 and 3.16 which give in the small e limit

$$\dot{h}_F = -F_r \frac{1}{an} \sin \lambda + F_\theta \frac{1}{an} 2 \cos \lambda \quad (3.17)$$

$$\dot{k}_F = F_r \frac{1}{an} \sin \lambda + F_\theta \frac{1}{an} 2 \cos \lambda. \quad (3.18)$$

Abrupt changes to ϖ may occur when h and k pass through the origin in the (h, k) plane. But this is clearly just a coordinate singularity rather than a problem with the physical system which changes smoothly on transition through the origin. The abrupt changes to the ϖ coordinate occur because very small perturbations to very nearly circular orbits produce large changes to this angle.

3.1.2 Multiple planets

Up to now we have considered a single planet. We now generalise the formalism so that it applies to a system of two planets. We follow closely the discussions in Papaloizou (2003) and Papaloizou & Szuszkiewicz (2005). Excluding stochastic forcing for the time being, we start from the Hamiltonian formalism describing their mutual interactions using Jacobi coordinates (Sinclair 1975). In this formalism the motion of the outer planet is described around the centre of mass of the star plus the inner planet rather than the star alone. Thus, the radius vector \mathbf{r}_2 , of the inner planet of mass m_2 is measured from the star with mass M and that of the outer planet, \mathbf{r}_1 , of mass m_1 is referred to the centre of mass of M and m_2 . The reduced masses of m_2 and m_1 are then defined as $\mu_2 = m_2 \cdot M / (M + m_2)$ and $\mu_1 = m_1 \cdot (M + m_2) / (M + m_2 + m_1)$. We also define $M_2 = M + m_2$ and $M_1 = M + m_2 + m_1$. From now on we consistently adopt subscripts 1 and 2 for coordinates related to the outer and inner planets respectively. Note that this is different from the previous chapter.

The required Hamiltonian, is given by (Murray & Dermott 2000, p.440ff):

$$H = \frac{1}{2} \mu_2 |\dot{\mathbf{r}}_2|^2 + \frac{1}{2} \mu_1 |\dot{\mathbf{r}}_1|^2 - \frac{GM_2 \mu_2}{|\mathbf{r}_2|} - \frac{GMm_1}{|\mathbf{r}_{01}|} - \frac{Gm_1 m_2}{|\mathbf{r}_{12}|}. \quad (3.19)$$

Here \mathbf{r}_{ij} is the relative position vector between the objects with subscript i and j , where 0 denotes the star. The Hamiltonian can be expressed in terms of $E_i, L_i, \varpi_i, \lambda_i, i =$

1, 2 and the time t . The energies are given by $E_i = -Gi\mu_i M_i/(2a_i)$ and the angular momenta $L_i = \mu_i \sqrt{GM_i a_i (1 - e_i^2)}$ with a_i and e_i denoting the semi-major axes and eccentricities respectively. The mean motions are $n_i = \sqrt{GM_i/a_i^3}$. As $m_i \ll M$, we replace M_i by M and μ_i by m_i from now on.

The interaction Hamiltonian (the term $\propto m_1 m_2$ in equation 3.19) can be expanded in a Fourier series involving linear combinations of the three angular differences $\lambda_i - \varpi_i$, $i = 1, 2$ and $\varpi_1 - \varpi_2$ (e.g. Brouwer & Clemence 1961). Near a first order $p+1 : p$ resonance, we expect that both $\phi_1 = (p+1)\lambda_1 - p\lambda_2 - \varpi_2$, and $\phi_2 = (p+1)\lambda_1 - p\lambda_2 - \varpi_1$, will be slowly varying. Following standard practice (see e.g. Papaloizou 2003; Papaloizou & Szuszkiewicz 2005) only terms in the Fourier expansion involving linear combinations of ϕ_1 and ϕ_2 as argument are retained because only these are expected to lead to large long term perturbations.

The resulting Hamiltonian may then be written in the general form $H = E_1 + E_2 + H_{12}$, where the interaction Hamiltonian is given by

$$H_{12} = -\frac{Gm_1 m_2}{a_1} \sum C_{k,l} \left(\frac{a_1}{a_2}, e_1, e_2 \right) \cos(l\phi_1 + k\phi_2), \quad (3.20)$$

where in the above and similar summations below, the sum ranges over all positive and negative integers (k, l) and the dimensionless coefficients $C_{k,l}$ depend on e_1, e_2 and the ratio of semi-major axes a_1/a_2 only.

Equations of motion for two planets

The equations of motion for each planet can now be easily derived, that take into account the contributions due to their mutual interactions (see Papaloizou 2003; Papaloizou & Szuszkiewicz 2005) and contributions from 3.9 - 3.13. The latter terms arising from external forcing are indicated with a subscript F . We obtain to lowest order in the perturbing masses:

$$\frac{dn_1}{dt} = \frac{3(p+1)n_1^2 m_2}{M} \sum C_{k,l} (k+l) \sin(l\phi_1 + k\phi_2) + \left(\frac{dn_1}{dt} \right)_F \quad (3.21)$$

$$\frac{dn_2}{dt} = -\frac{3pn_2^2 m_1 a_2}{Ma_1} \sum C_{k,l} (k+l) \sin(l\phi_1 + k\phi_2) + \left(\frac{dn_2}{dt} \right)_F \quad (3.22)$$

$$\begin{aligned} \frac{de_1}{dt} = & -\frac{m_2 n_1 \sqrt{1-e_1^2}}{e_1 M} \cdot \sum C_{k,l} \sin(l\phi_1 + k\phi_2) \\ & \cdot \left[k - (p+1)(k+l) \left(1 - \sqrt{1-e_1^2} \right) \right] + \left(\frac{de_1}{dt} \right)_F \end{aligned} \quad (3.23)$$

$$\begin{aligned} \frac{de_2}{dt} = & -\frac{m_1 a_2 n_2 \sqrt{1-e_2^2}}{a_1 e_2 M} \cdot \sum C_{k,l} \sin(l\phi_1 + k\phi_2) \\ & \cdot \left[l + p(k+l) \left(1 - \sqrt{1-e_2^2} \right) \right] + \left(\frac{de_2}{dt} \right)_F \end{aligned} \quad (3.24)$$

$$\frac{d\phi_2}{dt} = (p+1)n_1 - pn_2 - \sum (D_{k,l} + E_{k,l}) \cos(l\phi_1 + k\phi_2) + \left(\frac{d\phi_2}{dt}\right)_F \quad (3.25)$$

$$\frac{d\phi_1}{dt} = (p+1)n_1 - pn_2 - \sum (D_{k,l} + F_{k,l}) \cos(l\phi_1 + k\phi_2) + \left(\frac{d\phi_1}{dt}\right)_F. \quad (3.26)$$

Here

$$D_{k,l} = \frac{2(p+1)n_1a_1^2m_2}{M} \frac{\partial}{\partial a_1} (C_{k,l}/a_1) - \frac{2pn_2a_2^2m_1}{M} \frac{\partial}{\partial a_2} (C_{k,l}/a_1), \quad (3.27)$$

$$E_{k,l} = \frac{n_1m_2 \left((p+1)(1-e_1^2) - p\sqrt{1-e_1^2} \right) \frac{\partial C_{k,l}}{\partial e_1}}{e_1M} + \frac{pn_2a_2m_1 \left(\sqrt{1-e_2^2} - 1 + e_2^2 \right) \frac{\partial C_{k,l}}{\partial e_2}}{a_1e_2M} \quad (3.28)$$

and

$$F_{k,l} = \frac{(p+1)n_1m_2 \left(1 - e_1^2 - \sqrt{1-e_1^2} \right) \frac{\partial C_{k,l}}{\partial e_1}}{e_1M} + \frac{n_2a_2m_1 \left((p+1)\sqrt{1-e_2^2} - p(1-e_2^2) \right) \frac{\partial C_{k,l}}{\partial e_2}}{a_1e_2M}. \quad (3.29)$$

Note that $\phi_2 - \phi_1 = \varpi_2 - \varpi_1 \equiv \zeta$ is the angle between the two apsidal lines of the two planets. We also comment that, up to now, we have not assumed that the eccentricities are small and that, in addition to stochastic contributions, the external forcing terms may in general contain contributions from very slowly varying disc tides.

Modes of libration

We first consider two planets in resonance with no external forces, to identify the possible libration modes. In the absence of external forces, equations 3.21 - 3.26 can have a solution for which a_i and e_i are constants and the angles ϕ_1 and ϕ_2 are zero. In general, other values for the angles may be possible but such cases do not occur for the numerical examples presented below. When the angles are zero, equations 3.25 and 3.26 provide a relationship between e_1 and e_2 (see e.g. Papaloizou 2003).

We go on to consider small amplitude oscillations or librations of the angles about their equilibrium state. Because two planets are involved there are two modes of oscillation, which we find convenient to separate and describe as fast and slow modes. Assuming the planets have comparable masses, the fast mode has a libration frequency $\propto \sqrt{m}$ and the slow mode has a libration frequency $\propto m$. These modes clearly separate as the planet masses are changed while maintaining fixed eccentricities.

Fast mode

To obtain the fast mode we linearise equations 3.21 - 3.26 and neglect second order terms in the planet masses. This is equivalent to neglecting the variation of $D_{k,l}, E_{k,l}$

and $F_{k,l}$ in equations 3.25 and 3.26 which then require that $\phi_1 = \phi_2$ very nearly for this mode. Noting that for linear modes of the type considered here and in the next section, equations 3.21 - 3.24 imply that \dot{n}_i and \dot{e}_i are proportional to linear combinations of the librating angles, differentiation of either of equations 3.25 or 3.26 with respect to time then gives for small amplitude oscillations

$$\frac{d^2\phi_i}{dt^2} + \omega_{if}^2\phi_i = 0, \quad (i = 1, 2), \quad (3.30)$$

where

$$\omega_{if}^2 = -\frac{3p^2n_2^2m_2}{M} \left(1 + \frac{a_2m_1}{a_1m_2}\right) \cdot \sum C_{k,l}(k+l)^2, \quad (3.31)$$

and we have used the resonance condition that $(p+1)n_1 = pn_2$ which is satisfied to within a correction of order $\sqrt{m_1/M}$. Note that for this mode the fact that $\phi_1 = \phi_2$ very nearly, implies that $\varpi_2 - \varpi_1$ is small. Thus that quantity does not participate in the oscillation.

Slow mode

Now, we look for low frequency librations with frequency $\propto m_1$. Equations 3.25 and 3.26 imply that, for such oscillations, to within a small relative error of order m_1/M , $(p+1)n_1 = pn_2$ throughout.

Equations 3.21 and 3.22 then imply that the two angles are related by $\phi_2 = \beta\phi_1$, where $\beta = -\sum C_{k,l}(k+l)l / (\sum C_{k,l}(k+l)k)$. Subtracting equation 3.26 from equation 3.25, differentiating with respect to time and using this condition results in an equation for $\zeta = \phi_2 - \phi_1 = \varpi_2 - \varpi_1$

$$\frac{d^2\zeta}{dt^2} + \omega_{is}^2\zeta = 0, \quad (3.32)$$

where

$$\omega_{is}^2 = \alpha_1 \frac{n_1m_2\sqrt{1-e_1^2}}{e_1M(1-\beta)} \frac{\partial W}{\partial e_1} + \alpha_2 \frac{n_2a_2m_1\sqrt{1-e_2^2}}{a_1e_2M(1-\beta)} \frac{\partial W}{\partial e_2} \quad (3.33)$$

with

$$\begin{aligned} \alpha_1 &= \sum C_{k,l} \left[k - (p+1)(k+l) \left(1 - \sqrt{1-e_1^2}\right) \right] (k\beta + l), \\ \alpha_2 &= \sum C_{k,l} \left[l + p(k+l) \left(1 - \sqrt{1-e_2^2}\right) \right] (k\beta + l) \end{aligned}$$

and

$$W = \left(\frac{n_1a_2m_2\sqrt{1-e_2^2}}{a_1e_2M} \frac{\partial}{\partial e_2} - \frac{n_2m_1\sqrt{1-e_1^2}}{e_1M} \frac{\partial}{\partial e_1} \right) \cdot \sum C_{k,l}.$$

Although the expressions for the mode frequencies are complicated, the fast frequency scales as the square root of the planet mass and the slow frequency scales as the planet mass. Both frequencies scale with the characteristic mean motion of the system.

Librations with external forcing

When external forcing is included source terms appear on the right hand sides of equations 3.30 and 3.32. We assume that the forcing terms are small so that terms involving products of these and both the libration amplitudes and the planet masses may be neglected. Then, in the case of the slow mode, repeating the derivation given above including the forcing terms, we find that equation 3.32 becomes

$$\frac{d^2\zeta}{dt^2} + \omega_{ls}^2\zeta = \frac{d}{dt}(\dot{\varpi}_{2F} - \dot{\varpi}_{1F}). \quad (3.34)$$

The quantities $\dot{\varpi}_{iF}$ are readily obtained for each planet from equation 3.12. From this we see that for small eccentricities, $\dot{\varpi}_{iF} \propto 1/e_i$, indicating large effects when e_i is small. As already discussed, this feature arises from a coordinate singularity rather than physically significant changes to the system.

A similar description may be found for the fast mode. In this case, neglecting terms of the order of the square of the planet masses or higher, one may use equations 3.25 and 3.26 to obtain an equation for ϕ_1 in the form

$$\frac{d^2\phi_1}{dt^2} + \omega_{lf}^2\phi_1 = \frac{d}{dt}(\dot{\phi}_{1F}) + (p+1)\dot{n}_{1F} - p\dot{n}_{2F}. \quad (3.35)$$

Equations 3.35 and 3.34 form a pair of equations for the stochastically forced fast and slow modes respectively. This mode separation is not precise. However, it can be made so by choosing appropriate linear combinations of the above modes. Numerical results confirm that ϕ_1 predominantly manifests the fast mode and ζ the slow mode, so we do not expect such a change of basis to significantly affect conclusions.

We further comment that because $\dot{\phi}_{1F}$ contains $\dot{\varpi}_{2F}$ but not $\dot{\varpi}_{1F}$, for small eccentricities there are only potential forcing terms $\propto 1/e_2$ that occur when forcing is applied to the inner planet. As this planet has the larger eccentricity for the situations we consider, small eccentricities are not found to play any significant role in this case.

Each mode responds as a forced oscillator. The forcing contains a stochastic component which tends to excite the respective oscillator and ultimately convert libration into circulation. But we stress that the above formulation as well as developments below assume small librations, so we may only assess the initial growth of oscillation amplitude. However, inferences based on the structure of the non linear governing equations and an extrapolation of the linear results enable successful comparison with numerical results.

3.1.3 Stochastic forces

We assume that turbulence causes the external force per unit mass (F_r, F_θ) acting on each planet to be stochastic. For simplicity we shall adopt the simplest possible model.

Each component of the force satisfies the relation

$$F_i(t)F_i(t') = \langle F_i^2 \rangle g(|t - t'|) \quad (3.36)$$

where the auto-correlation function $g(x)$ is such that $\int_0^\infty g(x)dx = \tau_c$, where τ_c is the correlation time and $\sqrt{\langle F_i^2 \rangle}$ is the root mean square value of the i component. Note that an ensemble average is implied on the left hand side. Again, for simplicity we assume that different components acting on the same planet as well as components acting on different planets are uncorrelated. The root mean square values as well as τ_c may in general depend on t , but we shall not take this into account here and simply assume that these quantities are constant and the same for each force component.

The stochastic forces make quantities they act on undergo a random walk. Thus, if for example $\dot{A} = F_i$ for some quantity¹ A , the square of the change of A occurring after a time interval t is given by

$$\begin{aligned} (\Delta A)^2 &= \int_0^t \int_0^t F_i(t')F_i(t'')dt'dt'' \\ &= \int_0^t \int_0^t \langle F_i^2 \rangle g(|t' - t''|)dt'dt'' \rightarrow D_i t. \end{aligned} \quad (3.37)$$

Here we take the limit where t/τ_c is very large corresponding to an integration time of many correlation times and $D_i = 2 \langle F_i^2 \rangle \tau_c$ is the diffusion coefficient.

When the evolution of a stochastically forced planetary orbit is considered, it is more appropriate to consider a model governing equation for A of the generic form

$$\dot{A} = F_i \sin(nt), \quad (3.38)$$

where we recall that $2\pi/n$ is the orbital period (but note that a different value could equally well be considered). We note in passing that, by shifting the origin of time, an arbitrary phase may be added to the argument without changing the results given below. One readily finds that equation 3.37 is replaced by

$$\begin{aligned} (\Delta A)^2 &= \int_0^t \int_0^t F_i(t')F_i(t'') \sin(nt') \sin(nt'')dt'dt'' \\ &= \int_0^t \int_0^t \langle F_i^2 \rangle g(|t' - t''|) \sin(nt') \sin(nt'')dt'dt'' \\ &\rightarrow \frac{\gamma D t}{2}, \end{aligned} \quad (3.39)$$

where we introduce a new correction factor $\gamma(n) = \int_0^\infty g(x) \cos(nx)dx$. If $n\tau_c \ll 1$, corresponding to the correlation time being much less than the orbital period, then $\gamma \rightarrow 1$. For larger τ_c , $\gamma < 1$ gives a reduction factor for the amount of stochastic

¹Constants or slowly varying quantities originally multiplying F_i may be absorbed by a redefinition of A and so do not affect the discussion given below.

diffusion. For example if we adopt, an exponential form for the auto-correlation function such that

$$g(|t' - t''|) = \exp\left(-\frac{|t' - t''|}{\tau_c}\right),$$

we find

$$\gamma = \frac{1}{1 + n^2\tau_c^2}, \quad (3.40)$$

and for the purposes of simplicity and comparison with numerical work we shall use this from now on.

Stochastic forcing of an isolated planet

In the case of a stochastically forced single planet we may obtain a statistical estimate for the characteristic growth of the orbital parameters as a function of time by directly integrating equations 3.10, 3.12, 3.16, 3.17 and 3.18 with respect to time. We may then apply the formalism leading to the results expressed in generic form through equations 3.37 - 3.40 to obtain estimates for the stochastic diffusion of the orbital elements in the limit of small eccentricity in the form

$$(\Delta a)^2 = 4 \frac{Dt}{n^2} \quad (3.41)$$

$$(\Delta n)^2 = 9 \frac{Dt}{a^2} \quad (3.42)$$

$$(\Delta e)^2 = 2.5 \frac{\gamma Dt}{n^2 a^2} \quad (3.43)$$

$$(\Delta \varpi)^2 = \frac{2.5 \gamma Dt}{e^2 n^2 a^2} \quad (3.44)$$

$$(\Delta h)^2 = 2.5 \frac{\gamma Dt}{n^2 a^2} \quad (3.45)$$

$$(\Delta k)^2 = 2.5 \frac{\gamma Dt}{n^2 a^2}. \quad (3.46)$$

As mentioned before, the $1/e^2$ dependence of $(\Delta \varpi)^2$ which arises from the coordinate singularity does not appear for $(\Delta h)^2$ and $(\Delta k)^2$. Note that the definitions of h and k imply, consistently with the above, that

$$(\Delta h)^2 = (\Delta e)^2 \sin^2 \varpi + e^2 (\Delta \varpi)^2 \cos^2 \varpi \quad (3.47)$$

$$(\Delta k)^2 = (\Delta e)^2 \cos^2 \varpi + e^2 (\Delta \varpi)^2 \sin^2 \varpi. \quad (3.48)$$

The evolution of the longitude

Of special interest is also the evolution of the planet's mean longitude. In observations of Saturn's rings, for example, it is much easier to measure a shift of the longitude of an

embedded moonlet compared to a direct measurement of the change in its semi-major axis. The time derivative of the mean motion is given by

$$\dot{n} = -\frac{3}{2}\sqrt{\frac{GM}{a^5}}\dot{a} = -\frac{3 F_\theta}{a}. \quad (3.49)$$

Assuming a nearly circular ($e \ll 1$) orbit, the mean longitude is thus given by the double integral

$$\lambda(t) = \int_0^t (n + \Delta n(t')) dt' \quad (3.50)$$

$$= nt - \int_0^t \int_0^{t'} \frac{3F_\theta(t'')}{a} dt'' dt'. \quad (3.51)$$

The root mean square of the difference compared to the unperturbed orbit is

$$(\Delta\lambda)^2 = \langle (\lambda(t) - nt)^2 \rangle^{0.5} \quad (3.52)$$

$$= \int_0^t \int_0^{t'} \int_0^t \int_0^{t'''} \frac{9F_\theta(t'')F_\theta(t'''')}{a^2} dt'''' dt''' dt'' dt' \quad (3.53)$$

$$= \frac{9\langle F_\theta^2 \rangle}{a^2} \int_0^t \int_0^{t'} \int_0^t \int_0^{t'''} g(|t'' - t''''|) dt'''' dt''' dt'' dt' \quad (3.54)$$

$$= \frac{9\langle F_\theta^2 \rangle}{a^2} \left(-2\tau_c^4 + (2\tau_c^3 t + 2\tau_c^4 + \tau_c^2 t^2) e^{-t/\tau_c} + \frac{1}{3}\tau_c t^3 \right) \quad (3.55)$$

$$\stackrel{t \gg \tau_c}{\approx} \frac{9\langle F_\theta^2 \rangle \tau_c}{a^2} t^3 = \frac{3D}{2a^2} t^3 = (\Delta n)^2 \frac{t^2}{6}, \quad (3.56)$$

where we have taken the limit of $t \gg \tau_c$ in the last line. We also assume an exponentially decaying auto-correlation function g because the integral in equation 3.54 can not be solved analytically for an arbitrary function g . Note that on short timescales, other terms in equation 3.56 may dominate the growth of λ .

Instead of a stochastic migration, let us also assume a laminar migration with constant migration rate τ_a , given by

$$\tau_a = \frac{a}{\dot{a}} = -\frac{3n}{2\dot{n}}. \quad (3.57)$$

As above, we can calculate the longitude as a function of time as the following double integral

$$\lambda(t) = \int_0^t (n + \Delta n(t')) dt' \quad (3.58)$$

$$= nt - \int_0^t \int_0^{t'} \frac{3n}{2\tau_a} dt'' dt' = nt - \frac{3n}{4\tau_a} t^2 \quad (3.59)$$

and thus

$$(\Delta\lambda)^2 = \frac{9n^2}{8\tau_a^2} t^4 = (\Delta n)^2 \frac{t^2}{2}. \quad (3.60)$$

Note that equation 3.60 is an exact solution, whereas equation 3.56 is a statistical quantity, describing the root mean square value in an ensemble average. In the stochastic and laminar case, $(\Delta\lambda)^2$ grows like $\sim t^3$ and $\sim t^4$, respectively. This allows to discriminate the different mechanisms by observing $\Delta\lambda$ over an extended period of time.

Stochastic variation of the resonant angles in the two planet case

We now consider the effects of stochastic forcing on the resonant angles. The expressions are more complicated than in the previous section because there are more variables involved. However, we basically follow the same formalism.

While the libration amplitude is small enough for linearisation to be reasonable, the evolution is described by equations 3.34 and 3.35. These may be solved by the method of variation of parameters. Assuming the amplitude is zero at $t = 0$, the solution of equation 3.34 is given by

$$\zeta = \sin(\omega_{ls}t) \int_0^t \frac{S_\zeta \cos(\omega_{ls}t)}{\omega_{ls}} dt - \cos(\omega_{ls}t) \int_0^t \frac{S_\zeta \sin(\omega_{ls}t)}{\omega_{ls}} dt, \quad (3.61)$$

where $S_\zeta = d(\dot{\varpi}_{2F} - \dot{\varpi}_{1F})/dt$. Equation 3.61 may be regarded as describing a harmonic oscillator whose amplitude varies in time such that the square of the amplitude after a time interval t is given by

$$(\Delta\zeta)^2 = \left(\int_0^t \frac{S_\zeta \sin(\omega_{ls}t)}{\omega_{ls}} dt \right)^2 + \left(\int_0^t \frac{S_\zeta \cos(\omega_{ls}t)}{\omega_{ls}} dt \right)^2. \quad (3.62)$$

The corresponding expression for equation 3.35 is

$$(\Delta\phi_1)^2 = \left(\int_0^t \frac{S_\phi \sin(\omega_{lf}t)}{\omega_{lf}} dt \right)^2 + \left(\int_0^t \frac{S_\phi \cos(\omega_{lf}t)}{\omega_{lf}} dt \right)^2, \quad (3.63)$$

where $S_\phi = d(\dot{\phi}_{1F})/dt + (p+1)\dot{n}_{1F} - p\dot{n}_{2F}$.

We now evaluate the expectation values of these using the formalism of the previous section. For simplicity we specialise to the case when stochastic forces act only on the outer planet. This is also what has been considered numerically later. Taking equation 3.62, we perform an integration by parts, neglecting the end point contributions as these are sub-dominant (they increase less rapidly than t for large t), to obtain

$$(\Delta\zeta)^2 = \left(\int_0^t \dot{\varpi}_{1F} \sin(\omega_{ls}t) dt \right)^2 + \left(\int_0^t \dot{\varpi}_{1F} \cos(\omega_{ls}t) dt \right)^2. \quad (3.64)$$

In dealing with equation 3.63 we neglect $\dot{\phi}_{1F}$ in S_ϕ because after integration by parts this leads to a contribution on the order ω_{lf}/n smaller than that derived from \dot{n}_{1F} . Thus, we simply obtain

$$\frac{(\Delta\phi_1)^2}{(p+1)^2} = \left(\int_0^t \frac{\dot{n}_{1F} \sin(\omega_{lf}t)}{\omega_{lf}} dt \right)^2 + \left(\int_0^t \frac{\dot{n}_{1F} \cos(\omega_{lf}t)}{\omega_{lf}} dt \right)^2.$$

We again follow the procedures outlined in the previous section to obtain the final growth estimates

$$(\Delta e_1 e_2 \sin \zeta)^2 = 2.5 \frac{D e_2^2 \gamma_s t}{2 a_1^2 n_1^2} \quad \text{and} \quad (3.65)$$

$$\frac{(\Delta \phi_1)^2}{(p+1)^2} = \frac{9 D \gamma_f t}{a_1^2 \omega_{lf}^2}, \quad (3.66)$$

where the corrections factors are given by

$$\gamma_f = \frac{1}{1 + \omega_{lf}^2 \tau_c^2} \quad \text{and} \quad (3.67)$$

$$\gamma_s = \frac{1}{1 + (n_1 + \omega_{ls})^2 \tau_c^2} + \frac{1}{1 + (n_1 - \omega_{ls})^2 \tau_c^2}. \quad (3.68)$$

The correction factors γ_f and γ_s compare the relevant timescales of the system (here, the libration periods) to the correlation time of the stochastic force.

Growth of libration amplitudes

Equations 3.65 and 3.66 express the expected growth of the resonant angle libration amplitudes as a function of time. These expressions can be simply related to those obtained for a single planet. Thus equations 3.41 and 3.66 applied to the outer planet imply that

$$(\Delta \phi_1)^2 / (\Delta a_1)^2 = 9(p+1)^2 n_1^2 \gamma_f / (4 a_1^2 \omega_{lf}^2).$$

As we are interested in the case $p = 1$, the width of the libration zone is $\sim a_1 \omega_{lf} / n_1$, we see that the time for $(\Delta \phi_1)^2$ to reach unity is comparable for the semi-major axis to diffuse through the libration zone.

For fixed eccentricity of the inner planet e_2 , equation 3.65 indicates that ζ , being the angle between the apsidal lines of the two planets, diffuses in the same way as for an isolated outer planet subject to stochastic forces. Thus, in the small amplitude regime, the way this diffusion occurs would appear to be essentially independent of whether the planets are in resonance.

An important consequence of equation 3.65 is the behaviour of ζ for small e_1 . The latter quantity was assumed constant in the analysis. As already discussed earlier, abrupt changes to ζ are expected when the eccentricity of one planet gets very small. Then, even an initially small amplitude libration is converted to circulation. Thus if e_1 is small, then equation 3.65 indicates that a time $t \sim 4 a_1^2 n_1^2 e_1^2 / (5 D \gamma_s \zeta^2)$, is required to convert libration to circulation. This can be small if e_1 is small. Even if e_1 is not small initially, it is important to note that it also undergoes stochastic diffusion (see equation 3.43) as well as oscillations through its participation in libration. Should e_1^2 attain very small values through this process, then from equation 3.65 we expect the

onset of a rapid evolution of ζ . This is particularly important when e_1^2 already starts from relatively small values.

In fact, application of equations 3.65 and 3.66 to the numerical examples discussed below, adopting the initial orbital elements, indicate that the diffusion of ζ is significantly smaller than ϕ_1 unless e_1 starts out with a very small value. This would suggest that ϕ_1 reaches circulation before ζ . However, this neglects the coupling between the angles that occurs once the libration amplitudes become significant. It is readily seen that it is not expected that ϕ_1 could circulate while ζ remains librating as it was initially. One expects to recover standard secular dynamics for ζ from the governing equations 3.21 - 3.25, when these are averaged over an assumed ϕ_1 circulating with constant $\dot{\phi}_1$. As a libration of the initial form would not occur under those conditions, we expect, and find, large excursions or increases in the libration amplitude of ζ to be correlated with increases in the libration amplitude of ϕ_1 . This in turn increases the oscillation amplitude of the eccentricity e_1 , allowing it to approach zero. The consequent rapid evolution of ζ then enables it to pass to circulation. Thus, the breaking of resonance is ultimately found to be controlled by the excitation of large amplitude librations for ϕ_1 , which induce ζ to pass to circulation somewhat before ϕ_1 itself.

3.2 Numerical simulations

We have performed numerical simulations of one and two planet systems that allow for the incorporation of additional stochastic forces with the properties described above. These forces provide a simple prescription for estimating the effects of stochastic gravitational forces produced by density fluctuations associated with disc turbulence. The results have been obtained using the N-body code described in chapter 2. We have checked that results are converged and do not depend on the integrator used.

We first discuss the expected scaling of the stochastic forces with the physical parameters of the disc and their implementation in N-body integrations. In order to clarify the physical mechanisms involved, and to check the analytic predictions for stochastic diffusion given by equations 3.41 - 3.45, we consider simulations of a single planet undergoing stochastic forcing first. We then move on to consider two planet systems with and without stochastic forcing. We focus on the way a 2:1 commensurability is disrupted and highlight the various evolutionary stages a system goes through as it evolves from a state with a strong commensurability affecting the interaction dynamics, to one where the commensurability is completely disrupted. We find that in some cases a strong scattering occurs. We consider a range of different planet masses and eccentricities (see table 3.1).

3.2.1 Stochastic forces

In order to mimic the effects of turbulence, for example produced by the MRI, it is necessary to calibrate these forces with reference to MHD simulations. As described above, the basic parameters characterising the prescription for stochastic forcing that we have implemented are the root mean square value of the force components per unit mass (in cylindrical coordinates) $\sqrt{\langle F_i^2 \rangle}$ and the auto correlation time τ_c .

From our analytic considerations, we conclude that stochastic forces make the orbital parameters undergo a random walk that is dependent on the force model primarily through the diffusion coefficient $D = 2 \langle F_i^2 \rangle \tau_c$ but also through the dimensionless correction factors γ , γ_s and γ_f .

For planets under the gravitational influence of a proto-planetary disc, the natural scale for the force per unit mass components, F_i , is $F_0(r) = \pi G \Sigma(r) / 2$, where Σ is the characteristic disc surface density (see e.g. Papaloizou & Terquem 2006). $F_0(r)$ is the gravitational force per unit mass due to a small circular disc patch of radius r_Σ at a distance $\sqrt{2} r_\Sigma$ from its centre assuming that all its mass is concentrated there. See also figure 3.1. This is independent of r_Σ . The natural correlation time τ_c is the inverse of the orbital angular frequency $\tau_{c,0} = \Omega^{-1}$. We adopt a minimum mass solar nebula

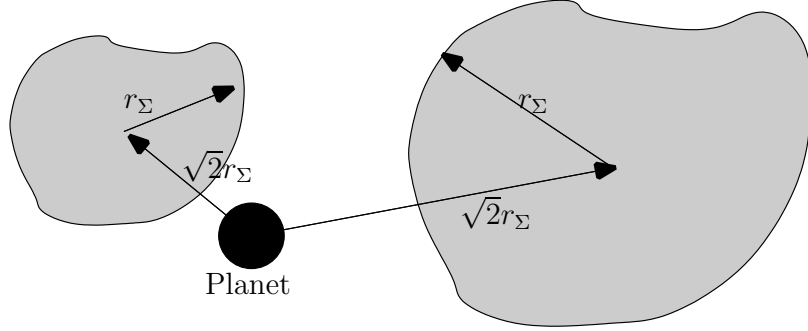


Figure 3.1: The planet is embedded in a proto-planetary disc with random density fluctuations. The force exerted by both clumps in the picture on the planet has the same strength. It is independent of the clump size in a two dimensional system, assuming that the clumps are randomly distributed.

model (MMSN, see Weidenschilling 1977b) with

$$\Sigma(r) = 4200 \frac{\text{g}}{\text{cm}^2} \left(\frac{r}{1 \text{ AU}} \right)^{-3/2}. \quad (3.69)$$

This provides a natural scale for D as a function of the local disc radius and the central stellar mass through²

$$D_0 = 2CF_0^2\tau_{c,0} = 1.95 C \frac{\text{cm}^2}{\text{s}^3} \left(\frac{r}{1 \text{ AU}} \right)^{-3/2} \left(\frac{M_*}{1 M_\odot} \right)^{-1/2}, \quad (3.70)$$

where C is a dimensionless constant. There are several factors which contribute to the value of C :

- The density fluctuations found in MRI simulations $\delta\rho/\rho \sim \delta\Sigma/\Sigma$ are typically of the order 0.1 (e.g. Nelson 2005).
- The presence of a dead zone in the mid plane regions of the disc, where the MRI is not active, has been found to cause reductions in the magnitude of F_0 by one order of magnitude or more, as compared to active cases (Oishi et al. 2007).
- Massive planets open a gap in the disc. Oishi et al. (2007) found that most of the contribution to the stochastic force comes from density fluctuations within a distance of one scale-height from the planet. When a gap forms, this region is cleared of material leading to a substantial decrease in the magnitude of turbulent density fluctuations. Consequently F_0 should be reduced on account of a lower ambient surface density. A factor of 0.1 seems reasonable, although it might be even smaller (de Val-Borro et al. 2006).

²The scaling in Rein & Papaloizou (2009) is incorrect due to a missing factor of π . The value in this thesis has been corrected.

Planet	m (M_J)	a (AU)	P (days)	e	ζ
GJ876 c	0.790	0.131	30.46	0.263	10°
b	2.530	0.208	60.83	0.031	
GJ876 LM c	0.13	0.131	30.46	0.263	10°
b	0.42	0.208	60.83	0.031	
GJ876 SE c	0.013	0.131	30.46	0.263	10°
b	0.042	0.208	60.83	0.031	
GJ876 E c	0.0013	0.0131	30.46	0.263	10°
b	0.0042	0.208	60.83	0.031	
GJ876 LM HE c	0.13	0.131	30.46	0.41	10°
b	0.42	0.208	60.83	0.09	
GJ876 SE HE c	0.013	0.131	30.46	0.41	10°
b	0.042	0.208	60.83	0.09	
HD128311 b	1.56	1.109	476.8	0.38	58°
c	3.08	1.735	933.1	0.21	

Table 3.1: Parameters of the model systems considered. Orbital elements of the system GJ876 are based on a fit by Rivera et al. (2005). LM, SE and E indicate that planet masses have scaled down by a factor of 6, 60 and 600, respectively. This is equivalent to a Jovian mass planet, a super-Earth and Earth mass planet around a solar mass star. HE indicates higher eccentricities than in the observed system. Orbital elements of the system HD128311 are taken from Vogt et al. (2005).

- The correlation time τ_c is found to be slightly shorter than an orbital period, namely $0.5 \Omega^{-1}$ (Nelson & Papaloizou 2004; Oishi et al. 2007).

If it is appropriate to include reduction factors to account for all of the above effects, one finds $C = 5 \cdot 10^{-7}$ and we expect a natural scale for the diffusion coefficient to be specified through

$$D_0 = 10^{-6} \left(\frac{r}{1 \text{ AU}} \right)^{-3/2} \left(\frac{M_*}{1 M_\odot} \right)^{-1/2} \frac{\text{cm}^2}{\text{s}^3}. \quad (3.71)$$

The same value of D may be equivalently scaled to the orbital parameters of the planets without reference to the disc by writing

$$D_0 = 3.5 \cdot 10^6 \left(\frac{r}{1 \text{ AU}} \right)^{-5/2} \left(\frac{M_*}{1 M_\odot} \right)^{3/2} \cdot \left(\frac{r^4 \langle F_i^2 \rangle \Omega \tau_c}{(GM_*)^2} \right) \frac{\text{cm}^2}{\text{s}^3}. \quad (3.72)$$

Thus, a value $D_0 = 10^{-5}$ in cgs units corresponds to a ratio of the root mean square stochastic force component to that due to the central star of about $\sim 10^{-6}$ for a central solar mass at 1 AU. It is a simple matter to scale to other locations.

Of course we emphasise that the value of this quantity is very uncertain, a situation that is exacerbated by its proportionality to the square of the magnitude of the stochastic force per unit mass. For this reason we perform simulations for a range of D , covering many orders of magnitude.

3.2.2 Numerical implementation of correlated noise

The procedure we implemented, uses a discrete first order Markov process to generate a correlated, continuous noise that is added as an additional force. This statistical process is defined by two parameters, the root mean square of the amplitude and the correlation time τ_c (Kasdin 1995). It has a zero mean value and has no memory. This has the advantage that previous values do not need to be stored in memory. The auto-correlation function decays exponentially and thus mimics the auto-correlation function measured in MHD simulations by Oishi et al. (2007). It is also consistent with the assumptions made in the previous sections.

The procedure for generating noise in a variable \mathbf{x} with an auto-correlation time τ and root mean square value of 1 is as follows. The update of \mathbf{x} from \mathbf{t} to $\mathbf{t}+\mathbf{dt}$ in pseudo code is

```

x *= exp( -dt / tau)
x += Xi * sqrt( 1 - exp( 2 * dt / tau ) )

```

where X_i is a random variable with normal distribution and a variance of unity.

3.2.3 Stochastic forces acting on a single planet

We first investigate the long-term effect of stochastic forces on a single isolated planet. The initial orbital parameters are taken to be the observed parameters of GJ876 b (see table 3.1). In this simulation, we use the reduced diffusion coefficients

$$D = 8.2 \cdot 10^{-5} \frac{\text{cm}^2}{\text{s}^3}, \quad \text{and} \quad D = 8.2 \cdot 10^{-3} \frac{\text{cm}^2}{\text{s}^3},$$

which can be represented by a correlation time of half the orbital period and a specific force with root mean square values $\sqrt{\langle F^2 \rangle} = 4.05 \cdot 10^{-6} \text{ cm/s}^2$, and $\sqrt{\langle F^2 \rangle} = 4.05 \cdot 10^{-5} \text{ cm/s}^2$, respectively (see also equation 3.72). In that case the correction factor γ evaluates to $\gamma = 0.0866$.

The growth rates of the root mean square values for Δa , $\Delta \varpi$ and Δe in 200 simulations are plotted in figure 3.2. We also plot the analytic predictions (equations 3.41, 3.45 and 3.43) as solid lines. The numerical simulations and the analytic model are in excellent agreement and scale as expected. We have performed simulations for a variety of diffusion coefficients and get results that are fully consistent in all cases.

We also plot the analytic growth rates coming from equations 3.45 and 3.43 while setting $\gamma = 1$, which corresponds to uncorrelated noise. The resulting curves (dashed lines) do not agree with simulation results. This shows clearly that correlation effects are important, and have to be taken into account. The model presented by Adams et al. (2008) makes use of such an uncorrelated force (random kicks), leading to an

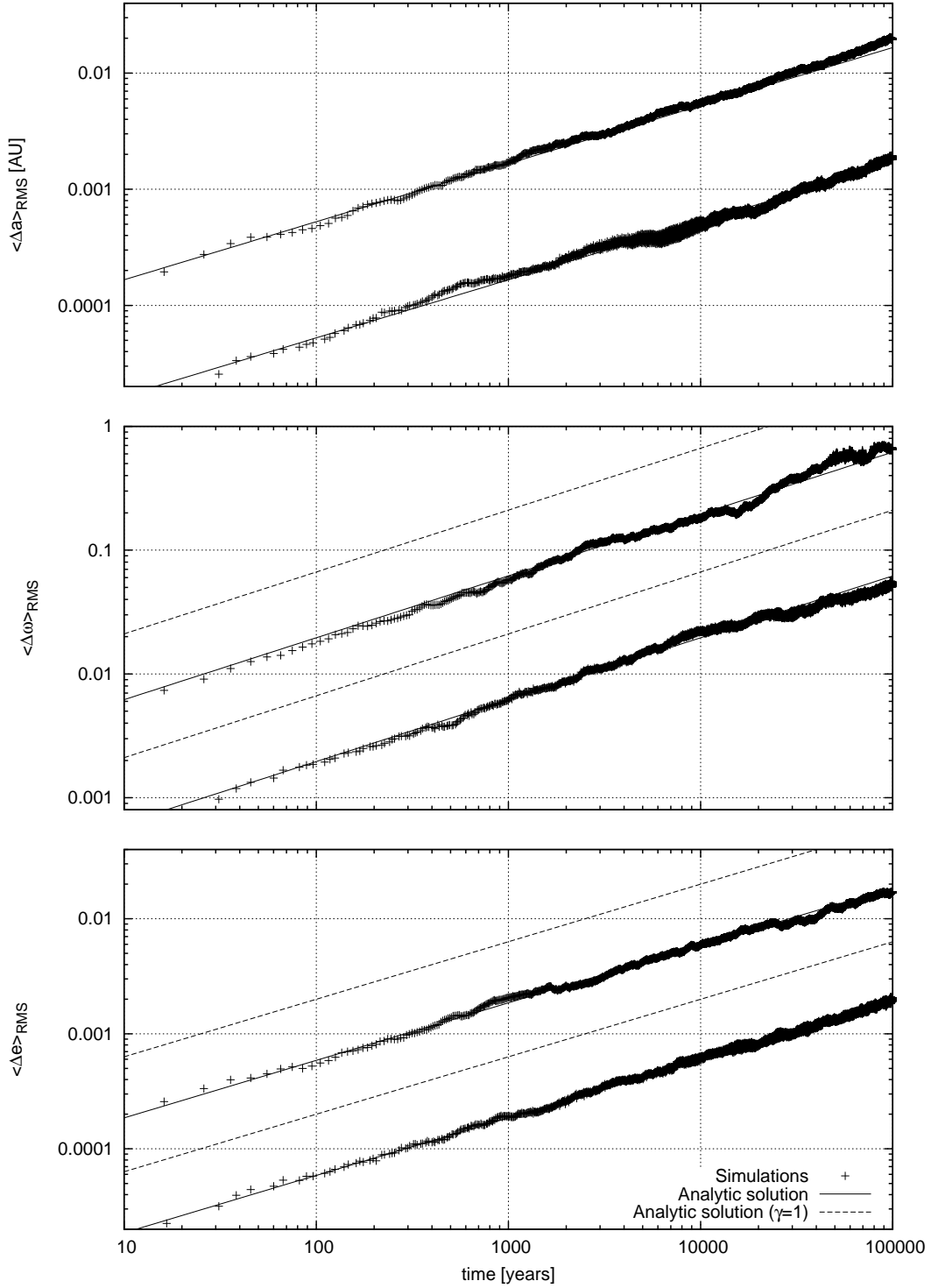


Figure 3.2: Growth of the semi-major axis Δa , the periastron $\Delta \varpi$ and the eccentricity Δe for a single planet as a function of time. The initial orbital parameters of the planet are taken to be those of GJ876 b (see table 3.1). One hundred simulations starting from the same initial conditions are averaged for each value of the diffusion coefficient. The diffusion coefficient D is $8.2 \cdot 10^{-3} \text{cm}^2/\text{s}^3$ for the upper and $8.2 \cdot 10^{-5} \text{cm}^2/\text{s}^3$ for the lower curves, respectively. Solid lines correspond to the analytic predictions, i.e., these are not fits. Dashed lines correspond to the analytic predictions for uncorrelated, random kicks.

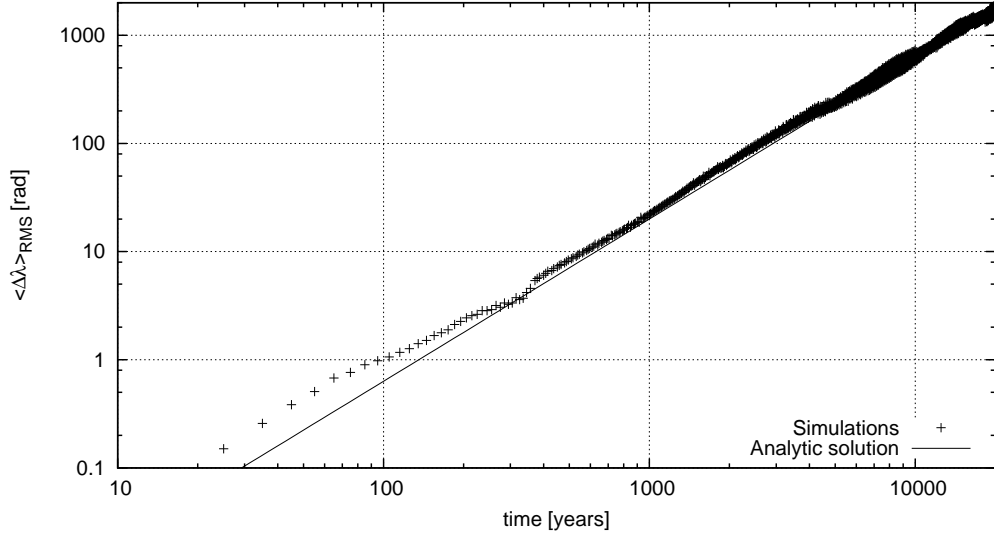


Figure 3.3: Growth of the difference in longitude $\Delta\lambda$ as a function of time for a single planet. The initial orbital parameters of the planet are taken to be those of GJ876 b (see table 3.1). One hundred simulations starting from the same initial conditions are averaged. Here, the diffusion coefficient is $D = 8.2 \cdot 10^{-5} \text{cm}^2/\text{s}^3$. The solid line corresponds to the analytic prediction, given by equation 3.56.

overestimated diffusion coefficient by almost a factor ~ 16 . Note that only orbital parameters involving the geometry of the orbit are affected, i.e., not the semi-major axis.

In figure 3.3, we plot the root mean square of the difference in longitude. One can clearly see that $(\Delta\lambda)^2$ does grow like $\sim t^3$, as expected from equation 3.56.

3.2.4 Illustration of the modes of libration in a two planet system

We now go on to consider two planet systems. As an illustrative example we discuss the GJ876 system (see table 3.1). We begin by considering the evolution of the system without stochastic forcing in order to characterise the modes of libration of the resonant angles and other orbital parameters. In particular, we identify the fast and slow modes discussed in section 3.1.2.

The time evolution of the resonant angles and the eccentricities of the unperturbed system is plotted in figure 3.4. Clearly visible are the slow and fast oscillation modes. The fast mode, which is seen to have a period of about 1.4 years, dominates the librations of e_2 and ϕ_1 while also being present in those of ϕ_2 . On the other hand the slow mode, which is seen to have a period of about 10 years, dominates the librations of ζ while also being present in those of e_1 and ϕ_2 .

We emphasise the fact that the eccentricities of the two planets participate in the

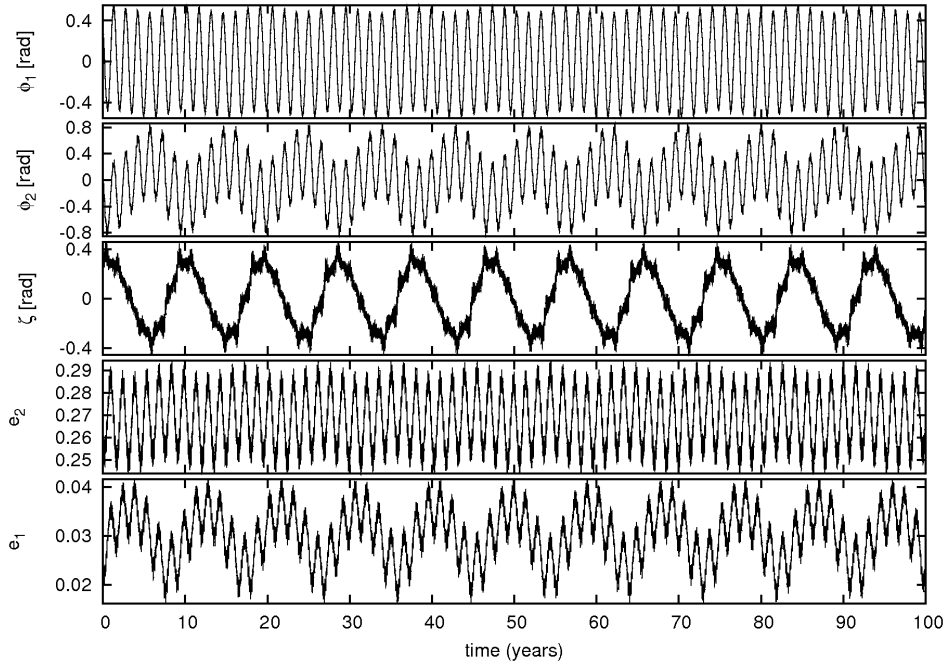


Figure 3.4: Time evolution of the resonant angles and the eccentricities in the system GJ876 without turbulent forcing. The dominance of the fast mode with period ~ 1.4 years in the oscillations of ϕ_1 , and the dominance of the slow mode with period ~ 10 years in ζ can be clearly seen.

librations, and are therefore not constant. In particular, the eccentricity of GJ876 b oscillates around a mean value of 0.03 with an amplitude $\Delta e \approx 0.01 - 0.02$. This behaviour involving the attainment of smaller values of the eccentricity has important consequences for stochastic evolution as discussed above (section 3.1.3) and also below.

We remark that similar behaviour occurs for all the systems we have studied, these having a wide range of eccentricities and planet masses. The fast and slow mode periods scale with the planet masses as given by equations 3.31 and 3.33 respectively. These indicate, as confirmed by our simulations, that if both masses are reduced by a factor Λ then the period of the fast mode scales as $\sqrt{\Lambda}$ and the period of the slow mode scales as Λ .

In figure 3.5 we plot the librations in h and k variables. The left plots show one period of the slow mode libration, corresponding to one complete circle around the origin. Super-imposed on that are slow mode librations with higher frequency. The frequency ratio is ~ 6 , thus the hexagon shape. The even higher frequency modes correspond to the orbital period itself. The right plots show many libration periods.

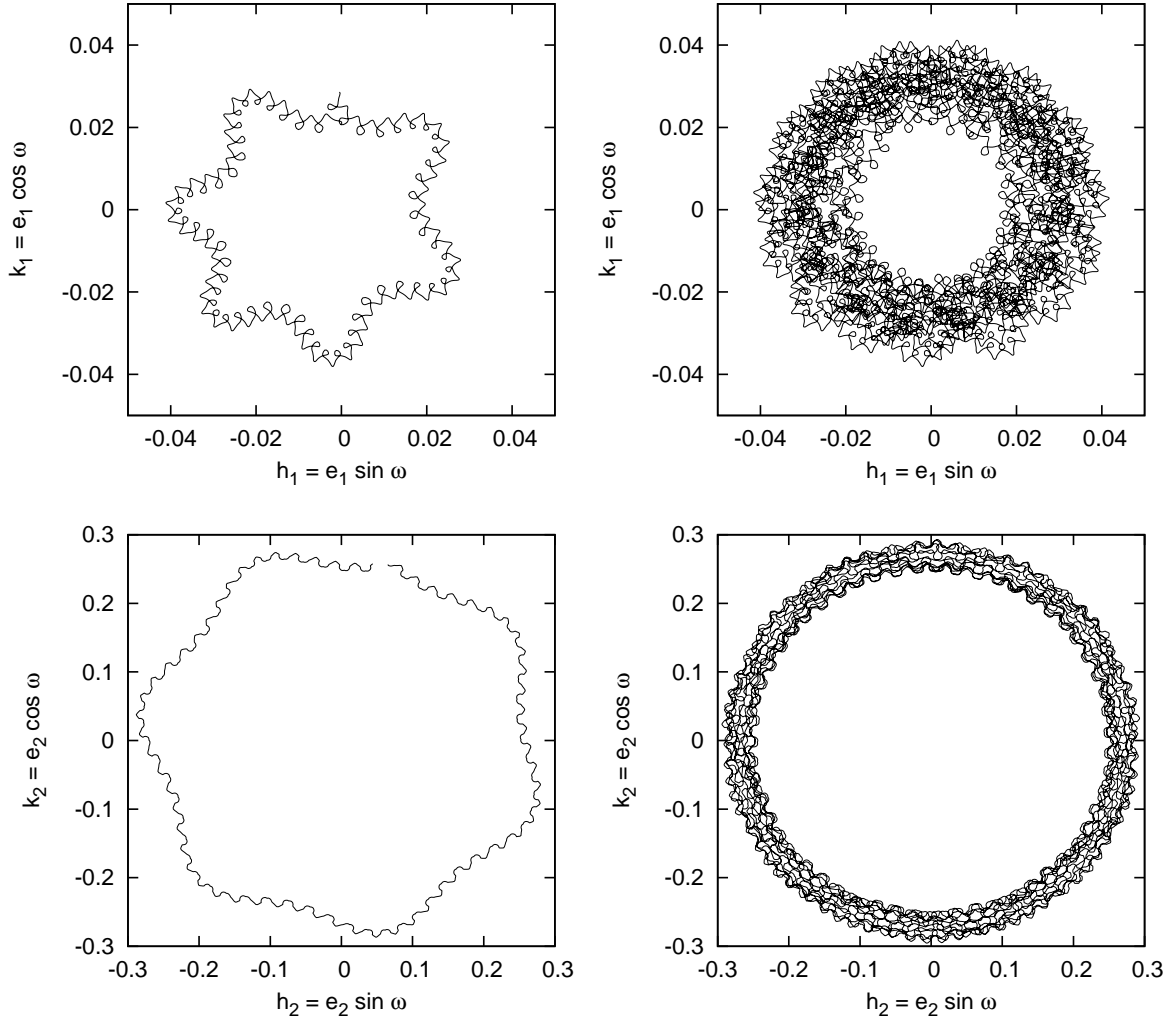


Figure 3.5: Librations in the GJ876 system, visualised using h and k variables. The initial conditions are the same as in figure 3.4. The left plots show the evolution during one slow mode period, which is equivalent to about 6 fast mode periods. The right plots show the evolution over many libration periods.

3.3 Two planets with stochastic forcing

We now consider systems of two planets with stochastic forcing. For simplicity we begin by applying additional forces only to the outer planet. We have found that adding the same form of forcing to the inner planet tends to speed up the evolution by approximately a factor of two without changing qualitative details. For illustrative purposes we again start with the GJ876 system and consider two diffusion coefficients $D = 8.2 \cdot 10^{-5} \text{cm}^2/\text{s}^3$ and $D = 8.2 \cdot 10^{-4} \text{cm}^2/\text{s}^3$. In all of our simulations a constant value of $D = 2\langle F_i \rangle^2 \tau_c$ is used by maintaining both parameters $\langle F_i \rangle$ and τ_c constant. For the cases considered here, there is little orbital migration so that this effect can be ignored.

The time evolution of the eccentricities is plotted for two runs in the first and third plot in figure 3.6. We see fast oscillations superimposed on a random walk. The amplitude of the oscillations, as well as the mean value, change with time.

Our simple analytic model assumes slowly changing background eccentricities and semi-major axes. Accordingly, it does not incorporate the oscillations of the eccentricity due to the resonant interaction of the planets. In order to make a comparison, we perform a time average over many periods to get smoothed quantities whose behaviour we can compare with that expected from equations 3.41 - 3.45. When this procedure is followed (see second and forth plot in figure 3.6), the evolution is in reasonable accord with that expected from the analytic model provided that allowance is made for the importance of small values of e_1 in determining the growth of the libration amplitude of the angle between the apsidal lines of the two planets (see equation 3.45). The presence of this feature results in the behaviour of the libration amplitude being more complex than that implied by a process governed by a simple diffusive random walk. This is discussed in the following sections.

3.3.1 Disruption of a resonance in stages

Systems with mean motion commensurabilities can be in many different configurations. Here we describe the important evolutionary stages as they appear in a stochastically forced system starting from a situation in which all the resonant angles show small amplitude libration. Observations of GJ876 suggest that the system is currently in such a state with the ratio of the orbital periods P_1/P_2 oscillating about a mean value of 2.

Attainment of circulation of the angle between the apsidal lines

When the initial eccentricity of the outer planet, e_1 , is small, the excitation of the libration amplitudes of the resonant angles readily brings about a situation where e_1 attains even smaller values. This then causes the periastron difference ζ to undergo large oscillations and eventually reach circulation (see equation 3.45). Should stochastic forces cause e_1 to reach zero, on account of the coordinate singularity, ϖ_1 becomes undefined. Note that this occurs without a large physical perturbation to the system. Thus, the occurrence of this phenomenon does not imply the system ceases to be in a commensurability.

In this context we note that the eccentricity of GJ876 b initially is such that $e_1 \sim 0.03$ with values $e_1 \sim 0.01$ often being attained during libration cycles. Thus only a small change may cause the above situation to occur. In all cases that we have considered,

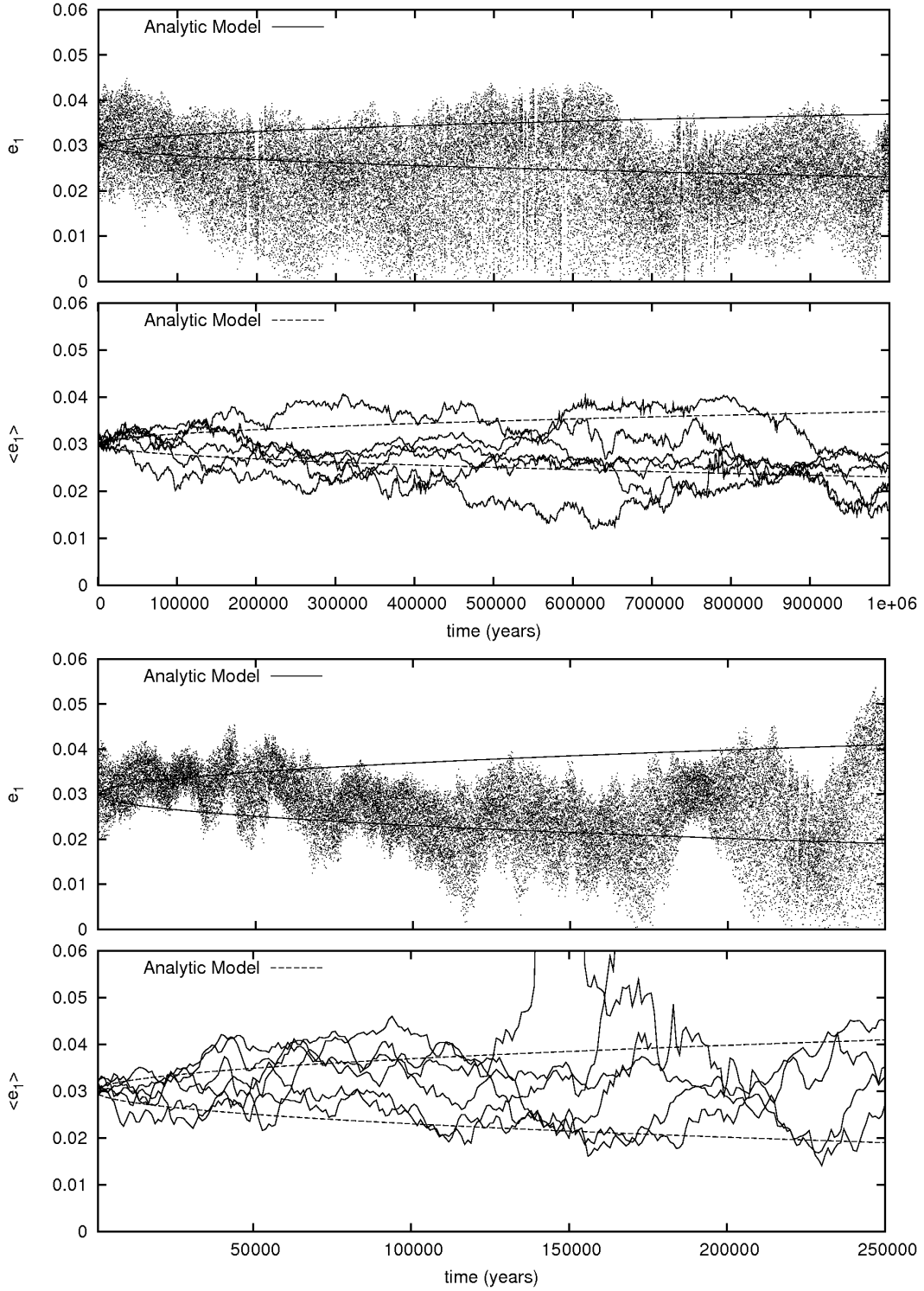


Figure 3.6: Time evolution of the eccentricities in the GJ876 system with turbulent forcing included. The diffusion coefficient is $D = 8.2 \cdot 10^{-5} \text{cm}^2/\text{s}^3$ for the two upper plots and $D = 8.2 \cdot 10^{-4} \text{cm}^2/\text{s}^3$ for the two lower plots. The first (uppermost) and the third plots each show a single run. The second and fourth (lowermost) plots show the time averaged eccentricities for six different runs. The averaging interval is 1000 years, corresponding to ~ 100 slow mode periods.

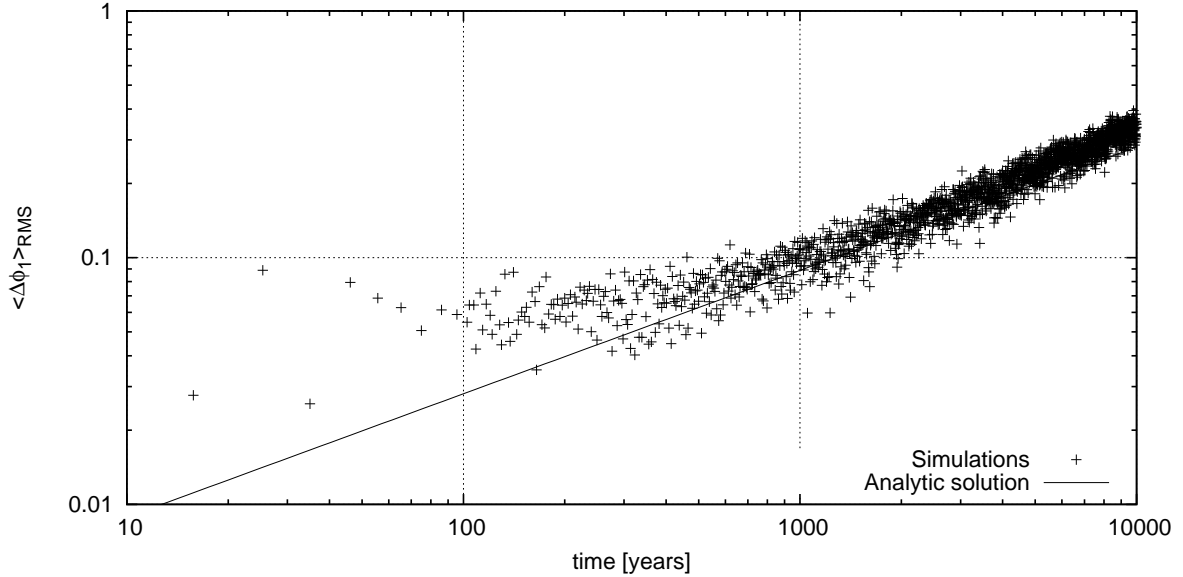


Figure 3.7: Growth of the difference in the resonance angle ϕ_1 as a function of time. The initial orbital parameters are those of GJ876 (see table 3.1). Here, the diffusion coefficient is $D = 8.2 \cdot 10^{-3} \text{cm}^2/\text{s}^3$. The solid line corresponds to the analytic prediction, given by equation 3.66.

we find that ζ enters circulation prior to the fast angle ϕ_1 , which may remain librating until that too is driven into circulation.

Attainment of circulation of the fast angle

Both before and after ζ enters circulation, stochastic forces increase the libration amplitude of the fast mode ϕ_1 . This mode dominates both the librations of the resonant angle ϕ_1 and the semi-major axes. Eventually ϕ_1 starts circulation. Shortly afterwards, commensurability is lost and P_1/P_2 starts to undergo a random walk with a centre that drifts away from 2. Note that it is possible for some realisations to re-enter commensurability. For systems with the masses of the observed GJ876 system, the most likely outcome is a scattering event that causes complete disruption of the system.

Because the eccentricities do not play an important role in the attainment of circulation of the fast angle, we can use equation 3.66 to calculate the growth rate. The root mean square values of $\Delta\phi_1$ as a function of time, taken from both, analytical and numerical results, are plotted in figure 3.7. Here, we use $D = 8.2 \cdot 10^{-3} \text{cm}^2/\text{s}^3$. Note that as mentioned above, ζ is circulating first (in the presented case this happens after ~ 1000 years). However, this does not influence the growth of $\Delta\phi_1$.

3.3.2 A numerical illustration

In order to illustrate the evolutionary sequence described above we plot results for two realisations of the evolution of the GJ876 system in figure 3.8. For these runs we adopted the diffusion coefficient $D = 0.42\text{cm}^2/\text{s}^3$. Note that increasing D only decreases the evolutionary time which has been found, both analytically and numerically to be $\propto 1/D$ (see below).

The times at which the transition from libration to circulation occurs for both the slow and fast angles, are indicated by the vertical lines in figure 3.8.

Several of the features discussed above and in section 3.1.3 can be seen in figure 3.8. In particular the tendency for the occurrence of very small values of e_1 to be associated with transitions to circulation of ζ can be seen for the realisation plotted in the lower panels at around $t = 80$ years and $t = 500$ years. Such episodes always seem to occur when the libration amplitude of the fast angle ϕ_1 is relatively boosted, indicating that this plays a role in boosting the slow angle. If the duration for which e_1 attains small values is small and ϕ_1 recovers small amplitude librations, the slow angle returns to circulation. Thus, the attainment of long period circulation for the slow angle is related to the diffusion time for ϕ_1 . We also see from figure 3.8 that the angle ϕ_2 , which has a large contribution from the slow mode, behaves in the same way as ζ as far as libration/circularisation is concerned. We have verified by considering the results from the simulations of GJ876 LM HE, which started with a larger value of e_1 , that, as expected, the attainment of circulation of the slow angle takes relatively longer in this case, the time approaching more closely the time when ϕ_1 attains circulation. Also as expected, the time when ϕ_1 attains circulation is not affected by the change in e_1 .

3.3.3 Dependence on the diffusion coefficient

We now consider the stability of the systems listed in table 3.1 as a function of D . These systems have a variety of masses and orbital eccentricities. In particular, in view of the complex interaction between the resonant angles discussed above, we wish to investigate whether the mean amplitude growth at a given time is indeed proportional to D . As also mentioned above, the value of the diffusion parameter D that should be adopted, is very uncertain. We have therefore considered values of D ranging over five orders of magnitude. The correlation time τ_c is always taken to be given by $\tau_c = 0.5\Omega^{-1}$ while the RMS value of the force is changed. In order to determine the *lifetime* of a resonant angle, we monitor whether it is librating or circulating. Numerically, libration is defined to cease when the angle is first seen to reach absolute values larger than 2. We note that the angle can in general regain small values afterwards. However, this is

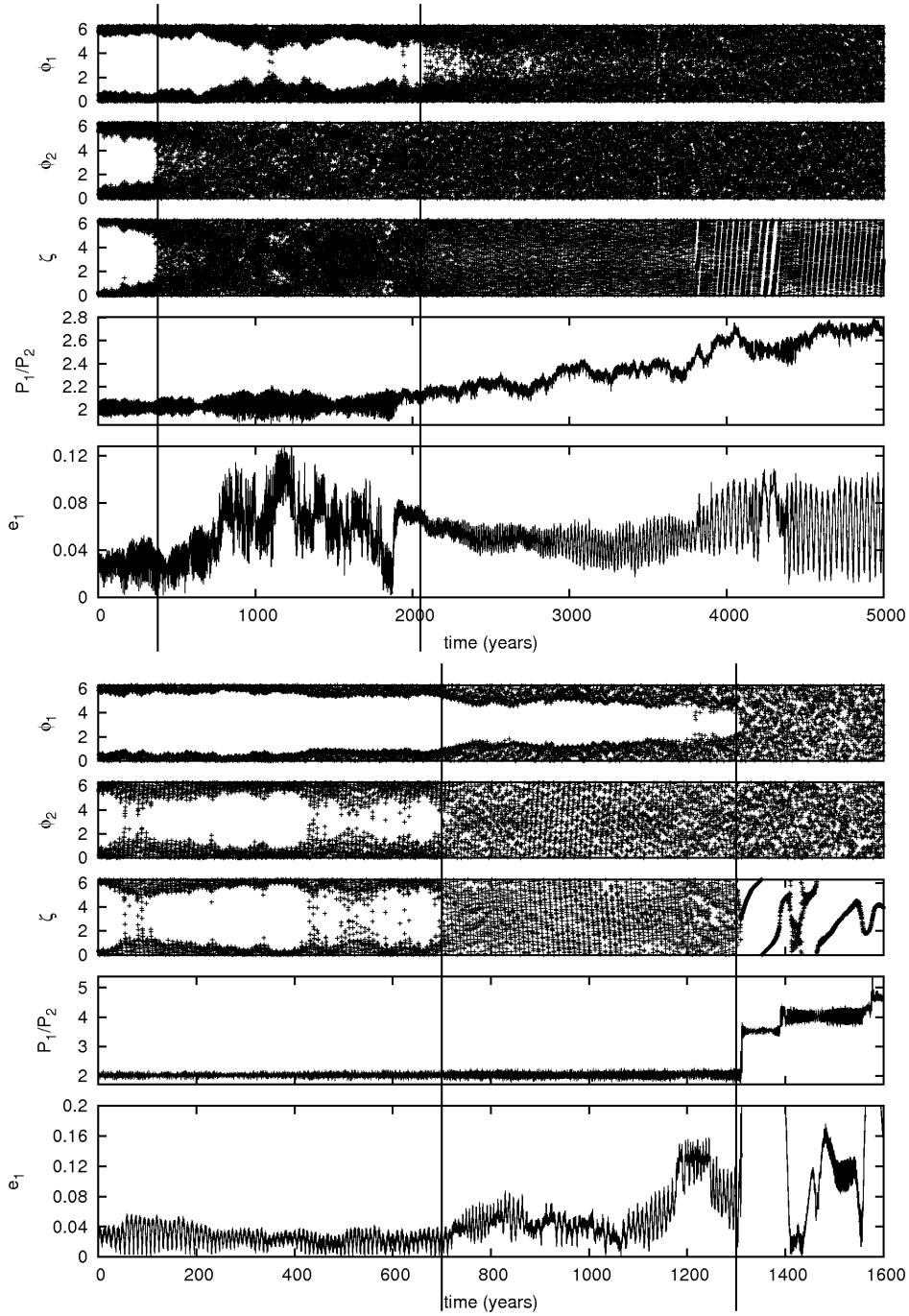


Figure 3.8: Time evolution of the resonant angles, the period ratio P_2/P_1 and the eccentricity, e_1 , in the GJ876 system with stochastic forcing corresponding to $D = 0.42\text{cm}^2/\text{s}^3$. The vertical lines indicate when the angles enter circulation for a prolonged period. The realisation illustrated in the lower panel scatters shortly after ϕ_1 goes into circularisation.

a transient effect and changes the lifetime by no more than a factor of ~ 2 in all our simulations.

In this context we consider the fast angle ϕ_1 and the slow angle ζ . As we saw above, the latter can be replaced by ϕ_2 which exhibits the same behaviour. Because ϕ_1 is the last to start circulating, the resonance is defined to be broken at that point.

Equations 3.66 and 3.65 estimate the spreading of the resonant angles as a function of time. We plot both the numerical and analytical results in figure 3.9. To remove statistical fluctuations and obtain a mean spreading time, the numerical values for a particular value of D were obtained by averaging over 60 realisations.

From figure 3.9 it is apparent that the evolutionary times scale is $\propto 1/D$ for D varying by many orders of magnitude. The analytic estimates for the libration survival times of ϕ_1 , dominated by the fast mode, obtained using equation 3.66 adopting the initial orbital elements and with the fast libration frequency determined from the simulations, are plotted in the upper panel of figure 3.9. These are in good agreement with the numerical results. However, the estimate for ϕ_2 based on equation 3.65 using the initial value of e_1 overestimates the lifetime by a factor of at least ~ 40 (see solid line in the lower plot of figure 3.9). Furthermore equation 3.65 has no dependence on planet mass which is in clear conflict with the numerical results. As discussed above, this is due to the temporary attainment of small eccentricities. This causes the disruption of the libration of ζ earlier than predicted assuming e_1 being constant. In fact this disruption occurs at times that can be up to 10 times shorter than those required to disrupt ϕ_1 . We estimate the lifetime of librations of ϕ_2 by calculating the time ϕ_1 needs to reach values close to 1 (see dashed lines in the lower plot of figure 3.9). As explained above in section 3.1.3, large amplitude variations of ϕ_1 are expected to couple to and excite the slow mode. Variations induced in the eccentricity e_1 allow e_1 to reach zero and we lose libration of ϕ_2 . These simple estimates are in good agreement with the numerical results and accordingly support the idea that ϕ_1 and ϕ_2 are indeed coupled in the non-linear regime. For low mass planets this simple analytic prediction underestimates the lifetime of ϕ_2 by a factor of ~ 2 , suggesting that the coupling between the two modes depends slightly on the planet masses.

To confirm our understanding of these processes, we have repeated the calculations with systems that are in the same state as the system discussed above but have higher eccentricities (see GJ876 LM HE and GJ876 SE HE in table 3.1). The lifetime of the librating state of ϕ_1 is unchanged, as this does not depend significantly on the eccentricity. However, the lifetime of the librating state of ϕ_2 is a factor of 2 – 3 longer. This is due to the fact that a larger excitation of ϕ_2 is needed to make e_1 reach small values in these simulations.

The random walk description breaks down completely when the anticipated disrup-

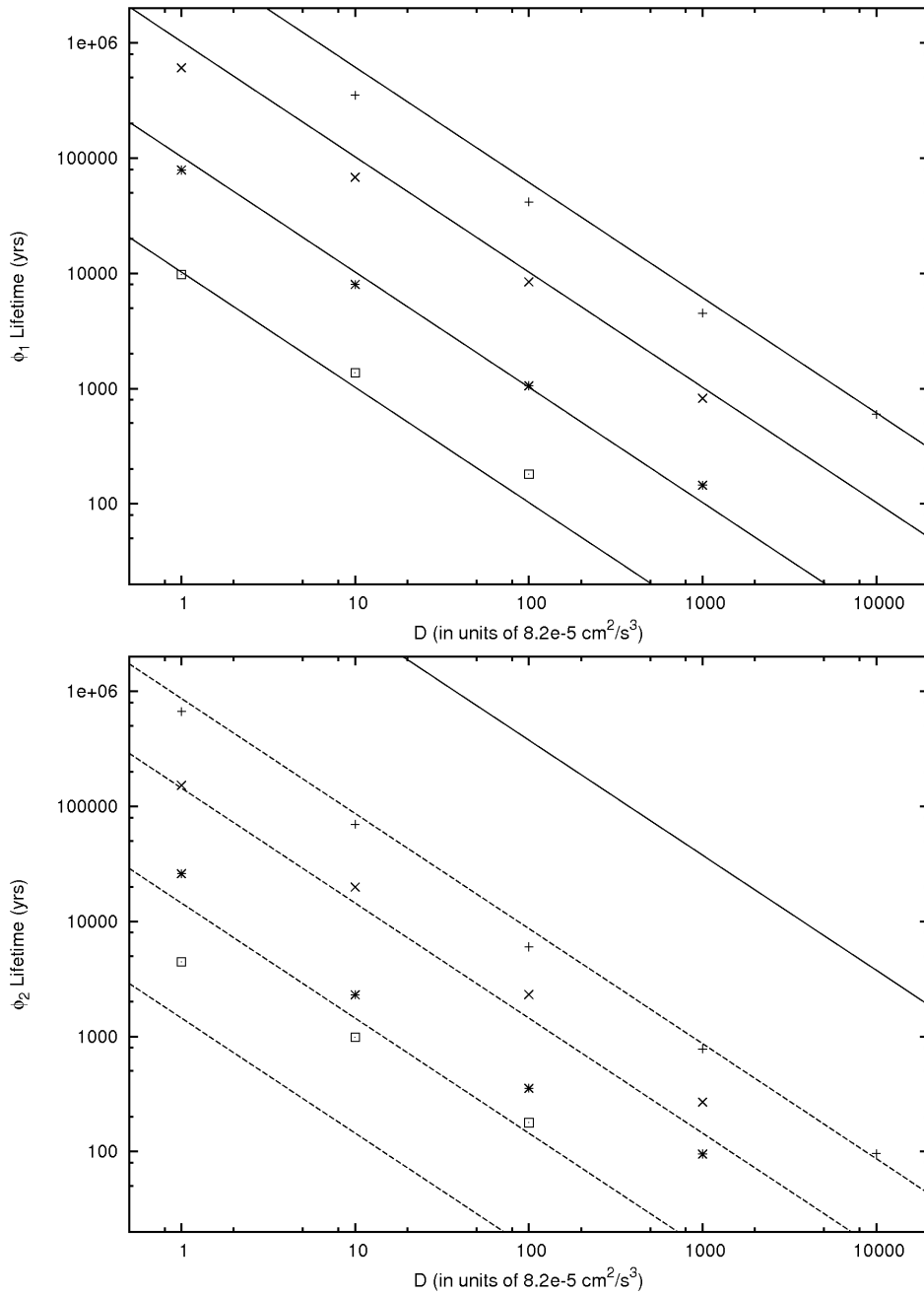


Figure 3.9: Average time until circulation of the resonant angles ϕ_1 (top) and ϕ_2 (bottom) in the systems GJ876 (indicated with +), GJ876LM (indicated with \times), GJ876SE (indicated with \star) and GJ876E (indicated with \square) as a function of the stochastic forcing diffusion coefficient D . In the case of the upper panel, the analytic curves explained in the text, are from top to bottom for the GJ876, GJ876LM, GJ876SE and GJ876E systems, respectively. In the lower panel the analytic curves, as explained in the text, are from top to bottom for the GJ876 (solid curve and top dashed curve), GJ876LM, GJ876SE and GJ876E systems, respectively.

tion time becomes shorter than the libration period. This is expected to happen for small enough masses as can be verified from figure 3.9. It is because the disruption time decreases linearly with the planet masses while the libration period increases as the square root of the planet masses. Then we cannot average over many libration periods. This situation is apparent in figure 3.9 for very short disruption times of the order 100-1000 years where survival times cease to vary linearly with $1/D$.

3.4 Formation of HD128311

Having understood the effects of stochastic forces on resonances, we now go on to discuss the application of these ideas to the formation of the orbital configuration of the planetary system HD128311. This is (with 99% confidence) in a 2:1 mean motion resonance, with the angle ϕ_1 librating and the angle ζ circulating so that there is no apsidal co-rotation (Vogt et al. 2005). However, the orbital parameters are not well constrained. The original Keplerian fit by Vogt et al. (2005) is such that the planets undergo a close encounter after only 2000 years. The values in table 3.1 have been obtained from a fit to the observational data that includes interactions between the planets. The values quoted have large error bars. For example the eccentricities e_1 and e_2 have an uncertainty of 33% and 21%, respectively. Although the best fit doesn't manifest apsidal co-rotation, the system could undergo large amplitude librations and still be stable.

According to Lee & Peale (2002) the planets should have apsidal co-rotation if the commensurability was formed by the two planets undergoing sufficiently slow convergent inward migration, and if they then both migrated inwards significantly while maintaining the commensurability (see also Snellgrove et al. 2001). Accordingly Sándor & Kley (2006) suggested a possible formation scenario with inward migration as described above, but with an additional perturbing event, such as a close encounter with an additional third planet occurring after the halting of the inward migration. This perturbation is needed to alter the behaviour of ζ , so that it undergoes circulation rather than libration and thus producing orbital parameters similar to the observed ones.

We showed above that stochastic forcing possibly resulting from turbulence driven by the MRI readily produces systems with commensurabilities without apsidal co-rotation if the eccentricities are not too large. This suggests that a scenario that forms the commensurability through disc-induced inward convergent migration might readily produce commensurable systems without apsidal co-rotation if stochastic forcing is included. Such scenarios are investigated in this section.

We present simulations of the formation of HD128311 that include migration and stochastic forcing due to turbulence but do not invoke artificial perturbation events

involving additional planets. We find that model systems with orbital parameters resembling the observed ones are readily produced and are better matches than those provided by Sándor & Kley (2006). The planets in this system are of the order of several Jupiter masses and the eccentricity of one planet can get very small during one libration period. The observed orbital parameters are given in table 3.1 and their time evolution (due to planet-planet interactions) is plotted on the right hand side of figures 3.10, 3.11 and 3.12. The mass of the star is $0.8 M_{\odot}$.

3.4.1 Migration forces

We incorporate the non-conservative forces exerted by a proto-stellar disc that lead to inward migration by following the approach outlined in appendix B. The migration process is characterised by migration and eccentricity damping timescales, $\tau_a = a/\dot{a}$ and $\tau_e = e/\dot{e}$, respectively. This procedure is now widely used (e.g. Sándor & Kley 2006; Crida et al. 2008). We also use the ratio of the above timescales, $K = |\tau_a|/\tau_e$, as defined in chapter 2. This ratio determines the eccentricities in the state of self-similar inward migration of the commensurable system that is attained after large times.

In this work we allow the planets to form a commensurability through convergent inward migration with stochastic forcing included. The disc is then removed through having its surface density reduced to zero on a 2000 year timescale. This reduces both the migration forces and the stochastic forces simultaneously. This procedure is very similar to that adopted by the above authors but we have included stochastic forcing and removed the disc on longer, more realistic, time-scales.

The stochastic forces need to have the right balance with respect to the migration rate. We have found that inward migration imparts stability to the resonant system. If the migration rate is too fast relative to the stochastic forcing the migration keeps down the libration amplitudes and we do not get circulation. On the other hand large eccentricity damping favours broken apsidal co-rotation. This might look counter intuitive at first sight, but remember that the diffusion of ζ depends on $1/e_1^2$ and $1/e_2^2$.

Due to the stochastic nature of the problem, it is hard to present a continuum of solutions so we restrict ourselves to the discussion of three representative examples. However, we comment that we are able to obtain similar end states for a wide range of migration parameters.

As above, the parameters $\langle F_i \rangle$ and τ_c are kept constant, so maintaining D constant, for the duration of the simulation, with τ_c being determined for the initial location of the outer planet. As discussed above, these values may scale with the radius of the planet and we thus expect them to change during migration. However, the semi-major axis of the outer planet changes only by $\sim 30\%$ during the simulation. Consequently, we ignore this effect.

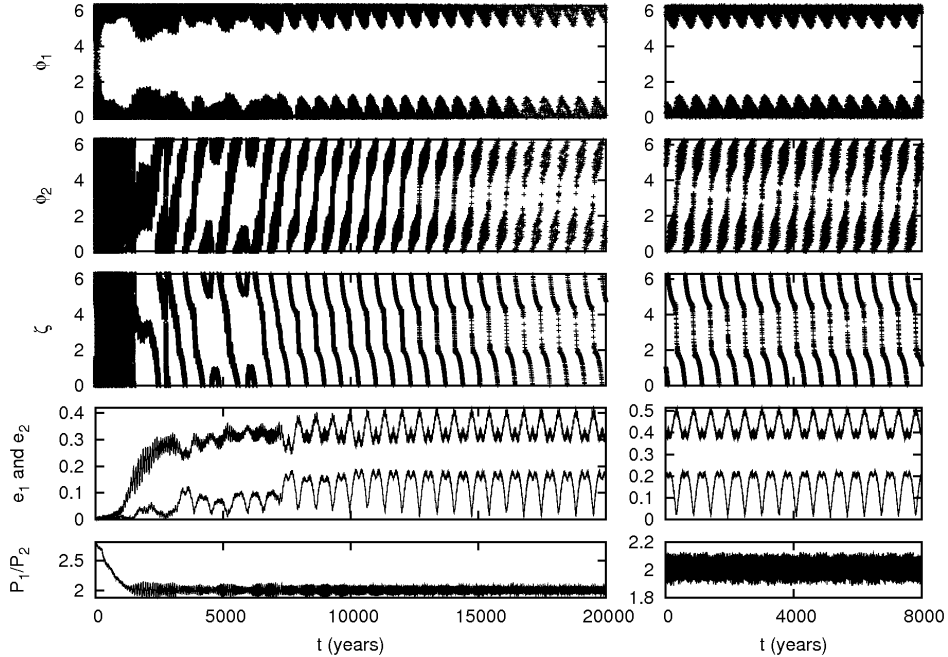


Figure 3.10: The plots on the left hand side show a possible formation scenario for the system HD128311 including turbulence and migration. We plot the observed system on the right hand side as a comparison (see table 3.1 and text). The plots show, from top to bottom, the resonant angles ϕ_1, ϕ_2, ζ , the eccentricities e_1, e_2 and the period ratio P_1/P_2 . Resonance capturing occurs after 2000 years.

3.4.2 Model 1

The planets are initially on circular orbits at radii $a_1 = 4$ AU and $a_2 = 2$ AU. Stochastic forcing is applied to the outer planet only, with a diffusion coefficient of $D = 6.4 \cdot 10^{-3} \text{cm}^2/\text{s}^3$. Note that although this value is 64 times larger than the scaling given by equation 3.71, corresponding to a force that is 8 times larger than the simple estimate given in section 3.2.1, corresponding to smaller reduction factors resulting from a gap or dead zone, it is too small for the angle ϕ_1 to be brought to circulation during our runs. The results given above and summarised in figure 3.9, and further tests, indicate that similar results would be obtained if D is reduced, but on a longer time-scale $\propto 1/D$, provided the migration rate is also ultimately reduced appropriately so that the system can survive for long enough to enable ζ to be driven into circulation.

The outer planet is made to migrate inwards on a timescale $\tau_{a_1} = 8000$ years. The inner planet migrates slowly outwards on a timescale of $\tau_{a_2} = -20000$ years. This results in convergent migration. For both planets we use an eccentricity to semi-major axis damping ratio of $K = 8$. The resulting evolutionary timescales are significantly larger than those used by Sándor & Kley (2006) and more easily justified by hydrodynamical simulations.

The time evolution is shown in the left plot of figure 3.10. After resonance capturing

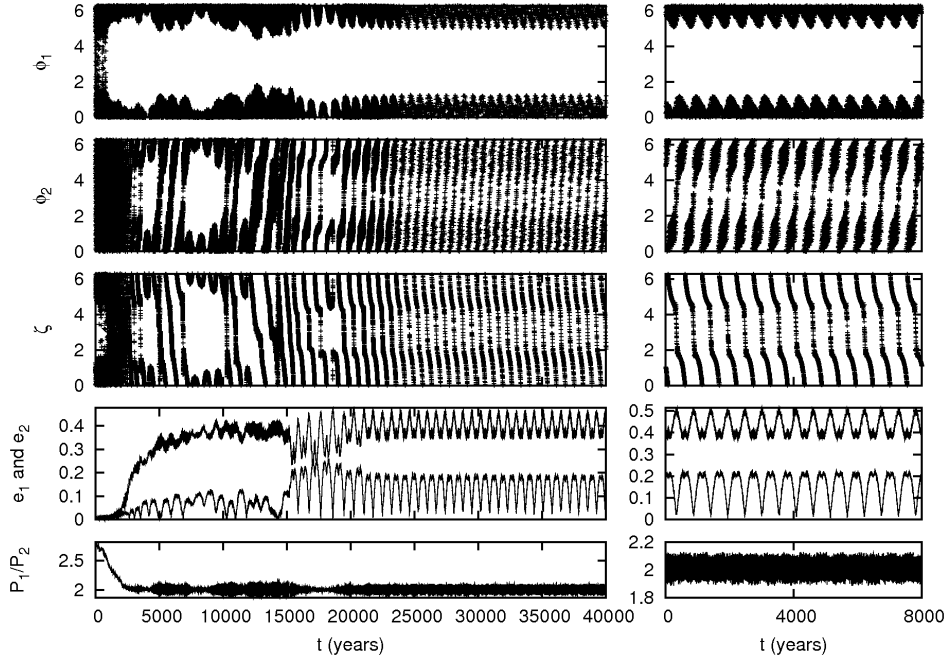


Figure 3.11: The plots on the left hand side show another possible formation scenario for the system HD128311. Again, we plot the observed system on the right hand side as a comparison (see table 3.1 and text). The migration timescales in this run are $\tau_{a,1} = 16000$, $\tau_{a,2} = -40000$ and $K = 5.5$. Note that the eccentricities are larger compared to figure 3.10 because K is smaller.

all angles are either initially librating or on the border between libration and circulation. The slow mode has a period of ~ 700 years, whereas the fast mode period is 20 times shorter.

It can be seen from figure 3.10 and other similar figures below, that while migration continues, libration amplitudes tend to be controlled apart from when e_1 becomes either zero or very close to zero. Then, due to stochastic forcing, ϕ_2 and ζ start circulating. Subsequently, libration is recovered over time intervals for which e_1 does not attain very small values but eventually additional stochastic forcing together with the repeated attainment of small values for e_1 causes ϕ_2 to remain circulating for the remainder of the simulation. After 13000 years, both the forces due to migration and turbulence are reduced smoothly on a timescale of 2000 years. The result is a stable configuration that resembles the observed system very well.

3.4.3 Model 2

For this simulation, we lengthen the migration timescales by a factor of 2 to show that the results are generic. We also decrease the value of K to 5.5. All other parameters are the same as for model 1. This results in larger eccentricities and the final state better resembled our representation of the observed system. However, it should be kept

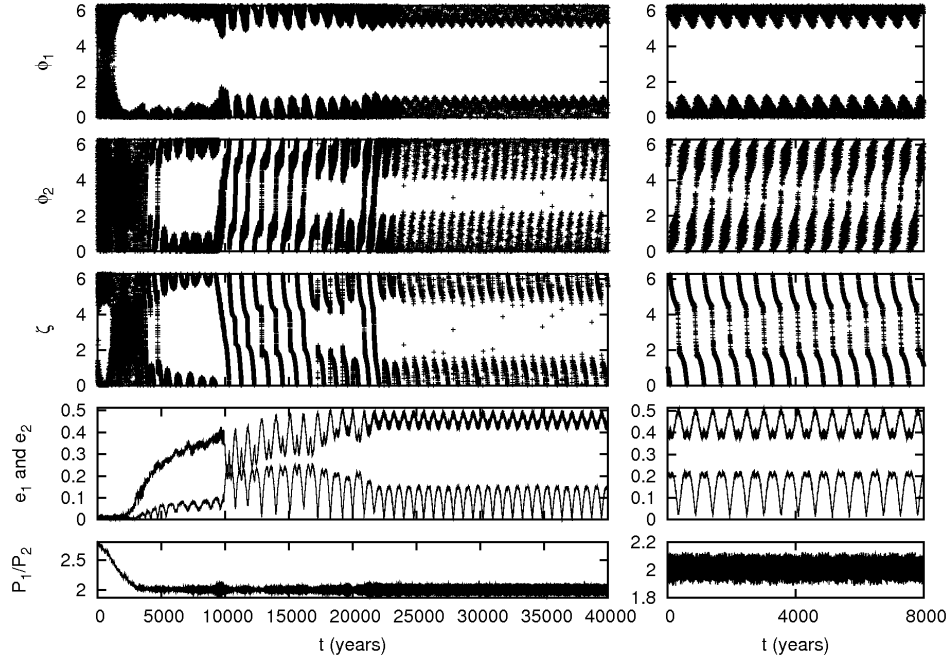


Figure 3.12: These plots show another possible formation scenario of HD128311. The damping parameters are the same as in figure 3.11.

in mind that the eccentricities are not well constrained by the observations.

The time evolution is plotted in figure 3.11. The resonant angles librate immediately after the capture into resonance, as predicted for sufficiently slow migration. However, in the same way as for model 1 described above, stochastic forces make ϕ_2 circulate soon afterwards. Once the migration forces and stochastic forces are removed between 20000 and 22000 years, the system stays in a stable configuration with no apsidal co-rotation.

3.4.4 Model 3

All parameters are the same as for model 2. Accordingly, model 3 represents another statistical realisation of that case. The time evolution is plotted in figure 3.12. The final state is very close to the boundary between libration and circulation of ζ . As discussed above, large uncertainties in the orbital parameters mean that the actual system could be in such a state.

Due to stochastic forces, which may result from local turbulence, we are able to generate a broad spectrum of model systems. Some of them undergo a strong scattering during the migration process. However, the surviving systems resemble the observed system very well. Although the orbital parameters are not well constrained yet, we showed that values in the right range are naturally produced by a turbulent disc.

3.5 Conclusions

In this chapter, we have presented a self-consistent analytical model of both a single planet, and two planets in a mean motion resonance, being subject to external stochastic forcing. The stochastic forces could result from MRI-driven turbulence within the protoplanetary disc but our treatment is equally applicable to any other source, for example from a gravitoturbulent disc such as Saturn’s A-ring (see chapter 4).

We considered the evolution of a stochastically forced two planetary system that is initially deep inside a MMR (i.e., the two independent resonant angles librate with small amplitude). Stochastic forces cause libration amplitudes to increase in the mean with time until all resonant angles are eventually driven into circulation, at which point the commensurability is lost. Often a strong scattering occurs soon afterwards for systems composed of planets in the Jovian mass range.

We isolated a fast libration mode which is associated with oscillations of the semi-major axes and a slow libration mode which is mostly associated with the motion of the angle between the apsidal lines of the two planets. These modes respond differently to stochastic forcing, the slow mode being more readily converted to circulation than the fast mode. This slow mode is sensitive to the attainment of small eccentricities, which cause rapid transitions between libration and circulation. The amplitude of the fast mode grows more regularly in the mean, with the square of the libration amplitude in most cases increasing linearly with time and being proportional to the diffusion coefficient D . Of course this discussion is simplified and there are limitations. For example if the total mass of the system is reduced, the disruption time eventually becomes comparable to the libration period. In that case the averaging process that we use in the derivation is no longer valid and the lifetime no longer scales as $1/D$.

The analytic model was compared to numerical simulations which incorporate stochastic forces. Those forces, parametrised by the mean square values of each component in cylindrical coordinates and the auto-correlation time, are applied in a continuous manner giving results that could be directly compared with the analytic model. The simulations are in broad agreement with analytic predictions and we presented illustrative examples of the disruption process. We performed the simulations for a large range of diffusion parameters, planet masses and initial eccentricities to verify the scaling law for the commensurability disruption time summarised hereafter.

To summarise our results, recalling that the slow angle is driven into circulation before the fast angle, so that the ultimate lifetime is determined by the time taken for the fast angle to achieve circulation, we determine the lifetime, t_f , using equation 3.66, setting $t = t_f$, $(\Delta\phi_1)^2 = (\Delta\phi_1)_0^2 = 4$, together with $\gamma_f = p = 1$, we obtain

$$t_f = \frac{a_1^2 \omega_{lf}^2 (\Delta\phi_1)_0^2}{36D}. \quad (3.73)$$

We showed above that this gives good agreement with our numerical results. Using $D = 2\langle F_i^2 \rangle \tau_c$, we can express this result in terms of the relative magnitude of the stochastic forcing in the form

$$t_f = 2.4 \times 10^{-4} \left(\frac{a_1^2 n_1^4}{\langle F_i^2 \rangle} \right) \left(\frac{(\Delta\phi_1)_0^2}{8n_1\tau_c} \right) \cdot \left(\frac{8.5\omega_{lf}\sqrt{q_{GJ}}}{n_1\sqrt{q}} \right)^2 \frac{q}{q_{GJ}} P_1, \quad (3.74)$$

where P_1 is the orbital period of the outer planet. Here the first quantity in brackets represents the ratio of the square of the central force per unit mass to the mean square stochastic force per unit mass acting on the outer planet. The other quantities in brackets, scaled to the GJ876 system are expected to be unity, while the last factor q/q_{GJ} is the ratio of the total mass ratio of the system to the same quantity for GJ876. Here, it is assumed that the two planets in the system have comparable masses.

From equation 3.74, we see that a non-migrating system such as GJ876 could survive in resonance for $t_f \sim 10^6$ years if the stochastic force amplitude is $\sim 10^{-5}$ times the central force. This expression enables scaling to other systems at other disc locations for other stochastic forcing amplitudes. Inference of survival probabilities for particular systems depends on many uncertain aspects, such as the proto-planetary disc model and the strength of the turbulence. However, the mass ratio dependence in equation 3.74 indicates that survival is favoured for more massive systems. At the present time the number of observed resonant systems is too small for definitive conclusions to be made. However, the fact that several systems exhibiting commensurabilities have been observed indicates that resonances are not always completely disrupted by stochastic forces due to turbulence, but rather may be modified as in our study of HD128311.

The most likely orbital configuration of the HD128311 system is such that the fast mode librates with the slow mode being near the borderline between libration and circulation. We found that such a configuration was readily produced in a scenario in which the commensurability was formed through a temporary period of convergent migration, with the addition of stochastic forcing. During a migration phase moderate adiabatic invariance applied to the libration modes together with eccentricity damping leads to increased stabilisation and a longer lifetime for the resonance. However, the time evolution of the eccentricity, and in particular the attainment of small values, plays an important role in causing the slow mode to circulate. This corresponds to the loss of apsidal co-rotation. Thus we expect that a large eccentricity damping rate does not necessarily stabilise the apsidal co-rotation of a system. Additional simulations have shown that this is lost more easily for large damping rates ($K \gg 10$). On the other hand, it should be noted that this has less significance when one of the orbits becomes nearly circular.

Further observations of extra-solar planetary systems leading to better statistics may lead to an improved situation for assessing the role of stochastic forcing.

Stochastic migration of small bodies in Saturn's rings

Have not the small particles of bodies certain powers, virtues, or forces, by which they act at a distance, not only upon the rays of light for reflecting, refracting, and inflecting them, but also upon one another for producing a great part of the Phenomena of nature?

Isaac Newton, *Optiks*, Query 31, 1729

In the previous chapter, we discussed the stochastic migration of planets, embedded in a circum-stellar disc. A very similar process also occurs in the circum-planetary disc known as Saturn's rings. However, both the length and time scales involved are three orders of magnitude smaller. The bodies of interest are small moonlets. These 20 m – 100 m sized bodies have been predicted both analytically and numerically (Spahn & Sremčević 2000; Sremčević et al. 2002; Seiß et al. 2005). They create propeller shaped structures due to their disturbance of the rings and have been observed only recently by the Cassini spacecraft in the A and B ring (Tiscareno et al. 2006, 2008).

They can migrate within the rings, similar to proto-planets which migrate in a proto-stellar disc. Depending on the disc properties and the moonlet size, this can happen in either a smooth or in a stochastic (random walk) fashion. We refer to those migration regimes as type I and type IV, respectively, in analogy to the terminology in disc-planet interactions (see section 1.4.1). Crida et al. (2010) showed that there is a laminar type I regime that might be important on very long timescales. This migration is qualitatively different to the migration in a pressure supported gas disc. However, the migration of moonlets in the A ring is generally dominated by type IV migration, at least on short timescales.

We here study their dynamical evolution in the type IV regime analytically, including important effects such as collisions which were not present in the discussion in chapter 3. We also perform realistic three dimensional collisional N-body simulations with up to a quarter of a million particles. A new set of *pseudo* shear periodic boundary conditions is used which reduces the computational costs by an order of magnitude compared to previous studies. The numerical simulations confirm our analytic estimates to within a factor of two.

For low ring surface densities, the main effects on the evolution of the eccentricity and the semi-major axis are found to be due to collisions and the gravitational interaction with particles in the vicinity of the moonlet. For large surface densities, the gravitational interaction with self-gravitating wakes becomes important. These stochastic forces are very similar to what has been discussed earlier, in chapter 3.

On short timescales the evolution is always dominated by stochastic effects caused by collisions and gravitational interaction with self-gravitating ring particles. These result in a random walk of the moonlet's semi-major axis. The eccentricity of the moonlet quickly reaches an equilibrium value due to collisional damping. The average change in semi-major axis of the moonlet after 100 orbital periods is 10-100m. This translates to an offset in the azimuthal direction of several hundred kilometres. We expect that such a shift is easily observable.

We start by reviewing the basic equations governing the moonlet and the ring particles in a shearing box approximation in section 4.1. Then, in section 4.2, we estimate the eccentricity damping timescale due to ring particles colliding with the moonlet and ring particles on horseshoe orbits as well as the effect of particles on circulating orbits. In section 4.3 we estimate the excitation of the moonlet eccentricity caused by stochastic particle collisions and gravitational interactions with ring particles. This enables us to derive an analytic estimate of the equilibrium eccentricity.

In section 4.4 we discuss and evaluate processes, such as collisions and gravitational interactions with ring particles and self-gravitating clumps, that lead to a random walk in the semi-major axis of the moonlet.

We describe our numerical setup and the initial conditions used in section 4.5. The results are presented in section 4.6. All analytic estimates are confirmed both in terms of qualitative trends and quantitatively to within a factor of about two in all simulations that we performed. We also discuss the long term evolution of the longitude of the moonlet and its observability, before summarising our results in section 4.7.

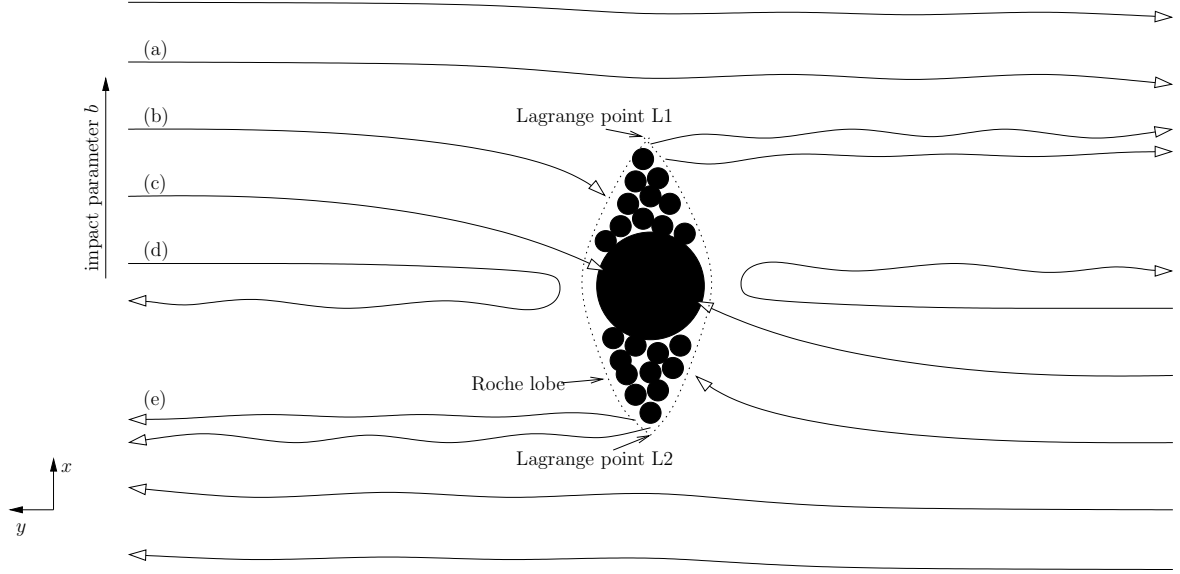


Figure 4.1: Trajectories of ring particles in a frame centred on the moonlet. Particles accumulate near the moonlet and fill its Roche lobe. Particles on trajectories labelled a) are on circulating orbits. Particles on trajectories labelled b) collide with other particles in the moonlet’s vicinity. Particles on trajectories labelled (c) collide with the moonlet directly. Particles on trajectories labelled (d) are on horseshoe orbits. Particles on trajectories labelled (e) leave the vicinity of the moonlet.

4.1 Basic equations governing the moonlet and ring particles

4.1.1 Epicyclic motion

We adopt a local right handed Cartesian coordinate system with its origin being in circular Keplerian orbit with semi-major axis a and rotating uniformly with angular velocity Ω . This orbit coincides with that of the moonlet when it is assumed to be unperturbed by ring particles. The x axis coincides with the line joining the central object of mass M_p and the origin. The unit vector in the x direction, \mathbf{e}_x , points away from the central object. The unit vector in the y direction \mathbf{e}_y points in the direction of rotation and the unit vector in the z direction, \mathbf{e}_z points in the vertical direction being normal to the disc mid-plane (see also appendix D).

In general, we shall consider a ring particle of mass m_1 interacting with the moonlet which has a much larger mass m_2 . A sketch of three possible types of particle trajectory in the vicinity of the moonlet is shown in figure 4.1. These correspond to three distinct regimes, a) denoting circulating orbits, b) and c) denoting orbits that result in a collision with particles in the vicinity of the moonlet and directly with the moonlet respectively, and d) denoting horseshoe orbits. All these types of trajectory occur for particles that are initially in circular orbits, both interior and exterior to the moonlet, when at large

distances from it.

Approximating the gravitational force due to the central object by its first order Taylor expansion about the origin leads to Hill's equations (see equations D.8-D.10), governing the motion of a particle of mass m_1 of the form

$$\ddot{\mathbf{r}} = -2\Omega\mathbf{e}_z \times \dot{\mathbf{r}} + 3\Omega^2(\mathbf{r} \cdot \mathbf{e}_x)\mathbf{e}_x - \nabla\Psi/m_1, \quad (4.1)$$

where $\mathbf{r} = (x, y, z)$ is position of a particle with mass m_1 and Ψ is the gravitational potential acting on the particle due to other objects of interest such as the moonlet.

The square amplitude of the epicyclic motion \mathcal{E}^2 can be defined through

$$\mathcal{E}^2 = \Omega^{-2}\dot{x}^2 + (2\Omega^{-1}\dot{y} + 3x)^2. \quad (4.2)$$

Note that neither the eccentricity e , nor the semi-major axis a are formally defined in the local coordinate system. However, in the absence of interaction with other masses ($\Psi = 0$), \mathcal{E} is conserved, and up to first order in the eccentricity we may make the identification $\mathcal{E} = ea$. We recall the classical definition of the eccentricity e in a coordinate system centred on the central object

$$e = \left| \frac{\mathbf{w} \times (\mathbf{s} \times \mathbf{w})}{\Omega^2 a^3} - \frac{\mathbf{s}}{|\mathbf{s}|} \right|. \quad (4.3)$$

Here, \mathbf{s} is the position vector $(a, 0, 0)$ and \mathbf{w} is the velocity vector of the particle relative to the mean shear associated with circular Keplerian motion as viewed in the local coordinate system plus the circular Keplerian velocity corresponding to the orbital frequency Ω of the origin. Thus

$$\mathbf{w} = \left(\dot{x}, \dot{y} + \frac{3}{2}\Omega x + a\Omega, \dot{z} \right). \quad (4.4)$$

All eccentricities considered here are very small ($\sim 10^{-8} - 10^{-7}$) so that the difference between the quantities defined through use of equations 4.2 and 4.3 is negligible, allowing us to adopt \mathcal{E} as a measure of the eccentricity throughout this chapter.

Let us define another quantity, \mathcal{A} , that is also conserved for non interacting particle motion, $\Psi = 0$, which is the x coordinate of the centre of the epicyclic motion and is given by

$$\mathcal{A} = 2\Omega^{-1}\dot{y} + 4x. \quad (4.5)$$

We identify a change in \mathcal{A} as a change in the semi-major axis a of the particle, again, under the assumption that the eccentricity is small.

4.1.2 Two interacting particles

We now consider the motion of two gravitationally interacting particles with position vectors $\mathbf{r}_1 = (x_1, y_1, z_1)$ and $\mathbf{r}_2 = (x_2, y_2, z_2)$. Their corresponding masses are m_1 and m_2 , respectively. The governing equations of motion are

$$\ddot{\mathbf{r}}_1 = -2\Omega\mathbf{e}_z \times \dot{\mathbf{r}}_1 + 3\Omega^2(\mathbf{r}_1 \cdot \mathbf{e}_x)\mathbf{e}_x - \nabla_{\mathbf{r}_1}\Psi_{12}/m_1 \quad (4.6)$$

$$\ddot{\mathbf{r}}_2 = -2\Omega\mathbf{e}_z \times \dot{\mathbf{r}}_2 + 3\Omega^2(\mathbf{r}_2 \cdot \mathbf{e}_x)\mathbf{e}_x + \nabla_{\mathbf{r}_1}\Psi_{12}/m_2, \quad (4.7)$$

where the interaction gravitational potential is $\Psi_{12} = -Gm_1m_2/|\mathbf{r}_1 - \mathbf{r}_2|$. The position vector of the centre of mass of the two particles is given by

$$\bar{\mathbf{r}} = \frac{m_1\mathbf{r}_1 + m_2\mathbf{r}_2}{m_1 + m_2}. \quad (4.8)$$

The vector $\bar{\mathbf{r}}$ also obeys equation 4.1 with $\Psi = 0$, which applies to an isolated particle. This is because the interaction potential does not affect the motion of the centre of mass. We also find it useful to define the vector

$$\mathcal{E}_i = (\Omega^{-1}\dot{x}_i, 2\Omega^{-1}\dot{y}_i + 3x_i) \quad i = 1, 2. \quad (4.9)$$

Then, consistently with our earlier definition of \mathcal{E} , we have $\mathcal{E}_i = |\mathcal{E}_i|$. The amplitude of the epicyclic motion of the centre of mass $\bar{\mathcal{E}}$ is given by

$$(m_1 + m_2)^2\bar{\mathcal{E}}^2 = m_1^2\mathcal{E}_1^2 + m_2^2\mathcal{E}_2^2 + 2m_1m_2\mathcal{E}_1\mathcal{E}_2\cos(\phi_{12}). \quad (4.10)$$

Here ϕ_{12} is the angle between \mathcal{E}_1 and \mathcal{E}_2 . It is important to note that $\bar{\mathcal{E}}$ is conserved even if the two particles approach each other and become bound. This is as long as frictional forces are internal to the two particle system and do not affect the centre of mass motion.

4.2 Effects leading to damping of the eccentricity of the moonlet

We begin by estimating the moonlet eccentricity damping rate associated with ring particles that either collide directly with the moonlet, particles in its vicinity, or interact only gravitationally with the moonlet.

4.2.1 The contribution due to particles impacting the moonlet

Particles impacting the moonlet in an eccentric orbit exchange momentum with it. Let us assume that a ring particle, identified with m_1 has zero epicyclic amplitude, so that

$\mathcal{E}_1 = 0$ far away from the moonlet. The moonlet is identified with m_2 and has an initial epicyclic amplitude \mathcal{E}_2 . The epicyclic amplitude of the centre of mass is therefore

$$\bar{\mathcal{E}} = \frac{m_2}{m_1 + m_2} \mathcal{E}_2 \simeq \left(1 - \frac{m_1}{m_2}\right) \mathcal{E}_2, \quad (4.11)$$

where we have assumed that $m_1 \ll m_2$.

The moonlet is assumed to be in a steady state in which there is no net accretion of ring particles. Therefore, for every particle that either collides directly with the moonlet or nearby particles bound to it (and so itself becomes temporarily bound to it), one particle must also escape from the moonlet. This happens primarily through slow leakage from locations close to the L_1 and L_2 points such that most particles escape from the moonlet with almost zero velocity (as viewed from the centre of mass frame) and so do not change its orbital eccentricity. However, after an impacting particle becomes bound to the moonlet, conservation of the epicyclic amplitude associated with the centre of mass motion together with equation 4.11 imply that each impacting particle will reduce the eccentricity by a factor $1 - m_1/m_2$.

It is now an easy task to estimate the eccentricity damping timescale by determining the number of particle collisions per time unit with the moonlet or particles bound to it. To do that, a smooth window function $W_{b+c}(b)$ is used, being unity for impact parameters b that always result in an impact with the moonlet or particles nearby that are bound to it, being zero for impact parameters that never result in an impact.

To ensure that the impact band is well defined, we assume that the epicyclic amplitude is smaller than the moonlet's Hill radius, which is the case in all simulations discussed below. However, if this were not the case, one could simply calculate the collisions per time units by other means, for example by using the velocity dispersion and the geometrical cross section of the moonlet.

The number of particles impacting the moonlet per time unit, dN/dt , is obtained by integrating over the impact parameter with the result that

$$\frac{dN}{dt} = \frac{1}{m_1} \int_{-\infty}^{\infty} \frac{3}{2} \Sigma \Omega |b| W_{b+c}(b) db. \quad (4.12)$$

We note that allowing b to be negative enables impacts from both sides of the moonlet to be taken into account.

Therefore, after using equation 4.11 we find that the rate of change of the moonlet's eccentricity e_2 , or equivalently of its amplitude of epicyclic motion \mathcal{E}_2 , is given by

$$\frac{d\mathcal{E}_2}{dt} = -\frac{\mathcal{E}_2}{\tau_{e,\text{collisions}}} = -\frac{\mathcal{E}_2}{m_2} \int_{-\infty}^{\infty} \frac{3}{2} \Sigma \Omega |b| W_{b+c}(b) db, \quad (4.13)$$

where $\tau_{e,\text{collisions}}$ defines the circularisation time arising from collisions with the moonlet. We remark that the natural unit for b is the Hill radius of the moonlet, $r_H =$

$(m_2/(3M_p))^{1/3}a$, so that the dimensional scaling for $\tau_{e,\text{collisions}}$ is given by

$$\tau_{e,\text{collisions}}^{-1} \propto G \Sigma r_H^{-1} \Omega^{-1} \quad (4.14)$$

which we find to also apply to all the processes for modifying the moonlet's eccentricity discussed below. If we assume that $W_{b+c}(|b|)$ can be approximated by a box function, being unity in the interval $[1.5r_H, 2.5r_H]$ and zero elsewhere, we get

$$\tau_{e,\text{collisions}}^{-1} = 2.0 G \Sigma r_H^{-1} \Omega^{-1}. \quad (4.15)$$

4.2.2 Eccentricity damping due the interaction of the moonlet with particles on horseshoe orbits

The eccentricity of the moonlet manifests itself in a small oscillation of the moonlet about the origin. Primarily ring particles on horseshoe orbits will respond to that oscillation and damp it. This is because only those particles on horseshoe orbits spend enough time in the vicinity of the moonlet, i.e. many epicyclic periods.

In appendix C, we calculate the amplitude of epicyclic motion \mathcal{E}_{1f} (or equivalently the eccentricity e_{1f}) that is induced in a single ring particle in a horseshoe orbit undergoing a close approach to a moonlet which is assumed to be in an eccentric orbit. In order to calculate the circularisation time, we have to consider all relevant impact parameters. Note that each particle encounter with the moonlet is conservative and is such that for each particle, the Jacobi constant, applicable when the moonlet is in circular orbit, is increased by an amount $m_1\Omega^2\mathcal{E}_{1f}^2/2$ by the action of the perturbing force, associated with the eccentricity of the moonlet, as the particle passes by. Because the Jacobi constant, or energy in the rotating frame, for the moonlet and the particle together is conserved, the square of the epicyclic amplitude associated with the moonlet alone changes by $\mathcal{E}_{1f}^2 m_1/m_2$. Accordingly the change in the amplitude of epicyclic motion of the moonlet \mathcal{E}_2 , consequent on inducing the amplitude of epicyclic motion \mathcal{E}_{1f} in the horseshoe particle, is given by

$$\Delta\mathcal{E}_2^2 = -\frac{m_1}{m_2}\mathcal{E}_{1f}^2. \quad (4.16)$$

Note that this is different compared to equation 4.11. Here, we are dealing with a second order effect. First, the eccentric moonlet excites eccentricity in a ring particle. Second, because the total epicyclic motion is conserved, the epicyclic motion of the moonlet is reduced.

Integrating over the impact parameters associated with ring particles and taking into account particles streaming by the moonlet from both directions by allowing negative impact parameters gives

$$\left. \frac{d\mathcal{E}_2^2}{dt} \right|_{\text{horseshoe}} = - \int_{-\infty}^{\infty} \frac{3\Sigma\mathcal{E}_{1f}^2\Omega |b| W_d(b) db}{2m_2} \equiv -\frac{2\mathcal{E}_2^2}{\tau_{e,\text{horseshoe}}}, \quad (4.17)$$

where $\tau_{e,\text{horseshoe}}$ is the circularisation time and, as above, we have inserted a window function, which is unity on impact parameters that lead to horseshoe orbits, otherwise being zero. Using \mathcal{E}_{1f} given by equation C.18, we obtain

$$\tau_{e,\text{horseshoe}}^{-1} = \frac{9}{128} \left(\frac{\Sigma r_H^2 \Omega}{m_2} \right) \int_{-\infty}^{\infty} \mathcal{I}^2 \eta^{4/3} W_d((2\eta r_h)^{1/6}) d\eta. \quad (4.18)$$

For a sharp cutoff of $W_d(|b|)$ at $b_m = 1.5r_H$ we find the value of the integral in the above to be 2.84. Thus, in this case we get

$$\tau_{e,\text{horseshoe}}^{-1} = 0.13 G \Sigma r_H^{-1} \Omega^{-1}. \quad (4.19)$$

However, note that this value is sensitive to the value of b_m adopted. For $b_m = 1.25r_H$, τ_e is a factor of 4.25 larger.

4.2.3 The effects of circulating particles

The effect of the response of circulating particles to the gravitational perturbation of the moonlet on the moonlet's eccentricity can be estimated from the work of Goldreich & Tremaine (1980) and Goldreich & Tremaine (1982). These authors considered a ring separated from a satellite such that co-orbital effects were not considered. Thus, their expressions may be applied to estimate effects due to circulating particles. However, we exclude their corotation torques as they are determined by the ring edges and are absent in a local model with uniform azimuthally averaged surface density. Equivalently, one may simply assume that the corotation torques are saturated. When this is done only Lindblad torques act on the moonlet. These tend to excite the moonlet's eccentricity rather than damp it.

We replace the ring mass in equation 70 of Goldreich & Tremaine (1982) by the integral over the impact parameter and switch to our notation to obtain

$$\left. \frac{d\mathcal{E}_2^2}{dt} \right|_{\text{circ}} = 9.55 \int_{-\infty}^{\infty} m_2 \Sigma G^2 \Omega^{-3} |b|^{-5} \mathcal{E}_2^2 W_a(b) db, \quad (4.20)$$

where $W_a(b)$ is the appropriate window function for circulating particles. Assuming a sharp cutoff of $W_a(|b|)$ at b_m , we can evaluate the integral in equation 4.20 to get

$$\frac{1}{\mathcal{E}_2} \left. \frac{d\mathcal{E}_2}{dt} \right|_{\text{circ}} = -\frac{1}{\tau_{e,\text{circ}}} = 0.183 G \Sigma r_H^{-1} \Omega^{-1}, \quad (4.21)$$

where we have adopted $b_m = 2.5r_H$, consistently with the simulation results presented below. We see that, although $\tau_{e,\text{circ}} < 0$ corresponds to growth rather than damping of the eccentricity, it scales in the same manner as the circularisation times in sections 4.2.1 and 4.2.2 scale (see equation 4.14).

This timescale and the timescale associated with particles on horseshoe orbits, $\tau_{e,\text{horseshoe}}$, are significantly larger than the timescale associated with collisions, given in equation 4.15. We can therefore ignore those effects for most of the discussion in this chapter.

4.3 Processes leading to the excitation of the eccentricity of the moonlet

In section 4.2 we assumed that the moonlet had a small eccentricity but neglected the initial eccentricity of the impacting ring particles. When this is included, collisions and gravitational interactions of ring particles with the moonlet may also excite its eccentricity.

4.3.1 Collisional eccentricity excitation

To see this, assume that the moonlet initially has zero eccentricity, or equivalently no epicyclic motion, but the ring particles do.

As above we consider the conservation of the epicyclic motion of the centre of mass in order to connect the amplitude of the final epicyclic motion of the combined moonlet and ring particle to the initial amplitude of the ring particle's epicyclic motion. This gives the epicyclic amplitude of the centre of mass after one impact as

$$\bar{\mathcal{E}} = \frac{m_1}{m_1 + m_2} \mathcal{E}_1 \simeq \left(\frac{m_1}{m_2} \right) \mathcal{E}_1. \quad (4.22)$$

Assuming that successive collisions are uncorrelated and occur stochastically with the mean time between consecutive encounters being τ_{ce} , the evolution of $\bar{\mathcal{E}}$ is governed by the equation

$$\left. \frac{d\bar{\mathcal{E}}^2}{dt} \right|_{\text{collisions}} = \left(\frac{m_1}{m_2} \right)^2 \langle \mathcal{E}_1^2 \rangle \tau_{ce}^{-1}, \quad (4.23)$$

where $\tau_{ce}^{-1} = dN/dt$ can be expressed in terms of the surface density and an impact window function $W_{b+c}(b)$ (see equation 4.12). The quantity $\langle \mathcal{E}_1^2 \rangle$ is the mean square value of \mathcal{E}_1 for the ring particles. Using equation 4.2, this may be written in terms of the mean squares of the components of the velocity dispersion relative to the background shear, in the form

$$\langle \mathcal{E}_1^2 \rangle = \Omega^{-2} \langle (\dot{x}_1^2 + 4(\dot{y}_1 + 3\Omega x_1/2)^2) \rangle. \quad (4.24)$$

We find in numerical simulations $\langle e_1 \rangle \sim 10^{-6}$ for almost all ring parameters. This value is mainly determined by the coefficient of restitution (see e.g. figure 4 in Morishima & Salo 2006).

4.3.2 Stochastic excitation due to circulating particles

Ring particles that are on circulating orbits, such as that given by path (a) in figure 4.1, exchange energy and angular momentum with the moonlet and therefore change its eccentricity. Goldreich & Tremaine (1982) calculated the change in the eccentricity of a ring particle due to a satellite. We are interested in the change of the eccentricity of the moonlet induced by a ring of particles and therefore swap the satellite mass with the mass of a ring particle. Thus, rewriting their results (equation 64 in Goldreich & Tremaine (1982)) in our local notation without reference to the semi-major axis, we have

$$\Delta\mathcal{E}_2^2 = 5.02 m_1^2 G^2 \Omega^{-4} b^{-4}. \quad (4.25)$$

Supposing that the moonlet has very small eccentricity, it will receive stochastic impulses that cause its eccentricity to undergo a random walk that will result in \mathcal{E}_2^2 increasing linearly with time, so that we may write

$$\left. \frac{d\mathcal{E}_2^2}{dt} \right|_{\text{circulating particles}} = \int_{-\infty}^{\infty} W_a(b) \Delta\mathcal{E}_2^2 d(1/t_b), \quad (4.26)$$

where $d(1/t_b)$ is the mean encounter rate with particles which have an impact parameter in the interval $(b, b + db)$. $W_a(b)$ is the window function describing the band of particles in circulating orbits. Setting $d(1/t_b) = 3\Sigma\Omega|b|db/(2m_1)$, we obtain

$$\left. \frac{d\mathcal{E}_2^2}{dt} \right|_{\text{circulating particles}} = 7.53 \int_{-\infty}^{\infty} W_a(b) m_1 |b|^{-3} \Sigma G^2 \Omega^{-3} db. \quad (4.27)$$

For high surface densities an additional effect can excite the eccentricity when gravitational wakes occur. The Toomre parameter Q is defined as

$$Q = \frac{\bar{v}\Omega}{\pi G\Sigma}, \quad (4.28)$$

where \bar{v} is the velocity dispersion of the ring particles¹. When the surface density is sufficiently high such that Q approaches unity, transient clumps will form in the rings. The typical length scale of these structures is given by the critical Toomre wave length (Daisaka et al. 2001)

$$\lambda_T = 4\pi^2 G\Sigma\Omega^{-2}, \quad (4.29)$$

which can be used to estimate a typical mass of the clump:

$$m_T \sim \pi \left(\frac{\lambda_T}{2} \right)^2 \Sigma = 4\pi^5 G^2 \Sigma^3 \Omega^{-4}. \quad (4.30)$$

¹The Toomre criterion used here was originally derived for a flat gaseous disc. To make use of it we replace the sound speed by the radial velocity dispersion of the ring particles.

Whenever strong clumping occurs, m_T should be used in the above calculation instead of the mass of a single particle m_1 :

$$\left. \frac{d\mathcal{E}_2^2}{dt} \right|_{\text{circulating clumps}} = 7.53 \int_{-\infty}^{\infty} W'_a(b) m_T |b|^{-3} \Sigma G^2 \Omega^{-3} db, \quad (4.31)$$

where $W'_a(b) \approx W_a(b)$ is the appropriate window function. For typical parameters used in section 4.6, this transition occurs at $\Sigma \sim 200 \text{kg/m}^2$.

4.3.3 Equilibrium eccentricity

Putting together the results from this and the previous section, we can estimate an equilibrium eccentricity of the moonlet. Let us assume the eccentricity e_2 , or the amplitude of the epicyclic motion \mathcal{E}_2 , evolves under the influence of excitation and damping forces as follows

$$\begin{aligned} \frac{d\mathcal{E}_2^2}{dt} = & -2 (\tau_{e,\text{collisions}}^{-1} + \tau_{e,\text{horseshoe}}^{-1} + \tau_{e,\text{circ}}^{-1}) \mathcal{E}_2^2 \\ & + \left. \frac{d\mathcal{E}_2^2}{dt} \right|_{\text{collisions}} + \left. \frac{d\mathcal{E}_2^2}{dt} \right|_{\text{circulating particles}} + \left. \frac{d\mathcal{E}_2^2}{dt} \right|_{\text{circulating clumps}}. \end{aligned} \quad (4.32)$$

The equilibrium eccentricity is then found by setting the above equation equal to zero and solving for \mathcal{E}_2 .

To make quantitative estimates we need to specify the window functions $W_a(b)$, $W_{b+c}(b)$ and $W_d(b)$ that determine in which impact parameter bands the particles are in (see figure 4.1). To compare our analytic estimates to the numerical simulations presented below, we measure the window functions numerically. Alternatively, one could simply use sharp cutoffs at some multiple of the Hill radius (see also section 4.6.1). We already made use of this approximation as a simple estimate in the previous sections. The results may vary slightly, but not significantly.

However, as the window functions are dimensionless, it is possible to obtain the dimensional scaling of \mathcal{E}_2 by adopting the length scale applicable to the impact parameter to be the Hill radius r_H and simply assume that the window functions are of order unity. As already indicated above, all of the circularisation times scale as $\tau_e \propto \Omega r_H G^{-1} \Sigma^{-1}$, or equivalently $\propto m_2 / (\Sigma r_H^2 \Omega)$. Assuming the ring particles have zero velocity dispersion, the eccentricity excitation is then due to circulating clumps or particles and the scaling of $d\mathcal{E}_2^2/dt$ due to this cause is given by equations 4.27 and 4.31 by

$$\frac{d\mathcal{E}_2^2}{dt} \propto m_i r_H^{-2} \Sigma G^2 \Omega^{-3}, \quad (4.33)$$

where m_i is either m_1 or m_T . We may then find the scaling of the equilibrium value of \mathcal{E}_2 from consideration of equations 4.32 and 4.13 as

$$\mathcal{E}_2^2 \propto \frac{m_i}{m_2} r_H^2. \quad (4.34)$$

This means that the expected kinetic energy in the non circular motion of the moonlet is $\propto m_i r_H^2 \Omega^2$ which can be viewed as stating that the non circular moonlet motion scales in equipartition with the mass m_i moving with speed $r_H \Omega$. This speed applies when the dispersion velocity associated with these masses is zero indicating that the shear across a Hill radius replaces the dispersion velocity in that limit.

In the opposite limit when the dispersion velocity exceeds the shear across a Hill radius and the dominant source of eccentricity excitation is due to collisions, equation 4.32 gives

$$m_2 \mathcal{E}_2^2 = m_1 \langle \mathcal{E}_1^2 \rangle \quad (4.35)$$

so that the moonlet is in equipartition with the ring particles. Results for the two limiting cases can be combined to give an expression for the amplitude of the epicyclic motion excited in the moonlet of the form

$$m_2 \Omega^2 \mathcal{E}_2^2 = m_1 \Omega^2 \langle \mathcal{E}_1^2 \rangle + C_i m_i \Omega^2 r_H^2, \quad (4.36)$$

where C_i is a constant of order unity. This indicates the transition between the shear dominated and the velocity dispersion dominated limits.

4.4 Processes leading to a random walk in the semi-major axis of the moonlet

We have established estimates for the equilibrium eccentricity of the moonlet in the previous section. Here, we estimate the random walk of the semi-major axis of the moonlet. In contrast to the case of the eccentricity, there is no tendency for the semi-major axis to relax to any particular value, so that there are no damping terms and the deviation of the semi-major axis from its value at time $t = 0$ grows on average as \sqrt{t} for large t .

Depending on the surface density, there are different effects that dominate the contributions to the random walk of the moonlet. For low surface densities, collisions and horseshoe orbits are most important. For high surface densities, the random walk is dominated by the stochastic gravitational force of circulating particles and clumps. In this section, we try to estimate the strength of each effect.

4.4.1 Random walk due to collisions

Let us assume, without loss of generality, that the guiding centre of the epicyclic motion of a ring particle is displaced from the orbit of the moonlet by \mathcal{A}_1 in the inertial frame, whereas in the co-rotating frame the moonlet is initially located at the origin with

$\mathcal{A}_2 = 0$. When the impacting particle becomes bound to the moonlet, the guiding centre of the epicyclic motion of the centre of mass of the combined object, as viewed in the inertial frame, is then displaced from the original moonlet orbit by

$$\Delta\bar{\mathcal{A}} = \frac{m_1}{m_1 + m_2} \mathcal{A}_1 \sim \frac{m_1}{m_2} \mathcal{A}_1. \quad (4.37)$$

This is the analogue of equation 4.22 for the evolution of the semi-major axis. For an ensemble of particles with impact parameter b , the average centre of epicyclic motion is $\langle \mathcal{A}_1 \rangle = b$. Thus we can write the evolution of $\bar{\mathcal{A}}$ due to consecutive encounters as

$$\left. \frac{d\bar{\mathcal{A}}^2}{dt} \right|_{\text{collisions}} = \left(\frac{m_1}{m_2} \right)^2 \langle \mathcal{A}_1^2 \rangle \tau_{ce}^{-1} \quad (4.38)$$

$$= \frac{m_1}{m_2^2} \int_{-\infty}^{\infty} \frac{3}{2} \Sigma \Omega |b|^3 W_{b+c}(b) db, \quad (4.39)$$

which should be compared to the corresponding expression for the eccentricity in equation 4.23.

4.4.2 Random walk due to stochastic forces from circulating particles and clumps

Particles on a circulating trajectory (see path (a) in figure 4.1) that come close the moonlet will exert a stochastic gravitational force. The largest contributions occur for particles within a few Hill radii. Thus, we can crudely estimate the magnitude of the specific gravitational force (acceleration) due to a single particle as

$$f_{cp} = \frac{G m_1}{(2r_H)^2}. \quad (4.40)$$

When self-gravity is important, gravitational wakes (or clumps) have to be taken into account, as was done in section 4.3.2. Then a rough estimate of the largest specific gravitational force due to self gravitating clumps is

$$f_{cc} = \frac{G m_T}{(2r_H + \lambda_T)^2}, \quad (4.41)$$

where $2r_H$ has been replaced by $2r_H + \lambda_T$. This allows for the fact that λ_T could be significantly larger than r_H , in which case the approximate distance of the clump to the moonlet is λ_T (see also figure 3.1 and discussion in section 3.2.1).

Following the formalism of chapter 3, we define a diffusion coefficient as $D = 2\tau_c \langle f^2 \rangle$, where f is an acceleration, τ_c is the correlation time and the angle brackets denote a mean value. We here take the correlation time associated with these forces to be the orbital period, $2\pi\Omega^{-1}$. This is the natural dynamical timescale of the system and has been found to be a reasonable assumption from an analysis of the simulations described

below. Using equation 3.41, we may estimate the random walk in $\bar{\mathcal{A}}$ due to circulating particles and self-gravitating clumps to be given by

$$\left. \frac{d\bar{\mathcal{A}}^2}{dt} \right|_{\text{circulating particles}} = 4D_{cp} \Omega^{-2} = 16\pi \Omega^{-3} f_{cp}^2 \quad (4.42)$$

$$= 16\pi \Omega^{-3} \left(\frac{G m_1}{(2r_H)^2} \right)^2 \quad (4.43)$$

$$\left. \frac{d\bar{\mathcal{A}}^2}{dt} \right|_{\text{circulating clumps}} = 4D_{cc} \Omega^{-2} = 16\pi \Omega^{-3} f_{cc}^2 \quad (4.44)$$

$$= 16\pi \Omega^{-3} \left(\frac{G m_T}{(2r_H + \lambda_T)^2} \right)^2. \quad (4.45)$$

This is only a crude estimate of the random walk undergone by the moonlet. In reality several additional effects might also play a role. For example, circulating particles and clumps are clearly correlated, the gravitational wakes have a large extent in the azimuthal direction and particles that spend a long time in the vicinity of the moonlet have more complex trajectories. Nevertheless, we find that the above estimates are correct up to a factor 2 for all the simulations that we performed (see below).

4.4.3 Random walk due to particles in horseshoe orbits

Finally, let us calculate the random walk induced by particles on horseshoe orbits. Particles undergoing horseshoe turns on opposite sides of the planet produce changes of opposite sign. Encounters with the moonlet are stochastic and therefore the semi-major axis will undergo a random walk. A single particle with impact parameter b will change the semi-major axis of the moonlet by

$$\Delta\bar{\mathcal{A}} = 2 \frac{m_1}{m_1 + m_2} b. \quad (4.46)$$

Analogous to the analysis in section 4.4.1, the time evolution of $\bar{\mathcal{A}}$ is then governed by

$$\left. \frac{d\bar{\mathcal{A}}^2}{dt} \right|_{\text{horseshoe}} = 4 \left(\frac{m_1}{m_2} \right)^2 b^2 \tau_{he}^{-1} \quad (4.47)$$

$$= 6 \frac{m_1}{m_2^2} \int_{-\infty}^{\infty} \Sigma \Omega |b|^3 W_d(b) db. \quad (4.48)$$

Note that this equation is identical to equation 4.39 except a factor 4, as particles with impact parameter b will leave the vicinity of the moonlet at $-b$.

Name	Σ	r_2	dt	$L_x \times L_y$	N
EQ5025	50 kg/m ²	25 m	4s	1000 m \times 1000 m	7.2k
EQ5050	50 kg/m ²	50 m	4s	1000 m \times 1000 m	7.2k
EQ20025	200 kg/m ²	25 m	4s	1000 m \times 1000 m	28.8k
EQ20050	200 kg/m ²	50 m	4s	1000 m \times 1000 m	28.8k
EQ40025	400 kg/m ²	25 m	4s	1000 m \times 1000 m	57.6k
EQ40050	400 kg/m ²	50 m	4s	1000 m \times 1000 m	57.6k
EQ40050DT	400 kg/m ²	50 m	40s	1000 m \times 1000 m	57.6k
EQ5050DTW	50 kg/m ²	50 m	40s	2000 m \times 2000 m	28.8k
EQ20050DTW	200 kg/m ²	50 m	40s	2000 m \times 2000 m	115.2k
EQ40050DTW	400 kg/m ²	50 m	40s	2000 m \times 2000 m	230.0k

Table 4.1: Initial simulation parameters. The second column gives the surface density of the ring. The third gives the moonlet radius. The fourth column gives the time step. The fifth and sixth columns give the lengths of the main box as measured in the xy -plane and the number of particles used, respectively.

4.5 Numerical Simulations

We perform realistic three dimensional simulations of Saturn’s rings with an embedded moonlet and verify the analytic estimates presented above. The nomenclature and parameters used for the simulations are listed in table 4.1.

4.5.1 Methods

We use the GravTree code and a symplectic integrator for Hill’s equations (Quinn et al. 2010). Both are described in more detail in appendix D. The gravitational forces are calculated with a Barnes-Hut tree (Barnes & Hut 1986).

To further speed up the calculations, we run two coupled simulations in parallel. The first adopts the main box which incorporates a moonlet. The second adopts an auxiliary box which initially has the same number of particles but which does not contain a moonlet. This is taken to be representative of the unperturbed background ring. We describe these so called *pseudo* shear periodic boundary conditions in more detail in appendix D.

The moonlet is allowed to move freely in the main box. However, in order to prevent it leaving the computational domain, as soon as the moonlet has left the innermost part (defined as extending one eighth of the box size), all particles are shifted together with the box boundaries, such that the moonlet is returned to the centre of the box. This is possible because the shearing box approximation is invariant with respect to translations in the xy plane (see equation 4.1).

Collisions between particles are resolved using the instantaneous collision model and

a velocity dependent coefficient of restitution given by Bridges et al. (1984):

$$\epsilon(v) = \min \left[0.34 \cdot \left(\frac{v_{\parallel}}{1\text{cm/s}} \right)^{-0.234}, 1 \right], \quad (4.49)$$

where v_{\parallel} is the impact speed projected on the axis between the two particles.

4.5.2 Initial conditions and tests

Throughout this chapter, we use a distribution of particle sizes, r_1 , ranging from 1m to 5m with a slope of $q = -3$. Thus $dN/dr_1 \propto r_1^{-q}$. The density of both the ring particles and the moonlet is taken to be 0.4g/cm^3 . This is at the lower end of what has been assumed reasonable for Saturn's A ring (Lewis & Stewart 2009). The moonlet radius is taken to be either 50 m or 25 m. We found that using a larger ring particle and moonlet density only leads to more particles being bound to the moonlet. This effectively increases the mass of the moonlet (or equivalently its Hill radius) and can therefore be easily scaled to the formalism presented here. Simulating a gravitational aggregate of this kind is computationally very expensive, as many more collisions have to be resolved each time-step.

The initial velocity dispersion of the particles is set to 1 mm/s for the x and y components and 0.4 mm/s for the z component. The moonlet is placed at a semi-major axis of $a = 130000$ km, corresponding to an orbital period of $P = 13.3$ hours. Initially, the moonlet is placed in the centre of the shearing box on a circular orbit.

The dimensions of each box, as viewed in the (x, y) plane, are specified in table 4.1. Because of the small dispersion velocities, the vertical motion is automatically strongly confined to the mid-plane. After a few orbits, the simulations reach an equilibrium state in which the velocity dispersion of particles does not change any more.

We ran several tests to ensure that our results are converged. Simulation EQ40050DT uses a ten times larger time step than simulation EQ40050. Simulations EQ5050DTW, EQ20050DTW and EQ40050DTW use a box that is twice the size of that used in simulation EQ40050. Therefore, four times more particles have been used. No differences in the equilibrium state of the ring particles, nor in the equilibrium state of the moonlet have been observed in any of those test cases.

A snapshot of the particle distribution in simulation EQ40050DTW is shown in figure 4.2. Snapshots of simulations EQ5025, EQ5050, EQ20025, EQ20050, EQ40025 and EQ40050, which use the smaller box size, are shown in figures 4.3, 4.4 and 4.5. In all these cases, the length of the wake that is created by the moonlet is much longer than the box size. Nevertheless, the pseudo shear periodic boundary conditions allow us to simulate the dynamical evolution of the moonlet accurately.

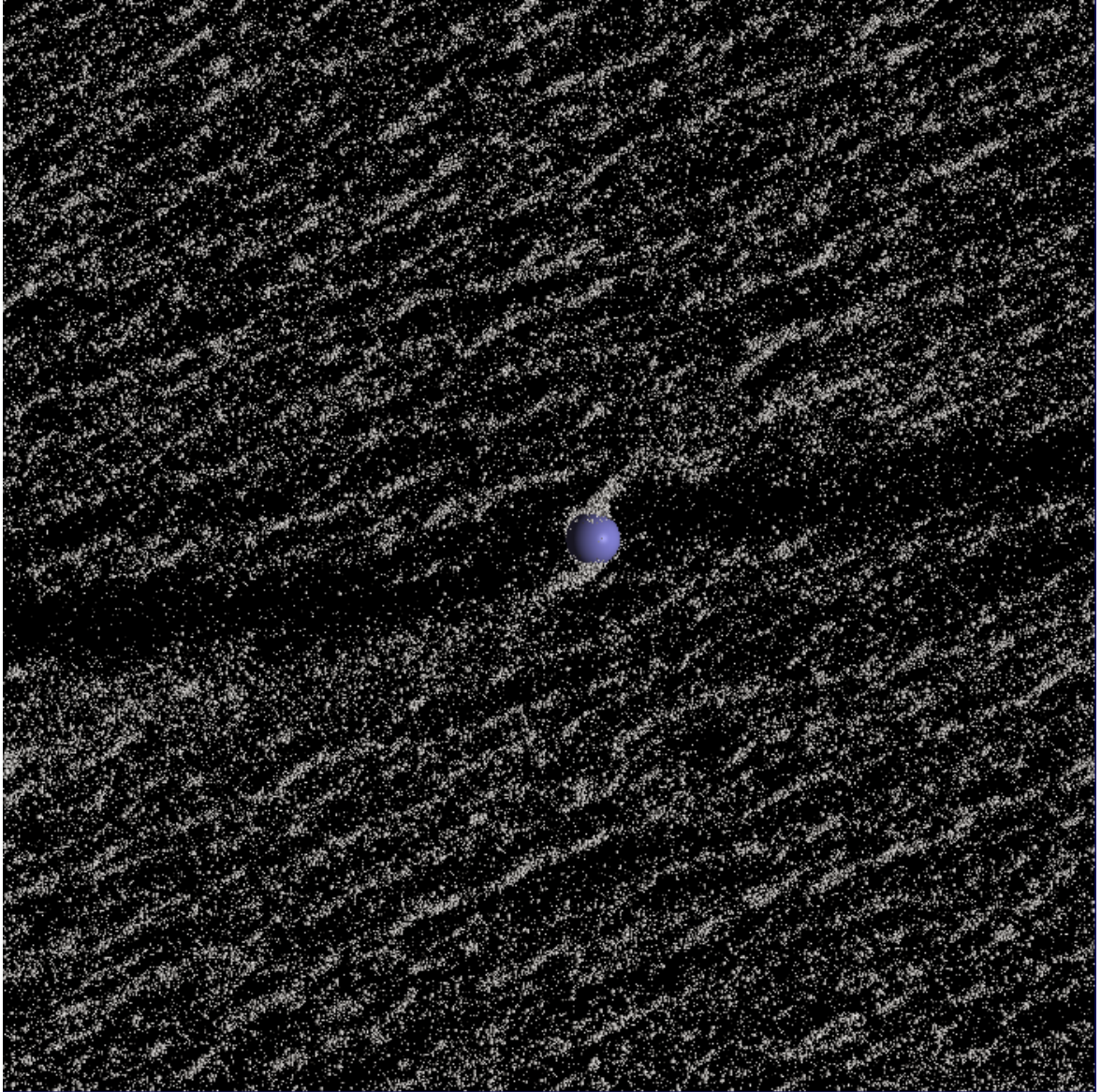
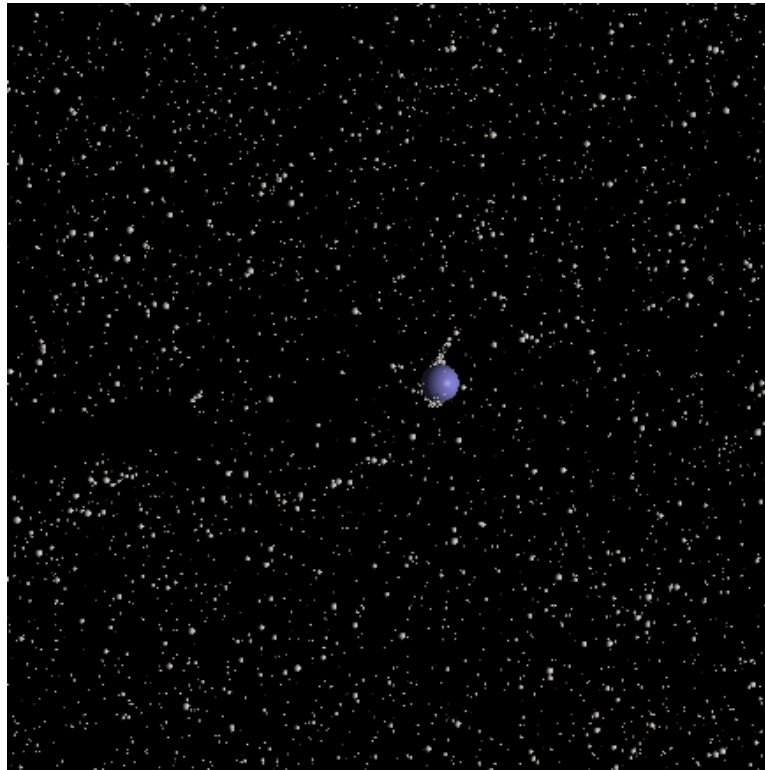


Figure 4.2: Particle distribution in the xy plane in simulation EQ40050DTW. The moonlet's wake is clearly visible.

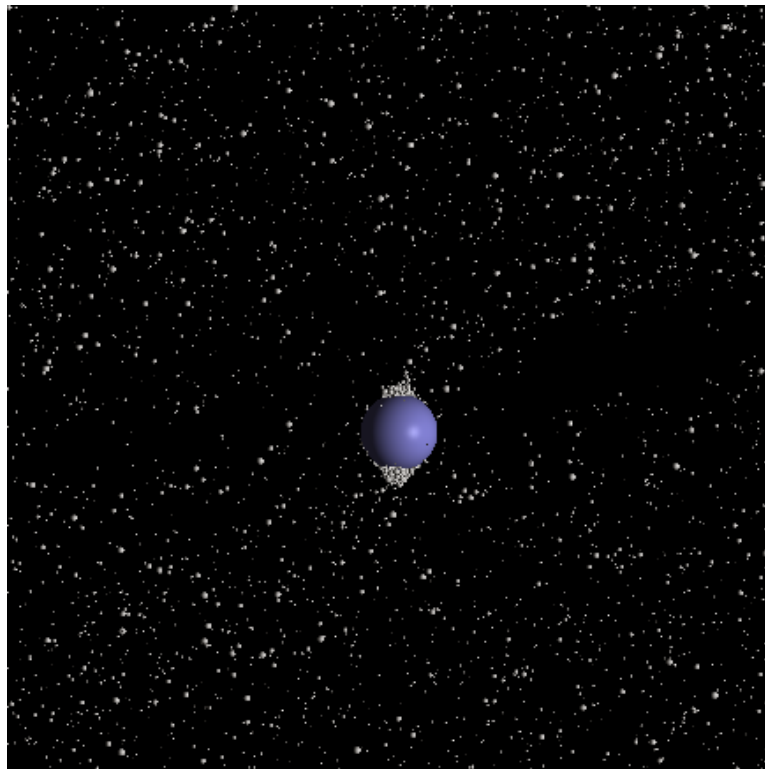
4.6 Results

4.6.1 Impact bands

The impact band window functions $W_a(b)$, $W_{b+c}(b)$ and $W_d(b)$ are necessary to estimate the damping timescales and the strength of the excitation. To measure those, each particle that enters the box is labelled with its impact parameter. The possible outcomes are plotted in figure 4.1: (a) being a circulating particle which leaves the box on the opposite side, (b) representing a collision with other ring particles close to the moonlet where the maximum distance from the centre of the moonlet has been taken to be twice the moonlet radius, (c) being a direct collision with the moonlet and finally (d) showing

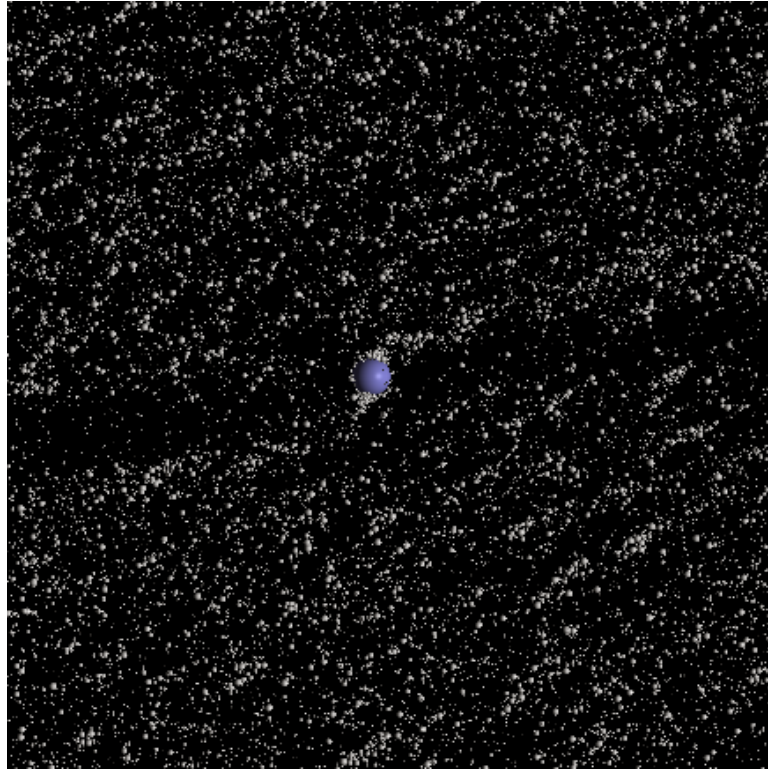


(a) $\Sigma = 50 \text{ kg/m}^2$, $r_2 = 25 \text{ m}$

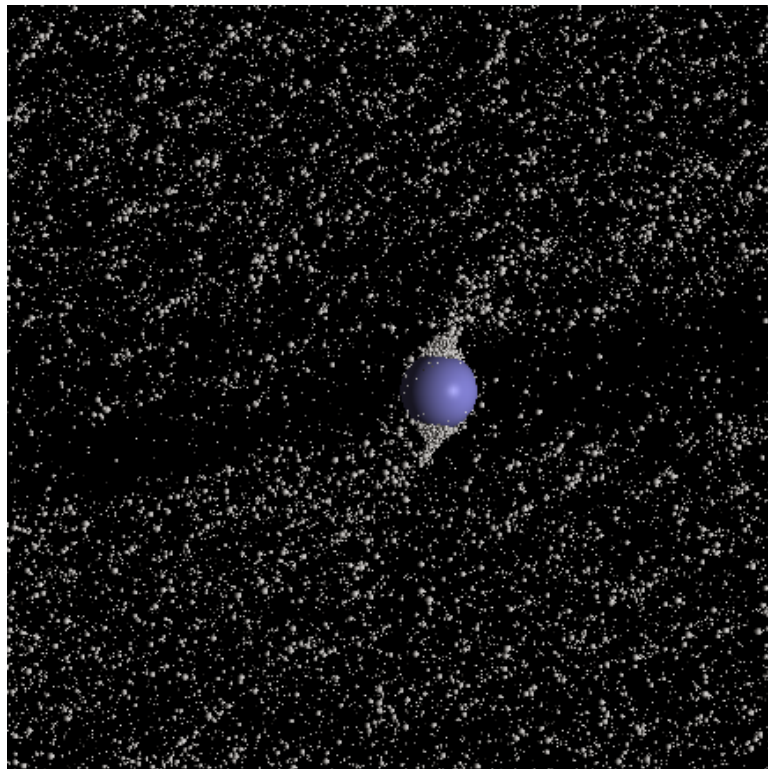


(b) $\Sigma = 50 \text{ kg/m}^2$, $r_2 = 50 \text{ m}$

Figure 4.3: Particle distribution in the xy plane in simulations EQ5025 and EQ5050 at a time when the moonlet and the ring particles are in equilibrium. The mean optical depth is $\tau = 0.04$.

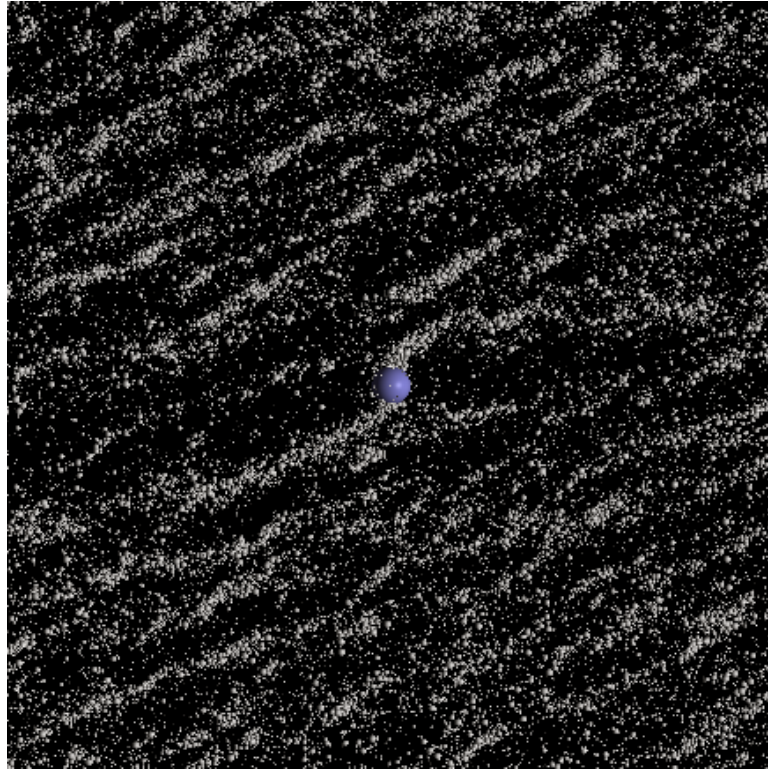


(a) $\Sigma = 200 \text{ kg/m}^2$, $r_2 = 25 \text{ m}$

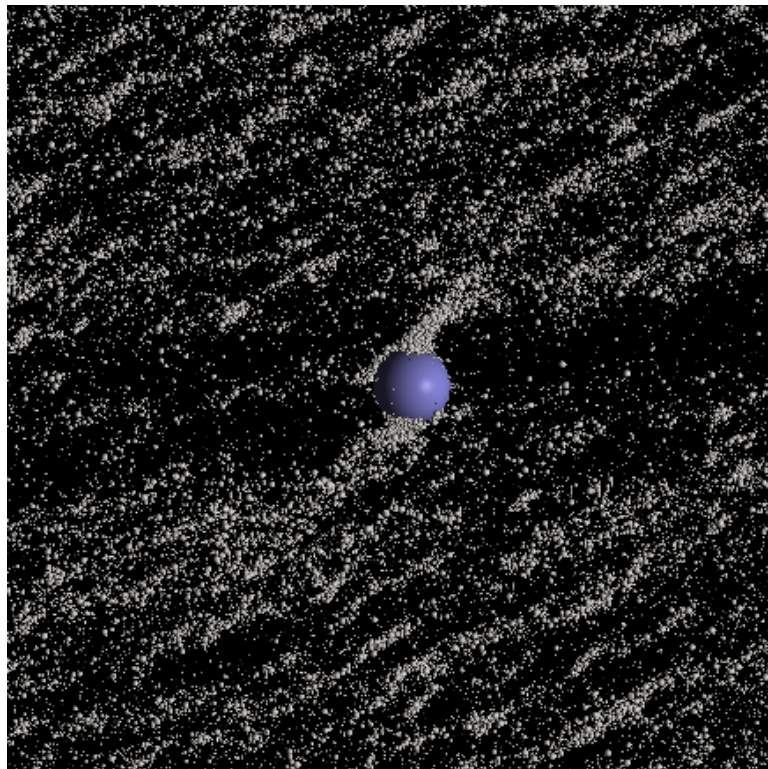


(b) $\Sigma = 200 \text{ kg/m}^2$, $r_2 = 50 \text{ m}$

Figure 4.4: Same as in figure 4.3 but for simulations EQ20025 and EQ20050. The mean optical depth is $\tau = 0.15$.



(a) $\Sigma = 400 \text{ kg/m}^2$, $r_2 = 25 \text{ m}$



(b) $\Sigma = 400 \text{ kg/m}^2$, $r_2 = 50 \text{ m}$

Figure 4.5: Same as in figure 4.3 but for simulations EQ40025 and EQ40050. The mean optical depth is $\tau = 0.30$.

a horseshoe orbit in which the particle leaves the box on the same side that it entered.

The impact band (b) is considered in addition to the impact band (c) because some ring particles will collide with other ring particles that are (temporarily) bound to the moonlet. Thus, these collisions take part in the transfer the energy and momentum to the moonlet. Actually, if the moonlet is simply a rubble pile of ring particles as suggested by Porco et al. (2007), then there might be no solid moonlet core and all collisions are in the impact band (b).

Figures 4.6 and 4.7 show the impact bands, normalised to the Hill radius of the moonlet r_H for simulations EQ5025, EQ20025, EQ40050, EQ5050, EQ20050 and EQ40050. For comparison, we also plot sharp cutoffs, at $1.5r_H$ and $2.5r_H$, as these have been used in same of the scaling laws presented above.

Note that $\sum_{i=a,b,c,d} W_i \gtrsim 1$ because ring particles are shifted from time to time when the moonlet is too far away from the origin (see section 4.5.1). In this process, particles with the same initial impact parameter might become associated with the more than one impact band.

Our results show no sharp discontinuity because of the velocity dispersion in the ring particles which is ~ 5 mm/s. The velocity dispersion corresponds to an epicyclic amplitude of $\mathcal{E}_{rp} \sim 20$ m or equivalently $\sim 0.4r_H$ and $\sim 0.8r_H$ (for $r_2 = 50$ m and $r_2 = 25$ m, respectively). Note that the Hill radius is approximately equal to the physical radius of the moonlet. This is because the moonlet will always fill its Roche lobe with ring particles (see also Porco et al. 2007).

The impact bands are almost independent of the surface density and depend only on the Hill radii and the mean epicyclic amplitude of the ring particles, or, more precisely, the ratio thereof. Thus we expect the impact bands to have a cutoff width of \mathcal{E}_{rp} . A simple approximation of the impact bands may then be given by

$$W_a(b) = \frac{1}{2} + \frac{1}{2} \operatorname{erf} \left(\frac{b/r_H - 2.5}{\mathcal{E}_{rp}/r_H} \right), \quad (4.50)$$

$$W_d(b) = \frac{1}{2} + \frac{1}{2} \operatorname{erf} \left(\frac{1.5 - b/r_H}{\mathcal{E}_{rp}/r_H} \right) \quad \text{and} \quad (4.51)$$

$$W_{b+c}(b) = 1 - W_a(b) - W_d(b). \quad (4.52)$$

These curves are plotted on the right hand side of figures 4.6 and 4.7, being qualitatively very similar to the measured impact bands. This approximation ignores the non-spherical shape of the Roche lobe and assumes $r_H = r_2$.

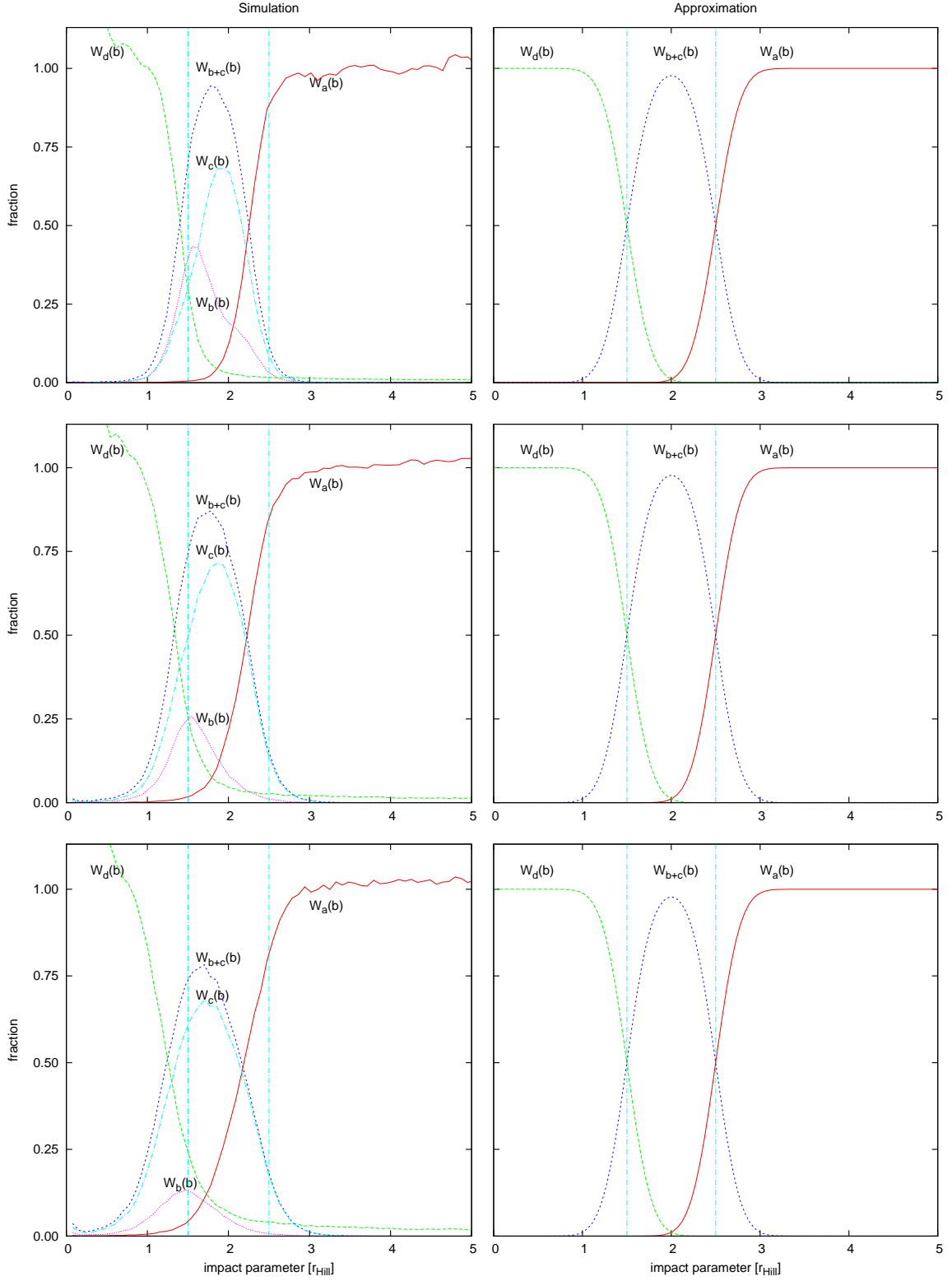


Figure 4.6: Impact bands for simulations with a moonlet radius $r_2 = 25$ m. Left and right columns show the window functions measured in simulations and approximations of those, respectively (see equations 4.50-4.52). The surface density of the ring is, from top to bottom, $\Sigma = 50$ kg/m², $\Sigma = 200$ kg/m² and $\Sigma = 400$ kg/m².

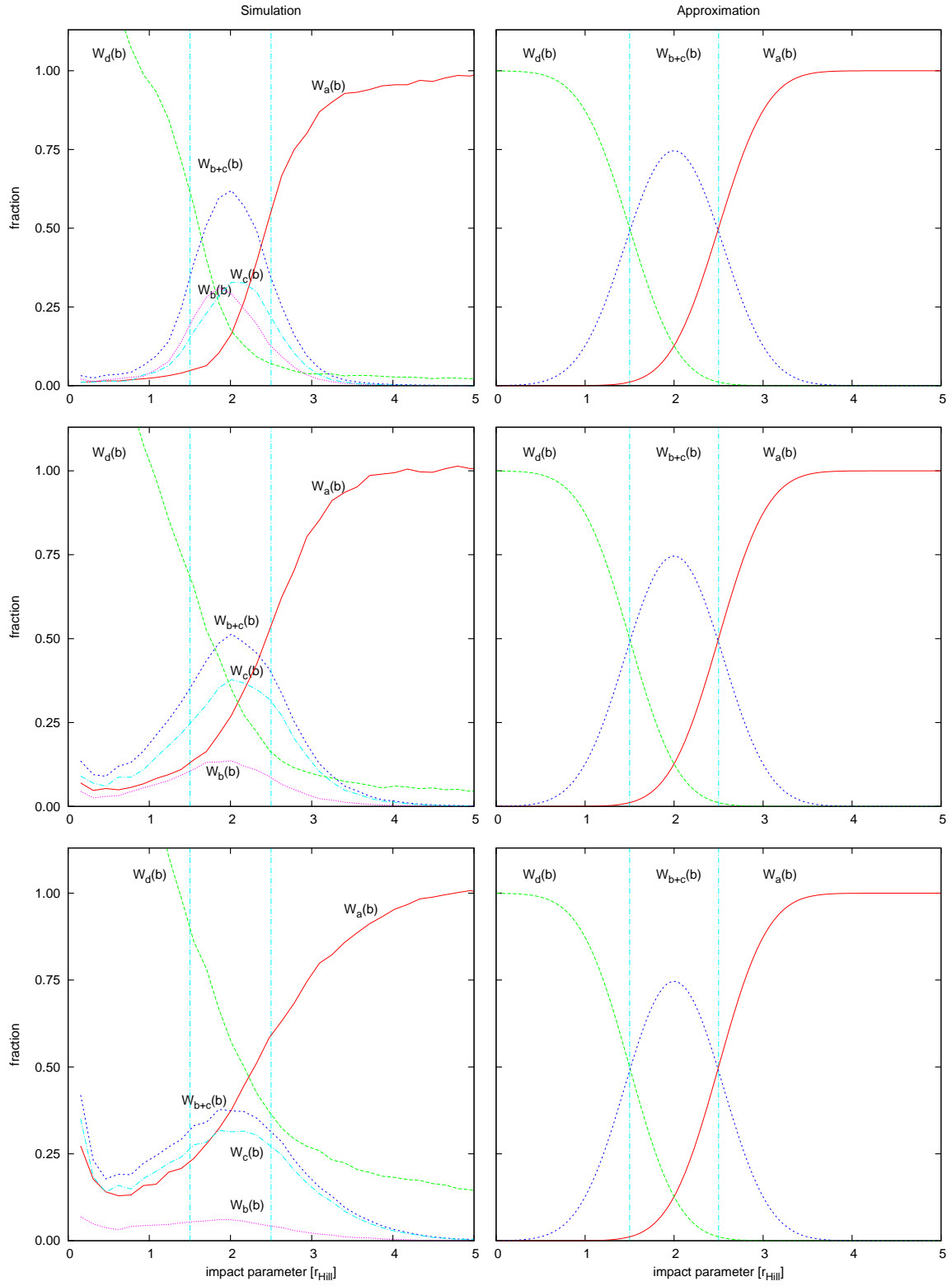


Figure 4.7: Same as in figure 4.6 but for simulations with a moonlet radius $r_2 = 50$ m.

Name	Numerical results	Analytic results	
		collisions	horseshoe
EQ5025	18.9	18.4	1712
EQ5050	27.6	33.8	3424
EQ20025	9.0	3.9	428
EQ20050	12.9	8.5	856
EQ40025	2.8	2.1	214
EQ40050	5.5	4.4	428

Table 4.2: Eccentricity damping timescale τ_e of the moonlet in units of the orbital period. The second column lists the simulation results. The third and fourth column list the analytic estimates of collisional and horseshoe damping timescales, respectively.

4.6.2 Eccentricity damping timescale

To measure the eccentricity damping timescale, we first let the ring particles and the moonlet reach an equilibrium and integrate them for 200 orbits. We then change the velocity of the moonlet and the ring particles within $2r_H$. The new velocity corresponds to an eccentricity of $6 \cdot 10^{-7}$, which is well above the equilibrium value. We then measure the decay timescale τ_e by fitting a function of the form

$$e_d(t) = \langle e_{eq} \rangle + (6 \cdot 10^{-7} - \langle e_{eq} \rangle) e^{-t/\tau_e}. \quad (4.53)$$

The results are given in table 4.2. They are in good agreement with the estimated damping timescales from section 4.2.1 and 4.2.2, showing clearly that the most important damping process, in every simulation considered here, is indeed through collisional damping as predicted by comparing equation 4.15 with equations 4.19 and 4.21.

4.6.3 Mean moonlet eccentricity

The time averaged mean eccentricity of the moonlet² is measured in all simulations after several orbits when the ring particles and the moonlet have reached an equilibrium state. To compare this value with the estimates from section 4.1 we set equation 4.32 equal to zero and use the analytic damping timescale listed in table 4.2. The analytic estimates of the equilibrium eccentricity are calculated for each excitation mechanism separately to disentangle their effects. They are listed in the third, fourth and fifth column in table 4.3. The sixth column lists the analytic estimate for the mean eccentricity using the sum of all excitation mechanisms.

For all simulations, the estimates are correct within a factor of about 2. For low surface densities, the excitation is dominated by individual particle collisions. For larger

²Here, we are calculating the mean eccentricity, not the root-mean-square eccentricity.

Name	Numerical results		Analytic results		
	collisions	circulating particles	circulating clumps	total	total
EQ5025	$6.1 \cdot 10^{-8}$	$1.9 \cdot 10^{-8}$	$0.3 \cdot 10^{-8}$	$4.9 \cdot 10^{-8}$	$4.9 \cdot 10^{-8}$
EQ5050	$4.3 \cdot 10^{-8}$	$1.4 \cdot 10^{-8}$	$0.2 \cdot 10^{-8}$	$2.1 \cdot 10^{-8}$	$2.1 \cdot 10^{-8}$
EQ20025	$6.4 \cdot 10^{-8}$	$1.7 \cdot 10^{-8}$	$2.0 \cdot 10^{-8}$	$5.3 \cdot 10^{-8}$	$5.3 \cdot 10^{-8}$
EQ20050	$4.9 \cdot 10^{-8}$	$1.4 \cdot 10^{-8}$	$1.6 \cdot 10^{-8}$	$2.7 \cdot 10^{-8}$	$2.7 \cdot 10^{-8}$
EQ40025	$11.3 \cdot 10^{-8}$	$2.5 \cdot 10^{-8}$	$8.4 \cdot 10^{-8}$	$9.9 \cdot 10^{-8}$	$9.9 \cdot 10^{-8}$
EQ40050	$7.2 \cdot 10^{-8}$	$1.6 \cdot 10^{-8}$	$4.9 \cdot 10^{-8}$	$5.4 \cdot 10^{-8}$	$5.4 \cdot 10^{-8}$

Table 4.3: Equilibrium eccentricity $\langle e_{\text{eq}} \rangle$ of the moonlet. The second column lists the simulation results. The third, fourth and fifth column list the analytic estimates of the equilibrium eccentricity assuming a single excitation mechanism. The last column lists the analytic estimate of the equilibrium eccentricity summing over all excitation mechanisms.

Name	Numerical results		Analytic results		
	horseshoe	collisions	circulating particles	circulating clumps	total
EQ5025	22.7m	9.0m	17.6m	0.3m	22.4m
EQ5050	12.6m	4.5m	4.4m	0.1m	7.9m
EQ20025	38.1m	18.1m	17.6m	15.7m	38.9m
EQ20050	22.7m	13.6m	4.4m	4.8m	14.7m
EQ40025	78.1m	25.6m	17.6m	86.6m	100.7m
EQ40050	45.6m	12.8m	4.4m	31.4m	36.7m

Table 4.4: Change in semi-major axis of the moonlet after 100 orbits, $\mathcal{A}(\Delta t = 100 \text{ orbits})$. The second column lists the simulation results. The third till sixth columns list the analytic estimates of the change in semi-major axis assuming a single excitation mechanism. The last column lists the total estimated change in semi-major axis summing over all excitation mechanisms.

surface densities, it is dominated by the excitation due to circulating self gravitating clumps (gravitational wakes). The estimates and their trends are surprisingly accurate, as we have ignored several effects (see below).

4.6.4 Random walk in semi-major axis

The random walk of the semi-major axis a (or equivalently the centre of epicyclic motion \mathcal{A} in the shearing sheet) of the moonlet in the numerical simulations are measured and compared to the analytic estimates presented in section 4.4. We run one simulation per parameter set. To get a statistically meaningful expression for the average random walk after a given time $\mathcal{A}(\Delta t)$, we average all pairs of $\mathcal{A}(t)$ and $\mathcal{A}(t')$ for which $t - t' = \Delta t$. In other words, we assume the system satisfies the Ergodic hypothesis.

$\mathcal{A}(\Delta t)$ then grows like $\sqrt{\Delta t}$ and we can fit a simple square root function (see chapter 3). This allows us to accurately measure the average growth in \mathcal{A} after $\Delta t = 100$ orbits by running one simulation for a long time and averaging over time, rather than running many simulations and performing an ensemble average. The measured values are given in the second column of table 4.4. The values that correspond to the analytic expressions in equations 4.48, 4.39, 4.43 and 4.45 are listed in columns three, four, five and six, respectively.

For low surface densities, the evolution of the random walk is dominated by collisions and the effect of particles on horseshoe orbits. For large surface densities, the main effect comes from the stochastic gravitational force due to circulating clumps (gravitational wakes).

The change in semi-major axis is relatively small, a few tens of metres after 100 orbits (= 50 days). The change in longitude $\Delta\lambda$ that corresponds to this is, however, is much larger.

Using the results from chapter 3, namely equations 3.56 and 3.60, we can predict the long term evolution of λ . In the stochastic and laminar case, $(\Delta\lambda)^2$ grows like $\sim t^3$ and $\sim t^4$, respectively. This behaviour allows us to discriminate between a stochastic and laminar migration by observing $\Delta\lambda$ over an extended period of time.

Results from individual simulations (i.e. not an ensemble average) are plotted in figure 4.8. Here, $\Delta\lambda$ is expressed in terms of the azimuthal offset relative to a Keplerian orbit. One can see that for an individual moonlet, the shift in azimuth can appear to be linear, constant or oscillating on short timescales (see curve for simulation EQ20025). This is partly because of the lower order terms in equation 3.55, though, on average, the azimuthal offset grows very rapidly, as $\sim t^{3/2}$ for $t \gg \tau$ (see equation 3.56).

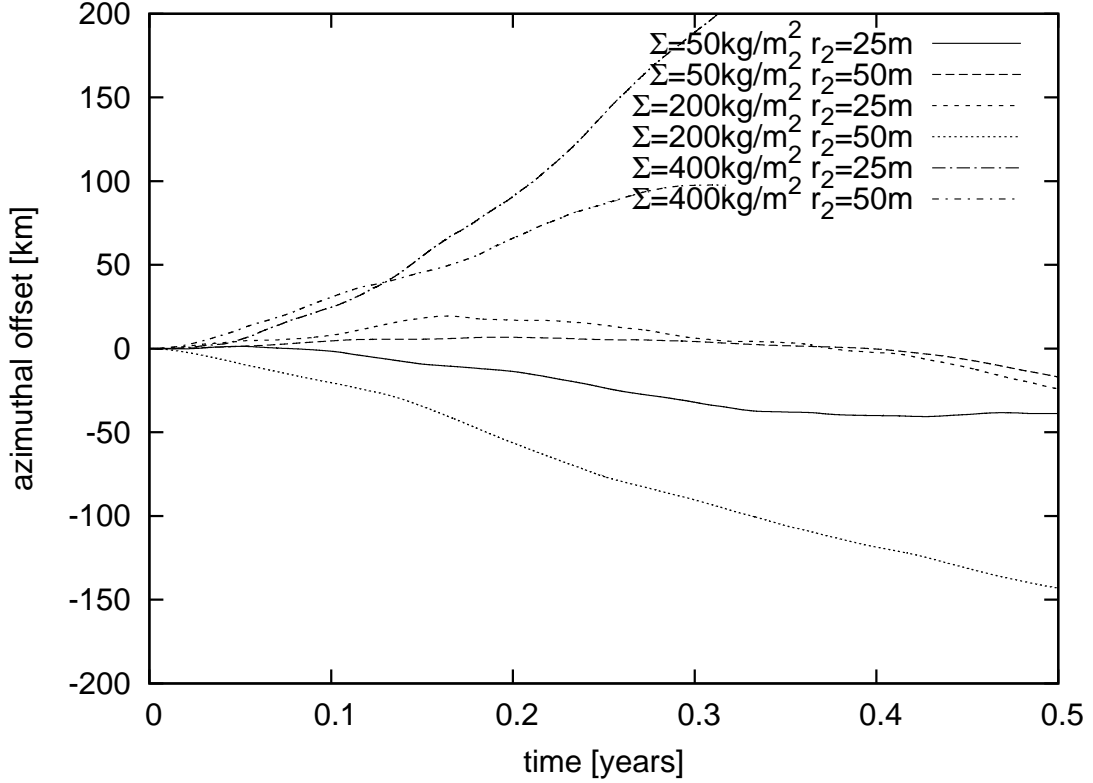


Figure 4.8: Offset in the azimuthal distance due to the random walk in the semi-major axis a measured in simulations EQ5025, EQ5050, EQ20025, EQ20050, EQ40025 and EQ40050. Individual moonlets may show linear, constant or oscillatory growth. On average, the azimuthal offset grows like $t^{3/2}$.

4.7 Conclusions

In this chapter, we have discussed the dynamical response of an embedded moonlet in Saturn’s rings to interactions with ring particles both analytically and by the use of realistic three dimensional many particle simulations. Both the moonlet and the ring particle density were taken to be 0.4g/cm^3 . Moonlets of radius 25 m and 50 m were considered. Particle sizes ranging between 1 m and 5 m were adopted.

We estimated the eccentricity damping timescale of the moonlet due to collisions with ring particles and due to the response of ring particles to gravitational perturbations by the moonlet analytically. We found the effects due to the response of particles on horseshoe and circulating orbits are negligible. On the other hand the stochastic impulses applied to the moonlet by circulating particles were found to cause the square of the eccentricity to grow linearly with time as did collisions with particles with non zero velocity dispersion. A balance between excitation and damping processes then leads to an equilibrium moonlet eccentricity.

We also estimated the magnitude of the random walk in the semi-major axis of the moonlet induced by collisions with individual ring particles and the gravitational

interaction with particles and gravitational wakes. There is no tendency for the semi-major axis to relax to any particular value, so that there are no damping terms. The deviation of the semi-major axis from its value at time $t = 0$ grows on average as \sqrt{t} for large t .

From our simulations we find that the evolution of the eccentricity is indeed dominated by collisions with ring particles. For large surface densities (more than 200kg/m^2) the effect of gravitational wakes also becomes important, leading to an increase in the mean steady state eccentricity of the moonlet. When the particle velocity dispersion is large compared to Ωr_H , we obtain approximate energy equipartition between the moonlet and ring particles as far as epicyclic motion is concerned.

Similarly, the random walk in the semi-major axis was found to be dominated by collisions for low surface densities and by gravitational wakes for large surface densities. In addition we have shown that on average, the difference in longitude $\Delta\lambda$ of a stochastically forced moonlet grows with time like $t^{3/2}$ for large t .

The radial distance travelled within 100 orbits (50 days at a distance of 130000km) is, depending on the precise parameters, of the order of $10\text{-}100\text{m}$. This translates to a shift in longitude of several hundred kilometres. The shift in λ is not necessarily monotonic on short timescales (see figure 4.8). We expect that such a shift should be easily detectable by the Cassini spacecraft. And indeed, Tiscareno et al. (2010) report such an observation, although the data is not publicly available yet, at the time when this thesis was submitted.

There are several effects that have not been included in this study. The analytic discussions in sections 4.2, 4.3 and 4.4 do not model the motion of particles correctly when their trajectories take them very close to the moonlet. Material that is temporarily or permanently bound to the moonlet is ignored. The density of both the ring particles and the moonlet are at the lower end of what is assumed to be reasonable (Lewis & Stewart 2009), which has the advantage that for our computational setup only a few particles (with a total mass of less than 10% of the moonlet) are bound to the moonlet at any given time.

Planetesimal formation in a turbulent disc

To explain all nature is too difficult a task for any one man or even for any one age. 'Tis much better to do a little with certainty, & leave the rest for others that come after you, than to explain all things by conjecture without making sure of any thing.

Isaac Newton, unpublished preface to *Opticks*, 1704

In chapter 3, we discussed the evolution of planets and planetary systems under the effect of stochastic forces resulting from turbulence. The stochastic migration of moonlets in Saturn's rings was discussed in chapter 4. In this chapter, we look at another system, in which turbulence is important, namely the formation of planetesimals, the building blocks of planets.

The formation mechanism of planetesimals in proto-planetary discs is hotly debated. Currently, the favoured model involves the accumulation of metre-sized objects within a turbulent disc. These high spatial densities then promote the formation of planetesimals, for example via gravitational instability as discussed in more detail in chapter 1. In numerical simulations that model this process, one can at most simulate a few million particles as opposed to the several trillion metre-sized particles expected in a real proto-planetary disc. Therefore, single particles are often used as super-particles to represent a distribution of many smaller particles. It is assumed that small-scale phenomena do not play a role and particle collisions are not modelled. However, the super-particle approximation can only be valid in a collision-less or strongly collisional system. In many recent numerical simulations this is not the case.

Here, a scaled system is studied that does not require the use of super-particles. We compare this new method to the standard super-particle approach. We find that the

super-particle approach produces unreliable results that depend on numerical artifacts such as the gravitational softening in both the requirement for gravitational collapse and the resulting clump statistics. Our results show that short-range interactions (collisions) have to be modelled properly.

The outline of this chapter is as follows. In section 5.1, we review the important timescales in the problem and show that the super-particle approach breaks down in high density regions. In section 5.2, we discuss both the super-particle and the scaled particle method. The numerical implementation and the initial conditions of the simulations are presented in section 5.3. Results of numerical simulations using both the super-particle approach and our scaling method are presented in section 5.4. We conclude with presenting resolution constraints for numerical simulations and discuss the implications for the planetesimal formation process through gravitational instability in section 5.5.

5.1 Orders of magnitude

5.1.1 Definition of timescales

The aim of this work is to simulate the dynamics of dust (or particles) interacting gravitationally inside a turbulent proto-planetary disc. Each particle is subject to five different physical processes, each operating on a typical timescale:

Stopping time τ_s

Each particle of size a feels the effects of the surrounding gas through a linear drag force. This force can be written as $\mathbf{F}_{\text{drag}} = \frac{m_p}{\tau_s}(\mathbf{v}_g - \mathbf{v}_p)$, where τ_s is the stopping time of a particle of mass m_p , \mathbf{v}_g is the velocity of the gas, and \mathbf{v}_p is the velocity of the particle (Weidenschilling 1977a). The stopping time depends on the degree of coupling to the gas (e.g. Chiang & Youdin 2009):

$$\tau_s = \begin{cases} \frac{\rho_p a}{\rho_g c_s} & a \leq \frac{9}{4}\lambda \quad \text{Epstein drag} \\ \frac{4\rho_p a^2}{9\rho_g c_s \lambda} & a \geq \frac{9}{4}\lambda \quad \text{Stokes drag,} \end{cases} \quad (5.1)$$

where ρ_p and ρ_g are the internal density of the particles and the density of the gas, respectively. λ is the mean free path of gas particles and c_s the sound speed.

Physical collision timescale τ_c

Dust particles will suffer a physical collision with another dust particle on a timescale of $\tau_c = (\sigma_c \bar{v}_p n)^{-1}$, where σ_c is the geometrical cross-section of the particles, \bar{v}_p is the particle velocity dispersion, and n is the number density of particles in a homogeneous medium.

Orbital timescale τ_e

The timescale associated with the particles orbiting the central object in a local shearing patch is the epicyclic period $\tau_e = 2\pi\Omega^{-1}$, where Ω is the angular velocity at the semi-major axis of the shearing box.

There are two limits for the gravitational interactions between dust particles, long and short range. The long-range interaction can be seen as a collective process involving interactions between clouds of particles. On the other hand, the short-range interaction is important for resolving close approaches between pairs of particles, i.e. gravitational scattering. For the sake of clarity, we separate these two processes.

Gravitational collapse timescale τ_{Gl}

On a length scale $\lambda \gg \delta_r$, where δ_r is the average distance between neighbouring dust particles, the long-range interaction of the dust particle distribution can be approximated by a continuous density ρ . The gravitational collapse timescale, which is of the order of the free fall time of the system, can be defined by $\tau_{Gl} = 1/\sqrt{G\rho}$.

Gravitational scattering timescale τ_{Gs}

Short-range gravitational interactions are interactions between a pair of single particles that can result in a scattering event. As with physical collisions, the timescale for a gravitational interaction depends on the cross-section, $\tau_{Gs} = (\sigma_G \bar{v}_p n)^{-1}$. Here, $\sigma_G \sim G^2 m_p^2 / \bar{v}_p^4$ is the gravitational cross-section of the particle. Note that the cross-section is velocity dependent, which makes it qualitatively different from physical (billiard ball) collisions between two particles.

Particles might also be affected by excitation from a turbulent background state on a timescale defined by the turbulence itself. Unlike in chapter 3, we here model the excitation in an even more simplified way, in which the turbulence is scale independent and has no timescale associated with it.

5.1.2 The real physical system

To identify the dominant physical processes in a proto-planetary disc, one has to quantify and compare the relevant timescales as defined above. In the following discussion and in the numerical simulations, we assume $R_0 = 1$ AU, a gas disc thickness of $H/R_0 = 0.01$, and a minimum mass solar nebula (MMSN) with surface gas density¹

¹Note that there are different values for MMSN in the literature. This value here is a factor 5 smaller than the one used in chapter 3.

$\Sigma = 890 \text{ g cm}^{-2}$. One usually assumes a solid to gas ratio of $\rho_s/\rho_g = 0.01$. We, however, assume a solid to gas ratio of unity. This value is justified by numerical simulations (Johansen et al. 2007, 2009) that demonstrate over-densities of the order of $10^1 - 10^2$ can easily occur because of the interaction with a turbulent gas disc, the streaming instability, or vertical settling. Thus, we are only interested in the late stages of the planetesimal formation process. The details of how the initial over-density has been achieved are not relevant for the discussion presented in this chapter. We also note that significantly different models of the solar nebula have been proposed (Desch 2007). However, all results can easily be scaled to different scenarios.

We simplify the system by assuming that all solid components of the disc are in metre-sized particles. We assume that these boulders have a typical velocity dispersion caused by gas turbulence $\bar{v}_p \sim 0.05c_s \sim 30\text{m/s}$, where c_s is the local sound speed, in accordance with numerical results (Johansen et al. 2007). Since $\bar{v}_p \ll c_s$, the particles tend to sediment toward the mid-plane, forming a finite thickness dust layer due to the non-zero velocity dispersion.

For metre-sized boulders, the physical cross-section is $\sigma_c \sim 1 \text{ m}^2$, whereas the gravitational scattering cross-section is $\sigma_G \sim 10^{-21} \text{ m}^2$ showing clearly that gravitational scattering is irrelevant to the dynamics of dust particles embedded in a disc. However, all other timescales are roughly equivalent. Metre-sized boulders are weakly coupled to the gas with a stopping time $\tau_s \sim \tau_e \sim \Omega^{-1}$ (Weidenschilling 1977a). The physical collision timescale is $\tau_c = 7.3 \Omega^{-1}$ and the long-range gravitational interaction timescales is $\tau_{Gl} \sim \Omega^{-1}$.

This physical system is expected to become gravitationally unstable, according to the Toomre criterion (Toomre 1964). The instability occurs when the gravitational collapse timescale τ_{Gl} is shorter than the transit time due to random particle motions λ/\bar{v}_p and the orbital timescale. Assuming that the particles can be modelled by an isotropic gas² with a sound speed \bar{v}_p , the system becomes unstable when $Q \sim 1$ (equation 4.28). In that case, the most unstable wavelength λ_T is given by equation 4.29. In the following, we compare the physical parameters from this section to their counterpart in numerical simulations. We first summarise the super-particle approach before presenting the scaling method.

²This is formally not valid in the studied regime, as it is not strongly collisional.

5.2 Methods

Two different kinds of simulation are considered in this chapter:

1. Particles are assumed to be point masses and have no physical size, the gravitational field of the particles being approximated with a smoothing length to avoid numerical divergences (see section 5.3.1).
2. Particles have a physical size and, therefore, no gravitational smoothing is required but physical collisions must be included.

We refer to the particles as super-particles and scaled particles, respectively.

5.2.1 Super-particle approximation

Let us quickly review the standard approach using super-particles before moving on to studying our favoured method that uses scaled particles.

A super-particle represents many smaller particles. The dynamics of the small particles are not calculated exactly. It is assumed that all particles behave similarly and in a collective manner. To simulate gravitational interactions between super-particles, one has to use a softened potential. Without this, the gravitational scattering cross-section of super-particles becomes too large and super-particles undergo gravitational scattering events, which are unphysical since these events never occur in a real system. Individual particle-particle collisions are not modelled.

There are various examples where this approach is used successfully. For example, smoothed particle hydrodynamics (SPH) uses the super-particle approximation to simulate many gas molecules (Lucy 1977). These systems are often assumed to be *strongly collisional* to ensure thermodynamical equilibrium inside each super-particle. One can therefore assign collective properties to clouds of particles such as pressure and temperature. Another example is the evolution of galaxies. When two galaxies collide, individual particles (stars) will usually not undergo gravitational scattering events or physical collisions. In that case, the super-particle approach models a *collision-less* system in which collective dynamics are the only important physical process. In both cases, the super-particle approximation is a valid approach for simulating the system numerically, but will break down as soon as the system is *marginally collisional*.

As an example, we consider two clouds of particles undergoing a “collision”. In the strongly collisional case, the clouds will slowly merge and the thermodynamic variables (e.g., temperature) will diffuse between the clouds, the particles inside each cloud following a random walk trajectory due to numerous collisions. On the other hand, in the collision-less regime, the two clouds simply do not see each other because there is no short-range interaction present between the particles. In a marginally collisional

regime, some particles will collide with particles of the other cloud, leading to a partial thermalisation of the velocity distribution, but some other particles will not have any collision at all and will follow approximately a straight line. Evidently, the outcome of this event cannot be described using a super-particle approach.

5.2.2 Scaling method

The idea of the scaling method is that one should keep all important timescales in a numerical simulation as close to those of the real physical system as possible and model all particle collisions explicitly.

The numerical system consists of N_{num} particles in a box with length H , simulating a patch of the disc at a fixed radius R_0 . The particle mass is $m_{\text{num}} = \Sigma H^2 / N_{\text{num}}$ (H is the box size and one scale height). Thus, the density in the box and the long-range gravitational interactions are unchanged compared to the real system.

The gravitational scattering cross-section of the numerical system is then given by

$$\sigma_{G,\text{num}} = \frac{G^2 \Sigma^2 H^4}{N_{\text{num}}^2 \bar{v}_p^4}. \quad (5.2)$$

For the initial surface density and velocity dispersion used in the simulation (see above), one finds

$$\sigma_{G,\text{num}} \simeq \frac{H^2}{N_{\text{num}}^2} \simeq \frac{0.0001 \text{ AU}^2}{N_{\text{num}}^2}. \quad (5.3)$$

The physical collision cross-section in the simulation is $\sigma_{c,\text{num}} = \pi a_{\text{num}}^2$ where a_{num} is the radius of the particles in the simulation. We derive two constraints from the physical and gravitational collision cross-sections:

1. *Same mean free path in simulation and real physical systems*

That means $N_{\text{num}} \sigma_{c,\text{num}} = N \sigma_c$, where σ_c and N are the geometrical cross-section and the number of particles in a region of size H^3 in a real disc, respectively. In other words, this condition ensures that the physical collision timescale in the simulation is exactly the same as in the real system.

2. *Negligible gravitational scattering*

When two particles approach each other, the outcome should be a physical collision, which means that $\sigma_{c,\text{num}} \gg \sigma_{G,\text{num}}$. The gravitational scattering timescale remains long compared to the physical collision timescale.

The first condition places a constraint on the particle size in the simulation. With $N = 4.7 \cdot 10^{18}$ and a particle radius of $a = 1$ m as found in a real disc within a box of

volume H^3 , using the parameters from above one finds that

$$a_{\text{num}} = \sqrt{\frac{\sigma_{c,\text{num}}}{\pi}} = \sqrt{\frac{N\sigma_c}{N_{\text{num}}\pi}} \simeq \frac{0.014}{\sqrt{N_{\text{num}}}} \text{AU}. \quad (5.4)$$

We note that once this condition is satisfied in the initial conditions it will be automatically satisfied at all times. In simulations, we typically find that the collision timescale is reduced by more than one order of magnitude during the gravitational collapse.

The second condition is then satisfied by changing the number of particles. An interesting result is that if $N_{\text{num}} > 10$, the second condition is easily satisfied if the first one is satisfied. However, $\sigma_{G,\text{num}}$ depends strongly on the velocity dispersion. In particular, a velocity dispersion 5 times smaller than the initial value (as found in some simulations) leads to an increase by a factor of 600 in the gravitational scattering cross-section. Therefore, we suggest using a large safety factor ($N_{\text{num}} > 10^5$) to ensure that the second condition is always satisfied, even for significantly smaller \bar{v}_p . This condition also allows us to estimate when our approach breaks down, namely when the number of clumps in the system is so low ($N < 10 \sim 100$) that gravitational scattering becomes important.

Although it would be helpful as a further simplification, it is not possible to perform the above mentioned simulation in two dimensions. In that case, the filling factor, which is defined to be the ratio of the volume (or area) of all particles to the total volume (or area), is of the order of one for the above parameters. We note that in 2D an increase in particle number (and decrease in particle size as required by equation 5.4) does not decrease the filling factor if the collisional lifetime remains constant.

5.3 Numerical simulations

We perform our simulations in a cubic box with shear periodic boundary conditions in the radial (x) and periodic boundary conditions in the azimuthal (y) and vertical (z) directions, as described in appendix D. In the local approximation, the force per mass on each particle is a sum of the contributions from Hill's equations (see equations D.8-D.10) and interaction terms. The interaction terms \mathbf{F}_{int} are divided into components related to self gravity (including vertical gravity), physical collisions between particles, or drag and excitation forces:

$$\mathbf{F}_{\text{int}} = \mathbf{F}_{\text{grav}} + \mathbf{F}_{\text{col}} + \mathbf{F}_{\text{drag}} + \mathbf{F}_{\text{turb}}. \quad (5.5)$$

We solve the resulting equations of motion with a leap frog (kick drift kick) time-stepping scheme. In the following subsections, we describe how each of these terms are calculated and what their physical relevance is.

The box size of 0.01 AU was chosen such that there are always several unstable modes λ_T in the box, when the system is pushed into the regime of gravitational collapse, as estimated by equation 4.29.

5.3.1 Self gravity

In the N -body problem that we consider, we have to solve Newton's equations of universal gravitation for a large number of particles N . Calculating the gravity for each particle from each other particle results in $O(N^2)$ operations. To reduce the number of operations, we use an approximation, namely a Barnes-Hut (BH) tree code (see appendix D).

We use 8 *rings* of ghost boxes in the radial and azimuthal direction. The system that we are interested in is only marginally gravitationally stable and due to the finite number of ghost boxes, we introduce a slight asymmetry that will become important after several orbits. In the beginning of our simulations, we integrate for many orbits in order to reach a stable equilibrium. We then push the system into a gravitationally unstable regime (see section 5.3.5 for details). During the stable phase, horizontal over-concentrations are to be expected and are indeed observed because of this asymmetry. However, since in a real proto-planetary disc the gravitational instability is considered to appear locally (e.g., inside a vortex or a similar structure), this effect of having a preferred location for gravitational instability is not unphysical and does not affect any conclusions made. We tested this by applying a linear cut-off to the gravitational force at a distance of one box length (A. Toomre, private communication). In this case, there was no preferred location in the box and the simulation evolved in exactly the same way.

5.3.2 Physical collisions

Physical collisions between particles are treated by checking whether any two particles are overlapping after each time-step. Using the already existing tree structure from the gravity calculation, one can again reduce the computational costs from $O(N^2)$ to $O(N \log N)$. There is a small probability that we might miss a collision if the time-step is too large. To ensure that our results are converged, we tested that a reduced time-step does not alter the outcome. See appendix D for more details on how collisions are resolved.

The particle radius is given by equation 5.4. In order to keep the collision timescale τ_c close to unity, which is numerically the worst case scenario because all timescales are equivalent, we increase the radius by a factor of 4 in all simulations.

5.3.3 Drag force

Each particle feels a drag force. The background velocity of the gas \mathbf{v}_g is assumed to be a steady Keplerian profile

$$\mathbf{v}_g = -\frac{3}{2}\Omega x \mathbf{e}_y. \quad (5.6)$$

Although accretion flows are turbulent, we choose to use a simple velocity profile so that the behaviour of self-gravitating particles can be understood in conditions that can be easily controlled.

5.3.4 Random excitation

The system of particles described above is dynamically unstable even without self-gravity, as the coefficient of restitution and the stopping time do not depend on the particle velocities. The particles can either settle down in the mid-plane and create a razor-thin disc if the stopping time is too short, or they can expand vertically forever if the stopping time is above some critical value and the excitation mechanism is provided only by collisions. Dust particles in accretion discs are found in the settling regime. However, a complete settling never occurs in accretion discs because the background flow is always turbulent due to the Kelvin-Helmholtz instability (Johansen et al. 2006), the MRI, or other hydrodynamic instabilities (see e.g. Lesur & Papaloizou 2009) which diffuse particles vertically (Fromang & Papaloizou 2006). This stirring process of turbulence is not present in the gas velocity field of the simulations presented here (see equation 5.6). To approximate the turbulent mixing, we add a random excitation (white noise in space and time) to the particles in the simulation. This allows us to have a well defined equilibrium in which the system is stable rather than starting from unstable initial conditions that might influence the final state.

We perturb the velocity components of each particle after each time-step by $\Delta v_i = \sqrt{\delta t} \xi$, where δt is the current time-step and ξ is a random variable with a normal distribution around 0 and variance s . This excitation mechanism heats up the particles and allows us to have a well defined three dimensional equilibrium as shown in section 5.4. In our simulations, we use a value of $s = 1.3 \cdot 10^{15} \text{ m}^2\text{s}^{-3}$ and $s = 8.9 \cdot 10^{14} \text{ m}^2\text{s}^{-3}$ for the simulations without and with collisions, respectively. These values were chosen such that the equilibrium state is approximately equivalent for both types of simulations.

In comparison to chapter 3, here we try to simplify things as far as possible. Thus, the description of stochastic forces used leads to uncorrelated and scale independent noise.

5.3.5 Initial conditions

All particles, which have equal mass, smoothing length, and physical size, are placed randomly inside the box in the xy plane. We note that particles have either a physical size or a smoothing length associated with them, depending on the type of simulation we perform. In the z -direction, the particles are placed in a layer with an initially Gaussian distribution about the mid-plane and a standard deviation of $0.05 H$. We allow the system to reach equilibrium by integrating it until $t = 30\Omega^{-1}$ (4.8yrs).

We tested various ways of pushing the system into the unstable regime. We here present two different scenarios. First, one can switch off the excitation mechanism. The system starts to cool down and thus becomes unstable. Second, one can shorten the stopping time, which leads to enhanced cooling.

Following one of the above descriptions, the system becomes gravitationally unstable and bound clumps form within a few orbits. We did not see any qualitative differences as long as we started from a well defined equilibrium state. This shows that, even though we simplified the treatment of turbulent stirring and gas drag, the results are generic.

5.4 Results

5.4.1 Super particles

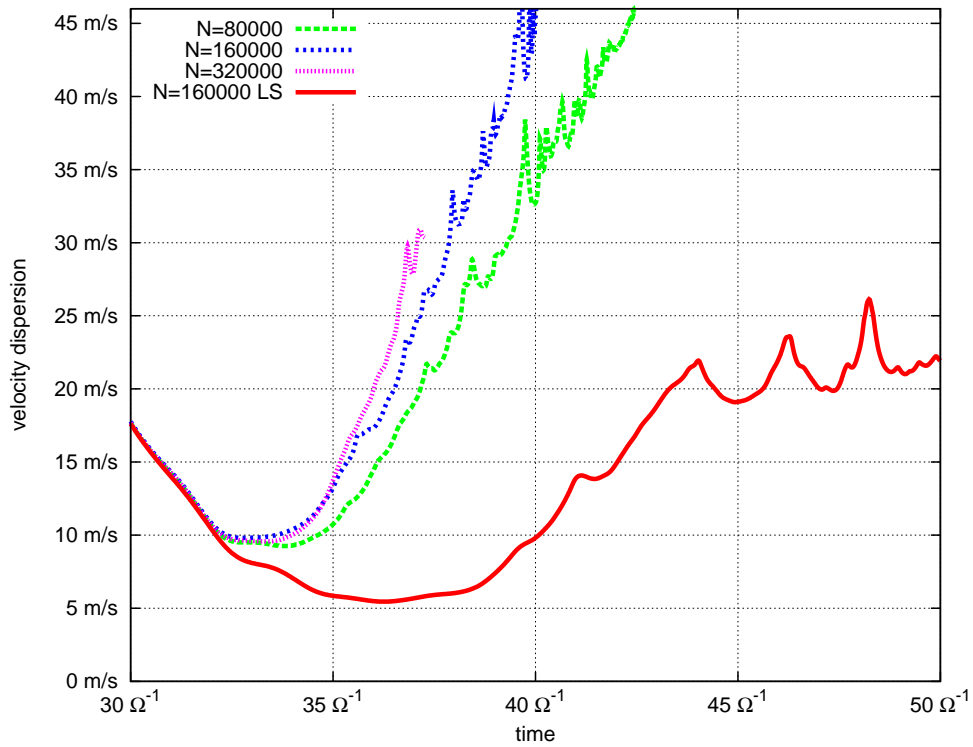
We first present simulations without physical collisions (super-particles) which rely on the smoothing length b to avoid any divergences. Although we use a tree code and a smoothed potential for the force calculation is assumed, the results are equivalent to an FFT-based method (Fast Fourier Transform) where the grid length acts as an effective smoothing length. In general, to check the numerical resolution, the particle number N_{num} is increased and the smoothing length b is reduced independently. A simulation is resolved when the result is independent of both N_{num} and b . This turns out to be impossible in the present situation. The main reason is that the smallest scale in a gravitational collapse will ultimately depend on the smoothing length. By varying both parameters at the same time, an empirical scaling of $b \sim 1/\sqrt{N_{\text{num}}}$ works fairly well if N_{num} is large enough. The square root in this scaling comes from the fact that we are basically treating a two dimensional system. However, this procedure is not justified and is unphysical. The smoothing length was introduced to avoid divergent terms and not to model any small-scale physical process. Therefore, it should *not* have any impact on the physical outcome of the simulation. Incidentally, the existence of this dependency indicates that short-range interactions are important for the result of these simulations and should be modelled with care.

In figure 5.1(a), we plot the velocity dispersion as a function of time. The simulations begin from the stable equilibrium described in section 5.2. After $t = 30 \Omega^{-1}$, we switch off the excitation mechanism. The system continues to cool and it becomes gravitationally unstable within one orbit, as estimated by equation 4.28. Once clumping occurs, the velocity dispersion begins to rise again. All simulations use the particle radius given by equation 5.4 as a smoothing length except the ones labelled LS, which use a value ten times larger. The larger softening length is approximately 128-th of the box length and illustrates the kind of evolution expected from an FFT method using a 128^3 grid. This is the resolution used in other studies, such as Johansen et al. (2007).

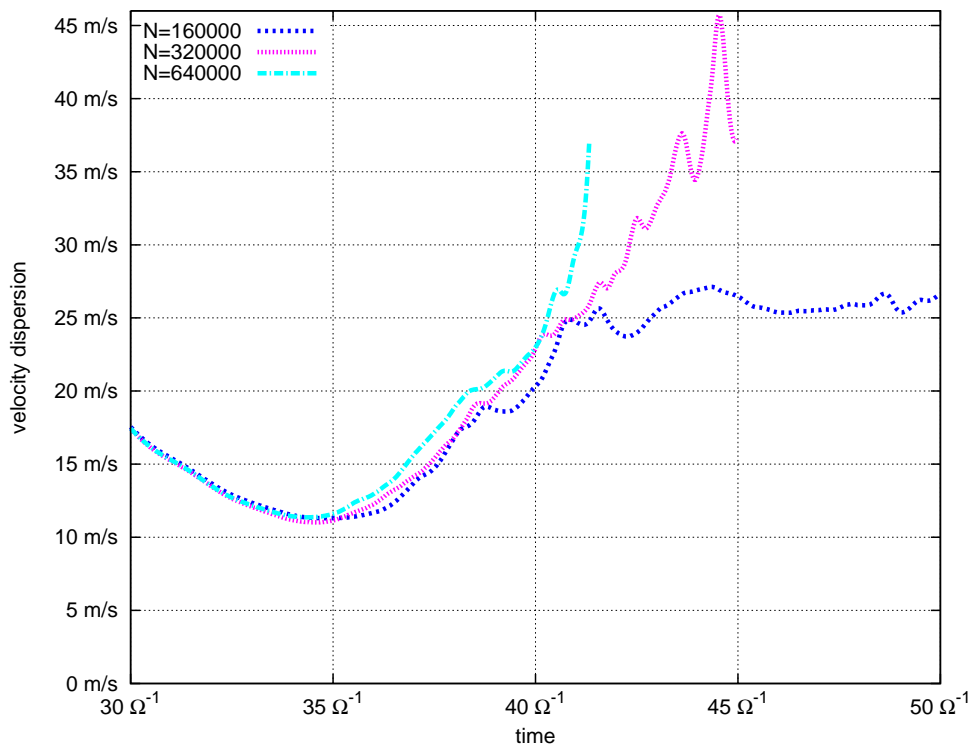
The velocity dispersion evolution is also plotted in figure 5.2(a) for those simulations, in which the damping timescale has been decreased while keeping the excitation unchanged. The results are qualitatively very similar to those presented in figure 5.1(a).

Snapshots of the particle distribution of two simulations are shown in figure 5.3. Both simulations use 160 000 particles and all parameters, except the smoothing length, are the same. The top row is the simulation with a smoothing length given by equation 5.4, whereas the bottom row uses a smoothing length that is ten times larger. The simulations correspond to the blue (medium dashed) and red (solid) curve in figure 5.1(a). We show the snapshots to illustrate the importance of the smoothing length in simulations without physical collisions. One can see that the simulations differ already before clumps form. Stripy structures appear on a scale given by equation 4.29. As soon as we enter the unstable regime at $t \sim 32\Omega^{-1}$ (i.e., the velocity dispersion begins to rise, see also figure 5.1(a)) the simulations evolve very differently. The simulation on the top row of figure 5.3 forms many clumps at an early time, whereas the bottom row simulation forms only a few, more massive clumps at later times.

This can be confirmed by looking at spectra of the same two simulations as shown in figure 5.5(a). These spectra were generated by mapping the particles onto a 128×128 grid in the xy plane and computing the fast Fourier transform of the mapping in the x direction. The resulting spectra were finally averaged in the y direction (see Tanga et al. 2004, for a complete description of the procedure). As suggested by the snapshots, the nonlinear dynamics of the gravitational instability strongly depends on the smoothing length used. In particular, one observes that smaller scales are amplified more slowly for larger smoothing lengths. The resulting spectra at $t = 40\Omega^{-1}$ also differ significantly. With a small enough smoothing length, the spectrum looks almost flat, whereas a large smoothing length introduces a cutoff at $k/2\pi \simeq 10$. We also note that the smoothing length in the latter case is of the order of the grid size ($k/2\pi \sim 100$). The cutoff observed clearly demonstrates that the smoothing length modifies the dynamics on scales up to 10 times larger than the smoothing length itself.

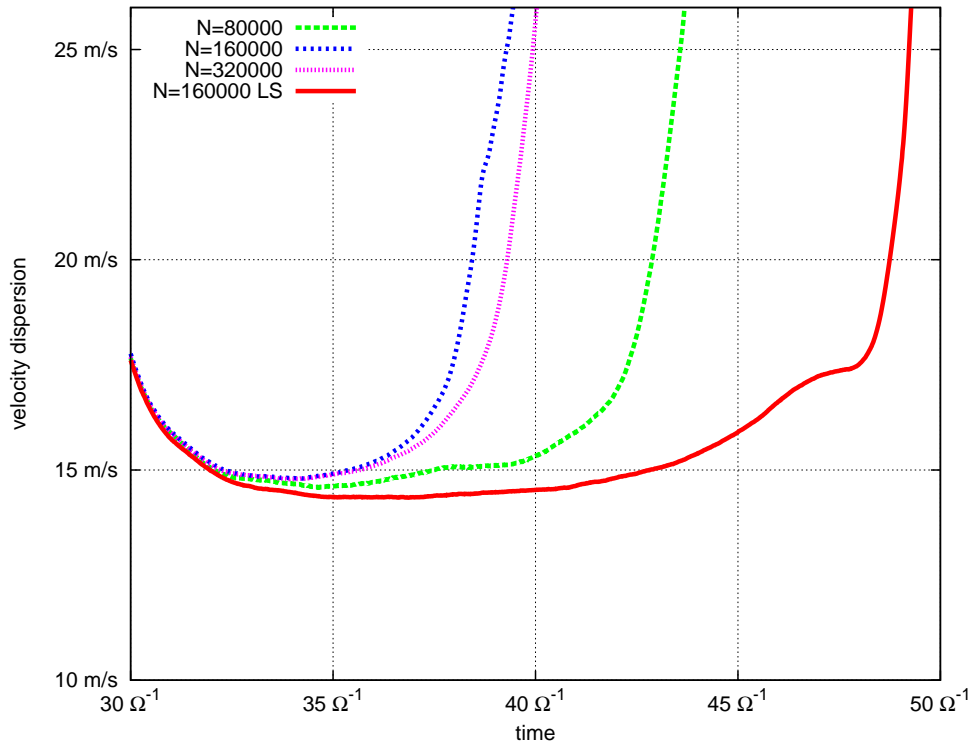


(a) Super-particles. The simulation labelled LS has a ten times larger smoothing length. The curves do not overlap because the simulations have not converged.

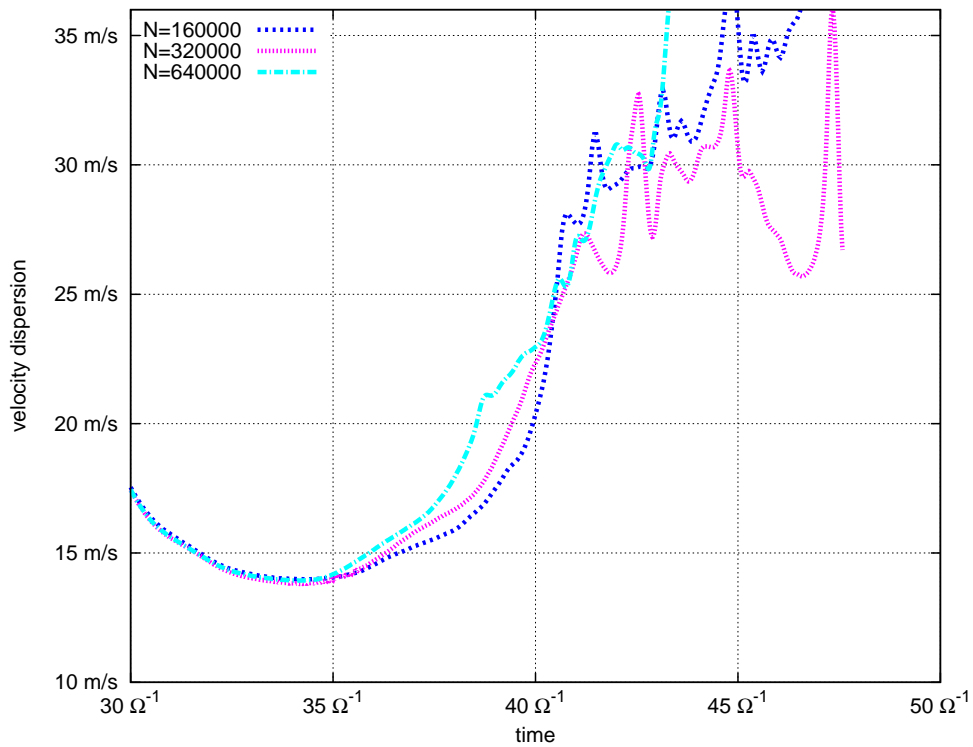


(b) Scaled-particles. All curves overlap at early times because the simulations are converged (see text).

Figure 5.1: The velocity dispersion as a function of time in different runs as an indicator of convergence. Simulations use super-particles (top) and scaled-particles (bottom).



(a) Super-particles. The simulation labelled LS has a ten times larger smoothing length. The curves do not overlap because the simulations have not converged.



(b) Scaled-particles. All curves overlap because the simulations are converged.

Figure 5.2: Same as in figure 5.1 but here the damping timescale is decreased while the excitation is unchanged. This leads to qualitatively very similar results.

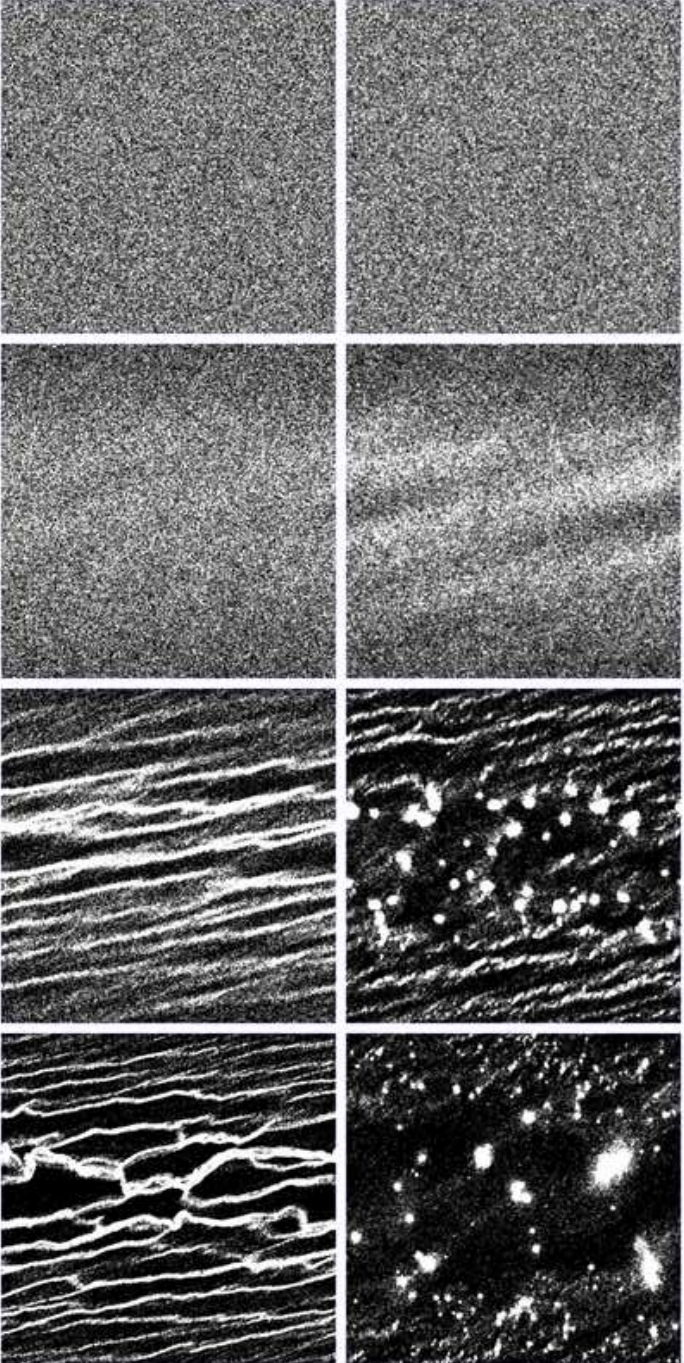


Figure 5.3: Super-particles: Snapshots of the particle distribution in the xy plane. Both simulations use 160 000 particles with different smoothing lengths. The simulation on the bottom uses smoothing length ten times larger than the one on the top. The snapshots were taken (from left to right) at $t = 0, 30, 37, 40 \Omega^{-1}$. With a large smoothing length, the outcome looks very different, the system is more stable, more stripy structure can be seen and clumps form later, if at all.

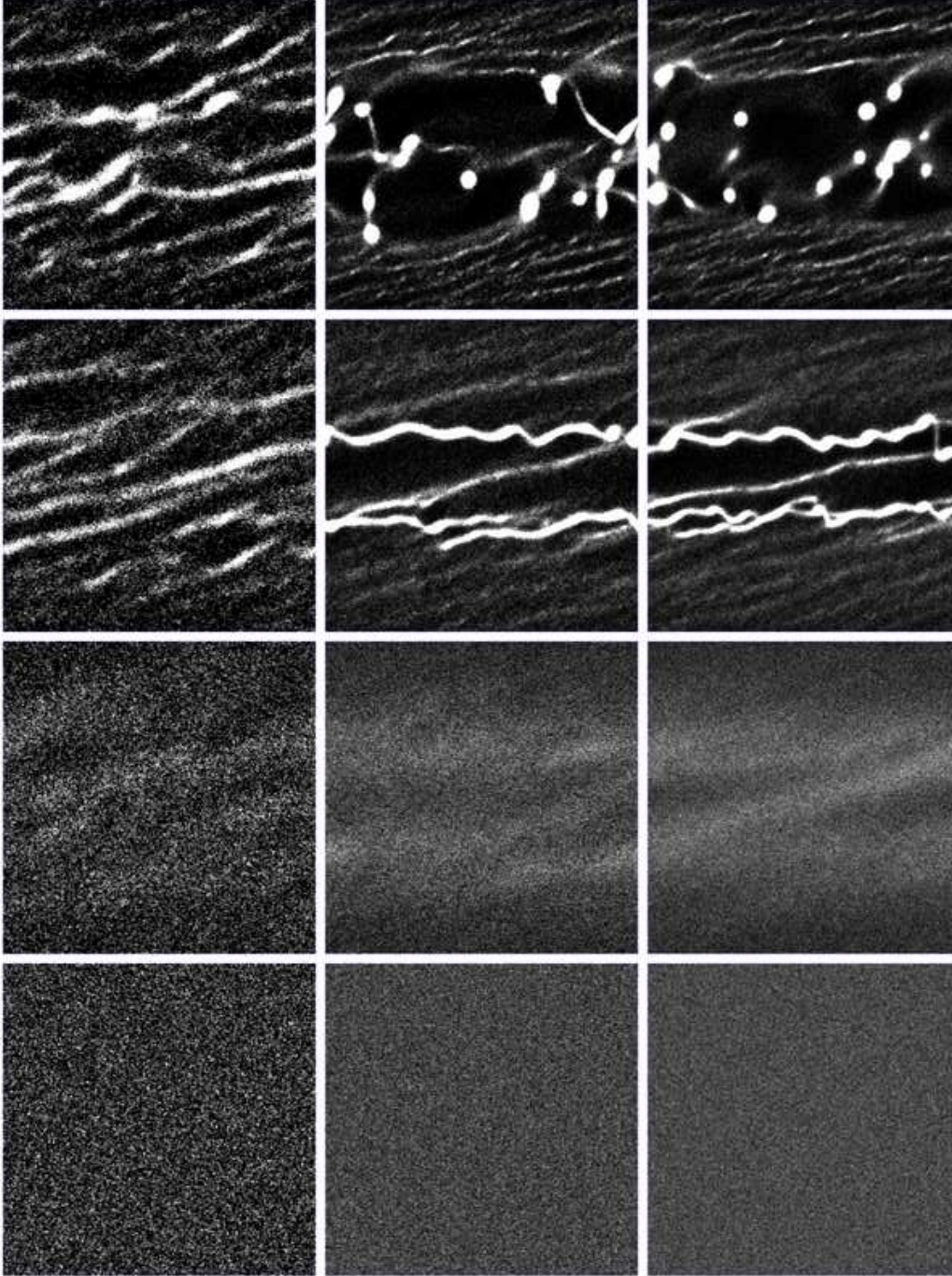


Figure 5.4: Scaled particles: Snapshots of the particle distribution in the xy plane. The simulations (from top to bottom) use 40 000, 320 000, 640 000 particles with their physical size given by equation 5.4. In all simulations, the collision timescale was kept constant. The snapshots were taken (from left to right) at $t = 0, 30, 37, 40 \Omega^{-1}$. The simulation with 40 000 particles has a large filling factor by the last frame, which prevents clumps from forming. The intermediate resolution simulation (middle row) and the highest resolution simulation (bottom row) have more and smaller particles and thus a smaller filling factor. The results (i.e., number of clumps in the last frame) are very similar in the intermediate and high resolution simulations.

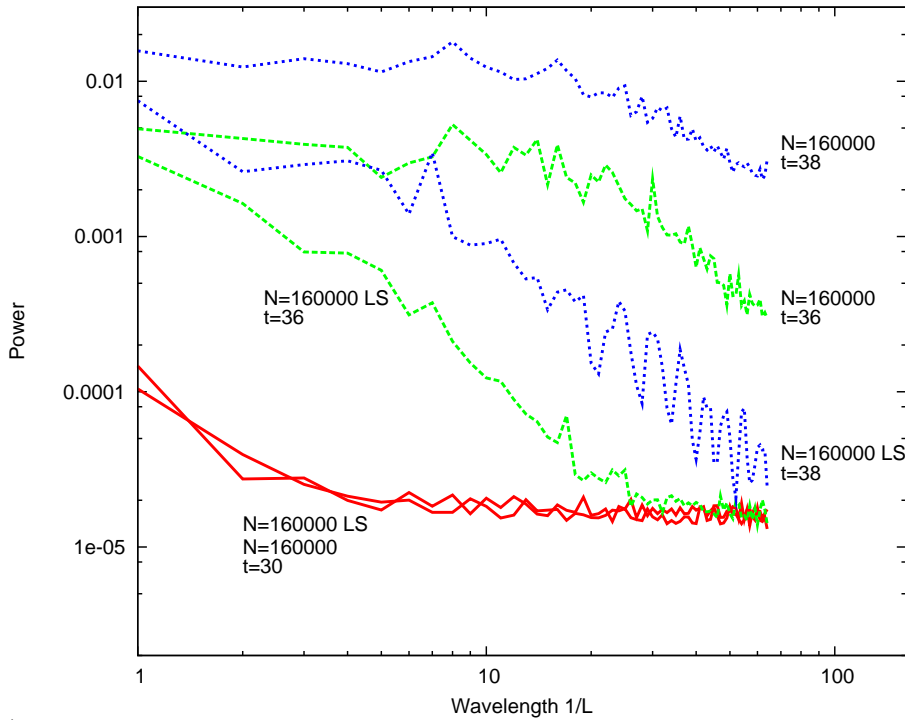
5.4.2 Scaled particles

The velocity dispersion evolution of simulations with $N = 160\,000, 320\,000, 640\,000$ particles including physical collisions is presented in figure 5.1(b) and figure 5.2(b). In these runs, no gravitational smoothing length is needed. Again, the simulations start from a stable equilibrium and after $t = 30 \Omega^{-1}$, we change the same parameters as in the non-collisional case to push the system into the gravitationally unstable regime. In figure 5.1(b) we increase the damping timescale, whereas we switch off the excitation in figure 5.2(b). Snapshots of the particle distribution for three runs are plotted in figure 5.4. The middle and bottom rows of snapshots correspond to the purple (medium dashed) and dark blue (long dashed) lines of figure 5.1(b).

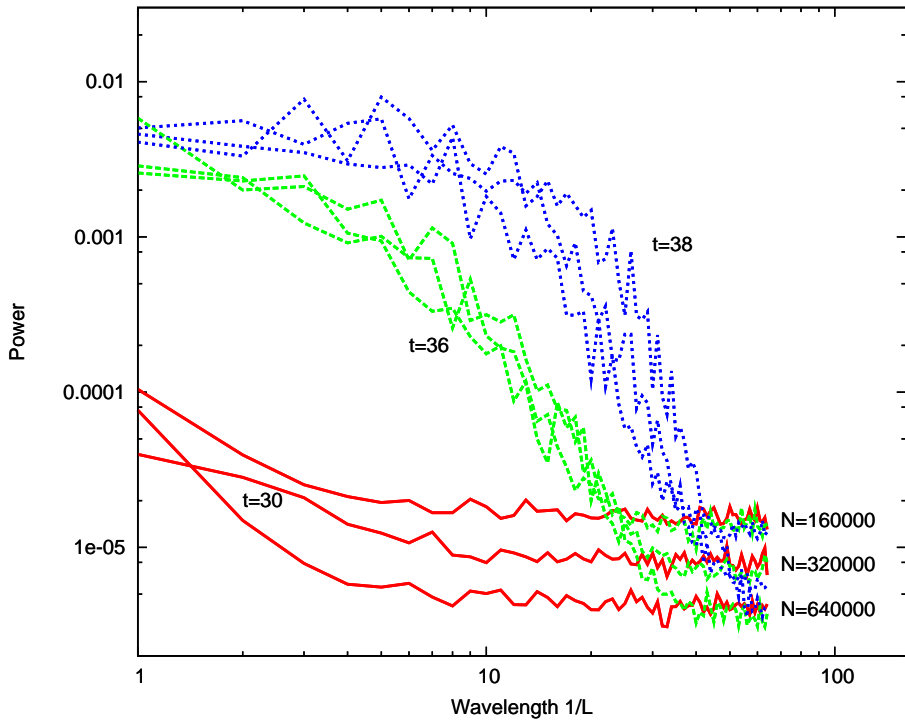
One can see in figures 5.1(b), 5.2(b) as well as figure 5.4 that the intermediate and high resolution runs produce very similar results. We call those simulations converged, as a change in particle number does not change the outcome. An additional, lower resolution run ($N = 40\,000$) has not converged because the filling factor is too large in dense regions, preventing clumps from being gravitationally bound. The problem does not occur in the non-collisional cases because particles are allowed to overlap. Since the filling factor scales with particle number as $1/\sqrt{N_{\text{num}}}$, this issue is resolved for runs with more than a few hundred thousand particles. We note that the velocity dispersion might differ at later stages for the converged runs because the final clump radius is still determined by the physical particle radius and therefore by the particle number. This can be seen in particular in figure 5.1(b) where the velocity dispersion of the 160 000 run reaches an equilibrium value before the runs with larger particle number. Note however, that up to that point, the results are converged.

We show the density distribution spectrum in figure 5.5(b) as a function of the number of particles. The resulting spectra do not depend on the number of particles in the system, as expected. In comparison with figure 5.5(a), the simulations with collisions are converged since the dynamic has not controlled by the numerical parameter N , which is the only free parameter in the system.

At very late times ($t \gtrsim 38\Omega^{-1}$), the spectra begin to show a systematic trend towards more structure on smaller scales for runs with larger N . This is due to the filling factor, already mentioned above. When the size of a clump in the simulation is only determined by the size of the individual scaled particles that it consists of, our approach breaks down. One can also see these clumps forming by looking at the velocity dispersion in figure 5.1(b). The particles inside a clump begin to dominate the velocity dispersion over the background after $t \sim 38\Omega^{-1}$. A clear indication of this is the spiky structure with a typical correlation time of $\sim \Omega^{-1}$ corresponding to different clumps interacting and merging with each other. One way around this issue, which will be considered in future work, is to allow particles to merge (Michikoshi et al. 2009). Using this specific



(a) Super-particles: Spectrum with 160 000 particles and two different smoothing lengths that differ by a factor 10 at times $t = 30$ (red, solid curve), $t = 36$ (green, long dashed curve), and $t = 38$ (blue, short dashed curve). The spectra at similar times are not on top of each other because the simulations have not converged.



(b) Scaled particles: Spectrum with 160 000, 320 000, and 640 000 particles (colours are equivalent to figure 5.5(a)). At each time, the spectra are converged, i.e., the spectra are on top of each other and independent of the particle number, besides the noise level on very small scales. At late times ($t \gtrsim 38$, blue curve), one begins to see more structure on small scales in simulations with larger number of particles (see text).

Figure 5.5: Density distribution spectrum

accretion model, the mass of the clump can then be used as an upper limit of the clump mass. Eventually, one should also worry about possible effects leading to the destruction of an already formed clump.

5.5 Discussion and implications

In this chapter, we have shown that convergence in N -body simulations of planetesimal formation via gravitational instability can be achieved when taking into account all relevant physical processes. It is absolutely vital to simulate gravity, damping, excitation, and physical collisions simultaneously, as the related timescales are of the same order and therefore all effects are strongly coupled.

A set of simulations is defined to be converged when the results do not depend on the particle number or any other artificial numerical parameter such as a smoothing length. As a test case, a box with shear periodic boundary conditions was used, containing hundreds of thousands of self-gravitating (super-)particles in a stratified equilibrium state. The particles were then pushed into a self-gravitating regime that eventually led to gravitational collapse. Simulations with and without physical collisions were studied for a range of particle numbers to test convergence.

In cases without physical collisions, convergence can not be achieved. However, it was possible to change multiple free simulation parameters at the same time, namely the particle number N and the smoothing length b , such that in special cases the results did not depend on the particle number. We note however that there is a free parameter in the simulation (i.e., the smoothing length) that effects the outcome and makes it impossible to find the *real* physical solution.

In the proto-planetary disc, physical collisions dominate over gravitational scattering. In the case of planetesimal formation, the system is marginally collisional. Physical collisions will partially randomise the particle distribution, whereas a smoothing length does not because the softening length is very large compared to the gravitational cross-section. Even if the gravitational particle-particle scattering becomes important, it can be seen from equation 5.2 that the velocity dependence of the cross-section σ_G differs fundamentally from the velocity independent cross-section σ_C . We therefore argue that the super-particle approach should not be used when collisions become important.

With collisions, the simulation outcome is both quantitatively and qualitatively very different from simulations with no physical collisions. The initial size of the clumps is larger and the number of clumps is smaller. As there is no smoothing length, there is effectively one fewer free parameter. Changing the particle number while keeping the collision time constant does not change the outcome. We therefore call these simulations converged.

Additional tests including inelastic collisions with a normal coefficient of restitution of 0.25 have been performed to confirm that the results do not depend on the way physical collisions are modelled. As expected, the qualitative outcome in terms of number of clumps and clump size is different because the physical properties of the system have been changed. However, once individual collisions are resolved the results converge in exactly the same manner as in those simulations presented above which have a coefficient of restitution of 1.

This chapter focused on the numerical requirements to study gravitational instability and the formation of planetesimals in proto-planetary discs. The initial conditions were chosen such that the equilibrium is a well defined starting point for the convergence study. The collision, damping, collapse and orbital timescales are all of the same order, which is effectively the worst case scenario. To provide any constraints on planetesimal formation itself, one would have to properly simulate the turbulent background gas dynamics which is a far bigger task.

However, we were able to determine the numerical resolution needed to resolve dust particles in a proto-planetary disc. Assuming that one wishes to simulate dust particles realistically, including collisions, and that the particles are uniformly distributed in a box of base L^2 and height H , the size of each particle is determined by the collision rate in the real disc (see equation 5.4)

$$a_{\text{num}} = \sqrt{\frac{N}{N_{\text{num}}}} a, \quad (5.7)$$

where a and N are the size and number of particles in the volume $L^2 H$ of the real disc. The number of particles in the simulation N_{num} has to be large enough to ensure that the filling factor is low until clumps form. The requirement that the filling factor is less than unity at $t = 0$ is given by

$$\frac{4}{3} \pi (a_{\text{num}})^3 \cdot N_{\text{num}} \leq C_f L^2 H, \quad (5.8)$$

where C_f is a safety factor. Although $C_f \lesssim 1$ would be enough to resolve collisions initially, it is insufficient to simulate the collapse phase. During the collapse, the filling factor rises rapidly. Assuming that one wishes to resolve collisions correctly when the particles have contracted by one order of magnitude, one has to include a safety factor of $C_f = 10^{-3}$. If the collapse occurs mainly in two dimensions, as in the simulations presented here, a factor of $C_f = 10^{-2}$ is sufficient. Furthermore, one has to ensure that the box contains at least a few unstable modes (see equation 4.29). All this together places tight numerical constraints on numerical simulations of planetesimal formation via gravitational instability.

In the future, the discussion should be expanded to include more physics, namely a proper treatment and feedback of the background gas turbulence. This will allow us

to further clarify the behaviour of planetesimals in the early stages of planet formation and eventually test the different formation scenarios.

Summary

If I have seen further it is only by standing on the shoulders of giants.

Issac Newton, in a letter to Robert Hooke, 1676

Several hundred extra-solar planets have been discovered in recent years. This led to a revival of planet formation theory. The remarkable differences of extra-solar planetary systems and our own solar system keep challenging long standing theories.

In this thesis, four main results are presented and summarised below. They can be categorised into two groups. One group is concerned with the formation of resonant multi-planetary systems. The other group discusses the effects of stochastic forcing on orbiting bodies such as planets, moonlets and dust.

6.1 Main results

6.1.1 Most resonant planetary systems are stable

In chapter 3, we develop a consistent framework for the treatment of stochastic forces in celestial mechanics. The growth rates of all orbital parameters are given as a function of the diffusion coefficient in the most generic way. Furthermore, several important correction factors which take into account a finite correlation time are included. Previous studies have overestimated the diffusion efficiency by more than an order of magnitude by ignoring these effects.

We apply this framework to a single, stochastically forced planet and to two planets that are in resonance. The results show that most planetary systems are stable against the random forces originating from MRI turbulence. This remains true even when we take into account the considerable uncertainties in the amplitude of those forces.

We find that resonant planetary systems have two different modes, which respond differently to stochastic forcing. Thus, systems that did undergo a random walk phase during their evolution should show evidence of that. One system, in which this might have been observed, is HD128311. We present several successful formation scenarios of this system which can reproduce the observed libration pattern. This cannot be obtained using laminar convergent migration alone.

The framework has a wide range of applications including Saturn's rings (see chapter 4) and promises to have a large impact on future studies involving stochastic forces of any type.

6.1.2 First prediction of orbital parameters of exo-planets

The planetary system HD45364 is in a 3:2 resonance. The system cannot be formed by convergent migration with moderate migration rates. The final configuration is always a 2:1 resonance, not the observed 3:2 resonance.

In chapter 2, we present a successful formation scenario that involves a short phase of rapid inwards type III migration. A disc with a mass about five times that of the minimum mass solar nebula is sufficient to drive type III migration. Furthermore, a large disc scale height is favourable for the long term sustainability of the resonance. These results imply that planets form in discs which are more massive than previously thought.

Finally, the outcome of hydrodynamical simulations are directly compared to the measured radial velocity curve. We find a new orbital solution, based on the simulation results, that has a lower χ^2 value than the previously reported *best fit*. The eccentricities of both planets are considerably smaller. The results are generic, as in all simulations we perform and that form a 3:2 commensurability, the orbital parameters are almost identical. This difference is the first prediction of the precise orbital configuration of an extra-solar planetary system. It can be verified with new radial velocity measurements within the next few years.

This study opens a new window to quantitative and predictive studies of the dynamics of planetary systems beyond our own solar system.

6.1.3 Moonlets in Saturn's rings migrate stochastically

An analytic estimate of both the random walk in semi-major axis and the mean equilibrium eccentricity of a small moonlet which is embedded in Saturn's rings is presented in chapter 4. We show that the most important effects that determine the dynamical evolution of the moonlet are collisions with ring particles. If the surface density of the rings is sufficiently large that gravitational wakes can form, then those exert an addi-

tional force on the moonlet which becomes dominant eventually. No matter how the moonlet is excited, it will migrate stochastically, with its semi-major axis changing on average like \sqrt{t} for large t .

We perform realistic three dimensional collisional N-body simulation of up to half a million self-gravitating ring particles and confirm the analytic estimates within a factor of two. New, pseudo shear periodic, boundary conditions are used which allow us to use a much smaller shearing patch than previous authors and we therefore get a large performance boost.

The random walk in semi-major axis leads to changes in the longitude that are observable with the Cassini spacecraft. If confirmed, this can be used to calculate an upper limit on the age of the propellers and eventually the ring system itself.

6.1.4 Physical collisions are vital in numerical simulations of planetesimal formation

In chapter 5, we revisit the numerical requirements in simulations of planetesimal formation via gravitational instability. We find that the inclusion of collisions is indispensable to obtain a consistent model. If collisions are not included, gravitational scattering is the only small scale process present. It will therefore become very important as soon as clumping occurs. Naively, one might think that gravitational close encounters could be treated as if these were physical collisions. However, properties such as the cross section are different compared to physical collisions and gravitational scattering can therefore not resemble the real system.

The results show that earlier studies should not be trusted beyond the initial clumping phase. Estimates on the minimum number of particles required for convergent results are given.

Future studies on planetesimal formation will have to address this issue and the method presented here shows a clear way on how to do that. This will lead to self-consistent results in future simulations.

6.2 Future work

6.2.1 Multi-planetary systems

The results on multi-planetary systems in this thesis, as successful as they might be, have been restricted to only two systems. However, over a third of the discovered planets are confirmed to be in multi-planetary systems.

Having developed all necessary tools in chapters 2 and 3, it is now an easy task to study many systems in a similar fashion. In the following years, I will select up to 15

multi-planetary systems and study their evolution with both N-body as well as two and three dimensional hydrodynamic simulations. This will be the first survey of realistic formation scenarios among multi-planetary systems. The results will be more precise and not as degenerate as population synthesis models of single planets.

New observations suggest that a substantial fraction of hot Jupiters might be in retrograde orbits (Triaud et al. 2010, in preparation). There are various ways to form these systems, such as Kozai Migration or planet-planet scattering (Fabrycky & Tremaine 2007; Nagasawa et al. 2008). So far, these methods have not been studied in combination with the traditional ideas of planet-disc interaction. I will use Prometheus to study highly inclined systems in the presence of gas discs.

I also want to continue studying the effects of MRI turbulence on planetary systems. The strength of stochastic forces coming from turbulence is not well constrained yet. For that reason a large interval of possible values of the diffusion coefficient had to be studied in chapter 3. Using the MHD module of Prometheus or a different MHD code such as Athena, I will explore the parameter space in a systematic way with global non-ideal MHD simulations. The measurements of statistical properties of MRI turbulence will improve the predictive capability of our analytic random walk model significantly.

One needs at least 16 (maybe 32 or even 64) grid cells per scale-height to simulate the turbulent proto-stellar disc accurately. Assuming one wants to simulate a radial domain ranging from 1 to 4 AU and 6 scale-heights in the vertical direction, one needs a 96x480x502 grid. This is a challenging task. During my PhD, I have gained knowledge on how to speed up calculations using CPU specific hardware features. If the performance of the code becomes an issue and it turns out that higher resolution is required to simulate the relevant scales in the system, I can implement these changes to speed up the simulations.

With these new results, I am going to show that a broad selection of systems can be formed in a turbulent disc and prove if there is statistically significant observational evidence of turbulence in the exo-planet distribution or not.

6.2.2 Saturn's rings

The work presented in chapter 4 was limited to a rather small subset of the parameter space. I plan to extend this study to a wider range of parameters, especially to higher internal densities and a broader size distribution to reduce granularity. As soon as observational data has been published, I will investigate the constraints arising from the measured random walk of moonlets. If the random walk is indeed as strong as predicted, it is possible to obtain an upper limit on the age of the ring system.

Direct simulations of planetary rings are constrained to a local model. Although this is a valid approximation in most circumstances, it has also certain drawbacks. For

example, simulations presented in chapter 4 capture the random walk in semi-major axis but do not capture the net migration over long timescales (Crida et al. 2010).

I plan to extend direct simulations of Saturn’s rings to a *global* model. Periodic boundary conditions in the azimuthal and pseudo shear periodic boundary conditions in the radial direction, in a similar manner to those presented in chapter 4 and appendix D, can be used to extend the shearing box to a wedge that extends radially over several tens or hundreds of kilometres. We can get rid of Hill’s equations and solve the planet’s gravitational force directly.

Numerically, this is a challenging task, as the number of particles will be very large. Therefore, the particles have to be distributed across processors. As outlined in some detail in appendix D, MPI is not ideally suited for parallelising tree structures. In this case, however, the fact that one dimension is much larger than the others comes in handy because boxes far away do not have to communicate directly with each other so that their interaction can be pre-calculated.

6.2.3 Planetesimal formation

The results on planetesimal formation presented in this thesis are preliminary, showing that it is indeed possible to simulate the gravitational collapse of a self-gravitating planetesimal population. To do this self consistently, one has to include collisions and gas dynamics. The former part has been completed in chapter 5. The latter part has been done by other authors (e.g. Johansen et al. 2007). A combination of both is the logical next step.

Many groups are currently working on planetesimal formation in a turbulent disc. I plan to focus on the differences between global simulations and the local shearing box approximation which has been used by most authors. This is essential to understand the importance of effects such as the streaming instability which rely on a large over-density in the solid to gas ratio. In a local simulation with periodic boundary conditions, this ratio is set by the initial conditions and cannot change. However, in a real proto-stellar disc, as well as in global models, the ratio is controlled by large scale structures in the disc such as pressure and temperature gradients.

To gain a better understanding of these global effects, I will couple the new method that treats particles correctly to a global MHD simulation. The method to solve the non-ideal MHD equations will be the same as for the study of multi-planetary systems. To simulate the self-gravity and collisions in the dust layer, I will re-use the GravTree code, presented in appendix D, which is ideally suited for this project and already fully developed and tested.

6.2.4 Numerical codes

The primary codes that have been written for this thesis, Prometheus and GravTree, will be made publicly available. Both codes will be hosted on github at <http://github.com/hannorein/> under the open source license GPL. They are easily portable to different architectures as they are written in C and C++, respectively, using only standard libraries such as OpenGL, OpenMP and libpng. Compilation is controlled by the GNU autotool suite.

Providing the source code is, in my opinion, a necessity as numerical codes are part of the initial conditions. All results should be easily reproducible. Firstly, this helps to make progress in the subject, and secondly, it also increases the chance to find bugs in the code. It is therefore a win-win situation.

Appendices

Orbital elements

In this appendix, the orbital elements of an elliptical orbit are defined. It is a solution to the two body problem, the simplest non-trivial problem in celestial mechanics.

We consider a test particle on an orbit around a central object with mass m at the origin. The specific force on the particle is given by $\mathbf{F} = -\frac{Gm}{r^3}\mathbf{r}$, where \mathbf{r} is the position of the particle. Thus, the equation of motion is simply

$$\ddot{\mathbf{r}} = -\frac{Gm}{r^3}\mathbf{r}. \quad (\text{A.1})$$

Taking the vector product of the above equation with \mathbf{r} evaluates to zero on the right hand side and gives after integrating

$$\mathbf{r} \times \dot{\mathbf{r}} = \mathbf{h}, \quad (\text{A.2})$$

where \mathbf{h} is a constant of motion. The absolute value of \mathbf{h} is the specific angular momentum. The position and velocity vectors are in the same plane and allowing us to restrict ourselves to the two dimensional case. By switching to polar coordinates r and ϕ , we can rewrite equation A.2, giving $h = r^2\dot{\phi}$. We also rewrite equation A.1, giving

$$\ddot{r} = r\dot{\phi}^2 - \frac{Gm}{r^2}. \quad (\text{A.3})$$

The solution to equation A.3 can then be written as

$$r = \frac{p}{1 + e \cos(\phi - \varpi)}, \quad (\text{A.4})$$

where e is the eccentricity, ϖ is the longitude of pericentre and p the semilatus rectum which can be written as $p = h^2(Gm)^{-1}$. We restrict the further discussion to an elliptic orbit for which $0 \leq e < 1$. In that case $p = a(1 - e^2)$, where a is the semi major axis. We define the true anomaly as $f = \phi - \varpi$. We can further more define an average angular velocity, $n = 2\pi/T$, called the mean motion, where T is the orbital period, given by

$$T^2 = \frac{4\pi^2}{Gm}a^3. \quad (\text{A.5})$$

For a circular orbit, the mean motion is simply v_c/a , where $v_c = \sqrt{Gm/a}$. Now that we have a mean angular velocity, we can also define a mean angle M (the mean longitude), measured from the pericentre of the planet, via

$$M = n(t - \tau). \tag{A.6}$$

Here, τ is the time of pericentre passage. M grows linearly in time.

Finally, we would like to get an equation for $r(t)$ and $\phi(t)$. The time dependence of equation A.4 is hidden in ϕ . It turns out that an explicit form does in general not exist and the solution can only be calculated iteratively. We can see this by introducing another angle, the eccentric anomaly E (see figure A.1). It can be shown (Murray & Dermott 2000) that a relation between the mean longitude and the eccentric anomaly exists such that

$$M = E - e \sin E. \tag{A.7}$$

This equation is transcendental but can be solved iteratively, for example with a Newton-Raphson method.

Most of the quantities defined above are plotted in figure A.1 for illustrative purposes.

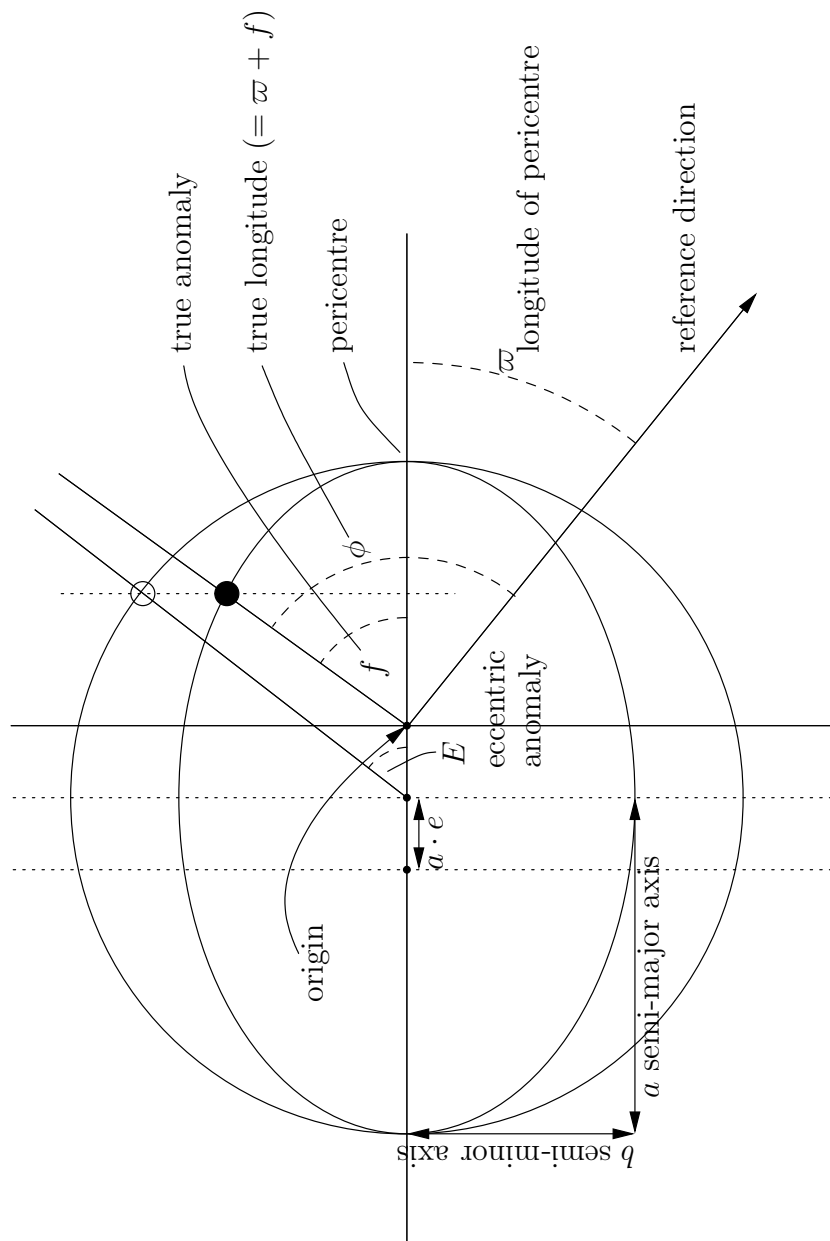


Figure A.1: Orbital elements of an elliptical orbit.

Dissipative forces

Additional terms can be added to the equations of motion in N-body simulations to describe eccentricity and semi-major axis damping. These forces could result from various sources, including a gaseous disc, a planetesimal disc or tides. The derivation follows Lee & Peale (2001) and some expressions are taken from Murray & Dermott (2000).

We have two additional, non-conservative terms in the equations for both the velocity and acceleration. In a Cartesian coordinate system, these are

$$\left. \frac{dx}{dt} \right|_{\dot{a}} + \left. \frac{dx}{dt} \right|_{\dot{e}} = \frac{\partial x}{\partial a} \dot{a} + \frac{\partial x}{\partial e} \dot{e} \quad \text{and} \quad (\text{B.1})$$

$$\left. \frac{d\dot{x}}{dt} \right|_{\dot{a}} + \left. \frac{d\dot{x}}{dt} \right|_{\dot{e}} = \frac{\partial \dot{x}}{\partial a} \dot{a} + \frac{\partial \dot{x}}{\partial e} \dot{e}. \quad (\text{B.2})$$

The expressions are analogue for the y and z coordinates. In order to differentiate with respect to a and e , we have to write the cartesian coordinates in terms of orbital elements. The positions can be expressed as

$$\begin{aligned} x &= r \cos \Omega \cos(\omega + f) - r \cos i \sin \Omega \sin(\omega + f), \\ y &= r \sin \Omega \cos(\omega + f) + r \cos i \cos \Omega \sin(\omega + f) \quad \text{and} \\ z &= r \sin i \sin(\omega + f), \end{aligned} \quad (\text{B.3})$$

which simply follow from the definition of the orbital parameters (see appendix A). By differentiating once, we get expressions for the velocities

$$\begin{aligned} \dot{x} &= \cos \Omega [\dot{r} \cos(\omega + f) - r \dot{f} \sin(\omega + f)] \\ &\quad - \cos i \sin \Omega [\dot{r} \sin(\omega + f) + r \dot{f} \cos(\omega + f)], \\ \dot{y} &= \sin \Omega [\dot{r} \cos(\omega + f) - r \dot{f} \sin(\omega + f)] \\ &\quad + \cos i \cos \Omega [\dot{r} \sin(\omega + f) + r \dot{f} \cos(\omega + f)], \\ \dot{z} &= \sin i [\dot{r} \sin(\omega + f) + r \dot{f} \cos(\omega + f)]. \end{aligned} \quad (\text{B.4})$$

We also need expressions for the radius r , the time derivative of the radius \dot{r} , and rf in terms of a , e , and f :

$$r = \frac{a(1 - e^2)}{1 + e \cos f} \quad (\text{B.5})$$

$$\dot{r} = \frac{r \dot{f} e \sin f}{1 + e \cos f} \quad (\text{B.6})$$

$$rf = \frac{na}{\sqrt{1 - e^2}}(1 + e \cos f). \quad (\text{B.7})$$

To complete the list of equations, we compute several other derivatives needed to calculate the partial derivatives in equation B.1 and B.2

$$\frac{\partial r}{\partial a} = \frac{r}{a},$$

$$\frac{\partial r}{\partial e} = \left[-\frac{2er}{1 - e^2} - \frac{r^2 \cos f}{a(1 - e^2)} \right],$$

$$\frac{\partial \dot{r}}{\partial a} = -\frac{\dot{r}}{2a},$$

$$\frac{\partial \dot{r}}{\partial e} = \frac{\dot{r}}{e(1 - e^2)}, \quad (\text{B.8})$$

$$\frac{\partial(rf)}{\partial a} = -\frac{rf}{2a},$$

$$\frac{\partial(rf)}{\partial e} = \frac{rf(e + \cos f)}{(1 - e^2)(1 + e \cos f)}.$$

Putting everything together, we arrive at the following expressions

$$\left. \frac{dx}{dt} \right|_{\dot{a}} + \left. \frac{dx}{dt} \right|_{\dot{e}} = \frac{x}{a} \dot{a} + \left[\frac{r}{a(1 - e^2)} - \frac{1 + e^2}{1 - e^2} \right] \frac{x}{e} \dot{e}, \quad (\text{B.9})$$

$$\left. \frac{dy}{dt} \right|_{\dot{a}} + \left. \frac{dy}{dt} \right|_{\dot{e}} = \frac{y}{a} \dot{a} + \left[\frac{r}{a(1 - e^2)} - \frac{1 + e^2}{1 - e^2} \right] \frac{y}{e} \dot{e}, \quad (\text{B.10})$$

$$\left. \frac{dz}{dt} \right|_{\dot{a}} + \left. \frac{dz}{dt} \right|_{\dot{e}} = \frac{z}{a} \dot{a} + \left[\frac{r}{a(1 - e^2)} - \frac{1 + e^2}{1 - e^2} \right] \frac{z}{e} \dot{e}. \quad (\text{B.11})$$

The additional terms for each of $d\dot{x}/dt$, $d\dot{y}/dt$, $d\dot{z}/dt$ are distinct for variations in e :

$$\begin{aligned} \left. \frac{d\dot{x}}{dt} \right|_{\dot{a}} + \left. \frac{d\dot{x}}{dt} \right|_{\dot{e}} &= -\frac{\dot{x}}{2a}\dot{a} + \cos \Omega \left[\frac{\partial \dot{r}}{\partial e} \cos(\omega + f) - \frac{\partial(r\dot{f})}{\partial e} \sin(\omega + f) \right] \dot{e} \quad (\text{B.12}) \\ &\quad - \cos i \sin \Omega \left[\frac{\partial \dot{r}}{\partial e} \sin(\omega + f) + \frac{\partial(r\dot{f})}{\partial e} \cos(\omega + f) \right] \dot{e}, \end{aligned}$$

$$\begin{aligned} \left. \frac{d\dot{y}}{dt} \right|_{\dot{a}} + \left. \frac{d\dot{y}}{dt} \right|_{\dot{e}} &= -\frac{\dot{y}}{2a}\dot{a} + \sin \Omega \left[\frac{\partial \dot{r}}{\partial e} \cos(\omega + f) - \frac{\partial(r\dot{f})}{\partial e} \sin(\omega + f) \right] \dot{e} \quad (\text{B.13}) \\ &\quad + \cos i \cos \Omega \left[\frac{\partial \dot{r}}{\partial e} \sin(\omega + f) + \frac{\partial(r\dot{f})}{\partial e} \cos(\omega + f) \right] \dot{e}, \end{aligned}$$

$$\left. \frac{d\dot{z}}{dt} \right|_{\dot{a}} + \left. \frac{d\dot{z}}{dt} \right|_{\dot{e}} = -\frac{\dot{z}}{2a}\dot{a} + \sin i \left[\frac{\partial \dot{r}}{\partial e} \sin(\omega + f) + \frac{\partial(r\dot{f})}{\partial e} \cos(\omega + f) \right] \dot{e}. \quad (\text{B.14})$$

The final equations B.9-B.14 are then used to calculate the dissipative forces and included in the N-body code (see section 2.2). Note that the orbital elements have to be calculated every sub-timestep. Depending on the integrator and the required number of force evaluations, this can be numerically expensive.

Response calculation of particles on horseshoe orbits

In this appendix, we calculate the amplitude of epicyclic motion that is induced by an eccentric moonlet in a small particle on a horseshoe orbit.

C.1 Interaction potential

Due to some finite eccentricity, the moonlet undergoes a small oscillation about the origin in the local Hill Cartesian coordinate system (see section 4.1.1). Its Cartesian coordinates then become (X, Y) , with these being considered small in magnitude. The components of the equation of motion for a ring particle with Cartesian coordinates $(x, y) \equiv \mathbf{r}_1$ are

$$\frac{d^2x}{dt^2} - 2\Omega \frac{dy}{dt} = 3\Omega^2 x - \frac{1}{m_1} \frac{\partial \Psi_{1,2}}{\partial x} \quad \text{and} \quad (\text{C.1})$$

$$\frac{d^2y}{dt^2} + 2\Omega \frac{dx}{dt} = -\frac{1}{m_1} \frac{\partial \Psi_{1,2}}{\partial y}, \quad (\text{C.2})$$

where the interaction gravitational potential due to the moonlet is

$$\Psi_{1,2} = -\frac{Gm_1m_2}{(r^2 + R^2 - 2rR \cos(\phi - \Phi))^{1/2}} \quad (\text{C.3})$$

with the cylindrical coordinates of the particle and moonlet being (r, ϕ) and (R, Φ) respectively. This may be expanded correct to first order in R/r in the form

$$\Psi_{1,2} = -\frac{Gm_1m_2}{r} - \frac{Gm_1m_2R \cos(\phi - \Phi)}{r^2}. \quad (\text{C.4})$$

The moonlet undergoes small amplitude epicyclic oscillations such that $X = \mathcal{E}_2 \cos(\Omega t + \epsilon)$, $Y = -2\mathcal{E}_2 \sin(\Omega t + \epsilon)$ where e is its small eccentricity and ϵ is an arbitrary phase. Then $\Psi_{1,2}$ may be written as

$$\Psi_{1,2} = -\frac{Gm_1m_2}{r} - \Psi'_{1,2}, \quad (\text{C.5})$$

where

$$\Psi'_{1,2} = -\frac{Gm_1m_2r \mathcal{E}_2(x \cos(\Omega t + \epsilon) - 2y \sin(\Omega t + \epsilon))}{r^3} \quad (\text{C.6})$$

gives the part of the lowest order interaction potential associated with the eccentricity of the moonlet.

We here view the interaction of a ring particle with the moonlet as involving two components. The first, due to the first term on the right hand side of equation C.4 operates when $\mathcal{E}_2 = 0$ and results in standard horseshoe orbits for ring particles induced by a moonlet in circular orbit. The second term, equation C.6, perturbs this motion when \mathcal{E}_2 is small. We now consider the response of a ring particle undergoing horseshoe motion to this perturbation. In doing so we make the approximation that the variation of the leading order potential equation C.4 due to the induced ring particle perturbations may be neglected. This is justified by the fact that the response induces epicyclic oscillations of the particle which are governed by the dominant central potential.

C.2 Response calculation

Setting $x \rightarrow x + \xi_x, y \rightarrow y + \xi_y$, where $\boldsymbol{\xi}$ is the small response displacement induced by equation C.6 and linearising equations C.2, we obtain the following equations for the components of $\boldsymbol{\xi}$

$$\frac{d^2\xi_x}{dt^2} - 2\Omega \frac{d\xi_y}{dt} = 3\Omega^2\xi_x - \frac{1}{m_1} \frac{\partial\Psi'_{1,2}}{\partial x} \quad \text{and} \quad (\text{C.7})$$

$$\frac{d^2\xi_y}{dt^2} + 2\Omega \frac{d\xi_x}{dt} = -\frac{1}{m_1} \frac{\partial\Psi'_{1,2}}{\partial y}, \quad (\text{C.8})$$

From these we find a single equation for ξ_x in the form

$$\frac{d^2\xi_x}{dt^2} + \Omega^2\xi_x = -\frac{1}{m_1} \frac{\partial\Psi'_{1,2}}{\partial x} - \int \frac{1}{m_1} \frac{\partial\Psi'_{1,2}}{\partial y} dt = F. \quad (\text{C.9})$$

When performing the time integral on the right hand side of the above, as we are concerned with a potentially resonant epicyclic response, we retain only the oscillating part.

The solution to equation C.9 which is such that $\boldsymbol{\xi}$ vanishes in the distant past ($t = -\infty$) when the particle is far from the moonlet may be written as

$$\xi_x = \alpha \cos(\Omega t) + \beta \sin(\Omega t), \quad (\text{C.10})$$

where

$$\alpha = -\int_{-\infty}^t \frac{F \sin(\Omega t)}{\Omega} dt \quad \text{and} \quad \beta = \int_{-\infty}^t \frac{F \cos(\Omega t)}{\Omega} dt. \quad (\text{C.11})$$

After the particle has had its closest approach to the moonlet and moves to a large distance from it it will have an epicyclic oscillation with amplitude and phase determined by

$$\alpha_\infty = - \int_{-\infty}^{\infty} \frac{F \sin(\Omega t)}{\Omega} dt \quad \text{and} \quad \beta_\infty = \int_{-\infty}^{\infty} \frac{F \cos(\Omega t)}{\Omega} dt. \quad (\text{C.12})$$

In evaluating the above we note that, although F vanishes when the particle is distant from the moonlet at large $|t|$, it also oscillates with the epicyclic angular frequency Ω which results in a definite non zero contribution. This is the action of the co-orbital resonance. It is amplified by the fact that the encounter of the particle with the moonlet in general occurs on a horseshoe libration time scale which is much longer than Ω^{-1} . We now consider this unperturbed motion of the ring particles.

C.3 Unperturbed horseshoe motion

The equations governing the unperturbed horseshoe motion are equations C.2 with

$$\Psi_{1,2} = \Psi_{1,2}^0 = -\frac{Gm_1m_2}{r}. \quad (\text{C.13})$$

We assume that this motion is such that x varies on a time scale much longer than Ω^{-1} so that we may approximate the first of these equations as $x = -[2/(3\Omega)](dy/dt)$. Consistent with this we also neglect x in comparison to y in equation C.13. From the second equation we then find that

$$\frac{d^2y}{dt^2} = \frac{3}{m_1} \frac{\partial \Psi_{1,2}^0}{\partial y}, \quad (\text{C.14})$$

which has a first integral that may be written

$$\left(\frac{dy}{dt}\right)^2 = -\frac{6Gm_2}{|y|} + \frac{9\Omega^2b^2}{4}, \quad (\text{C.15})$$

where as before b is the impact parameter, or the constant value of $|x|$ at large distances from the moonlet. The value of y for which the horseshoe turns is then given by $y = y_0 = 24Gm_2/(9\Omega^2b^2)$. At this point we comment that we are free to choose the origin of time $t = 0$ such that it coincides with the closest approach at which $y = y_0$. Then in the approximation we have adopted, the horseshoe motion is such that y is a symmetric function of t .

C.4 Evaluation of the induced epicyclic amplitude

Using equations C.6, C.9 and C.15 we may evaluate the epicyclic amplitudes from equation C.12. In particular we find

$$F = -\frac{Gm_2 \mathcal{E}_2 \cos(\Omega t + \epsilon)}{r^3} \left(5 - \frac{(3x^2 + 12y^2)}{r^2}\right). \quad (\text{C.16})$$

When evaluating equation C.12, consistent with our assumption that the epicyclic oscillations are fast, we average over an orbital period assuming that other quantities in the integrands are fixed, and use equation C.15 to express the integrals with respect to t as integrals with respect to y . We then find $\alpha_\infty = -A_\infty \sin \epsilon$ and $\beta_\infty = -A_\infty \cos \epsilon$ where

$$A_\infty = \int_{y_0}^{\infty} \frac{\sqrt{6Gm_2 y_0} \mathcal{E}_2}{6\Omega r^3 \sqrt{1 - y_0/y}} \cdot \left[5 - \left(\frac{8Gm_2}{\Omega^2} \left(\frac{1}{y} - \frac{1}{y_0} \right) + 12y^2 \right) r^{-2} \right] dy, \quad (\text{C.17})$$

with $r^2 = 8Gm_2/(3\Omega^2 y_0)(1 - y_0/y) + y^2$. From this we may write

$$|A_\infty| = \mathcal{E}_{1f} = \frac{Gm_2 \mathcal{E}_2}{y_0^3 \Omega^2} |\mathcal{I}|, \quad (\text{C.18})$$

where \mathcal{E}_{1f} is the final epicyclic motion of the ring particle and the dimensionless integral \mathcal{I} is given by

$$\mathcal{I} = \sqrt{\frac{\Omega^2 y_0^3}{6Gm_2}} \int_{y_0}^{\infty} \frac{y_0^2 r^{-3}}{\sqrt{1 - y_0/y}} \cdot \left(5 - \frac{\left(\frac{8Gm_2}{\Omega^2} \left(\frac{1}{y} - \frac{1}{y_0} \right) + 12y^2 \right)}{r^2} \right) dy. \quad (\text{C.19})$$

We remark that the dimensionless quantity $\eta = 8Gm_2/(3\Omega^2 y_0^3) = 8(r_H/y_0)^3$, with r_H being the Hill radius of the moonlet. It is related to the impact parameter b by $\eta = 2^{-6}(b/r_H)^6$. Thus for an impact parameter amounting to a few Hill radii, in a very approximate sense, η is of order unity, y_0 is of order r_H and the induced eccentricity \mathcal{E}_{1f} is of order \mathcal{E}_2 .

C.5 Numerical verification

We verify the analytic calculation with the numerical code GravTree (see appendix D). A moonlet with Hill radius $r_H = 32$ m is setup on an eccentric orbit with $\mathcal{E}_2 = 130$ m and $\Omega = 0.0001314 \text{ s}^{-1}$. A ring particle is placed on an initially circular orbit far away from the moonlet with different impact parameters b that all lead to horseshoe orbits.

The amplitude of epicyclic motion of the ring particle, \mathcal{E}_1 , is plotted in figure C.1 for four test cases with $b = 0.25r_H$, $b = 0.5r_H$, $b = 0.75r_H$ and $b = r_H$. We also plot the analytic estimates of the final epicyclic motion given by equation C.18 as straight lines. The agreement is very good, showing some differences at large b . Note that an impact parameter greater than $1r_H \sim 2r_H$ leads to impacts so that the departure from the analytic estimate does not influence the circularisation time calculated in chapter 4 significantly.

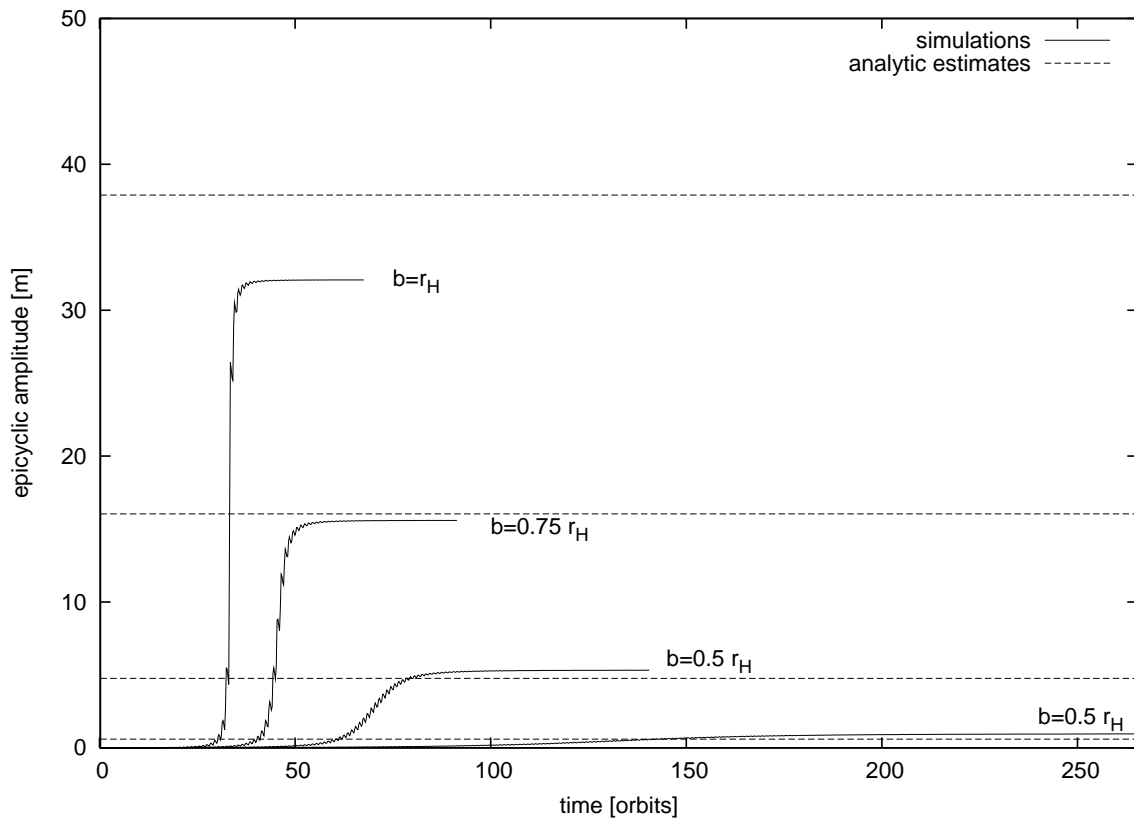


Figure C.1: Epicyclic amplitude \mathcal{E}_1 of a ring particle on a horseshoe orbit as a function of time for different impact parameters b . The horizontal lines are the estimate given by equation C.18.

N-body simulations with GravTree

This appendix describes the GravTree code that has been written to solve many body systems. The particles might interact gravitationally and through physical collisions. Modules incorporating gas drag and stochastic forces have also been implemented.

First, the relevant equations of motions are presented, followed by a description of the special symplectic integrator used for these. Second, the Barnes Hut tree code is explained. Finally, tests and optimisation strategies that have been implemented are discussed.

D.1 Hill's equations

In many situations it is impossible to simulate an entire accretion disc or planetary ring. For example, in the case of a proto-planetary disc there are about one trillion (10^{12}) metre-sized particles. Numerically, we can only simulate a few million, at most.

Fortunately, it is usually sufficient to simulate a small patch of the disc that includes most of the physics. In such a patch (also known as a shearing sheet) the shear is linearised and geometric effects are ignored. This leads to a well defined set of equations with shear periodic boundary conditions in the radial and azimuthal directions (Wisdom & Tremaine 1988).

Let us start from the equations of motion of a test particle around a single star at the origin with mass M such that the gravitational force can be described by

$$\ddot{r} = -\frac{GM}{r^2}, \quad (\text{D.1})$$

where r is the distance from the star. We now move to a non-inertial frame, rotating with angular frequency $\Omega = |\mathbf{\Omega}|$. The time derivative of a vector quantity \mathbf{v} in the new frame is given by

$$\dot{\mathbf{v}}_{\text{r}} = \dot{\mathbf{v}}_{\text{i}} - \mathbf{\Omega} \times \mathbf{v}, \quad (\text{D.2})$$

where subscripts i and r denote the inertial and rotating frames, respectively. The acceleration in the rotating frame is thus given by

$$\mathbf{a}_r = \mathbf{a}_i - 2 \boldsymbol{\Omega} \times \mathbf{v}_r - \boldsymbol{\Omega} \times (\boldsymbol{\Omega} \times \mathbf{r}_r), \quad (\text{D.3})$$

where \mathbf{v}_r is the velocity and \mathbf{r}_r is the position vector in the rotating frame. Adopting a coordinate system in the rotating frame where x corresponds to the radial direction, y to the azimuthal direction and z to the rotation axis, setting the origin at a distance a away from the star, we can simplify the above equation to get

$$\ddot{x} = \ddot{r}_i + 2\Omega \dot{y}_r + \Omega^2 (x + a)_r \quad \text{and} \quad (\text{D.4})$$

$$\ddot{y} = -2\Omega \dot{x}_r + \Omega^2 y_r. \quad (\text{D.5})$$

Linearising equation D.1 around $r = a + x$ gives

$$\ddot{r} = -\frac{GM}{r^2} = -\frac{GM}{(a+x)^2} = -\frac{GM}{a^2} + 2\frac{GM}{a^3}x + \dots \quad (\text{D.6})$$

$$= -\Omega^2 a + 2\Omega^2 x + \dots \quad (\text{D.7})$$

where we have assumed a Keplerian rotation, $\Omega^2 r^3 = GM$. Thus, the linearised equations of motion for an unperturbed particle orbiting in the rotating frame are

$$\ddot{x} = 3\Omega^2 x + 2\Omega \dot{y} \quad \text{and} \quad (\text{D.8})$$

$$\ddot{y} = -2\Omega \dot{x}, \quad (\text{D.9})$$

where we have dropped the subscript r. We can also linearise the gravity in the vertical direction to get

$$\ddot{z} = -\Omega^2 z. \quad (\text{D.10})$$

This set of local approximations is known as Hill's equations. We solve these with a symplectic leap frog, kick drift kick, time-stepping scheme which is discussed in more detail in the next section.

D.2 Symplectic integrator

Symplectic integrators in celestial mechanics have several attractive features, such as conservation of energy up to machine precision. We would therefore like to use such an integrator for solving Hill's equations numerically. A widely used standard symplectic integrator is leap-frog which can be described by a kick, followed by a drift and another kick sub-time-step (KDK). A possible C implementation of one full time-step with length \mathbf{dt} is

```

void kdk(double* x, double* v, double* a, double dt){
    // Kick
    v[0] += 0.5 * dt * a[0];
    v[1] += 0.5 * dt * a[1];
    v[2] += 0.5 * dt * a[2];

    // Drift
    x[0] += dt * v[0];
    x[1] += dt * v[1];
    x[2] += dt * v[2];

    // Kick
    update_force(x,v,a);
    v[0] += 0.5 * dt * a[0];
    v[1] += 0.5 * dt * a[1];
    v[2] += 0.5 * dt * a[2];
}

```

Here, x , v and a are pointers to the position, velocity and acceleration vectors, respectively. This integrator is symplectic if the forces calculated in `update_force(x,v,a)` do not depend on the velocities. However, Hill's equations do depend on the velocities (see equations D.8 and D.9). Note that the z component (equation D.10) does not depend on the velocities and thus can be integrated with a standard method. Quinn et al. (2010) describe a new symplectic integrator for Hill's equations. The changes to the KDK algorithm are minimal and only one additional value per particle has to be saved. A modified version of the above code is

```

void kdk_quinn(double* x, double* v, double* a, double* Py, double dt){
    // Kick
    v[0] += -0.5*dt * (OMEGA*OMEGA * r[0] - a[0]);
    Py    = v[1] + 2.0*OMEGA * r[0] + 0.5*dt * a[1];
    v[0] += dt * OMEGA * Py;
    v[1]  = Py - OMEGA * r[0] - OMEGA * (r[0] + dt * v[0]);
    v[2] += 0.5*dt * a[2];

    // Drift
    x[0] += dt * v[0];
    x[1] += dt * v[1];
    x[2] += dt * v[2];
}

```

```

// Kick
update_force(x,a);
v[0] += dt * OMEGA * Py;
v[0] += -0.5*dt * (OMEGA*OMEGA * r[0] - a[0]);
v[1] = Py - 2.0*OMEGA * r[0] + 0.5*dt * a[1];
v[2] += 0.5*dt * a[2];
}

```

Here, `OMEGA` is the orbital frequency and `Py` is initialised to `v[1] + 2.0*OMEGA * r[0]`. `Py` is a conserved quantity for an unperturbed orbit. Note that the drift step is unmodified. This allows for an unchanged collision detection algorithm, usually performed during the drift sub-time-step. The function `update_force()` does not include the terms due to Hill's equation anymore, only additional forces (e.g. gravity from other particles, gas drag, ...).

The symplectic integrator has proven to be very useful for integrations of moonlets in Saturn's rings, where the eccentricity is generally very small ($\sim 10^{-8}$) and the system is integrated for hundreds of orbits.

D.3 Gravity calculation

In the N -body problem that we are considering here, we have to solve Newton's equations of universal gravitation for a large number of particles N . The gravitational force on the i -th particle is given by

$$\mathbf{F}_{\text{grav}} = \sum_{j \neq i} G \frac{m_i m_j}{(r_{ij} + b)^2} \mathbf{e}_{ij}, \quad (\text{D.11})$$

where b is the smoothing length used to avoid divergencies in numerical simulations. In simulations where particles have a finite size and physical collisions are included we can safely set $b = 0$. The unit vector in the direction of the gravitational force between the i -th and j -th particle is \mathbf{e}_{ij} . Calculating the gravity for each particle from each other particle results in $O(N^2)$ operations. To reduce the number of operations, one can use different approximations to equation D.11. Here, we use a Barnes-Hut (BH) tree code (Barnes & Hut 1986). The BH tree reduces the number of calculations to $O(N \log N)$.

A tree code in three dimensions works by sub-dividing the original box into eight smaller cells with half the length of the original box. This can be done iteratively, by adding one particle to the box at a time. The new particle is given to the root box first. If the root box has already been sub-divided into smaller boxes, the particle is passed down to the next level. If the particle ends up in a box that has not yet been

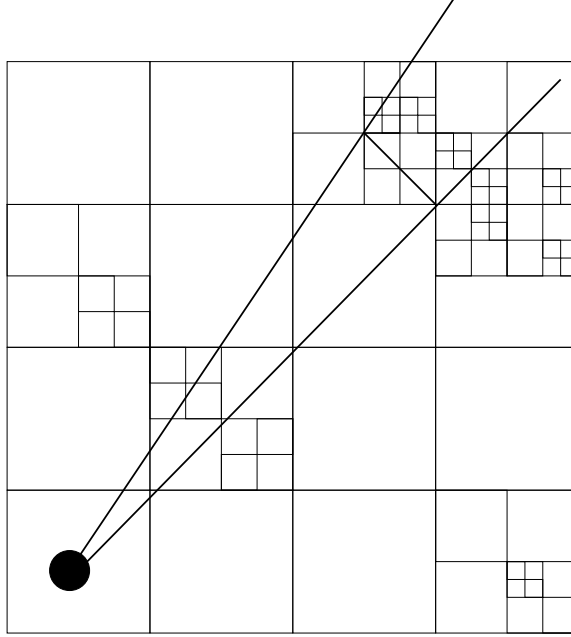


Figure D.1: The opening angle θ is the acute angle in the triangle and defined as the ratio of cell width divided by the distance from the particle to the cell. If $\theta \leq 0.5$, the cell is sufficiently large away and any substructure can be ignored.

sub-divided, but already contains a particle, then this box is divided into smaller boxes and the particle that was in this cell is removed. The original and the new particles are then re-added. This process is repeated until all particles are inserted. The depth of the tree in a homogeneous medium is approximately $\log_8 N$. The next step is to pre-calculate the total mass and the centre of mass for each cell at each level of the tree.

To get the force acting on a particle, one starts at the top of the tree and descends into the tree as far as necessary to achieve a given accuracy. If the current cell is far away from the particle for which the force is calculated, then the detailed density structure within this cell is not important. All that matters is the box's monopole moment (total mass and centre of mass)¹. One therefore does not have to descend into this branch any further. This criteria can be quantified by an opening-angle θ , which is defined as the ratio of the box width and the distance from the particle to the centre of the box, as shown in figure D.1. In all simulations we use $\theta \leq 0.5$.

D.4 Boundary conditions

Our implementation can handle arbitrary aspect ratios of the box, which is especially useful if a small annulus has to be simulated. We use ghost rings made of ghost boxes

¹This could be easily extended to include higher order moments.

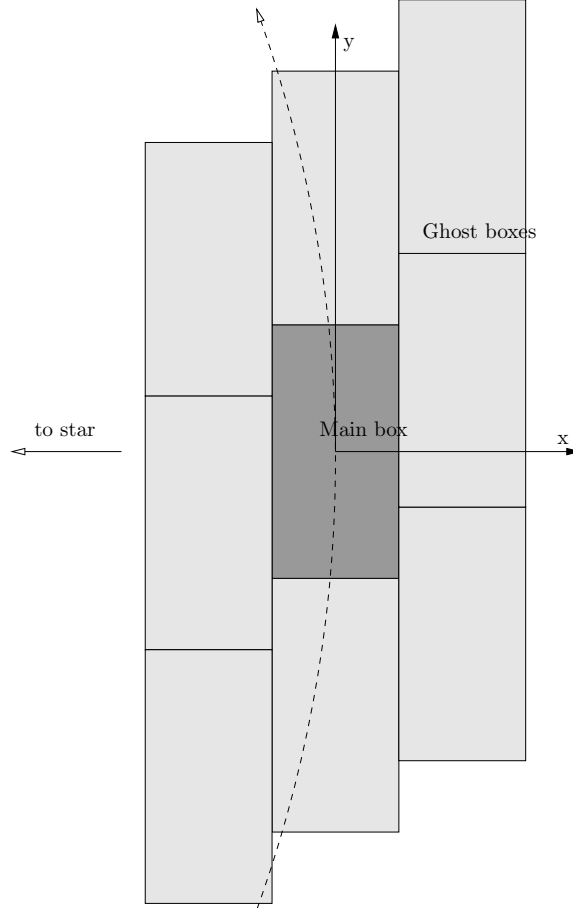


Figure D.2: Shearing box and ghost boxes. The ghost-boxes move in the y direction, following the mean shear, leading to *shear-periodic* boundary conditions. Here, the boxes have an aspect ratio of 2, but any other aspect ratio is possible.

in the radial and azimuthal directions as shown in figure D.2. The figure shows one ghost ring. A ghost box is either simply a shifted copy of the main box or a completely separate simulation, depending on the type of simulation (see below).

The gravity on each particle is then calculated by summing over contributions from each (ghost) box. This setup approximates a medium of infinite horizontal extent and avoids large force discontinuities at the boundaries. In general no ghost boxes are used in the vertical direction because the disc is stratified.

D.4.1 Shear periodic boundary conditions

In a standard simulation, we consider the main box together with eight ghost boxes that are all identical copies of the main box shifted according to the mean shear. On account of this motion ghost boxes are removed when their centres are shifted in azimuth by more than 1.5 times their length from the centre of the main box and then reinserted in the same orbit on the opposite side of the main box so that the domain under

consideration is prevented from shearing out.

If a particle in the main box crosses one of its boundaries, it is reinserted on the opposite side so that the total number of particles is conserved. The gravity acting on a particle in the main box, is calculated by summing over the particles in the main box and all ghost boxes.

A finite number of ghost rings can only act as an approximation of an infinite medium and the gravitational force will tend to concentrate particles horizontally in the centre of the box. In simulations of planetesimals (see chapter 5), we use 8 ghost rings, corresponding to 63 ghost boxes. The asymmetry of the gravitational force between the centre and the faces of the box is reduced by a factor of 20 compared to using no ghost rings at all. Note, however, that a small asymmetry remains in every simulations and leads to higher a concentration of particles in the box centre. In other simulations, such as Tanga et al. (2004), this effect can not be seen because the system is initially gravitationally unstable and integrated for only one orbit. Some systems that we are interested in are marginal gravitationally unstable and this slight asymmetry might become important after many orbits (see chapter 5).

D.4.2 Pseudo shear periodic boundary conditions

If a strong perturber is present in the simulation, such as a moonlet in chapter 4, we use a different setup that we call *pseudo* shear periodic boundary conditions. In that case, all ghost, or auxiliary, boxes are identical copies whose centres are shifted according to the background shear as in a normal shearing sheet. However, the auxiliary boxes are a completely separate simulation, mimicking the background state of the ring system without a perturber.

If a particle in the main box crosses one of its boundaries, it is discarded. If a particle in the auxiliary box crosses one of its boundaries, it is reinserted on the other side of this box, according to normal shear periodic boundary conditions. But in addition it is also copied into the corresponding location in the main box.

Other simulations (Lewis & Stewart 2009) use a very long box (about 10 times longer than the typical box size that we use) to ensure that particles are completely randomised between encounters with the moonlet. We are in general not interested in the long wavelength response that is created by the moonlet. Effects that are most important for the moonlet's dynamical evolution are found to happen within a few Hill radii. Using the pseudo shear periodic boundary conditions, we ensure that incoming particles are uncorrelated and do not contain prior information about the perturber.

The gravity acting on a particle in the main box, which also contains the moonlet, is calculated by summing over the particles in the main box and all auxiliary boxes.

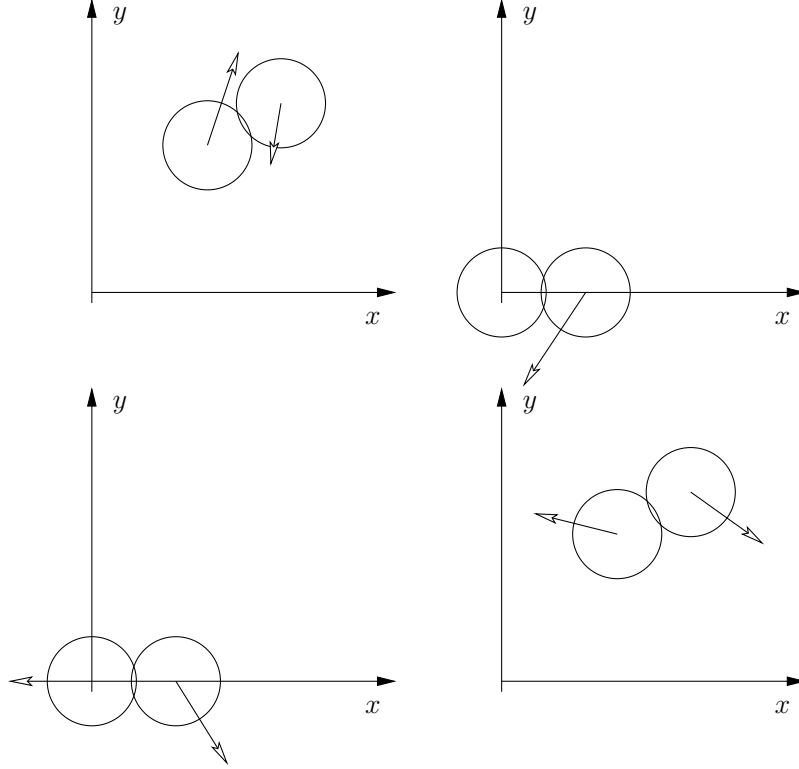


Figure D.3: Resolving collisions. Top left: An overlap has been detected in the original frame. Top right: Reference frame where one particle is at the origin and at rest. Bottom left: Collision is resolved using momentum and energy conservation. Bottom right: Back in original frame.

The gravity acting on a particle in the auxiliary box is calculated the standard way, by using ghost boxes which are identical copies of the auxiliary box.

This setup speeds up our calculations by more than an order of magnitude.

D.5 Collision detection

The collision detection algorithm makes use of the already existing tree structure to search for nearest neighbours. Again, this reduces the complexity from $O(N^2)$ to $O(N \log N)$, and can easily be done in parallel. We search for overlapping particles that are approaching each other. The order in which multiple collisions involving the same particle are resolved are not important in our case. We can ignore this effect as long as the time-step is sufficiently small.

This approach might lead to another problem. Consider two particles that are constantly touching; they might sink into each other over long timescales due to numerical errors and other dissipative effects. To avoid this fate, we limit the minimal impact velocity $v_{|\min}$ to a tiny fraction of the random velocity dispersion. $v_{|\min}$ has to be small enough to not affect the global evolution of the system.

Collisions are then resolved using energy and angular momentum conservation and a (velocity dependent) coefficient of restitution. This is done by moving to a reference frame in which one particle is at rest at the origin and the other particle is on the x -axis, as shown in figure D.3.

D.6 Optimisations

Cache

The tree structure leads to a large number of random memory accesses. This can potentially harm the performance of the code if many cache misses occur. When a cache miss occurs, the CPU has to request the data from the main memory, which is much slower than a request that can be handled by the cache. Using a simple heuristic branch prediction, one can speed up the calculation. We do this by pre-caching lower level tree branches before working on the current level. In C++, using non-standard MMX extensions, a typical tree walking subroutine looks as follows:

```
#include <xmmintrin.h>
void cell::walk_tree(){
    // Try to cache position and tree structures of next lower level
    for (int i =0; i<8; i++) {
        if (d[i]!=NULL){
            _mm_prefetch((const char*) &(d[i]->pos), _MM_HINT_NTA);
            _mm_prefetch((const char*) d[i]->d,      _MM_HINT_NTA);
        }
    }

    // Do calculations here
    // ...

    // Then descent into next level
    for (int i =0; i<8; i++){
        if (d[i]!=NULL){
            d[i]->walk_tree();
        }
    }
}
```

While calculations on the current level are performed, the CPU can try to cache data for future calculations in idle CPU cycles. This trick can give a performance boost of

up to 20%.

MPI

Parallelising tree codes on distributed memory systems is hard. This is not a shortcoming of the algorithm itself but rather the implementation of interconnect libraries such as MPI. A standard MPI program knows in advance when to send and receive data. This is a reasonable approach for grid based hydrodynamic codes for example, where exactly the same boundary cells have to be transmitted each time-step.

In a tree code, as described above, the situation is different. It is not possible to predict which cells will have to be opened during the calculation of the gravitational force for one particle. Thus, if the cell structures are distributed over many machines, we have to *pull* the required data instantaneously.

With the current implementations of the MPI library, this is not possible without large overhead. Thus, we use a brute force method to do calculations on distributed memory machines.

Each machine holds an exact copy of the entire tree. The tree construction and reconstruction is done on a single node and only the computationally expensive calculations are done in parallel. These include gravity calculation and collision detection.

This kind of parallelisation is limited by the number of particles, as the memory usage of each node scales with $N \log N$. Furthermore, the communication (usually all-to-all and one-to-all) scale also as $N \log N$. Nevertheless, it has proven to be very practical up to $N \sim 10^6 - 10^7$.

D.7 Tests

We begin with testing several conserved quantities. In figure D.4 the amplitude and the centre of epicyclic motion of a test particle in the shearing box are plotted as a function of time. One can see that both quantities are conserved accurately without any asymmetry over many dynamical timescales, as expected for the symplectic integrator. Furthermore, we made sure that the treatment of collisions is working correctly, especially across ghost cell boundaries.

Next, we present a comparison between GravTree and the results obtain by Schmidt et al. (2009). This is a comprehensive sample of runs including of both self-gravity and collisions. In every simulation, the particle density is $\rho = 0.9 \text{ g/cm}^3$, and the box width corresponds to four critical Toomre wavelengths. The coefficient of restitution is 0.5. By changing the optical depth and semi-major axis of the planetary ring, one can sweep through different regimes. Snapshots of the density distribution are plotted in figure D.5. Those should be compared to figure 14.7 in Schmidt et al. (2009).

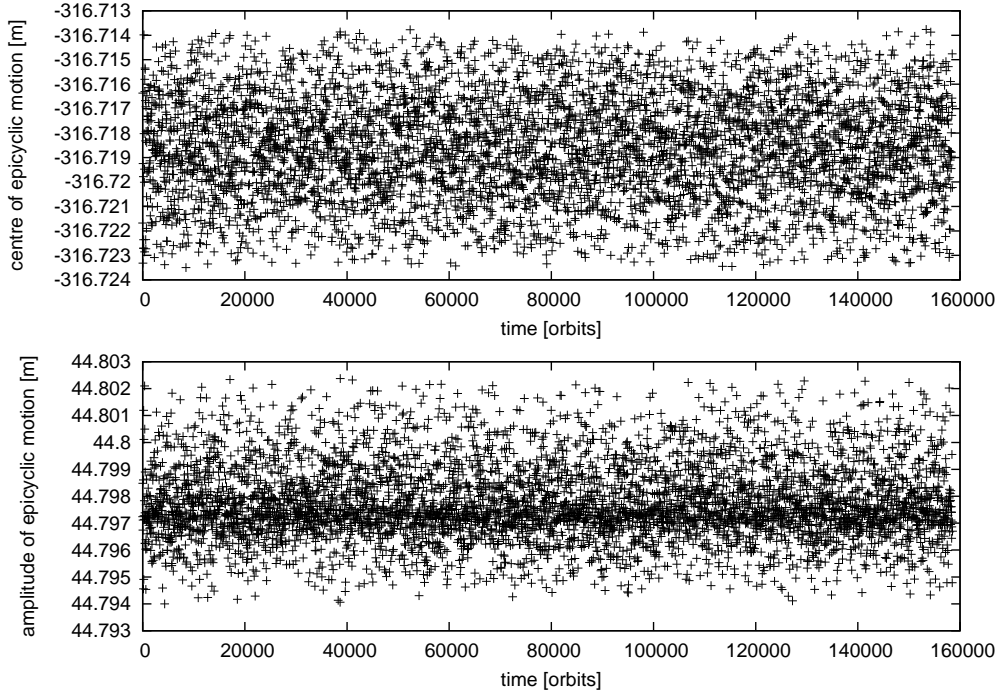


Figure D.4: Conserved quantities in the shearing box. The top panel shows the centre of epicyclic motion relative to the centre of the box. The bottom panel shows the amplitude of epicyclic motion.

One can clearly see different regimes. On the right hand side of the plot, particles clump into aggregates. On the top right boundary, strong gravitational wakes are visible. For $\tau = 1.8$, $a = 70000$ km and simulations close by, viscous overstability can be observed as strong azimuthal structures. Overall, the agreement with Schmidt et al. (2009) is very good. For large a , the simulations performed with GravTree have a trend to form aggregates slightly earlier.

As a further, more quantitative test, we reproduce the results from Daisaka et al. (2001). Therefore, the translational, collisional and gravitational components of the ring viscosity are measured, as defined by equation 19 in said paper. The results are shown in figure D.6 and should be compared to the left hand side of figure 7 in Daisaka et al. (2001). The viscosity is in units of the particle radius and the orbital frequency, the Hill radius (we here use the slightly different convention $r_h = (2m_p/(3M))^{1/3} a$) is normalised by the particle radius. One can see that for small Hill radii (low density particles), the effects of self-gravity are not important. Again, very good agreement with the previous study is achieved.

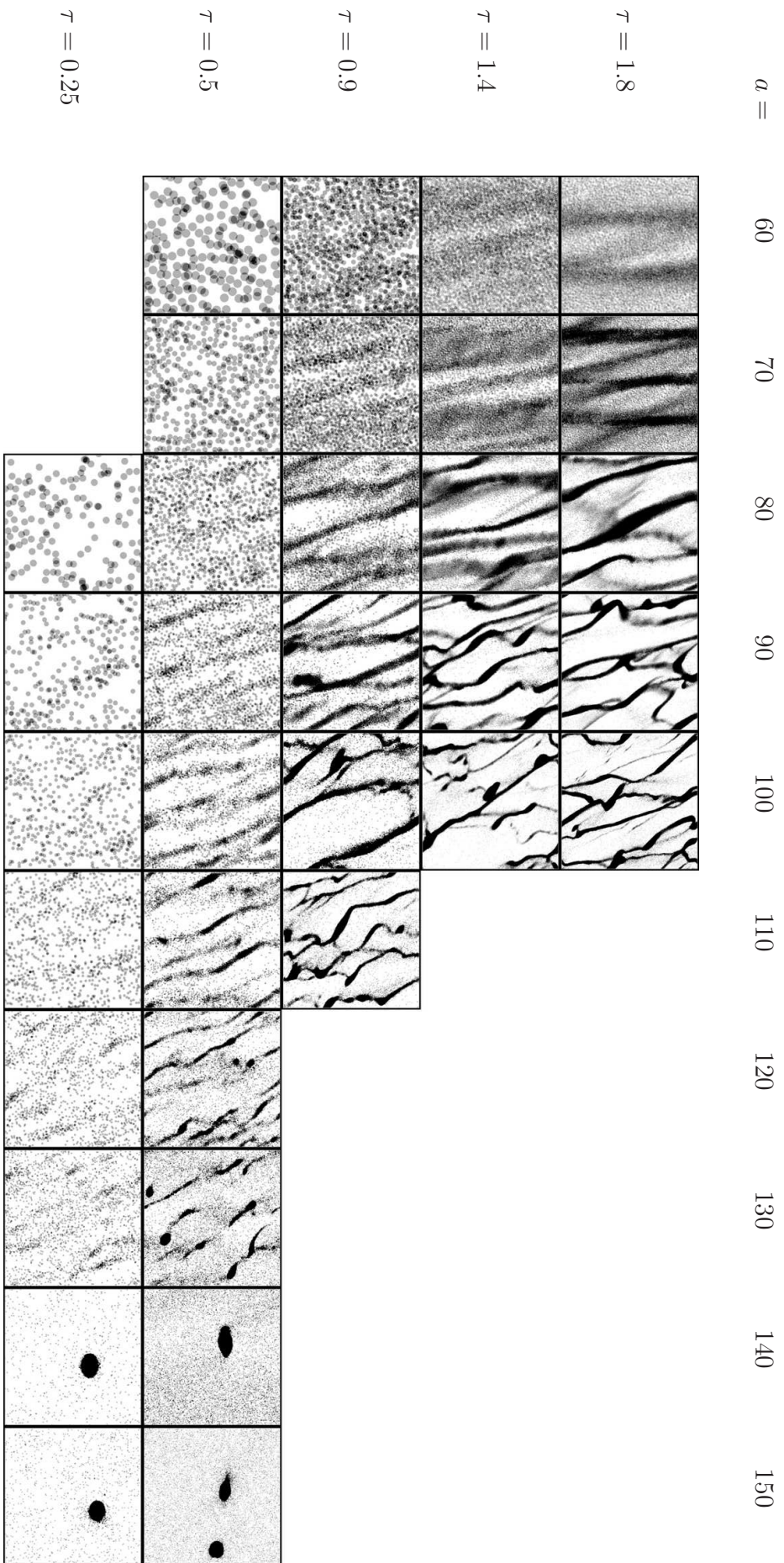


Figure D.5: Dependence of self-gravity wakes on the geometrical optical depth τ and the semi major axis a (in units of 1000km).

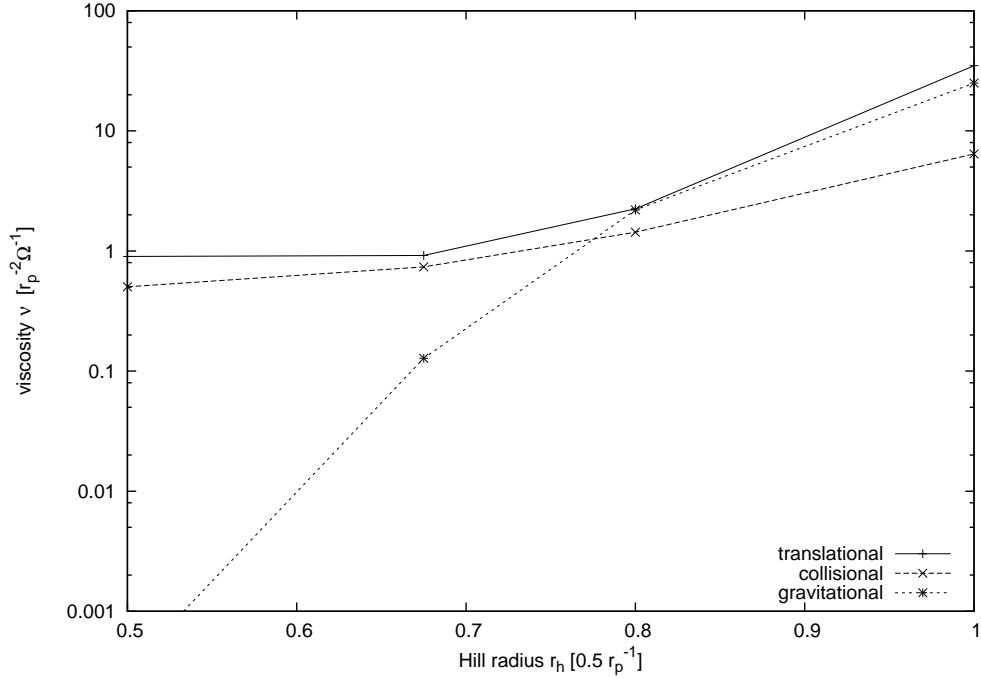


Figure D.6: Translational, collisional and gravitational viscosity components as a function of normalised Hill radius of the ring particles.

D.8 Visualisations

The visualisation of large data sets plays an increasingly important role in the scientific process. GravTree comes with a visualisation module, based on the OpenGL API. It can be used to visualise simulations in real time while they are running or in a standalone playback mode. The real time mode has proven to be especially useful during the development process.

Beside the particle distribution itself, average quantities such as the velocity dispersion and the filling factor can be shown as a transparent overlay. The tree structure can also be plotted. All graphic routines are easily expandable to incorporate any diagnostic that the current project requires. Two screenshots are shown in figures D.7 and D.8.

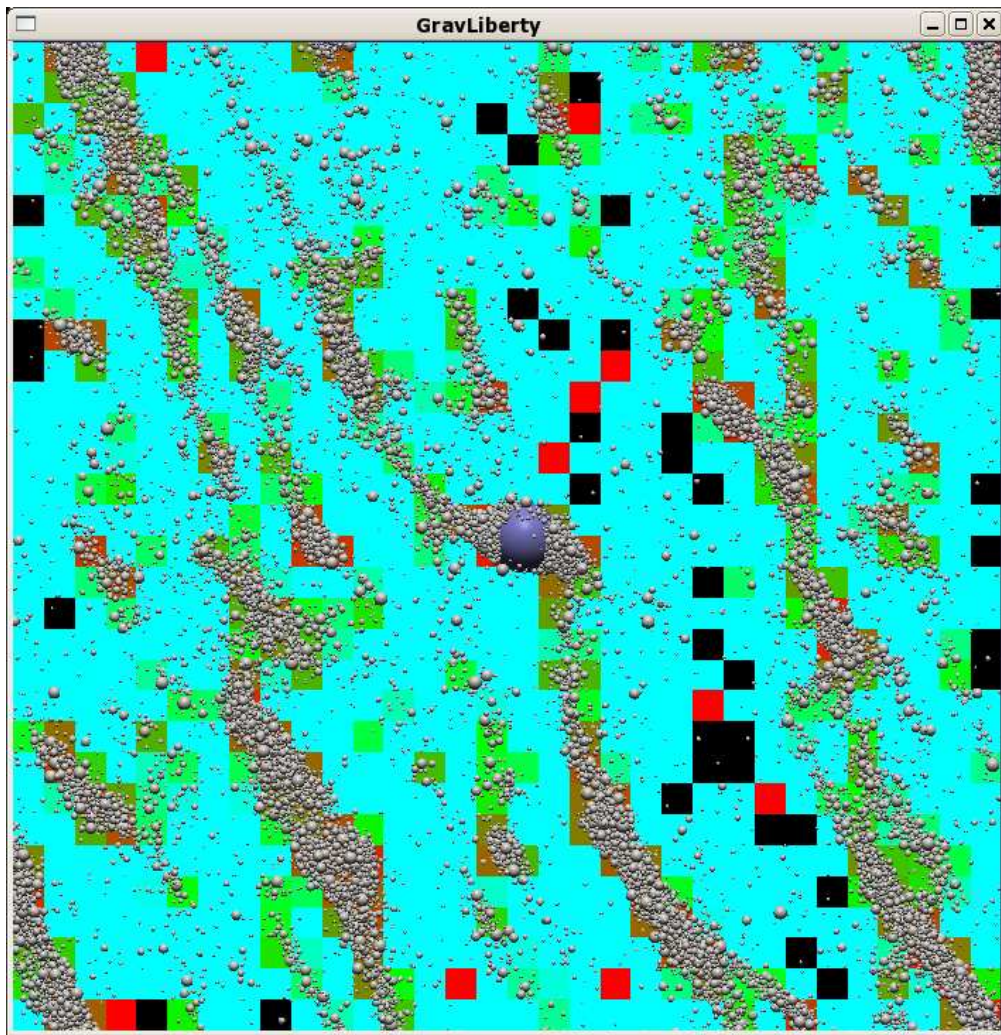


Figure D.7: Screenshot of the OpenGL visualisation module of GravTree, showing a simulation of a moonlet embedded in Saturn's rings. The entire computational domain is shown with an overlay, showing the Toomre Q parameter as coloured squares.

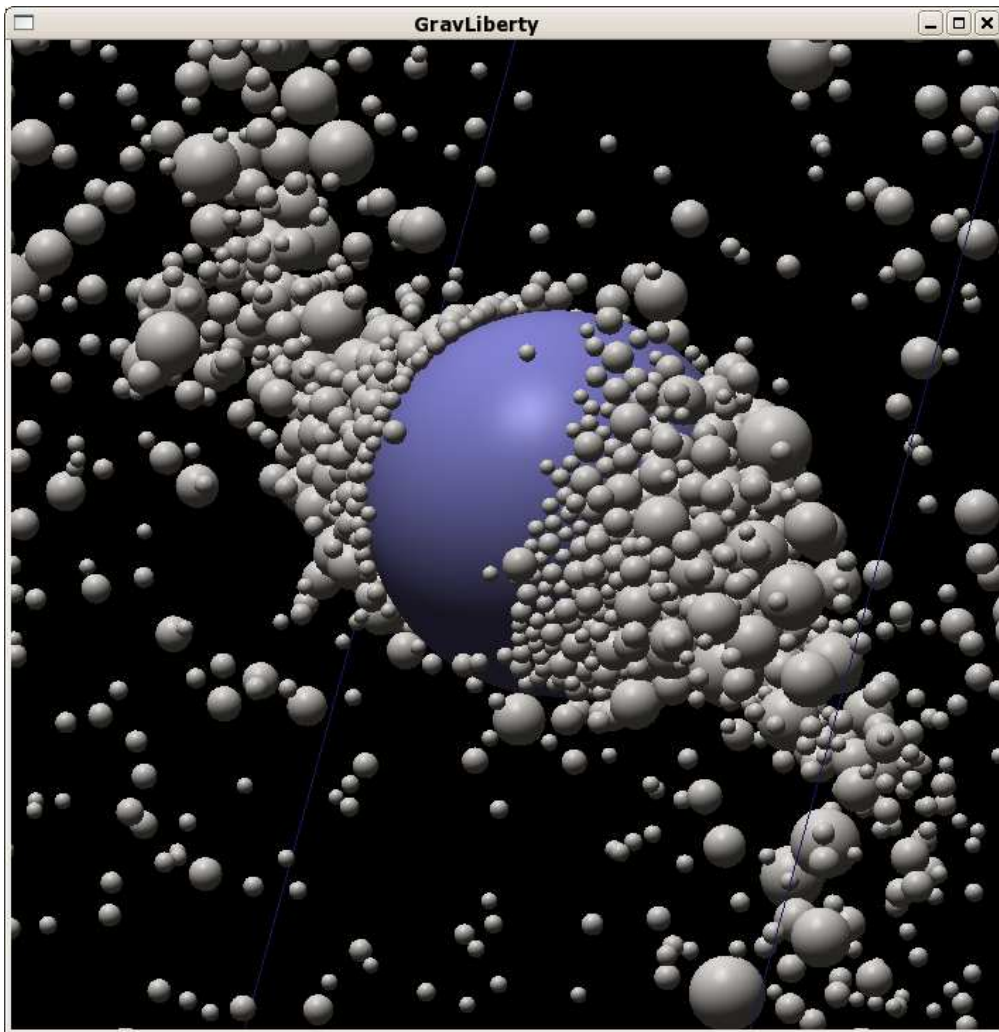


Figure D.8: Screenshot of the OpenGL visualisation module of GravTree, showing a simulation of a moonlet embedded in Saturn's rings. A closeup of the moonlet with particles resting on the moonlet's surface (blue) is shown.

Hydrodynamical simulations with Prometheus

Simulations of planets embedded in an accretion disc have been performed by a large number of authors in recent years. There are two main types of algorithm that can be used to simulate gas dynamics: finite difference methods such as ZEUS (Stone & Norman 1992), NIRVANA (Ziegler & Yorke 1997) and FARGO (Masset 2000) or Godunov methods like RODEO (Paardekooper & Mellema 2006) and ATHENA (Stone et al. 2008). As the name suggests, finite difference codes evaluate partial derivatives with a finite difference approximation. Godunov methods solve (exactly or approximately) a Riemann problem at every cell interface.

In this appendix, the code Prometheus is presented, which is a finite difference code in spherical coordinates, specialised for planet disc interactions. It is similar to the FARGO code but can also run simulations in three dimensions and has a module for solving the full MHD equations. This appendix can not be a comprehensive discussion of finite difference codes in general and merely lists the main concepts and implementation specific features of Prometheus.

Prometheus is written entirely in C and requires no external libraries. It can be compiled with a visualisation module, in which case it has to be linked to OpenGL, GLUT and libpng. Prometheus will be made publicly available at <http://github.com/hannorein/prometheus>.

E.1 Navier-Stokes equations

For many astrophysical processes collisions between gas particles are frequent enough such that a continuum description can be used. Here, the proto-planetary disc is treated as a gas whose motion is described by the Navier-Stokes equations. Although an MHD module has already been written for this code, it is not described here, due to current

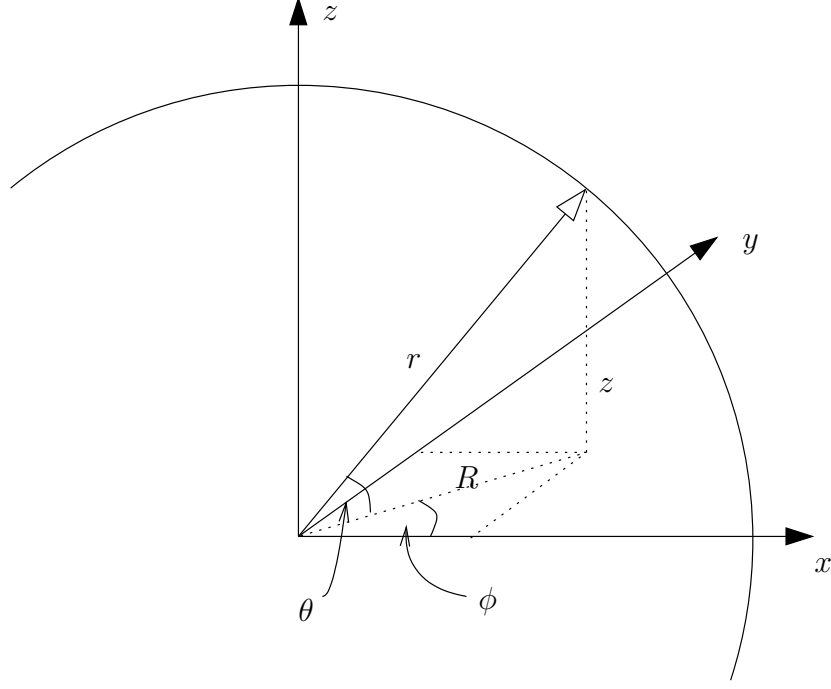


Figure E.1: Spherical coordinate system used in Prometheus

lack of testing and it has also not been used in scientific runs yet. We therefore restrict this discussion to the classical Navier-Stokes equations without magnetic fields, which we list in the following for both two and three dimensions.

E.1.1 Three dimensions

In spherical coordinates as defined in figure E.1, the inviscid Navier-Stokes equations in conservative form are

$$\frac{\partial \rho}{\partial t} + \nabla \cdot (\rho \mathbf{u}) = 0 \quad (\text{E.1})$$

$$\frac{\partial \rho u_r}{\partial t} + \nabla \cdot (\rho u_r \mathbf{u}) = \rho \frac{u_\theta^2 + u_\phi^2}{r} - \frac{\partial p}{\partial r} + \rho a_r \quad (\text{E.2})$$

$$\frac{\partial \rho r u_\theta}{\partial t} + \nabla \cdot (\rho r u_\theta \mathbf{u}) = -\rho \tan \theta u_\phi^2 - \frac{\partial p}{\partial \theta} + \rho a_\theta r \quad (\text{E.3})$$

$$\frac{\partial \rho r u_\phi \cos \theta}{\partial t} + \nabla \cdot (\rho r u_\phi \cos \theta \mathbf{u}) = -\frac{\partial p}{\partial \phi} + \rho a_\phi r \cos \theta. \quad (\text{E.4})$$

Here, ρ is the density, $\mathbf{u} = (u_r, u_\phi, u_\theta)$ the velocity, p the pressure and $\mathbf{a} = (a_r, a_\phi, a_\theta)$ the acceleration due to the star, planets or other forces (e.g. from a rotating coordinate system). The terms on the left hand side describe advection, the terms on the right hand side are source terms. Equations E.1-E.4 are the continuity equation, the radial momentum equation, the meridional momentum equation and the angular momentum equation, respectively. The system of equations is closed with an equation of state,

determining the pressure p . All simulations presented in this thesis use an isothermal equation of state $p = c_s^2 \rho$, where the sound speed c_s might vary with radius.

E.1.2 Two dimensions

One can simplify the equations in the previous section by averaging over the θ component, or z for cylindrical coordinates, to obtain a two dimensional system of equations. The vertically averaged surface density is given as the integral over the density

$$\Sigma(r, \phi) = \int \rho(r, \phi, z) dz. \quad (\text{E.5})$$

Thus, in two dimensional polar coordinates the Navier-Stokes equations can be written as

$$\frac{\partial \Sigma}{\partial t} + \nabla \cdot (\Sigma \mathbf{u}) = 0 \quad (\text{E.6})$$

$$\frac{\partial \Sigma u_r}{\partial t} + \nabla \cdot (\Sigma u_r \mathbf{u}) = \Sigma \frac{u_\phi^2}{r} - \frac{\partial p}{\partial r} + \Sigma a_r \quad (\text{E.7})$$

$$\frac{\partial \Sigma r u_\phi}{\partial t} + \nabla \cdot (\Sigma r u_\phi \mathbf{u}) = - \frac{\partial p}{\partial \phi} + \Sigma a_\phi r. \quad (\text{E.8})$$

Here, \mathbf{u} is the velocity two-vector (u_r, u_ϕ) , sometime also written as (u, v) . Equation E.6 is the two dimensional continuity equation, equation E.7 is the radial momentum equation and equation E.8 is the angular momentum equation.

In general the two dimensional system is a good approximation in planet disc simulations. In two dimensions, a smoothed planet potential is used to simulate the vertical structure of the circum-planetary disc (see equation D.11). The smoothing length b is approximately half the local disc scale height.

E.1.3 Viscosity

Strong physical viscosity is often used to model the effective viscosity resulting from turbulence (see section 1.3.1). This can be achieved by an additional source term in equations E.1-E.4 and E.7-E.8. Here, we restrict ourselves to the two dimensional case in which the additional terms to equations E.7 and E.8 are given by (see e.g. Masset 2002)

$$f_r = \frac{1}{r} \frac{\partial r \tau_{rr}}{\partial r} + \frac{1}{r} \frac{\partial \tau_{r\phi}}{\partial \phi} - \frac{\tau_{\phi\phi}}{r} \quad (\text{E.9})$$

$$f_\phi = \frac{1}{r} \frac{\partial r \tau_{\phi r}}{\partial r} + \frac{1}{r} \frac{\partial \tau_{\phi\phi}}{\partial \phi} + \frac{\tau_{r\phi}}{r}. \quad (\text{E.10})$$

The components of the symmetric viscous stress tensor τ are given by

$$\tau_{rr} = 2\Sigma\nu D_{rr} - \frac{2}{3}\Sigma\nu \nabla\mathbf{u}, \quad (\text{E.11})$$

$$\tau_{\phi\phi} = 2\Sigma\nu D_{\phi\phi} - \frac{2}{3}\Sigma\nu \nabla\mathbf{u} \quad \text{and} \quad (\text{E.12})$$

$$\tau_{r\phi} = \tau_{\phi r} = 2\Sigma\nu D_{r\phi}, \quad (\text{E.13})$$

where we have used

$$D_{rr} = \frac{\partial u_r}{\partial r} \quad (\text{E.14})$$

$$D_{\phi\phi} = \frac{1}{r} \frac{\partial u_\phi}{\partial \phi} + \frac{u_r}{r} \quad (\text{E.15})$$

$$D_{r\phi} = \frac{1}{2} \left(r \frac{\partial (u_\phi/r)}{\partial r} + \frac{1}{r} \frac{\partial u_r}{\partial \phi} \right). \quad (\text{E.16})$$

Here, ν is the shear viscosity and the bulk viscosity has been assumed to be zero. ν can be expressed in terms of the α parameter (Shakura & Syunyaev 1973) via $\alpha = \nu/(c_s^2/\Omega)$, with c_s being the local sound speed and $2\pi/\Omega$ being the orbital period.

E.2 Discretisation

To solve equations E.1-E.4 or E.6-E.8 numerically, we discretise them on a grid. A staggered grid, where the velocities are face-centred and the densities are cell-centred has been used, as illustrated in the two dimensional case in figure E.2. The discretisation is identical to that used in the ZEUS code. A staggered grid has the advantage that spacial derivatives are automatically second order accurate, but does also add some complexity, especially in three dimensions.

In the radial direction, the boundary conditions can be chosen to be either reflecting or damping. In the azimuthal direction, the boundary conditions are periodic. It is also possible to simulate only a wedge of the disc (without any planets). In three dimensions, periodic boundary conditions are used in the θ direction.

E.2.1 Operator splitting

Prometheus makes use of the operator splitting technique, where the equations are solved in small chunks. To do that, a time-step is divided into several sub-time-steps. Figure E.3 illustrates the main loop in Prometheus, including the additional function calls for the MHD module, which are not discussed any further here.

First, the source terms (right hand side of equations E.1-E.4 and E.6-E.8) are added. Then, the advection terms (left hand side of equations E.1-E.4 and E.6-E.8) are solved using the half updated values after the source step, ignoring all terms on the right

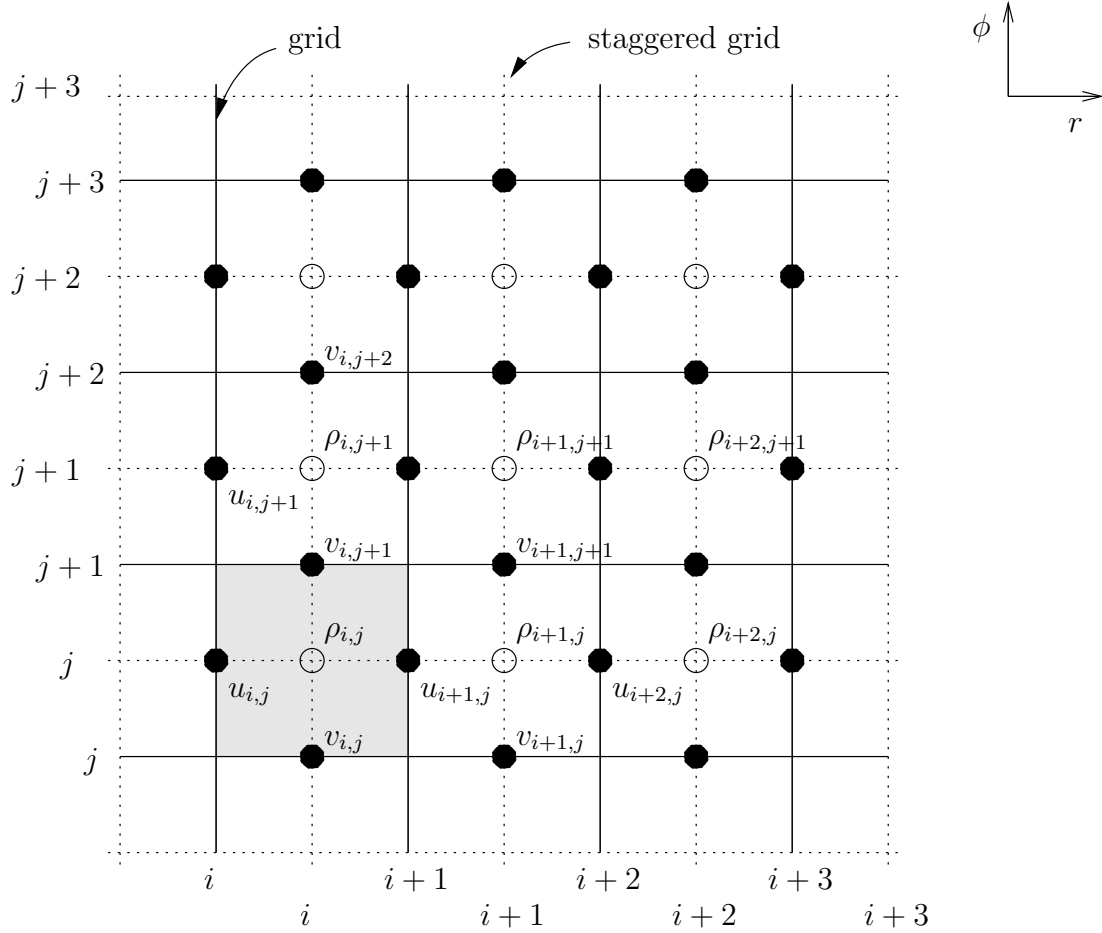


Figure E.2: Discretisation and staggered grid in two dimensions, showing the location of the cell and face centred variables.

hand side. We further use dimensional splitting, solving the advection in the radial, azimuthal and meridional directions consecutively.

This method is only a simplified approximation to the real solution, but has proven to be more accurate than a single time-step. It is (approximately) second order accurate in time. Furthermore, it has the advantage that new physics can be easily incorporated as additional sub-time-steps. In this code we make use of this when an MHD module is added. However, operator splitting can also lead to spurious results in special circumstances, as shown in section E.3.2.

E.2.2 Constrained transport

The transport step is solved using the integral representation of equations E.1-E.4 and E.6-E.8 to ensure conservation of mass and (angular-)momentum up to machine precision. We therefore need to have the fluxes at cell boundaries. There are different ways of estimating the cell faced, time centred flux at each interface, whose discussion goes beyond the scope of this section. In general, higher order methods are less diffusive

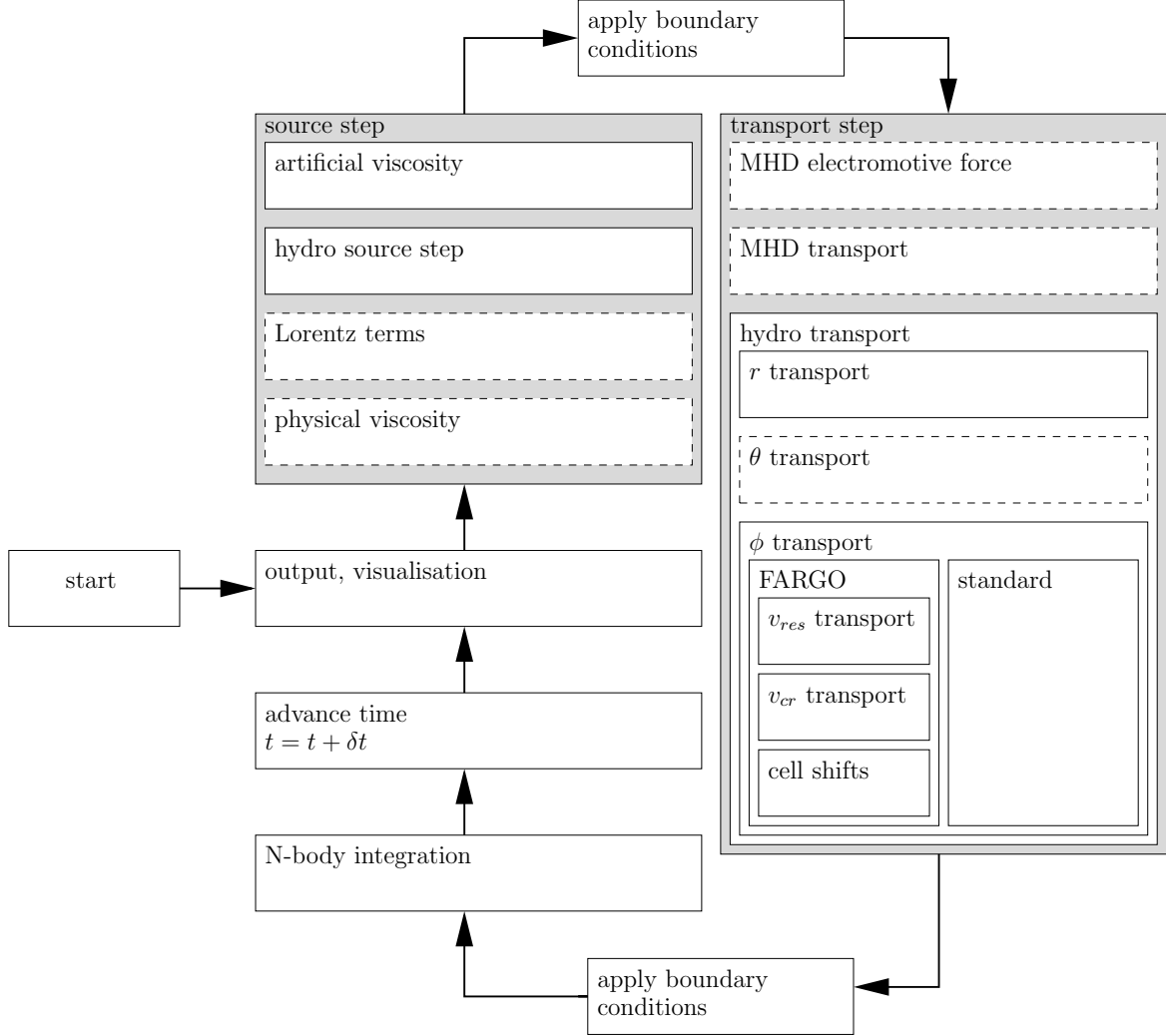


Figure E.3: A full time-step performed by Prometheus. Dashed boxes represent optional modules.

but computationally more expensive. Both the first order donor cell method and the second order van Leer method have been implemented.

Additionally, a concept called constrained transport is used, where the momentum flux calculations are constrained, such that they are consistent with the mass flux. This leads to improved conservation properties. It is physically motivated, as all conserved quantities are advected by the fluid.

E.2.3 Splitting the angular momentum equation

Masset (2000) proposes a method, called FARGO (Fast Advection in Rotating Gaseous Objects), to speed up calculations in which there is a large mean background flow, as it is the case in a sheared accretion disc. The idea is to rewrite the advection terms, the second column in equations E.1-E.4 and E.6-E.8, by replacing the angular velocity

u_ϕ by the sum $\bar{u}_\phi + \hat{u}_\phi + u'_\phi$. We choose \bar{u}_ϕ to be the mean angular velocity of the annulus, rounded such that $\bar{u}_\phi \delta t$ is an integer multiple of the grid spacing $\delta\phi$. \hat{u}_ϕ is the remainder of the rounding operation and thus less or equal than $0.5 \delta\phi/\delta t$. Both \bar{u}_ϕ and \hat{u}_ϕ are independent of ϕ and defined for an annulus with constant r . The residual velocity is given by u'_ϕ . Thus, the contribution from the ϕ component in a generic advection term of the form $\nabla \cdot (a \mathbf{u})$ can be written as

$$\frac{\partial}{\partial\phi} (a (\bar{u}_\phi + \hat{u}_\phi + u'_\phi)) = \underbrace{\bar{u}_\phi \frac{\partial}{\partial\phi} (a)}_{(a)} + \underbrace{\hat{u}_\phi \frac{\partial}{\partial\phi} (a)}_{(b)} + \underbrace{\frac{\partial}{\partial\phi} (a u'_\phi)}_{(c)}, \quad (\text{E.17})$$

where a can be any quantity. The term (c) is just like the old advection term, but with a different velocity, as if we were in a rotating frame. The terms (a) and (b) can be interpreted as a simple shift. Because we've chosen \bar{u}_ϕ such that $\bar{u}_\phi/\delta t$ is an integer multiple of the grid spacing $\delta\phi$, the term (a) corresponds to shifting the whole ring of cells, which is numerically very inexpensive. Because $|u'_\phi| \ll |u_\phi|$ and $|\hat{u}_\phi| \ll |u_\phi|$ the time-step constraint arising from the CFL condition allows us now to use much larger time-steps and the terms (b) and (c) can be solved using a standard advection algorithm. The splitting of the advection term gives an efficiency boost of a factor ~ 10 , in a typical simulation.

E.3 Tests

E.3.1 Shock-tube problems

Shock-tube problems are a standard test in numerical codes (see e.g. Stone & Norman 1992). Even though these test are in general not very thorough and easy to pass, we present a one dimensional example in Cartesian geometry, mainly for comparison with a low Mach number shock in section E.3.2.

The Mach number of the shock front is $v/c_s = 2.9$. An equidistantly spaced grid with 256 grid points, a CFL condition of 0.5 and a sound speed of $c_s = 0.05$ is used. The density profile after $t = 10$ together with the analytic solution is plotted in figure E.4. One can see that the artificial viscosity smears out the discontinuity over several grid cells. Furthermore, the rarefaction wave results in some undershooting. These effects are expected and present in any finite difference code.

E.3.2 Dispersion error

Finite difference codes are known to have a numerical dispersion error because they do not, contrary to Godunov methods, solve the equations along wave characteristics. The fluid equations are solved using operator splitting. Each part, namely the source

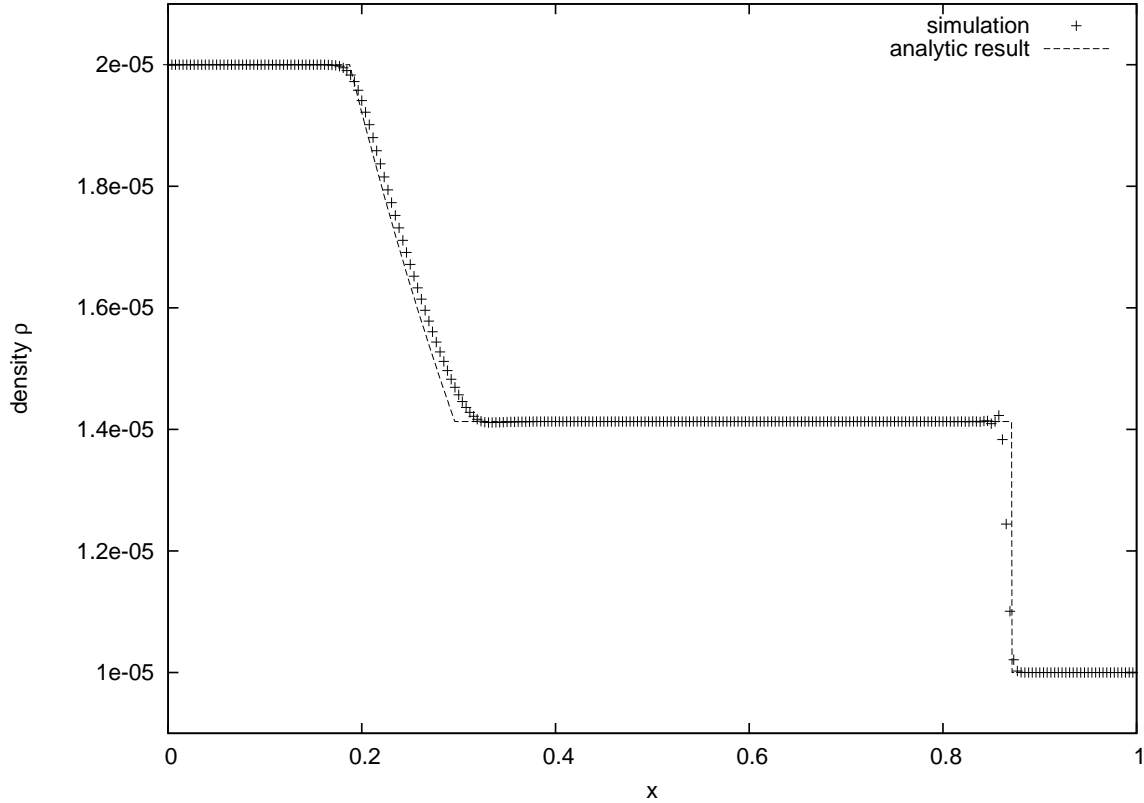


Figure E.4: Density profile for a strong shock-tube problem at time $t = 10$ with Mach number $v/c = 2.9$.

and transport step, are evaluated successively. Propagating sound waves involve both operators. The advection of a passive scalar, contrariwise, requires only one operator.

In most situations, this does not create any problems, as the error associated with the operator splitting is small and mostly affects the highest frequency modes which appear on the grid scale. However, if there is a discontinuity in the flow, large frequencies are present that can lead to a large dispersion error. For supersonic shocks, the artificial viscosity takes care of this, by smearing out discontinuities over a few grid cells, as shown in section E.3.1. For low amplitude, *subsonic* shocks this might not be the case. The shock behaves like a travelling wave package, where the package includes a discontinuity.

Unfortunately, we are exactly in this situation for a low mass planet being embedded in an accretion disc. The wake of the planet contains a discontinuity and its amplitude depends on the planet's mass. For sufficiently small masses, the discontinuity becomes subsonic and we expect noticeable numerical dispersion to occur. Since the wake is stationary in a frame co-rotating with the planet, the result will also be a stationary pattern.

In the following, we will first illustrate the problem with a shock tube test in a Cartesian box. We will then show that the same pattern appears in simulations of

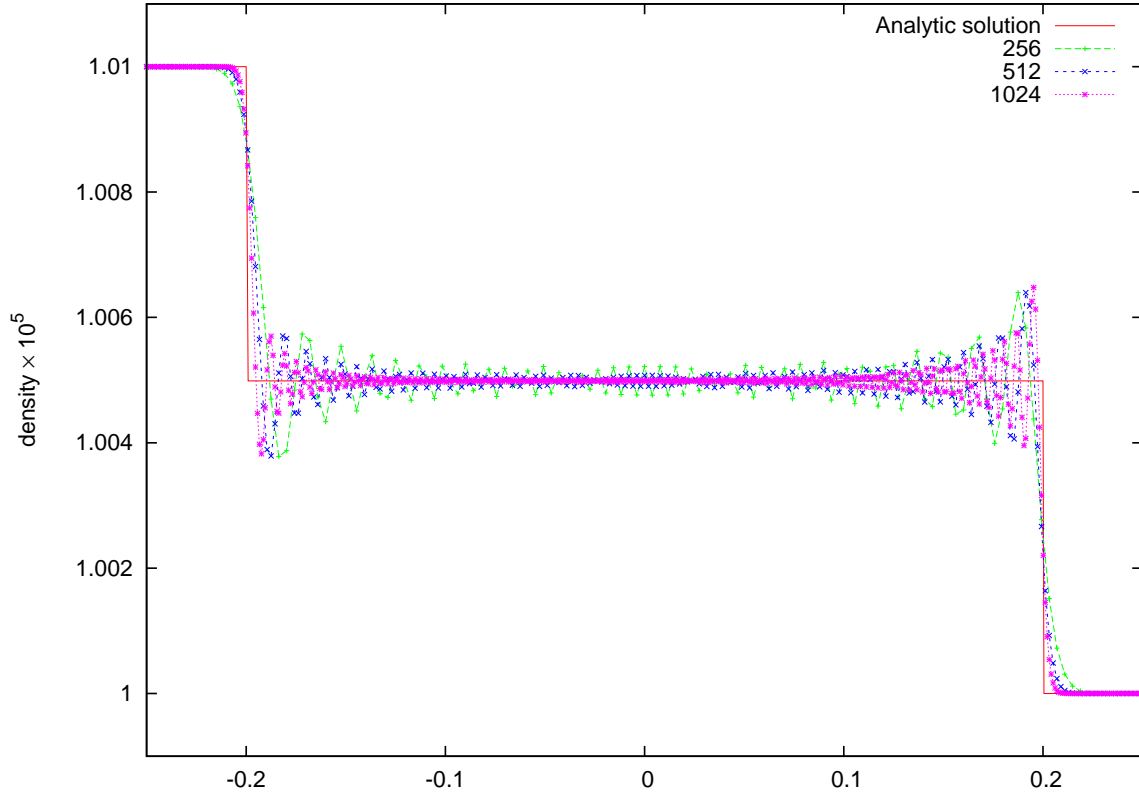


Figure E.5: Density profiles for different grid resolutions in the isothermal ($c_s = 0.05$) shock-tube problem at time $t = 4$. The initial density perturbation is 1%.

low mass planets and outline possible solutions such as physical viscosity and Godunov methods.

Low Mach number shock-tube tests

We set up a simple test problem that shows the problematic behaviour. We work in a Cartesian grid with resolutions 256×256 , 512×512 and 1024×1024 and use an isothermal equation of state with sound speed $c_s = 0.05$ in dimensionless units. The box has periodic boundary conditions and we set up a shock-tube problem by increasing the density in the left part of the box by 1%. The analytic solution after $t = 4$ is plotted as a solid line in figure E.5. Due to the low amplitude of the initial perturbation, the waves are basically sound packages travelling at the speed of sound, i.e. the rarefaction wave is very steep. Large ringing can be observed in the numerical solutions, which are also plotted in figure E.5. This is because the numerical dispersion error is largest for the smallest wavelength. As expected for a Gibbs-like phenomenon, the over and under-shoots do not die out with increasing resolution. However, they get more concentrated near the discontinuity.

Note that in all simulations, the Neumann and Richtmyer artificial viscosity is

switched on. The artificial viscosity does not kill the overshoots as it is quadratic in the velocities. This is reasonable approach in strong shocks (Stone & Norman 1992, section E.3.1). However, the velocity perturbations are very small compared to the sound speed in this case.

Low mass planets

A similar phenomenon can be observed in simulations of planet disc interactions. All integrations were performed with Prometheus. The results have been confirmed with a variety of codes (FARGO, NIRVANA and RH2D) and do not depend on the implementation.

The phenomenon is stronger for low mass planets, as the shocks that appear in the wake are weaker and eventually become subsonic. Therefore, a planet with a very low mass of $m_p = 1.26 \cdot 10^{-6} M_\odot = 0.42 M_{\text{earth}}$ is used in these simulations. The cylindrical grid is spaced equidistantly in the radial direction and has a resolution of 128x384. We plot the surface density contours of one simulation with and without physical viscosity in figure E.6. We over-plot the analytic position of the wake (Ogilvie & Lubow 2002).

One can clearly see that there are over-shootings occurring, similar to those discussed above. Including a small amount of physical viscosity smears out the phenomenon. Increasing the resolution also helps to reduce the strength of the over-shootings. Numerical diffusion becomes more important if more grid cells, and therefore also a smaller time-step, are used.

For reasonable resolutions ($N_\phi > 512$), the torque on the planet is not significantly affected by this effect for two reasons. Firstly, the over-shootings appear a few scale heights away from the planet. Secondly, the gravitational torque from the over and under-shootings cancel and give almost no net effect. However, note that this is not necessarily the case for multi planetary systems or situations in which the saturation of co-rotation torques plays an important role (Paardekooper & Papaloizou 2009). In those cases, finite difference codes should only be used with great care and possibly with explicit physical viscosity.

The phenomenon described here does not occur in Godunov codes such as RODEO (S.-J. Paardekooper, private communication). This is expected, as those schemes do solve the hydrodynamical equations along characteristics and therefore do not have a dispersion error.

E.3.3 Planet torques

As a further test, we calculate the torques for low mass planets in various disc models. A planet mass of $q = 1.26 \cdot 10^{-5}$ and a smoothing length of $b = 0.6$ is used, so that the

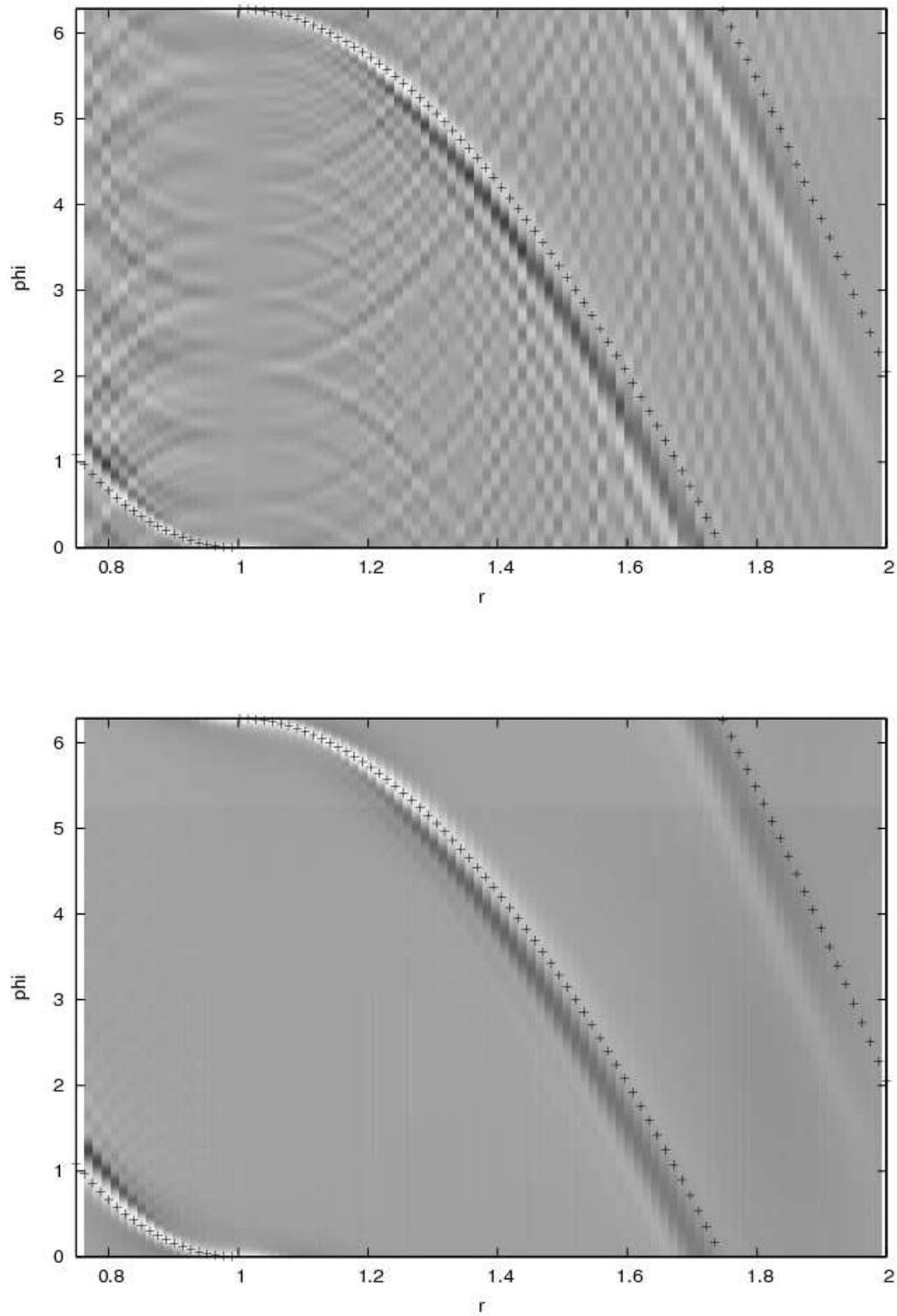


Figure E.6: Surface density after 10 orbits in simulations with a resolution of 128x384. The simulation on the top uses no physical viscosity, whereas the simulation on the bottom uses $\nu = 2 \cdot 10^{-5}$.

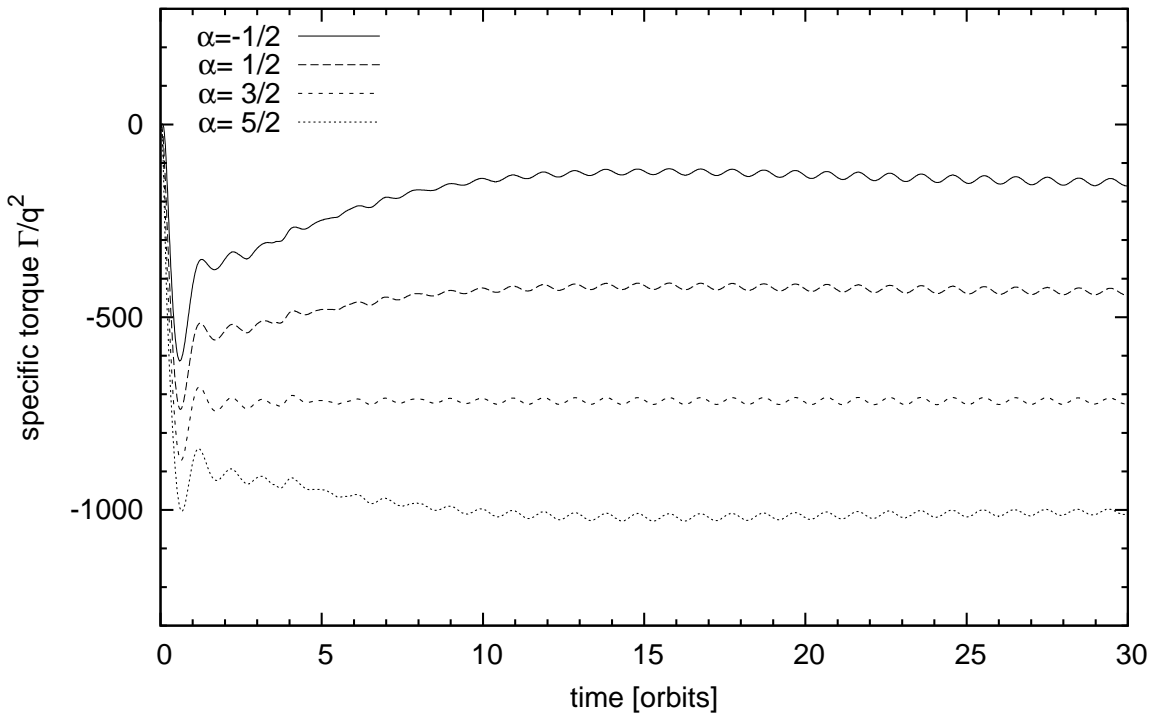


Figure E.7: Specific torque felt by a planet with mass $q = 1.26 \cdot 10^{-5}$ in an inviscid disc with varying surface density slope α . The results are in good agreement with Paardekooper & Papaloizou (2009).

simulations can be easily compared to those performed by Paardekooper & Papaloizou (2009). We first test the two dimensional version of Prometheus without physical viscosity. The specific torque $\Gamma = |\mathbf{f} \times \mathbf{r}|$ felt by the planet is plotted in figure E.7, normalised by the square of the planet mass ratio time the disc surface density for four different surface density profiles with slope α . It can be seen by comparing figure E.7 to figure 7 in Paardekooper & Papaloizou (2009) that the measured torques (and therefore the migration rates) are in very good agreement. In particular the case $\alpha = 3/2$ is in accord with linear theory (since it does not vary on a libration timescale). The long term trend visible towards the end of the simulation is due to different boundary conditions used (damping).

E.3.4 Planet disc interaction in three dimensions

We now go on and test a three dimensional simulation of planet disc interaction. Therefore, the results from Prometheus are compared to those of Kley et al. (2009).

A 20 Earth mass planet is set up on an eccentric and inclined orbit ($e = 0.2$, $i = 5^\circ$) and embedded in a stratified, three dimensional disc. The disc mass in the computational domain ($r = 0.4 \dots 2.5$) is $0.01 M_\odot$ and the aspect ratio of the disc is 0.05. The grid resolution used is $128 \times 384 \times 34$. We use no viscosity and a planet potential which

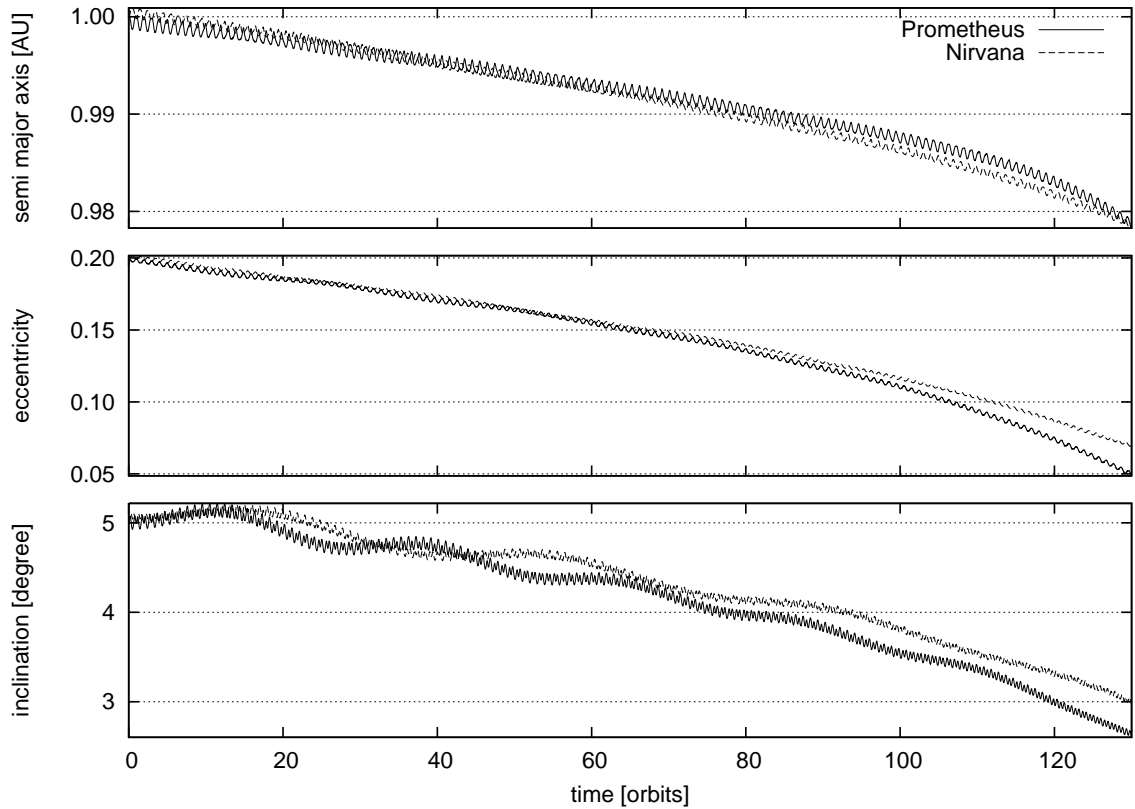


Figure E.8: Orbital parameters of a planet embedded in a three dimensional disc. The solid curves have been obtained with Prometheus, the dashed curves have been obtained with Nirvana by Kley et al. (2009).

is smoothed over a fraction (0.43) of a scale height. Note that this is a slightly different setup, compared to Kley et al. (2009).

Both, the results from Prometheus and those of Kley et al. (2009) are plotted in figure E.8. They are in good agreement and show only some small variation at large times.

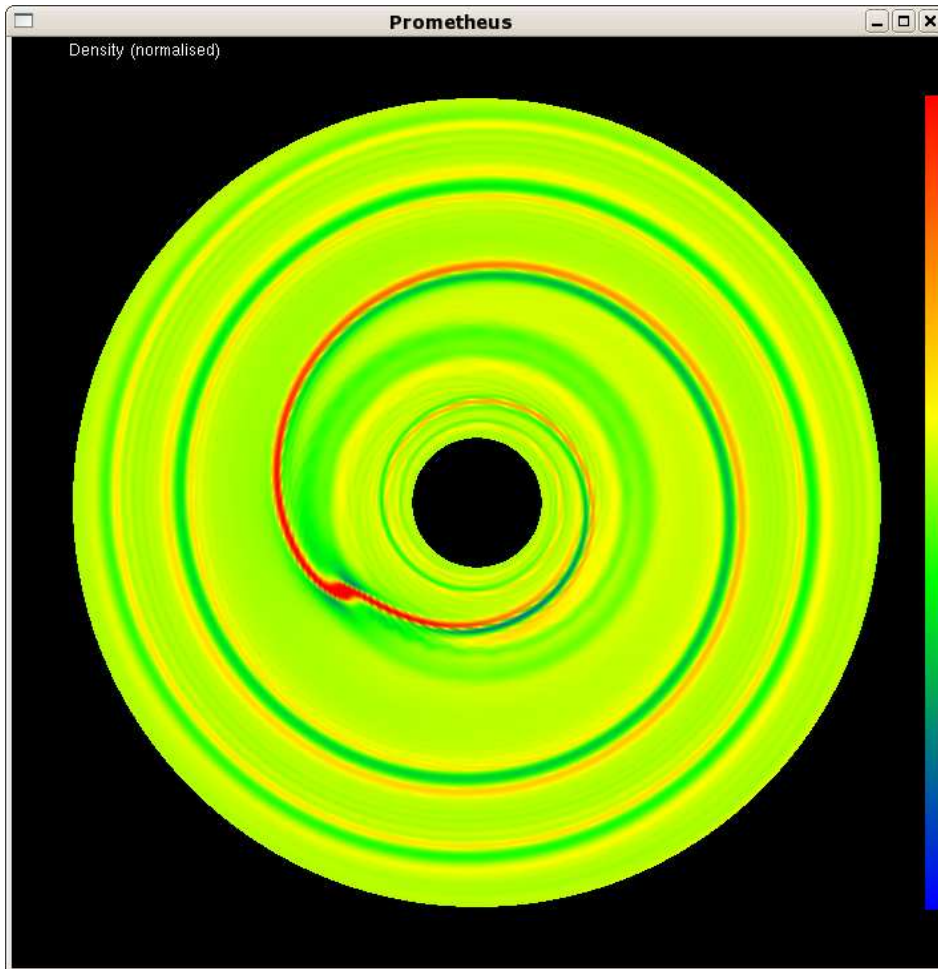


Figure E.9: Screenshot of the OpenGL visualisation module of Prometheus, showing the surface density in a two dimensional simulation with an embedded planet.

E.4 Visualisations

Similar to the visualisation module presented in appendix D, Prometheus comes with a visualisation module, based on the OpenGL API. It can be used to visualise simulations in real time while they are running or in a standalone playback mode. Standard quantities, such as density, velocity, divergence of velocity and vorticity can be plotted in both, two and three dimensional simulations in either a cylindrical/spherical or Cartesian representation. Two screenshots are shown in figures E.9 and E.10.

The visualisation module is also easily adaptable to allow for direct user interaction with the simulation. For example, this can be used to add perturbations or additional planets to the simulation and watch the simulation change instantaneously. This provides an astonishing new way to easily understand physical phenomena.

Furthermore, an iPhone version of Prometheus is available on the Apple AppStore at <http://itunes.apple.com/us/app/hydro/id341643251?mt=8>.

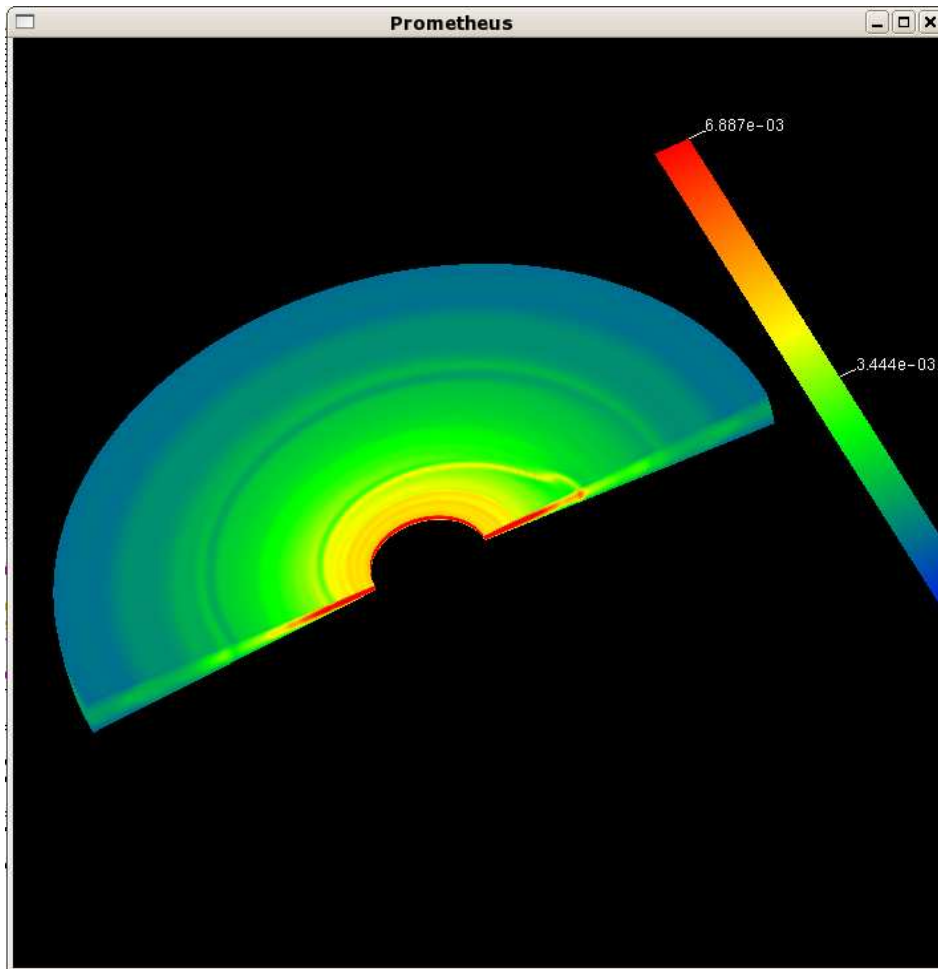


Figure E.10: Screenshot of the OpenGL visualisation module of Prometheus, showing the density in a three dimensional simulation of a stratified proto-planetary disc with an embedded planet.

Bibliography

- Adams, F. C. & Bloch, A. M. 2009, *ApJ*, 701, 1381
- Adams, F. C., Laughlin, G., & Bloch, A. M. 2008, *ApJ*, 683, 1117
- Alexander, R. D., Clarke, C. J., & Pringle, J. E. 2006, *MNRAS*, 369, 229
- Anderson, D. R., Hellier, C., Gillon, M., et al. 2010, *ApJ*, 709, 159
- Balbus, S. A. & Hawley, J. F. 1991, *ApJ*, 376, 214
- Barge, P. & Sommeria, J. 1995, *A&A*, 295, L1
- Barnes, J. & Hut, P. 1986, *Nature*, 324, 446
- Blum, J. & Wurm, G. 2008, *ARA&A*, 46, 21
- Bodenheimer, P. & Pollack, J. B. 1986, *Icarus*, 67, 391
- Bond, I. A., Udalski, A., Jaroszynski, M., et al. 2004, *The Astrophysical Journal*, 606, L155
- Boss, A. P. 2001, *ApJ*, 563, 367
- Bridges, F. G., Hatzes, A., & Lin, D. N. C. 1984, *Nature*, 309, 333
- Brouwer, D. & Clemence, G. M. 1961, *Methods of celestial mechanics* (New York: Academic Press, 1961)
- Chauvin, G., Lagrange, A.-M., Dumas, C., et al. 2004, *A&A*, 425, L29
- Chiang, E. & Youdin, A. 2009, *ArXiv e-prints*
- Chiang, E. I. & Goldreich, P. 1997, *ApJ*, 490, 368
- Correia, A. C., Udry, S., Mayor, M., et al. 2008, *â*
- Cresswell, P. & Nelson, R. P. 2008, *A&A*, 482, 677
- Crida, A. 2009, *ApJ*, 698, 606
- Crida, A., Baruteau, C., Kley, W., & Masset, F. 2009, *A&A*, 502, 679

- Crida, A., Papaloizou, J. C. B., Rein, H., Charnoz, S., & Salmon, J. 2010, ArXiv e-prints
- Crida, A., Sándor, Z., & Kley, W. 2008, A&A, 483, 325
- Cumming, A., Butler, R. P., Marcy, G. W., et al. 2008, PASP, 120, 531
- Cuzzi, J. N., Dobrovolskis, A. R., & Champney, J. M. 1993, Icarus, 106, 102
- Cuzzi, J. N., Hogan, R. C., & Shariff, K. 2008, ApJ, 687, 1432
- Daisaka, H., Tanaka, H., & Ida, S. 2001, Icarus, 154, 296
- de Val-Borro, M., Edgar, R. G., Artymowicz, P., et al. 2006, MNRAS, 370, 529
- Desch, S. J. 2007, ApJ, 671, 878
- Enoch, M. L., Evans, II, N. J., Sargent, A. I., et al. 2008, ApJ, 684, 1240
- Fabrycky, D. & Tremaine, S. 2007, ApJ, 669, 1298
- Fehlberg, E. 1969, Low-order Classical Runge-Kutta Formulas with Step-size Control and Their Application to Some Heat Transfer Problems (NASA)
- Fromang, S. & Papaloizou, J. 2006, A&A, 452, 751
- Fromang, S. & Papaloizou, J. 2007, A&A, 476, 1113
- Fromang, S., Papaloizou, J., Lesur, G., & Heinemann, T. 2007, A&A, 476, 1123
- Gammie, C. F. 1996, ApJ, 457, 355
- Goldreich, P. 1965, MNRAS, 130, 159
- Goldreich, P. & Tremaine, S. 1979, ApJ, 233, 857
- Goldreich, P. & Tremaine, S. 1980, ApJ, 241, 425
- Goldreich, P. & Tremaine, S. 1982, ARA&A, 20, 249
- Goldreich, P. & Ward, W. R. 1973, ApJ, 183, 1051
- Hayashi, C. 1981, Progress of Theoretical Physics Supplement, 70, 35
- Hayashi, C., Nakazawa, K., & Adachi, I. 1977, PASJ, 29, 163
- Ida, S. & Lin, D. N. C. 2004, ApJ, 604, 388
- Johansen, A., Henning, T., & Klahr, H. 2006, ApJ, 643, 1219
- Johansen, A., Oishi, J. S., Low, M.-M. M., et al. 2007, Nature, 448, 1022
- Johansen, A., Youdin, A., & Mac Low, M. 2009, ApJ, 704, L75
- Kalas, P., Graham, J. R., Chiang, E., et al. 2008, Science, 322, 1345
- Kasdin, N. J. 1995, Proceedings of the IEEE, 83

- Kipping, D. M., Fossey, S. J., & Campanella, G. 2009, *MNRAS*, 400, 398
- Kley, W., Bitsch, B., & Klahr, H. 2009, *A&A*, 506, 971
- Kley, W., Peitz, J., & Bryden, G. 2004, *A&A*, 414, 735
- Knutson, H. A., Charbonneau, D., Allen, L. E., et al. 2007, *Nature*, 447, 183
- Konacki, M., Torres, G., Jha, S., & Sasselov, D. D. 2003, *Nature*, 421, 507
- Laughlin, G., Steinacker, A., & Adams, F. C. 2004, *ApJ*, 608, 489
- Lee, M. H. & Peale, S. J. 2001, in *Bulletin of the American Astronomical Society*, Vol. 33, *Bulletin of the American Astronomical Society*, 1198
- Lee, M. H. & Peale, S. J. 2002, *ApJ*, 567, 596
- Lesur, G. & Papaloizou, J. C. B. 2009, *ArXiv e-prints*
- Lewis, M. C. & Stewart, G. R. 2009, *Icarus*, 199, 387
- Lin, D. N. C. & Papaloizou, J. 1986, *ApJ*, 309, 846
- Lucy, L. B. 1977, *AJ*, 82, 1013
- Lyra, W., Johansen, A., Klahr, H., & Piskunov, N. 2009, *A&A*, 493, 1125
- Malhotra, R. 1993, *Icarus*, 106, 264
- Masset, F. 2000, *A&AS*, 141, 165
- Masset, F. & Snellgrove, M. 2001, *MNRAS*, 320, L55
- Masset, F. S. 2002, *A&A*, 387, 605
- Masset, F. S. & Papaloizou, J. C. B. 2003, *ApJ*, 588, 494
- Mayor, M., Bonfils, X., Forveille, T., et al. 2009, *A&A*, 507, 487
- Mayor, M. & Queloz, D. 1995, *Nature*, 378, 355
- Michikoshi, S., Inutsuka, S.-i., Kokubo, E., & Furuya, I. 2007, *ApJ*, 657, 521
- Michikoshi, S., Kokubo, E., & Inutsuka, S.-i. 2009, *ApJ*, 703, 1363
- Mizuno, H. 1980, *Progress of Theoretical Physics*, 64, 544
- Morishima, R. & Salo, H. 2006, *Icarus*, 181, 272
- Murray, C. D. & Dermott, S. F. 2000, *Solar System Dynamics* (Cambridge University Press)
- Nagasawa, M., Ida, S., & Bessho, T. 2008, *ApJ*, 678, 498
- Nelson, R. P. 2005, *A&A*, 443, 1067
- Nelson, R. P. & Papaloizou, J. C. B. 2002, *MNRAS*, 333, L26

- Nelson, R. P. & Papaloizou, J. C. B. 2004, MNRAS, 350, 849
- Nelson, R. P., Papaloizou, J. C. B., Masset, F., & Kley, W. 2000, MNRAS, 318, 18
- Ogilvie, G. I. & Lubow, S. H. 2002, MNRAS, 330, 950
- Oishi, J. S., Mac Low, M.-M., & Menou, K. 2007, ApJ, 670, 805
- Paardekooper, S., Baruteau, C., Crida, A., & Kley, W. 2010, MNRAS, 401, 1950
- Paardekooper, S. & Mellema, G. 2006, A&A, 450, 1203
- Paardekooper, S. & Papaloizou, J. C. B. 2009, MNRAS, 394, 2283
- Papaloizou, J. C. B. 2003, Celestial Mechanics and Dynamical Astronomy, 87, 53
- Papaloizou, J. C. B. & Szuszkiewicz, E. 2005, MNRAS, 363, 153
- Papaloizou, J. C. B. & Terquem, C. 1999, ApJ, 521, 823
- Papaloizou, J. C. B. & Terquem, C. 2006, Reports of Progress in Physics, 69, 119
- Pepliński, A., Artymowicz, P., & Mellema, G. 2008a, MNRAS, 386, 164
- Pepliński, A., Artymowicz, P., & Mellema, G. 2008b, MNRAS, 386, 179
- Pepliński, A., Artymowicz, P., & Mellema, G. 2008c, MNRAS, 387, 1063
- Pierens, A. & Nelson, R. P. 2008, A&A, 482, 333
- Pollack, J. B., Hubickyj, O., Bodenheimer, P., et al. 1996a, Icarus, 124, 62
- Pollack, J. B., Hubickyj, O., Bodenheimer, P., et al. 1996b, Icarus, 124, 62
- Porco, C. C., Thomas, P. C., Weiss, J. W., & Richardson, D. C. 2007, Science, 318, 1602
- Press, W. et al. 1992, Numerical recipes in C (Cambridge University Press Cambridge)
- Pringle, J. E. 1981, ARA&A, 19, 137
- Quinn, T., Perrine, R. P., Richardson, D. C., & Barnes, R. 2010, AJ, 139, 803
- Rein, H. & Papaloizou, J. C. B. 2009, A&A, 497, 595
- Rein, H., Papaloizou, J. C. B., & Kley, W. 2010, A&A, 510, A260000+
- Rivera, E. J., Lissauer, J. J., Butler, R. P., et al. 2005, ApJ, 634, 625
- Sándor, Z. & Kley, W. 2006, A&A, 451, L31
- Sano, T., Miyama, S. M., Umebayashi, T., & Nakano, T. 2000, ApJ, 543, 486
- Sasselov, D. D. & Lecar, M. 2000, ApJ, 528, 995

- Schmidt, J., Ohtsuki, K., Rappaport, N., Salo, H., & Spahn, F. 2009, Dynamics of Saturn's Dense Rings, ed. Dougherty, M. K., Esposito, L. W., & Krimigis, S. M., 413–458
- Schneider, J. 2010, <http://exoplanet.eu>
- Seiß, M., Spahn, F., Sremčević, M., & Salo, H. 2005, *Geophys. Res. Lett.*, 32, 11205
- Shakura, N. I. & Syun'yaev, R. A. 1973, *A&A*, 24, 337
- Sinclair, A. T. 1975, *MNRAS*, 171, 59
- Snellgrove, M. D., Papaloizou, J. C. B., & Nelson, R. P. 2001, *A&A*, 374, 1092
- Spahn, F. & Sremčević, M. 2000, *A&A*, 358, 368
- Sremčević, M., Spahn, F., & Duschl, W. J. 2002, *MNRAS*, 337, 1139
- Stewart, S. T. & Leinhardt, Z. M. 2009, *ApJ*, 691, L133
- Stoer, J. & Bulirsch, R. 2002, *Introduction to Numerical Analysis* (Springer)
- Stone, J. M., Gardiner, T. A., Teuben, P., Hawley, J. F., & Simon, J. B. 2008, *ApJS*, 178, 137
- Stone, J. M. & Norman, M. L. 1992, *ApJS*, 80, 753
- Tanaka, H., Takeuchi, T., & Ward, W. R. 2002, *ApJ*, 565, 1257
- Tanga, P., Weidenschilling, S. J., Michel, P., & Richardson, D. C. 2004, *A&A*, 427, 1105
- Tiscareno, M. S., Burns, J. A., Hedman, M. M., & Porco, C. C. 2008, *AJ*, 135, 1083
- Tiscareno, M. S., Burns, J. A., Hedman, M. M., et al. 2006, *Nature*, 440, 648
- Tiscareno, M. S., Burns, J. A., Sremčević, M., et al. 2010, *ApJ*, 718, L92
- Toomre, A. 1964, *ApJ*, 139, 1217
- Vogt, S. S., Butler, R. P., Marcy, G. W., et al. 2005, *ApJ*, 632, 638
- Ward, W. R. 1997, *Icarus*, 126, 261
- Weidenschilling, S. J. 1977a, *MNRAS*, 180, 57
- Weidenschilling, S. J. 1977b, *Ap&SS*, 51, 153
- WGESP. 2003, <http://www.dtm.ciw.edu/boss/definition.html>
- Wisdom, J. & Tremaine, S. 1988, *AJ*, 95, 925
- Wolszczan, A. & Frail, D. A. 1992, *Nature*, 355, 145
- Wuchterl, G. 1993, *Icarus*, 106, 323
- Youdin, A. N. & Goodman, J. 2005, *ApJ*, 620, 459
- Ziegler, U. & Yorke, H. W. 1997, *Computer Physics Communications*, 101, 54

